Marine productivity estimates from dissolved gas measurements in the Southern Ocean

by

Karel Castro Morales

Thesis submitted in fulfilment of the requirements
for the degree of

Doctor of Philosophy

University of East Anglia
School of Environmental Sciences

October, 2010

Abstract

This work presents biogeochemical estimates of marine biological production in the mixed layer of the Drake Passage (DP) and Bellingshausen Sea (BS) regions of the Southern Ocean. During two oceanographic cruises on board the *RRS James Clark Ross* in summer and autumn 2007, continuous underway measurements of O_2 by optode and O_2/Ar ratios by membrane inlet mass spectrometry were performed. Discrete samples were also analysed for O_2 isotopologues to quantify the ^{17}O anomaly ($^{17}\Delta$) of dissolved oxygen. These measurements together with wind-speed gas exchange parameterizations give estimates of biological oxygen air-sea fluxes (F_{bio}) and gross photosynthetic oxygen production (G) in the mixed layer (MLD).

Here, I also propose a criterion to define MLD based on vertical oxygen concentrations. From this, the MLD is defined as the depth where the dissolved O_2 concentration has changed by at least 0.5 % compared to its value at 10 m. This criterion is suitable for other studies on air-sea gas exchange.

Biological O_2 fluxes were obtained in high temporal (few minutes) and spatial (0.1 km) resolution. This, together with estimates of G, revealed high spatial heterogeneity of biological O_2 production in both areas of study. High productivity was observed along the coast of the BS and in the upwelling areas of the DP. In contrast, negative F_{bio} values were found mainly in open ocean waters of the BS and in the Antarctic Coastal Zone of the DP during autumn.

In the absence of vertical mixing, F_{bio} can be used as a proxy for mixed layer net community production (N). However, physical processes may play an important role. The negative F_{bio} values were associated with the mixed-layer deepening and subsequent entrainment of low-oxygen subsurface waters. Net heterotrophy may also have contributed to the negative F_{bio} values. Diapycnal flux of oxygen across the base of the mixed layer had little effect.

The results presented here are the first high-resolution estimates of marine productivity in the BS and DP regions. These provide valuable information to understand the heterogeneity of the productivity distribution in the Southern Ocean in a changing climate.

Contents

List of figures

List of Tables

Acknowledgements

I would like to express my deep and sincere gratitude to my supervisor Jan Kaiser for his encouragement, guidance and support from the beginning to the end on the PhD journey. At sea, virtually or on land, during the data analysis or commenting on this thesis, thank you for believing in me and for teaching me that I can achieve anything with perseverance and confidence. It is my pleasure to have been the first PhD student of the Kaiser group.

Thanks to my incredible and supportive advisory committee Professor Peter Liss, Professor Andrew Watson and Professor Corinne LeQuéré. To Peter, thanks for the dedicated time and advice provided. To Andy, thanks for the very valuable comments and the time given during *impromptu* meetings. I express my sincere gratitude to Corinne for the recommendations, support and meticulous observations during the writing process. You are all an inspiration to follow.

This work would not have been possible without the financial support of the Mexican council for science and technology, CONACyT. Thank you for the scholarship provided to achieve this dream.

Special thanks to the long list of scientists and crew that made my life on the cold sea warmer and more enjoyable. Particular thanks to the principal investigators Karen Heywood and Deborah Shoosmith for allowing me on board to have the great experience of being in Antarctica.

I am extremely grateful to Michael Bender and Bruce Barnett for allowing me to do the analysis of samples at Princeton University. Particular thanks to Nicolas Cassar for his advice and patience especially when I nearly set fire to the lab.

Thanks to all the people in ENV for making my stay at UEA more pleasant.

I am indebted to my many friends in Norwich for their informal support and encouragement. Particularly, I would like to thank Agnieszka Latawiec, without her positive energy and strength this would not have been possible.

Thanks to Sarah Wexler, Arlette Covarrubias, Frida Güiza, Jorge Luis Vazquez, Elena Palacios, Alba Gonzalez-Posada, Suzanne Palminteri, Johanna Glöel, Maribel Velasco, Elizabeth Jones and Alessia Freddo who listened and supported me always at my many moments of desperation, filling the gaps of loneliness with warm love.

Many thanks also to Sue, Johanna, Sarah and Aga for the critical proof-reading of some sections of this thesis that helped enormously to improve it.

“Mil gracias” to my friends in Mexico for their encouragement to pursue this dream that has reached its reality. Thanks for providing the sunshine and flavour very indispensable particularly during the long nights and cold days while they were at work.

Thanks to my lovely cat Tigger for his warm company and patience during my absences. Thanks for coming with me to England, we did it!

I owe my most profound gratitude to Thomas Wichard for sharing his endless passion for science. Thanks for providing the inspiration and motivation to keep the energy levels on the positive side of the plot. Thanks for believing in me, for the warm support and for being next to me with endurance and courage at all times.

Chapter 1

Introduction

The determination of marine primary production is crucial because it is fundamental for understanding the global carbon cycle. Various current methods have tried to improve estimates of primary production in order to identify changes in phytoplankton communities as a response to changes in oceanic CO_2 inventories.

The distribution of CO_2 in the oceans depends mainly on biological and physical pumps. The exchange of gases at the boundary between the ocean and atmosphere by physical dissolution and chemical reaction are the main processes that take part in the physical pump. On the other hand, the biological pump is basically the production of organic carbon and its subsequent transport to the deep ocean, delivering large quantities of carbon away from contact with the atmosphere (Liss, 2001; Hamme and Emerson, 2006). The balance between these biological and physical pumps is a key for understanding the global carbon balance, combined with anthropogenic CO_2 contribution.

The Southern Ocean (SO) plays a critical role in the global carbon cycle because it is considered a major sink of anthropogenic CO_2 from the atmosphere. Its influence on global circulation of water masses is important because it acts as a link to other ocean basins delivering deep, cold nutrient-rich water towards northern latitudes.

The exchange of gas between the atmosphere and the ocean surface regulates atmospheric CO_2. General circulation model simulations have shown that the Southern Ocean is the most important high-latitude region controlling preindustrial atmospheric CO_2 because it serves as a lid to a larger volume of the deep ocean (Sarmiento and Orr, 2001). Various long-term studies have been carried out to obtain global observational CO_2 time series and to monitor changes in ocean and atmosphere carbon chemistry via research cruises or moorings. The main goal has been to acquire data at high spatial and temporal resolution to constrain the magnitude and variability of air-sea CO_2 flux and the ocean anthropogenic CO_2

inventory. The main example is the PMEL (Pacific Marine Environmental Laboratory) CO_2 program, conducted by NOAA, Washington, USA. Other programs carried out were WOCE (World Ocean Carbon Experiment) and JGOFS (Joint Global Ocean Flux Study), conducted by the USA during 1991 to 1998. New programs such as CDIAC (Carbon Dioxide Information Analysis Center) have been created in order to gather the data (discrete and from underway measurements) collected from previous and other programs around the world. New international cooperative efforts have been created, such as the CARBOOCEAN consortium, with the aim of accurately assess the oceanic carbon sources and sinks in space and time and to constrain the rate of uptake of anthropogenic CO_2.

In 2003, the International Ocean Carbon Coordination Project Workshop (IOCCP) identified the urgent need for studies focusing on the role of primary productivity, carbonate chemistry above and below the thermocline, and the identification of appropriate remote sensing products to improve the estimates of inter-annual variability in sea-air CO_2 fluxes.

Because of the link between CO_2 and O_2 via photosynthesis and respiration, marine biological production can also be estimated from oxygen measurements. However, the presence of dissolved O_2 in seawater is due to both biological (i.e. photosynthesis, respiration) and physical processes (i.e. air-sea gas exchange and mixing).

Measurements of O_2/Ar ratios can be used to constrain the physical contributions (i.e. changes in seawater temperature, barometric pressure variations, injection of bubbles) to dissolved O_2 supersaturation which are translated into biological O_2 supersaturations (ΔO_2/Ar). This approach is based on the similar solubility properties in seawater of oxygen and argon and that the latter has no biological sources or sinks (Craig and Hayward, 1987; Emerson, 1987). From ΔO_2/Ar and a suitable gas transfer coefficient, the biological O_2 flux (F_{bio}) is calculated. Because of the stoichiometric relationship between CO_2 and O_2 by photosynthesis and respiration and under the assumption of a mixed layer in steady-state, F_{bio} approximates net community production in terms of oxygen (N).

This approximation is possible only if the vertical transfer of gas between the mixed layer and the waters below is neglected (i.e. vertical mixing, eddy diffusivity, entrainment and upwelling of subsurface low-oxygenated waters).

In the oceans, *N* is defined as the difference between the rate of oxygen produced by photosynthesis (gross oxygen production, *G*) and the rate of oxygen consumption (respiration, *R*) by all metabolic processes (i.e. dark respiration, Mehler reaction, photorespiration, chlororespiration, alternative pathway and nitrification) (Reuer *et al.*, 2007a). In section 1.8 of this chapter, a detailed description for the calculation of F_{bio} is presented.

Gross O_2 production (*G*) can be derived from the triple O_2 isotopes in dissolved O_2 ($^{17}O/^{16}O$ and $^{18}O/^{16}O$). Thus, *G* represents the rate of oxygen that has been produced by photosynthesis. In the oceans, photosynthesis produces O_2 with the isotopic composition of the source water, bearing a mass-dependent isotopic fractionation (MDF) (Guy *et al.*, 1993). On the other hand, atmospheric oxygen from stratospheric photochemical reactions bears a mass-independent fractionation (MIF) (Luz *et al.*, 1999; Luz and Barkan, 2000). The oxygen dissolved in the mixed layer exchanges rapidly with the oxygen in the atmosphere; therefore, the stratospheric O_2 contribution will balance the production by photosynthesis and consumption by respiration.

The estimates of *G* in the ocean can be done from measurements of the triple oxygen isotopes composition of dissolved O_2. For this, it is necessary the estimation of the ^{17}O anomaly ($^{17}\Delta$). The latter is given by the change in the oxygen isotopic abundance, as photosynthesis adds O_2 to the mixed layer, diminishing the magnitude of the ^{17}O abundance associated with dissolved O_2 molecules from air (Luz *et al.*, 1999; Luz and Barkan, 2000; Barkan and Luz, 2003; Reuer *et al.*, 2007a). Details regarding the estimates of *G* from $^{17}\Delta$ are presented below in section 1.10.

1.1 Marine productivity estimates from traditional methods.

In order to understand the method used here to estimate marine biological productivity, it is important to first differentiate among the following definitions.

Primary Productivity (*PP*), is the rate of formation of organic carbon compounds from inorganic matter. Most of the *PP* is produced from photosynthesis, with a small portion from chemosynthetic bacteria (Nybakken and Bertness, 2005).

Gross primary production (*GPP*), is the total amount of organic material fixed in the *PP* process, meaning the total rate at which CO_2 is fixed into organic carbon by the dark reactions of photosynthesis (Nybakken and Bertness, 2005).

Net Primary Productivity (*NPP*), is the organic carbon that is used by plants themselves (plant respiration) and the remaining organic carbon available to support other trophic levels. In other words, it is the result of phytoplankton autotrophy (*GPP*) and heterotrophy (i.e. respiration, *R*) (Emerson and Hedges, 2008).

The rates of *GPP* and *NPP* are expressed in terms of grams of carbon fixed per unit area or volume of seawater per interval of time (g C m^{-2} yr^{-1}) representing the production integrated over the euphotic zone.

In addition to primary producers, other members of the "community" also fix inorganic carbon into organic carbon.
Net Community Carbon Production (*NCP*), represents the difference between the rate of gross C production and metabolic CO_2 release. Thus, *NCP* represents the net metabolic balance between photosynthesis and respiration (by both autotrophic and heterotrophic organisms) occurring in the water; thus, it describes the net rate at which CO_2 is transformed to particulate and dissolved organic carbon (new and regenerated carbon production) (Cassar *et al.*, 2007; Emerson and Hedges, 2008).

Primary production can also be estimated in terms of oxygen; therefore:
Net Community Production in terms of oxygen (*N*), is the difference between the rate of gross O_2 production (*G*) and the rate of O_2 consumption by respiration (*R*) by all metabolic processes (i.e. dark respiration, Mehler reaction, photorespiration, chlororespiration, alternative pathway and nitrification) (Reuer *et al.*, 2007a). Furthermore, *N* is a proxy of export production from the surface to deep ocean (Cassar *et al.*, 2007). In this regard, more work is still needed to characterize the

relationship between *N* and export production in specific regions of the world's oceans.

Gross oxygen production (*G*), is the rate at which O_2 is produced by the splitting of water. This is also obtained by adding the O_2 being respired to the *N* (Nybakken and Bertness, 2005; Reuer *et al.*, 2007a).

Most studies have focused on the use of tracers to characterize global carbon fluxes and marine productivity. Some examples are: particle fluxes, seasonal nitrate and oxygen variations, ^{14}C assimilation in bottle incubations and ^{18}O isotope dilution technique (e.g. Legendre *et al.*, 1983; Kana, 1990; Bender *et al.*, 1999; Luz and Barkan, 2002), the use of chlorophyll distribution from *in situ* measurements or sea surface ocean colour by remote sensing (e.g. Müller-Karger *et al.*, 2004; Marrari *et al.*, 2006) and modelling studies (e.g. Tans *et al.*, 1990; Heimann, 1995; Nakata and Doi, 2006).

The method most commonly used to estimate primary production is based on incubation experiments using ^{14}C as a tracer. In this method, the rate of primary production (*PP*) is measured by incubating samples in bottles attached to a floating mooring. The samples are labelled with ^{14}C-DIC (Dissolved Inorganic Carbon) and exposed to different levels of light irradiation (i.e. at different depths in the water column) for a specific time (i.e. on the order of 12 - 24 h). After the incubation time, the amount of ^{14}C that has been taken up into the particulate material is measured (Emerson and Hedges, 2008). This method has been shown to have significant problems associated with: bottle effects (i.e. influence of the lack of mixing of growing bacteria and phytoplankton and the exclusion of large grazers that affect the biomass of the phytoplankton), loss of labelled ^{14}C as CO_2 and DOC (Dissolved Organic Carbon), and assimilation of unlabelled CO_2 (Legendre *et al.*, 1983; Bender *et al.*, 1999). In this method it is assumed that the ^{14}C was only metabolized by phytoplankton and that the zooplankton is not fast enough to affect the results by grazing. Also, as photosynthetic organisms are both autotrophic during the day and heterotrophic during day and night, the interpretation of results is complex (Emerson and Hedges, 2008). Thus, results using this method may underestimate gross production, in comparison to estimates derived from O_2 production, due to

photorespiration, respiratory losses and excretion of dissolved organic ^{14}C (Shulenberger and Reid, 1981; Bender *et al.*, 1999; Robinson *et al.*, 2009).

Measurements of dissolved O_2 by bottle incubations in light and dark conditions has been an alternative method for the estimation of marine primary productivity (Gaarder and Gran, 1927). Although this method is free of tracer loss, problems have been experienced with it, such as the lack of measurement of the light-dependent respiration (Kana, 1990). In 1987, Bender *et al*. proposed a method to measure gross primary production (*GPP*) using ^{18}O as a tracer in natural plankton communities. For this, seawater samples are spiked with $H_2{}^{18}O$ and incubated, which allows the amount of the ^{18}O-labelled O_2 produced from the ^{18}O-labelled H_2O to be determined (Bender *et al.*, 1999). However, it relies on the measurement of the total O_2 production by metabolic processes, including the O_2 that is not related to the assimilation of organic carbon (Robinson *et al.*, 2009); therefore, it tends to overestimate gross production of carbon (Juranek and Quay, 2005). To solve this, Kana (1990) proposed a technique based on ^{18}O isotope dilution to measure changes in isotope enrichment and oxygen concentration with time. It has the advantage of requiring smaller quantities of isotope and sample to be analyzed in a more reliable way by a quadrupole mass spectrometer, compared to the traditional ^{18}O-tracer technique. However, both ^{14}C and ^{18}O incubation methods experience analytical uncertainties due to the bottle effect and face a limited *in situ* sampling scheme which is not able to resolve changes in marine productivity over low spatial resolution.

The method based on satellite imagery to estimate *NPP* is based on the indirect estimation of global oceanic primary production by combining chlorophyll data (derived from space observations of sea surface ocean colour) with sea surface temperature and photosynthetic available radiation. The main satellite sensors during the past two decades have been CZCS (Costal Zone Colour Scanner) and SeaWiFS (Sea-viewing Wide-Field-of-view Sensor). The productivity estimates from satellite observations are useful to obtain an overview of *NPP* at a global scale due to the afforded high spatial coverage. The derived algorithms for primary productivity from satellite data have been successful for annually averaged observations; however,

those are not accurate enough to estimate production at seasonal time scales (Campbell *et al.*, 2002).

Some of the main disadvantages to estimate marine productivity from space are cloud coverage, limiting the observations in some parts of the world's oceans, and the identification of the surface ocean colour only over the first few centimetres. The latter leads to an underestimation of marine productivity in the entire euphotic zone; however, the use of mathematical models has made it possible to extrapolate the surface observations into a vertical distribution (Balch *et al.*, 1992; Behrenfeld *et al.*, 2005). On the other hand, the coarse spatial resolution (~1 km^2/pixel) reached from satellite observations is a limiting factor for the identification of mesoscale processes important for the understanding of biogeochemical cycles. Furthermore, comparison with *in situ* measurements is needed in order to validate the satellite-derived productivity data.

The methods used so far have analytical limitations, such as restricted observations from space due to ice and cloud coverage or sparse sampling and bottle effects in the seawater incubation methods (Bender *et al.*, 1999). Improved *in situ* measurements of marine biological productivity over high spatial and temporal resolution are needed to identify changes associated with small and meso-scale processes such as the effect over the phytoplankton communities due to the increasing production rates of sea-ice melt water.

1.2 Aims and thesis structure.

In this thesis, I present estimates of net community production (N) from F_{bio} based on shipboard measurements of O_2/Ar ratios made in some areas of the Southern Ocean (i.e. Bellingshausen Sea and Drake Passage) during two oceanographic research cruises. I also present gross oxygen production (G) from the isotopic abundance of dissolved oxygen in discrete samples of surface seawater.

The method to estimate marine productivity from the mixed layer-O_2 budget is relatively recent and it is still under evaluation. It relies on continuous shipboard measurements and therefore offers higher spatial and temporal resolution of mixed

layer net community production than the estimates from traditional methods such as bottle incubations.

In order to improve the method used in here for marine productivity estimates from O_2 measurements more data are needed for validations by comparing new results with those of previous studies using the same method and those derived from other productivity methods such as *in vitro* incubations. While various previous studies have applied the O_2 budget method in different parts of the world's oceans, few have used it in the Southern Ocean (Hendricks et al., 2004; Reuer et al., 2007a) previous to the present work.

In **Chapter 2**, I present a thorough description of the method as used here including calibration procedures and uncertainties. The method used in field and laboratory work was not greatly modified from previous applications made by other authors (i.e. Hendricks *et al,*. 2004; Reuer *et al.,* 2007a) except by the type of degassing membrane used as an inlet for the shipboard measurements by mass spectrometry (Kaiser *et al.*, 2005).

Both *N* and *G* characterize rates of productivity in term of fluxes integrated in the mixed layer over weekly timescales (typically between 10 and 30 days) (Bender *et al.*, 1994b; Kaiser *et al.*, 2005). The latter timescale represents the typical residence time of oxygen in the mixed layer given by the time the gas takes to equilibrate with the atmosphere in a specific mixed layer thickness.

The *N* and *G* estimates from the O_2 budget rely on several assumptions leading to the main uncertainties of this method, which are mainly due to the selected gas transfer coefficient parameterization and measurements of the isotopic abundance of O_2. However, an adequate criterion to define mixed layer depth (MLD) is of great importance to *N* and *G* estimates. Typically, MLD is defined on the basis of profiles of temperature or potential density; however, how reliable is the estimation of mixed-layer marine productivity from oxygen measurements in a depth defined by conservative water properties? What is the most reliable MLD criterion to use for the marine productivity estimates from the O_2 budget method?

In **Chapter 3**, I propose a criterion to better define mixed layer depth from the vertical distribution of dissolved oxygen (MLD-O_2). This criterion improves upon previous criteria based on temperature or potential density in representing the sea-air gas fluxes in the coastal areas of the Southern Ocean.

In **Chapter 4**, I present the first high-resolution estimates of *N* and *G* in the Bellingshausen Sea (BS) area west of the Antarctic Peninsula using the O_2 budget method. As a step forward, I apply the MLD criterion based on vertical O_2 distribution. Additionally in Chapter 4, I quantify the vertical contribution of O_2 to the mixed layer due only to two physical processes: vertical diffusion (i.e. diapycnal flux, F_v) and vertical entrainment of O_2 by convection (F_e) after deepening of the oxygen-mixed layer. This step was done to improve the assumption of a steady state mixed layer to better approximate F_{bio} to *N*. Finally F_v and F_e, together with *G* and F_{bio}, are included in a simple O_2 mass balance to quantify the contribution of these physical processes for *N* estimates in the Bellingshausen Sea.

In **Chapter 5**, *N* and *G* estimates are shown for three transects in Drake Passage (DP). Here, in the absence of vertical oxygen profiles, the mixed layer depth is obtained from climatological data defined using the vertical distribution of potential density. The latter, was the best approximation to MLD-O_2, this comparison is presented in Chapter 3. The DP is a highly dynamic oceanographic region; thus, in Chapter 5 I show the reliability of the O_2 budget method in identifying fast changes in marine biological production of the DP and the inter-seasonal variability of marine biological production of the DP associated with its frontal zones.

Finally, in **Chapter 6** I draw the general conclusions of the earlier chapters with recommendations for future applications.

The application of the O_2 budget method for estimating marine productivity provides a timely contribution to our understanding of the current state of marine biological production in the SO in response to the warming of the surface ocean and to the increase of dissolved CO_2. The results of this work complement other continuous O_2/Ar measurements previously made by others the Drake Passage, and this is the first time it has been used in the Bellingshausen Sea.

The importance of estimating marine productivity in the Southern Ocean in greater detail and the basis of the method applied here are explained in sections below.

1.3 Marine biological production in the Southern Ocean.

The Southern Ocean plays a major role in the climate system. It is recognized as the most sensitive oceanic body to climate change (Blain *et al.*, 2007) due to its size, nutrient concentrations and close link to the deep ocean, with a consequent major influence on the global carbon cycle (e.g. Hendricks *et al.*, 2004; Verdy *et al.*, 2007).

The SO is the largest high-nutrient low-chlorophyll (HNLC) region of the global ocean, with high surface concentration of macronutrients (i.e. NO_x, PO_4 and SiO_2) largely unused. In this region, natural phytoplankton blooms occur mainly in the vicinity of the Antarctic coastline and Southern Ocean islands (Blain *et al.*, 2007). Thus, high values of chlorophyll can be found along the coast of the Antarctic Continent in contrast to the open waters of the Southern Ocean (Figure 1.1).

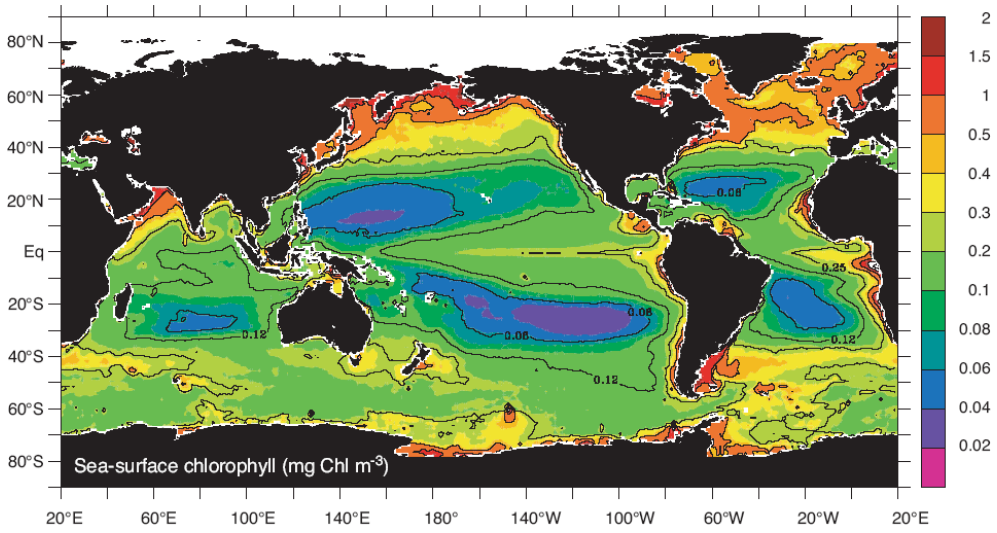

Figure 1.1 – Average sea-surface chlorophyll concentration (mg m^{-3}) for 1998 to 2002 estimated from satellite measurements of surface ocean colour from SeaWiFS, NASA/ Goddard Space Flight Center and ORBIMAGE (Taken from Sarmiento and Gruber, 2006 ; Chapter 4, pag. 229).

Recently, Kahru *et al.*, (2007) used satellite data to identify oceanic eddies, generated at the Southern Antarctic Circumpolar Current Front, associated with increased

phytoplankton biomass. After observations of the spatial distribution of surface ocean colour from satellite images, the authors found agreement between chlorophyll *a* concentration and the distribution of eddies. Eddies are common physical features in the SO that enhance the distribution of nutrients; their presence therefore contributes to the increase of chlorophyll *a*. Cyclonic eddies (spinning clockwise in the Southern Hemisphere) contain normally elevated chlorophyll *a* in the core, while anticyclonic eddies (spinning counter clockwise) have low chlorophyll *a* in the core but often elevated chlorophyll *a* on their periphery.

Phytoplankton production in the SO is known to be iron (Martin *et al.*, 1990a), light, grazing and silicate (SiO_2) limited. Iron concentrations in the SO are relatively low (~0.14 nM in the surface water column) compared with the rest of the world's oceans (e.g. Sohrin *et al.*, 2000; Coale *et al.*, 2004; Kahru *et al.*, 2007; Meskhidze *et al.*, 2007). This has been demonstrated by various iron addition experiments (e.g. Southern Ocean Iron Release Experiment, SOIREE; Southern Ocean Iron Experiments, SOFeX and CROZet natural iron bloom and Export experiment, CROZEX, to mention some) (Boyd *et al.*, 2000; Coale *et al.*, 2004; Pollard *et al.*, 2007). As a result, rates of photosynthesis (primary production) and biological carbon export in Antarctic waters are relatively low.

Temporal variability of air-sea fluxes of carbon dioxide and oxygen in the upper Southern Ocean have been evaluated with biogeochemical models in order to understand their causes (e.g. Le Quéré *et al.*, 2007; Lenton and Matear, 2007; Verdy *et al.*, 2007). It has been suggested that variability in the circulation and biological processes of the SO impacts local air-sea exchange of carbon dioxide (Watson and Naveira, 2006; Lovenduski *et al.*, 2007). Deep waters in the SO are rich in DIC and depleted in oxygen. Export production (biological carbon export) transfers nutrients to the deep ocean, influencing the nutrient concentrations in intermediate waters in the global oceans; however, export production is reduced due to strong grazing pressure and limited SiO_2 and light (Coale *et al.*, 2004; Meskhidze *et al.*, 2007; Reuer *et al.*, 2007a). When circulation brings these waters into the upper mixed layer, the soluble gases are exchanged at the air-sea interface (Verdy *et al.*, 2007).

These characteristics have the potential to affect global atmospheric CO_2 levels. Therefore, to constrain the uncertainties of the magnitude of the SO as a CO_2 sink, evaluate its variability in and control upon atmospheric CO_2 uptake, high-precision estimates of rates of primary production and respiration are needed. Furthermore, the high spatial and temporal resolution in *N* achieved from O_2/Ar ratios and the *G* estimates from triple oxygen isotopes will contribute to the understanding of marine phytoplankton distribution and the SO carbon cycle.

1.4 Hydrographic features of the Southern Ocean.

The dominant hydrographic feature of the SO is the eastward-flowing Antarctic Circumpolar Current (ACC) driven by the westerly wind field. The westerlies are found approximately between 45° and 65° S; these winds keep the Antarctic continent isolated from warming and have a strong impact on the SO hydrography, sea-ice distribution and biological production. The ACC has the largest mass transport of all ocean currents. Considering its northernmost limit as the Subtropical Front (Figure 1.3), the surface area of the SO represents approximately 22 % of the world's ocean surface (Tomckzak and Godfrey, 1994).

Antarctic waters are the global southern component source of the deepest, densest waters of the global overturning circulation in the world's oceans. The ACC flows freely around the Antarctic continent with no physical boundaries in the east, west and north. Thus, the SO acts as a global link among all major ocean basins (i.e. Pacific, Atlantic and Indian Oceans) (Orsi *et al.*, 1995) allowing a global overturning circulation to occur (Figure 1.2). Previously, a very close link has been observed between Antarctic temperatures and atmospheric CO_2 (Watson and Naveira, 2006) which could be due to the natural unlimited circulation of the ACC around the Antarctic continent.

In cold polar regions, changes in salinity affect ocean water density more than changes in temperature. As sea-ice forms, salt is ejected to the surrounding water, increasing its density and causing the water to sink. As the dense, cold and saline water sinks in down-slope gravity currents adjacent to the Antarctic continent, it is mixed through convection with warmer and fresher circumpolar deep water.

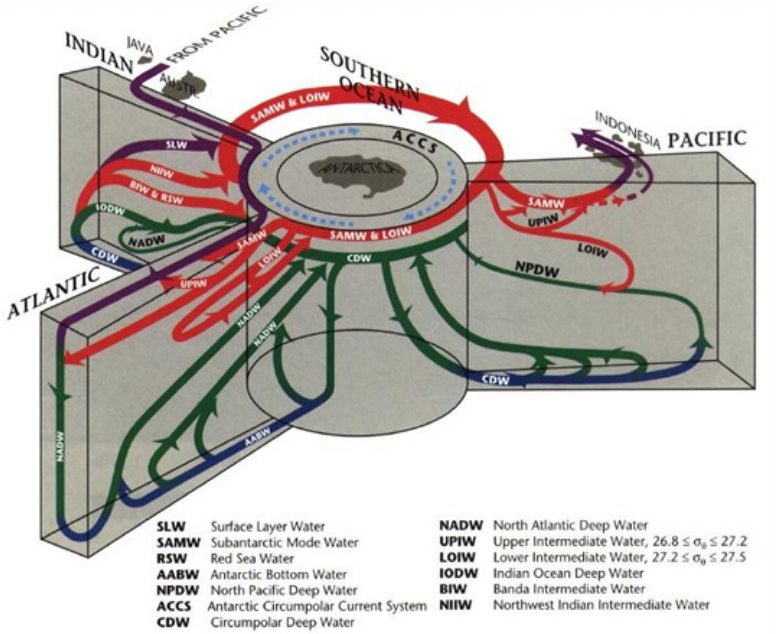

Figure 1.2 – Three-dimensional representation of global overturning circulation with the representation of the main ocean basins (three vertices are Pacific, Indian and Atlantic Oceans) connected by the Southern Ocean (cylinder in the middle). The main water masses involved are indicated in the figure; colours of the arrows resemble the approximate density ranges of the water masses: blue = dense bottom water; green = deep water; red = intermediate water and purple = less dense surface water (Schmitz Jr., 1996).

This pattern is the origin of the Antarctic Bottom Water (AABW), which flows northwards into each of the three major basins of the subpolar Southern Ocean (Figure 1.2, blue arrow in the Atlantic Ocean basin). The AABW is mixed with less dense waters while crossing the SO; a fraction is returned towards the surface, while another escapes northward into the Atlantic, Pacific and Indian Ocean basins, forming the bottom waters there. The flow into the Southern Atlantic Ocean moves eastwards below the tip of southern Africa to enter the Indian Ocean via the ACC, which is also the vehicle that carries cold deep waters into the Pacific Ocean (Chester, 2000; Watson and Naveira, 2006).

The North Atlantic Deep Water (NADW) is produced by convective sinking in the northern North Atlantic and moves towards the south. It is less dense, warmer and more saline than the AABW.

The Antarctic Intermediate Water (AAIW) is formed by the convergence and mixing of Antarctic surface waters. The AAIW penetrates northward to form the thermocline waters of much of the world's oceans. In the Southern Ocean, it is freshened by net precipitation and sea-ice melt and is transported northward by a net Ekman drift under the influence of the westerly winds and warmer upper-ocean waters to the north.

The dynamics of the Antarctic waters are dominated by geostrophy due to the small variations in density with depth; as a result, there is generally an evenly distributed pressure gradient over the water column (Tomckzak and Godfrey, 1994).

1.4.1 Oceanic regimes of the Southern Ocean.

The topography of the Southern Ocean has a much larger impact on currents than in other oceans. Most of the ACC transport is concentrated in frontal jets; their number, strength, and latitudinal locations are influenced by bathymetry (Kahru *et al.*, 2007). The Southern Ocean is characterized by meridional gradients that extend to the ocean floor. The properties of the surface waters are therefore clearly different from the warmer and saltier waters of the northern subtropical circulations. Three different oceanic regimes, limited by circumpolar fronts, are generally observed in the ACC. The frontal positions define the boundaries of the currents, and their presence marks rapid changes in surface and subsurface temperature and salinity in short distances (i.e. on the order of tenths of kilometres). From north to south, the main Southern Ocean fronts in the ACC are: Subtropical Front (STF), Subantarctic Front (SAF), Polar Front (PF), Southern ACC Front (SACCF) and Southern boundary of the ACC (SB) (e.g. Orsi *et al.*, 1995; McNeil *et al.*, 2007) (Figure 1.3).

The position of the SO fronts defines the limit of the frontal zones. From north to south, the most important frontal zones are:
1) The Subantarctic Zone (SAZ) which is limited to the north by the STF and to the south by the SAF and characterized by strong convergence,

2) The Polar Frontal Zone (PFZ) is located between the SAF and PF to the south and is the core of the ACC. The PFZ is regarded as a convergence zone due to strong

subduction. The main properties of the PFZ are strong lateral mixing and low biological production,

3) The Antarctic Zone (AZ) lies south of the PF and is bounded to the south by the SACCF. This area is characterized by upwelling (Antarctic divergence) due to the compensation of the equatorward Ekman transports (Orsi *et al.*, 1995; Hendricks *et al.*, 2004; McNeil *et al.*, 2007).

(4) The Southern Antarctic Circumpolar Current Zone (SACCZ) is located south of the AZ and is bounded to the south by the SB.

(5) Finally, the Antarctic Continental Zone (ACZ) is limited to the north by the SB and to the south by the Antarctic continent, and represents a separate water mass of uniform temperature and low salinity (Tomckzak and Godfrey, 1994; Orsi *et al.*, 1995) (Figure 1.3).

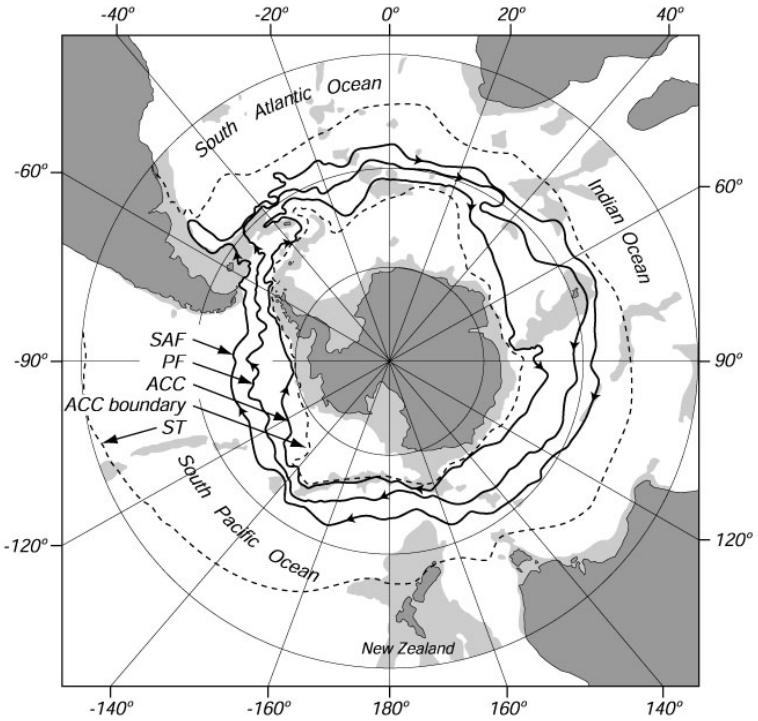

Figure 1.3 – Circumpolar representation of the Southern Ocean fronts according to their average historical location (Orsi *et al.*, 1995). Subtropical Front (STF) (outer dashed line, represented in the figure as "ST"); thick black circumpolar lines with arrows indicating the direction of the flow: Subantarctic Front (SAF), Polar Front (PF) and Southern Antarctic Circumpolar Current Front (SACCF, represented in the figure only as "ACC"). The Southern boundary of the ACC is represented by the inner dashed line indicated as "ACC boundary".

The upward transport of deep water masses (i.e. NADW, LCDW and UCDW) are the core part of the Southern Ocean meridional overturning circulation (Figure 1.4) and it plays an important role in the formation and distribution of water at intermediate and surface depths within the ACC zones. The distribution of biological communities within the ACC zones is therefore strongly linked to changes in local physical processes. A better understanding of the distribution of marine biological production in the SO will allow us to evaluate the implications of changes in the global carbon cycle.

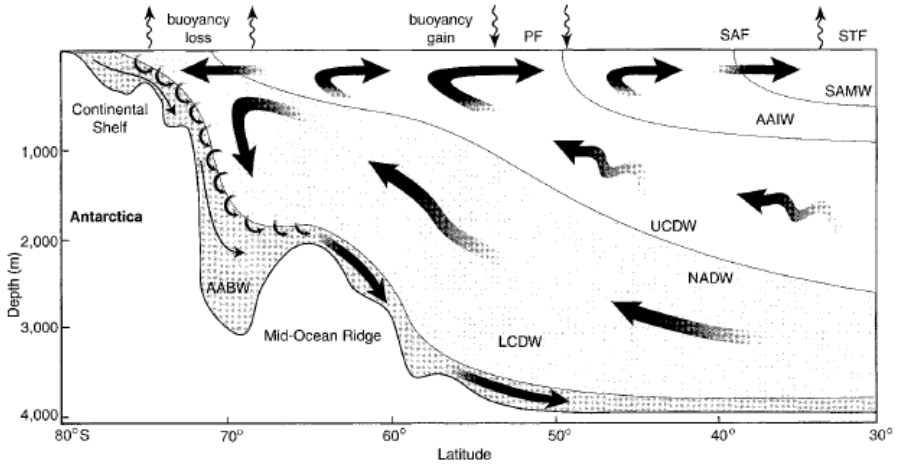

Figure 1.4 – Two-dimensional schematic representation of the Meridional Overturning Circulation in the Southern Ocean (Speer *et al.*, 2000). The key water masses are shown: North Atlantic Deep Water (NADW), Upper and Low Circumpolar Deep Waters (UCDW and LCDW, respectively); along the Antarctic continent the formation of the Antarctic Bottom Water (AABW) by sinking is observed. Antarctic Intermediate Water (AAIW) and Southern Annular Mode Water (SAMW) are represented at mid depth (<1000 m) and latitude (between 30 to 50 ºS).

In Chapter 5, I present more details about the physics and water properties of the SO fronts and zones associated with the marine biological production in the Drake Passage.

1.5 Dissolved oxygen as a proxy for marine productivity estimates.

Dissolved O_2 and CO_2 are reactive gases that play a role in marine physical, biological and chemical processes. In oceanic biogeochemical cycles, the two gases are essentially coupled by photosynthesis and respiration. Also, they are consumed and produced in the combustion process by the burning of fossil fuels or biomass.

In order to resolve the marine productivity estimates using alternative tracers of CO_2, there is growing interest in the quantification of the production and consumption of dissolved O_2. Therefore, measurements of dissolved O_2 act as a proxy to better understand rates of carbon fixation and CO_2 changes in the surface ocean and the atmosphere (Luz and Barkan, 2005).

Dissolved CO_2 and O_2 behave differently during the exchange between the surface ocean and the atmosphere due to differences in the solubility properties and reactivity levels of each gas. The Bunsen coefficient (β) is an index used to evaluate the solubility of gases in water and is defined as the volume of gas dissolved in a unit of volume of solution (seawater) at a specific temperature (T) when total pressure and fugacity are 1 atm (Wanninkhof, 1992). The O_2 is less soluble in seawater than CO_2. In terms of β at 24 ºC and salinity of 35, the solubility of O_2 is 23.7 $cm^3\ l^{-1}$ and the solubility of CO_2 is 666 $cm^3\ l^{-1}$ (Weiss, 1970; Broecker and Peng, 1982). Despite the higher solubility of CO_2, its equilibration rate and the rate of air-sea exchange in seawater are slower compared to O_2; this is due to the buffer capacity of seawater by the carbonate chemistry. Thus, estimates of marine biological productivity based on CO_2 measurements and its isotopic composition in the atmosphere and ocean have produced uncertain results (Bender *et al.*, 1994a).

Simultaneous measurements of both O_2 and CO_2 in air provide a better estimate of CO_2 fluxes and help to diminish the uncertainties in the air-sea CO_2 exchange. In 1992, Keeling and Shertz showed that the O_2 concentration of air constrains the seasonal rate of net production in the upper water column on a hemispheric scale. Furthermore, the long-term rate of decrease in atmospheric O_2 concentration can help to elucidate the rate of oceanic CO_2 uptake (Keeling and Shertz, 1992).

From the quantification of dissolved O_2, it is therefore possible to estimate the rate of marine biological production. The air-to-sea oxygen flux (F_g in mmol $m^{-2}\ d^{-1}$) can be estimated from the quantification of the total concentration of oxygen ($c(O_2)$ in µmol kg^{-1}) in surface waters using the appropriate gas exchange coefficient (k in m d^{-1}). However, oxygen concentration in the upper water column is affected by both biological (i.e. production by photosynthesis and consumption by respiration) and

physical processes (i.e. vertical and horizontal mixing, temperature and barometric pressure changes, wind velocity, exchange of bubbles); therefore in order to estimate the oxygen produced by biological communities, it is necessary to identify its sources.

In 1927, the approach for determining primary productivity using dissolved oxygen was first proposed by Gaarder and Gran. The authors developed a technique based on the *in vitro* variation of oxygen concentration, determined by Winkler titration, under different experimental conditions (Gaarder and Gran, 1927). This technique provided sensitive results for a limited analytical design (i.e. several hours of incubation, enough phytoplanktonic communities to be incubated and adequate illumination levels).

However, in order to reduce the uncertainties from the technique of Gaarder and Gran, various other techniques were proposed (e.g. polarographic, microgasometric and manometric techniques); all of these vary in the instrumentation and principles, with differences in the achieved precision and accuracies (Mountford, 1969). In 1987, Craig and Hayward proposed a method based on measurements of the ratio of oxygen to argon (O_2/Ar) to distinguish between the biological and physical components of dissolved O_2 in the mixed layer. Dissolved Ar is an inert analogue of O_2 in the oceanic mixed layer; however it is only affected by physical mechanisms due to temperature and salinity-dependent solubility effects (i.e. diffusive and bubble-mediated gas exchange, pressure, temperature and salinity changes, lateral mixing and vertical diffusion) (Craig and Hayward, 1987; Emerson *et al.*, 1999).

With the measurements of O_2/Ar ratios, and subsequent biological O_2 supersaturation (ΔO_2/Ar), it is possible to estimate the rate of net O_2 community production in terms of oxygen (N in mmol m^{-2} d^{-1}) and the gas exchange coefficient (k). This is complemented by the gross oxygen production (G in mmol m^{-2} d^{-1}) from the ^{17}O anomaly ($^{17}\Delta$ in per meg) given by the isotopic abundance of dissolved O_2 in the mixed layer.

The following sections describe the calculation of the gas transfer coefficient (*k*) for the productivity estimates. Below are also described the estimates of F_g from $c(O_2)$ and how measurements of O_2/Ar ratios and triple oxygen isotopes were performed in order to estimate *N* and *G*.

1.6 Gas transfer coefficient (*k*).

The rates of net community oxygen (*N*) and gross oxygen production (*G*), both in terms of gas fluxes, are representative for the mixed layer. Thus, the *k* calculation for this research is crucial.

The net flux of a gas between the air and the sea surface depends on the driving force, which for this process is the concentration of the gas (given by its molecular diffusion through the interface) and a transfer coefficient or velocity (*k*) in terms of length over time (m d^{-1}) (Emerson and Hedges, 2008). According to Liss and Slater (1974), *k* is proportional to the molecular diffusion coefficient (*D*) of the gas and the thickness of the water layer (*z*) at the air-sea interface at which the molecular diffusion takes place ($k = D/z$). Most of the transfer of the gas occurs in the top few centimetres of the water layer; this process is therefore limited mainly to the film thickness (Liss and Slater, 1974).

Since the work of Liss and Slater, several parameterizations for *k* as a function of wind speed (*u*) have been proposed. It has been challenging work, due to *k* is mainly driven by the near-surface turbulence or sea surface roughness, a parameter still difficult to measure in natural systems since it is dependent not only on *u*, but also in the state of the waves like their height and wavelength, as the main forcing parameters (Drennan *et al.*, 2005). Various empirical relations between *u* and *k* have been proposed in order to better estimate the value of the latter in natural systems. The three relationships used most commonly — Liss and Merlivat, 1986 (hereinafter referred to as LM86), Wanninkhof, 1992 (W92) and Nightingale, 2000 (N00) — all propose a relationship between *k* and *u*.

The LM86 parameterization was obtained from laboratory wind tunnel experiments and normalized with field measurements on a lake using SF_6 as a tracer. The relationship between *k* and *u* was defined by three surface regimes characterizing a

particular wind speed range and associated wave field: smooth surface, rough surface and breaking waves regimes (Liss and Merlivat, 1986; Liss *et al.*, 2004).

The study made by Liss and Merlivat is based on laboratory and small-scale field experiments; thus in 1992, Wanninkhof made public a quadratic fit for the calculation of *k* based on a field dual tracer experiment. The author took into account the disequilibrium between the natural and bomb radiocarbon inventory (^{14}C) and the proposed relationship is useful for short-term steady winds at a fine scale and for areas free of perturbations (i.e. floating ice) (Wanninkhof, 1992).

In 2000, Nightingale proposed a parameterization for *k* deduced from *in situ* non-toxic gaseous tracer measurements (SF_6 and ^3He) released at sea in a small area. A second-order polynomial described the relationship between *k* and *u* from the change in the ratio of the two tracers over time. This parameterization was suitable for short-term wind formulation (3 to 20 days) (Nightingale *et al.*, 2000).

Since substantial investigation has been done for air-sea CO_2 exchange, the *k* parameterizations are typically normalized by the Schmidt number for CO_2 in freshwater (600) and in seawater (660) (both at 20 ºC) and by the wind speed at 10 m above sea level (u_{10}). The Schmidt number (*Sc*) is the ratio between the kinematic viscosity (ν_c) and the diffusion coefficient (*D*) (Emerson and Hedges, 2008).

In 2007, a parameterization for *k* was proposed by Sweeney *et al.* (S07) based on radiocarbon measurements with a larger database than the one used for W92. It included dissolved inorganic carbon, a general circulation model and an inverse model to include the global ocean circulation. The S07 parameterization led to the following quadratic fit:

$$k = 0.27(u_{10}^2)(Sc/660)^{-0.5} \qquad (1.1)$$

This parameterization assumes that the flux into a given region has a time story very similar to the overlying atmospheric perturbation.

Several advantages and disadvantages must be considered for S07 parameterization. Probably the main disadvantage for air-sea boundary gas exchange is that it was constructed without taking into account the top 30 m of the water column due to limitations in the transport models to reproduce the high temporal and spatial variability of this top layer. However, the advantages are that it was based on a large dataset of ocean measurements including some regions of the Southern Ocean. The wind field used to formulate the S07 is based on long term variability at global and local scale from the historical record of winds (Sweeney *et al.*, 2007).

The next figure was taken from Sweeney *et al*. (2007). Here the author compares the different *k*-*u* relationships previously discussed. An underestimation of *k* for CO_2 in seawater is shown from the LM86 and N00 fits, compared to the values given by W92 and S07.

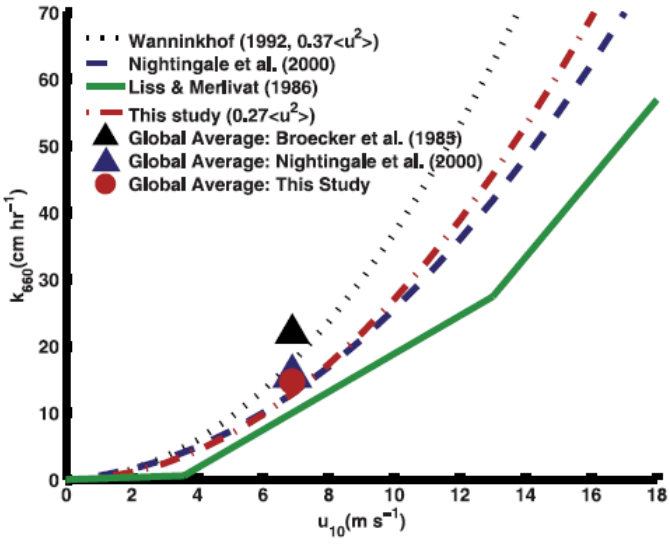

Figure 1.5 – Gas transfer coefficient for CO_2 in seawater (k_{660} in cm h^{-1}) as a function of wind speed (u_{10} in m s^{-1}) from different parameterizations (see label within the figure). "This study" refers to Sweeney *et al*., 2007, the source of this figure).

The S07 parameterization is therefore a major improvement over the previous short-term and small-scale parameterizations. Deriving a reliable estimate of *k* for the Southern Ocean is a challenge due to consistently high wind speeds. Despite the disadvantages of the S07 parameterization, in this work it was the preferred

parameterization to estimate *k* values. The error produced by the calculation of *k* from the W92 is 30 %. From S07 this error is reduced up to 15 %.

Following the estimate of *k*, a weighted gas transfer coefficient (k_w in m d^{-1}) is calculated in this work. The k_w is calculated following Reuer *et al.* (2007a) and it is considering the historical record of wind speeds previous to the sampling time and a fixed mixed layer depth.

1.7 Sea-air flux of oxygen (F_g).

The total net rate of sea-to-air O_2 exchange (F_g in mmol m^{-2} d^{-1}) is calculated from the O_2 supersaturation (ΔO_2 in %) and the gas transfer coefficient (Sweeney *et al.*, 2007) weighted to the historical record of wind speeds (k_w in m d^{-1}) (Reuer *et al.*, 2007a).

$$F_g = k_w \times \Delta O_2 \times c_{eq}(O_2) \qquad (1.2)$$

where ΔO_2 is calculated following:

$$\Delta O_2 = \frac{c(O_2)}{c_{eq}(O_2)} - 1 \qquad (1.3)$$

where $c(O_2)$ (µmol kg^{-1}) is the total surface concentration of oxygen. The term $c_{eq}(O_2)$ is the concentration of O_2 at equilibrium with the atmosphere at the *in situ* temperature and salinity calculated according to Garcia and Gordon (1992) and Benson and Krause (1984).

1.8 Estimates of biological O_2 flux (F_{bio}) as a proxy of net community oxygen production.

The normalization of O_2 with Ar is used to differentiate between the biological and physical oxygen and is based on their similar solubility pattern in natural waters. The responses of these two gases to changes in temperature and pressure, bubble-mediated gas exchange and the equilibration kinetics between bubbles and the solution is similar (Craig and Hayward, 1987; Kaiser *et al.*, 2005). The Bunsen coefficient of solubility at a temperature of 24 °C in seawater (35 of salinity) is 23.7 cm^3 l^{-1} for O_2 and 26 cm^3 l^{-1} for Ar (Broecker and Peng, 1982).

Figure 1.6 depicts a relationship between the supersaturation of N_2 (ΔN_2) and O_2 (ΔO_2) compared to Ar (ΔAr). Vertical and positive portions of the horizontal axes in

both figures represent supersaturation of each gas with respect to their concentration at equilibrium with the atmosphere. The latter is the zero on each plot, as given by the concentration at 25 ºC and 35 of salinity at atmospheric pressure (oxygen, Garcia and Gordon, 1992 with re-analysis by Benson and Krause, 1984b; nitrogen and argon, Hamme and Emerson, 2004).

Both figures present the changes in the saturation concentration due to the change on individual variables: pressure, temperature, salinity, bubble injection and mixing. The ΔO_2 and ΔAr vary similarly as a response to changes in the variables mentioned above. Bubble injection and mixing are the most sensitive processes to the supersaturation of water with both gases (Figure 1.6, left panel). In contrast, nitrogen responds less linearly to argon, particularly when injection of air from bubbles increases the supersaturation levels (Figure 1.6, right panel).

In the atmosphere, the O_2/Ar ratio in air is approximately 22.42 and is approximately 9 % greater than the equilibrium O_2/Ar in seawater. The latter corresponds to 20.47 at 10 °C and salinity of 35 using the solubility equations of Weiss (1970) (Reuer *et al.*, 2007a).

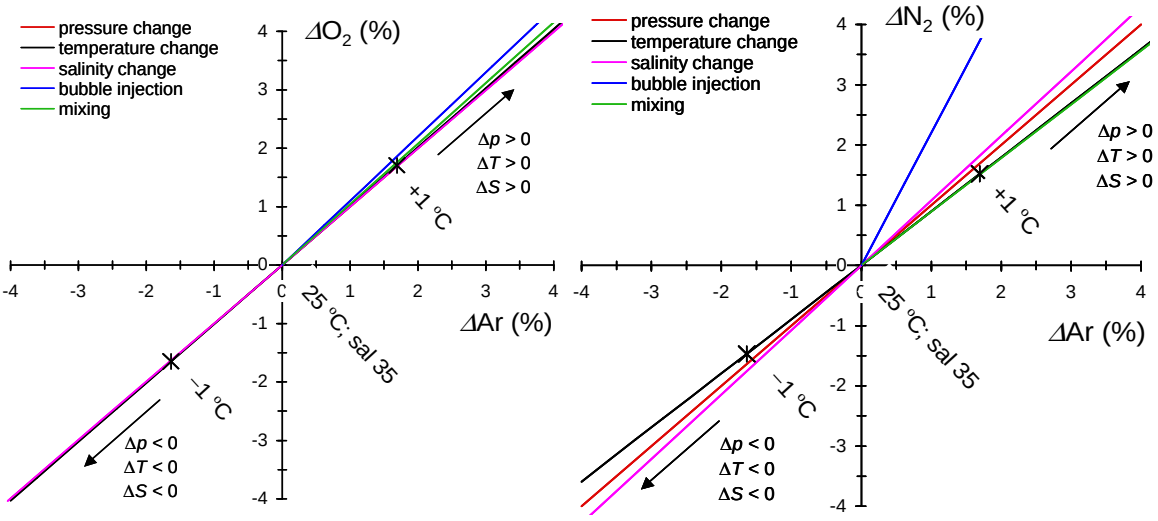

Figure 1.6 – Response of O_2 and N_2 supersaturations (ΔO_2 – left panel; ΔN_2 –right panel, respectively) in relation to Ar supersaturation (ΔAr) due to changes in pressure (red), temperature (black), salinity (pink), bubble injection (blue) and mixing (green). Supersaturations represent the % above (positive) or below (negative) the value at equilibrium with the atmosphere (*Courtesy of J. Kaiser*).

The biological O_2 supersaturation ($\Delta O_2/Ar$) is an estimate of the O_2 production by photosynthesis and is given by the percent deviation of the measured O_2/Ar from the concentration of the gases at equilibrium with the atmosphere (Craig and Hayward, 1987) as follows:

$$\Delta O_2/Ar = \frac{O_2 / Ar}{(O_2/Ar)_{eq}} - 1 \qquad (1.4)$$

where O_2/Ar represents the measured concentration ratio in seawater and $(O_2/Ar)_{eq}$ represents the saturation concentration ratio ($c_{eq}(O_2)$ / $c_{eq}(Ar)$; both in μmol kg^{-1}) determined by the solubility equations for O_2 (Benson and Krause, 1984; Garcia and Gordon, 1992; Garcia and Gordon, 1993) and for Ar (Hamme and Emerson, 2004) as functions of temperature, pressure and salinity.

In the absence of physical processes in a steady state mixed layer, the $\Delta O_2/Ar$ can constrain the balance between photosynthetic O_2 production and respiration. When $\Delta O_2/Ar = 0$, it represents the equilibrium between these two processes; while $\Delta O_2/Ar < 0$ represents a state where O_2 consumption is greater than production during the sampling time, and vice versa with values $\Delta O_2/Ar > 0$ integrated in the mixed layer (Hendricks *et al.*, 2004; Reuer *et al.*, 2007a).

From the $\Delta O_2/Ar$ it is calculated the rate of biological O_2 production, here referred as to biological O_2 flux (F_{bio} in mmol m^{-2} d^{-1}) integrated in the mixed layer and is calculated as:

$$F_{bio} = k_w \times \Delta O_2/Ar \times c_{eq}(O_2) \qquad (1.5)$$

F_{bio} can be approximated to N if steady state in the mixed layer is assumed and there is a negligible vertical flux of oxygen through the base of the mixed layer, as well as horizontal and vertical mixing (Reuer *et al.*, 2007a).

As mixed layer Ar is only affected by physical saturation mechanisms, Ar supersaturation (ΔAr) can be derived from the known dissolved oxygen supersaturation (ΔO_2) and the ΔO_2/Ar values (Kaiser *et al.*, 2005) according to:

$$\Delta \mathrm{Ar} = \frac{\left(\Delta \mathrm{O}_2 - \Delta \mathrm{O}_2/\mathrm{Ar}\right)}{\left(1 + \Delta \mathrm{O}_2/\mathrm{Ar}\right)} \qquad (1.6)$$

The ΔAr would therefore provide an estimate of the influence of solely physical processes in the mixed layer.

The method used in this thesis to measure shipboard *in situ* O_2/Ar ratios in natural waters by Membrane Inlet Mass Spectrometry (MIMS) is described in the following section.

1.9 Membrane Inlet Mass Spectrometry (MIMS) for *in situ* measurements of O_2/Ar ratios.

In 1999, Emerson *et al.* proposed an approach for determining dissolved gases (O_2, Ar and N_2) and their ratios using mass spectrometry (MS), which obtained accuracies better than ±0.1 to 0.3 % (Emerson *et al.*, 1999).

Typically, the measurements of dissolved gases by gas chromatography with a thermal conductivity detector (GC-TCD) provide a precision from 0.3 to 1 % for N_2, O_2 and Ar extracted from water (Craig and Hayward, 1987). The normalization of O_2 and N_2 measurements using a biologically inert gas eliminates the sensitivity of the absolute concentration estimations and gas ratios estimated from MS provide a precision on the order of 0.05% for N_2/Ar or O_2/Ar (Emerson *et al.*, 1991; Kana *et al.*, 1994). However, the method proposed by Emerson, was only for the analysis of discrete water samples followed by gas phase equilibration.

In order to improve the spatial resolution of the gas measurements it has been develolped a technique known as Membrane Inlet Mass Spectrometry (MIMS) for the continuous measurement of dissolved gases and their ratios in natural waters (Kana *et al.*, 1994; Kaiser *et al.*, 2005; Tortell, 2005a).

In the MIMS method, a continuous flow of water is exposed to a semi-permeable membrane where the dissolved gases are selectively diffused through it. The flow of gases is then passed into the vacuum inlet of a mass spectrometer for their separation and detection on the basis of their charge to mass ratio (*m/z*). The amount of the gas flow into the MS depends on its vapour pressure, solubility and diffusivity in the membrane material (Johnson *et al.*, 2000).

The next schematic (taken from Johnson *et al.*, 2000) is a representation of the typical components of the MIMS method, from the source containing the analyte of interest in the solvent, passing by the degassing membrane to the vacuum system of the MS for the detection of the analyte. In the following schematic is shown two alternative types of membrane inlet systems that differ on the use (or not) of a pneumatic transport and jet separator to introduce and enrich the analyte into the mass spectrometer after it was permeated by the membrane.

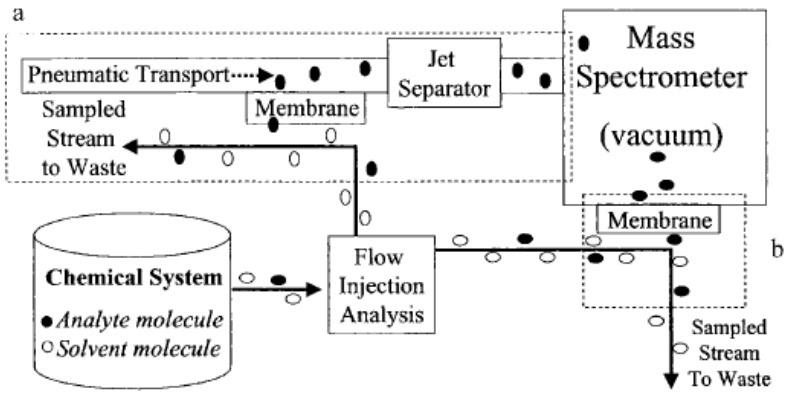

Figure 1.7 – Schematic of the components of the MIMS method showing two types of interface by using (a) or not (b) a pneumatic and jet separator to introduce the analyte to the MS for detection once it has been extracted from the solvent by the membrane (taken from Johnson *et al.*, 2000).

With the MIMS method measurements of both major and trace dissolved gases and their ratios are done almost instantaneously and in high-precision from a single water sample. The use of the degassing membrane as a preparation step of the water sample eliminates the need for the traditional headspace equilibration for discrete samples (Tortell, 2005a). Because the flow of the water through the membrane is proportionally smaller than the flow of the dissolved gases, the latter are enriched after the degassing process (Ketola *et al.*, 2002). The results obtained by MIMS

provide levels of detection as low as nmol l^{-1} of dissolved gases in water; this allows the identification of fine-scale structures in the distribution of gases in natural waters. MIMS has been shown to be a powerful tool for real time high-frequency gas measurements in several applications for environmental samples as in: sediment porewaters (Cartaxana and Lloyd, 1999; Hartnett and Seitzinger, 2003), air (Ketola *et al.*, 1997), urban wastewater monitoring and marine hydrothermal vents (Kibelka *et al.*, 2004).

1.9.1 Membrane interface for dissolved gas measurements in oceanographic applications.

The MIMS method has become a well-established method for measurements of dissolved gases in the ocean. It has been successful to measure DMS (dimethyl sulphide), the major gases in seawater (N_2, O_2, CO_2 and Ar) and their ratios (i.e. O_2/Ar and N_2/Ar) (e.g. Kaiser *et al.*, 2005; Tortell, 2005a; Tortell, 2005b), as well as for stable-isotope tracer addition experiments (e.g. An *et al.*, 2001). For oceanographic applications, the high frequency measurements from MIMS allow the identification of low scale temporal and spatial variability in the dissolved gas distribution, particularly in the highly variable upper water mixed layer or in coastal waters.

The measurement of O_2/Ar ratios with MIMS has been used in order to achieve estimates of marine productivity in the mixed layer (e.g. Kana *et al.*, 1994; Kaiser *et al.*, 2005; Tortell, 2005a). In the present work, this technique is applied for continuous *in situ* estimates of *N* on board oceanographic ships in the Southern Ocean.

The membrane is the most important element in the MIMS method. In order to improve the continuous measurements of different gas species in oceanographic applications, several materials, designs and sizes have been tested (Kana *et al.*, 1994; Kaiser *et al.*, 2005; Tortell, 2005a).

The efficiency of the membrane for the extraction of dissolved gases relies on the analytical sensitivity for the diffusion of gases across the material of the membrane. Therefore, the diffusion of gas is proportional to the ratio of the surface area of the

membrane to its wall thickness, and the flow rate of the sample through the membrane (Tortell, 2005a; Sarma *et al.*, 2006b).

In 1994, Kana *et al*. tested a semi-permeable membrane interface of bore silicone tubing (*Silastic, Dupont*®) with a length of 5 cm and an internal diameter of 0.33 mm and a wall thickness of 0.15 mm. The total sample flow rate was 0.75 ml min^{-1} (Kana *et al.*, 1994). This experimental design showed a high stable laminar flow across the membrane with good signal stability and precision. However, drifts in the data over time were observed due to the dependence between the signal intensity and the speed of the pump used to feed the water sample. The flow rate was a limiting factor due to its dependence with the signal stabilization time. The thickness of the membrane walls and its length were found to be key factors to obtain a good analytical sensitivity. The membrane material used by Kana *et al.* was very permeable for H_2O vapour and CO_2. Thus, in order to remove these interferences before the sample gas enters the ionization step in the MS, a liquid nitrogen trap was recommended after the degassing process.

In 2005, Tortell developed a membrane with dimethylsilicone membrane plate (*Silastic Sheeting, Dupont*®) with a diameter of 3 cm and thickness of 0.025 mm. The aim of the author was to compare the efficiency and performance of the membrane by variation of water flow rates (from 100 to 1200 ml min^{-1}). Tortell concluded that during the degassing process, the stability of the flow rate becomes more important for poorly soluble gases, such as N_2, Ar and O_2. To achieve a good performance of degasification process in the membrane, a constant flow rate of the water flow should be maintained; this is particularly important for gases with low solubility properties. Variations in the sample flow rate through the membrane during the analysis can cause fluctuations in the absolute gas concentration determinations. The instability in the water flow rate also can cause significant fractionation for isotopic determinations (Sarma *et al.*, 2006b). About 80 % of these fluctuations can be eliminated using the normalization of the gases of interest (i.e. O_2 and N_2) with argon (Tortell, 2005a).

For the research presented in this thesis, a membrane developed by Kaiser *et al.* (2005) built of *Teflon AF*® (*Random Technologies*, *Dupont*®) was used. The dimensions of the membrane are an internal diameter of 0.6 mm and a length of 10 cm and it was connected to a quadrupole mass spectrometer (QMS). During Kaiser's experimental design, the sample flow rate of the membrane was about 12 ml min^{-1}. The membrane was kept at constant temperature in order to reduce variations of the water flow due to temperature and pressure effects from the presence of water vapour.

An important advantage of the membrane built of *Teflon AF*® over other materials is the lack of interferences that remain trapped after the degassing process. The *Teflon AF*® is a polymer less permeable to water but highly permeable to other gases over a wide range of temperatures (up to 300 ºC). *Teflon AF*® has also high compressibility and low thermal conductivity, which accounts for a good stability even during fast temperature changes in the water flow. In a comparison of the precision gained after repetitive measurements of ion current ratio for gases from Isotope Ratio Mass Spectrometry (IRMS) compared to MIMS, the first showed a precision of 0.1 % for O_2/Ar, while the last showed a precision of 0.05 % for short-term stability measurements every 10 to 30 s (Kaiser *et al.*, 2005).

In order to improve the continuous shipboard measurements of O_2/Ar by MIMS, Cassar *et al.* (2009) proposed a modification of the MIMS method by using an equilibrator cartridge of the water sample before entering the degassing membrane and the mass spectrometer (Cassar *et al.*, 2009). The authors called it "Equilibrator Inlet Mass Spectrometry" (EIMS). The equilibration step allows the dissolved gases to reach equilibrium and instead of using an alternate preparation of air-equilibrated water as standard, it collects periodically samples of atmospheric air transferred into the system. However, the EIMS method has a response time significantly longer than the one reached by MIMS and is not ideal for high spatial heterogeneity as in high-productivity coastal ecosystems (i.e. west Antarctic Peninsula) or as in dynamic regions (i.e. Drake Passage). Although the MIMS requires more physical space, preparation of equilibrated waters as standard and more daily attention compared to EIMS, the MIMS is recommended over the EIMS for applications in the Southern Ocean due to its faster response time.

1.9.2 Advantages and disadvantages of the MIMS method.

Several advantages are attributed to the use of MIMS. As mentioned before, the quantification of dissolved gases by MIMS is in real-time, with the lack of time-consuming previous steps for collection, extraction and concentration of the gas before its analysis in the MS. With the lack of a preparation step, the efficiency of the method increases in both time and precision.

The MIMS method is suitable for fieldwork for a wide spectrum of applications. For oceanographic on board high-resolution measurements of dissolved gases, the basic requirements for the MIMS method are a stable water pump, vacuum inlet and membrane interface coupled to a QMS for the detection of gas species connected to a computer controller. In Chapter 2 is presented the detailed description of the main components and specifications of the MIMS method as used on board in the cruises subject of this research.

Compared to QMS, the gas measurements by IRMS provide higher precision achieved by dual-inlet systems. However, this analysis is restricted to discrete samples in laboratories due to the high level of technical requirements for its installation and inaccessibility to mobilize it into oceanographic campaigns.

On the other hand, QMS are easy to handle with low cost maintenance providing good signal stability for residual gas analysis. Dual mass spectrometer detectors (i.e. electron multiplier and Faraday cup) can be used in order to monitor simultaneously both major and minor gases on board oceanographic ships. This procedure allows modifications directly during the field work at sea (Kana *et al.*, 1994; Tortell, 2005a).

Other important advantages offered by MIMS are: the cost per sample is low, solvents are not used and MIMS can be used for long-term continuous monitoring of environmental, biochemical and chemical processes (Ketola *et al.*, 2002). Besides, MIMS offers a fast time response (i.e. on the order of seconds to few minutes), being an advantage for applications in spatially heterogeneous oceanic regions subject to fast environmental changes (Cassar *et al.*, 2009). The estimation of the gas ratios by MIMS, offers a better precision than the absolute gas concentrations. The precision gained by measuring the gas absolute concentration with the MIMS method is one

order of magnitude higher (0.5 %) than the one reached estimating the gas ratios (0.05 %).

The difference in the precisions from absolute and gas ratios is due to the effect of changes in pressure. The variability of the atmospheric pressure has a greater effect for single gas measurements. By calculating the ratio of two gases the variability of the atmospheric pressure in the environment is diminished in the way that the changes in pressure affect both gases similarly. Thus, for high accuracy measurements a good pressure control during standard preparation must be considered (Emerson *et al.*, 1991; Kana *et al.*, 1994).

The process of delivering the flow of water from the surface ocean to the degassing membrane in oceanographic ships can have implications over the dissolved gas content of the water. The collection pump in the intake systems can cause a warming of the water flow. Furthermore, an outgassing or gas loss to the walls of the intake pipes is likely to happen if the material is not impermeable enough. These effects must be evaluated and taken into account for MIMS applications in oceanographic campaigns; however, the ratio between the dissolved gases would remain unchanged despite the changes in their absolute concentrations. This applies for gases like N_2, O_2 and Ar with similar solubility behaviour to changes in temperature, pressure and bubble-mediated gas exchange (Kaiser *et al.*, 2005).

The MIMS method has also some limitations. Measurements of gas supersaturated water due to an excess of entrainment of bubbles, or simply due to the high production of gas in the water (i.e. by photosynthesis in eutrophic waters), can lead to inefficient performance due to perturbations in the uniform gas flow needed across the membrane for an efficient degassing process. The membranes based on silicone capillary are especially susceptible to this process.

The application of MIMS in high productive waters (i.e. oceanic gyres or coastal waters) can also be sensitive due to the high loads of particulate material in the water flow. As a result, clogging of the membrane with loss on the degassing efficiency over time can occur. To avoid the loss of efficiency in the membrane in eutrophic waters, a pre-step to filter the water before it enters the membrane is recommended.

The main interference for gas measurements by the MIMS method is the presence of water vapour in the vacuum line that later on is diffused through the membrane. The presence of water vapour can account for up to 50 % of the total gas load, significantly decreasing the ionization efficiency of other gases in the ionization beam. Also, water vapour can account for some background contamination of O_2 and CO_2 in the ion source which becomes significant for measurements of water with low O_2 content (Tortell, 2005a).

Finally, an important limitation on the use of MIMS for dissolved gases in seawater is during the calibration of the MS. The standardization of the measurements by MIMS preferentially must be done by using absolute standards of the dissolved gases of interest. However, there is a lack of absolute standards based on gravimetrically or volumetrically prepared techniques. Traditionally, air-equilibrated water at known temperature and salinity is used, providing an accessible standard to be used during the analysis. However, over the basis of several days the stability of the standard can vary due to changes in temperature and bacterial growth; therefore, it is important to monitor the standard in a well controlled system (Kana *et al.*, 1994).

The limitations discussed above must be taken into account in order to reach long term stability for high precision measurements of dissolved gases. The on-board MIMS method poses the challenge of reaching a stable water inflow in the membrane using a stable pumping system, temperature control of the water sample, as well as assuring efficient control of interferences such as water vapour.

1.10 Estimates of gross oxygen production from the isotopic composition of dissolved oxygen.

To complement the observations of *N* from $\Delta O_2/Ar$, the determination of the ^{17}O anomaly ($^{17}\Delta$) is performed from the quantification of the isotopic abundance of the three oxygen isotopes in dissolved O_2. The $^{17}\Delta$ is used to estimate mixed-layer marine gross production in terms of oxygen (*G* in mmol m^{-2} d^{-1}) (Sarma *et al.*, 2006a). This approach poses the main advantage of not requiring bottle incubations as in the ^{18}O assimilation method. In the following sections are presented a detailed description of the measurement of the triple isotopic abundance of dissolved O_2 in seawater samples (section 1.10.1), the fundamentals, definition of $^{17}\Delta$ and standardization of isotopic measurements (sections 1.10.2 and 1.10.3). The range of $^{17}\Delta$ values in natural aquatic systems, together with the definition of *G* from $^{17}\Delta$ estimates, is presented in section 1.10.4.

1.10.1 Measurements of the dissolved oxygen isotopic abundance by Isotope Ratio Mass Spectrometry (IRMS).

In nature, elements can be present in different forms known as "*stable isotopes*", depending on the number of neutrons in their nucleus with different natural abundance. Oxygen has three stable isotopes with mass numbers 16, 17 and 18. The most stable and abundant oxygen isotope is ^{16}O (99.758 %) with minor abundance from ^{17}O (0.038 %) and ^{18}O (0.204 %).

After nitrogen, oxygen is the second most abundant gas in the Earth's atmosphere and as dissolved air in water bodies with an abundance of 20.946 % of the total air mixture (Chester, 2000; Luz and Barkan, 2005). The relative isotopic abundance, or enrichment of a sample to a reference material for any given isotope in the natural environment, is defined by the δ-notation as the ratio of the abundance of a lighter isotope over the heavier isotope in a sample (sa) with respect to the same ratio in a standard or reference (ref) expressed in per mille (‰).

For oxygen isotopes the relative abundance of the isotopes referenced to a known standard can be expressed according to the following equation; where $^{i}O/^{16}O$ denotes the relative abundance of ^{17}O or ^{18}O relative to ^{16}O.

$$\delta^{i}\mathrm{O} = R_{\mathrm{sa}}({}^{i}\mathrm{O}/{}^{16}\mathrm{O})/R_{\mathrm{ref}}({}^{i}\mathrm{O}/{}^{16}\mathrm{O}) - 1 \qquad (1.7)$$

where, i is equal to 17 or 18 (i.e. $\delta^{17}O$ and $\delta^{18}O$). The fractionation of the isotopic abundance of $^{17}O/^{16}O$ relative to $^{18}O/^{16}O$ for a sample with respect to a reference material, after a chemical or physical process in the environment, can be expressed in terms of the absolute ratios, ^{i}R. The preferred reference material is Vienna Standard Mean Ocean Water (VSMOW).

According to the isotopic relative abundance notation the absolute ratio can be expressed as:

$$\delta^{i}\mathrm{O} = ({}^{i}R_{\mathrm{sa}}/{}^{i}R_{\mathrm{ref}}) - 1 \qquad (1.8)$$

For convenience, the factor 10^3 is omitted, but the $\delta\,^{i}O$ results are reported in per mille. In the biological process of O_2 production and consumption, the fractionation of oxygen isotopes follows a 'mass-dependent' relationship (MDF) between $^{17}O/^{16}O$ and $^{18}O/^{16}O$ abundances. The MDF process for oxygen follows the classical theory of the "oxygen three isotope distributions" where the isotopes are controlled by the respective masses of the reactants. This theory was established by Urey in 1947 and followed by Bigeleisen and Mayer in the same year (Bigeleisen and Mayer, 1947; Urey, 1947). The work of these authors contributed in a significant way to the calculations of the equilibrium constants for isotope exchange reactions directly from the small difference in free energy of the isotopically substituted molecules.

For MDF natural processes, the relative ^{17}O enrichment would be approximately one half of the ^{18}O enrichment relative to ^{16}O (Luz *et al.*, 1999; Luz and Barkan, 2005). The main source of molecular oxygen fractionated in a mass dependent way to the atmosphere is from biological production by photosynthesis in terrestrial and aquatic plants. The isotopic composition of atmospheric O_2 is then controlled by biological

mechanisms (photosynthetic production and uptake by respiration), the hydrological cycle and stratospheric photochemistry (Luz *et al.*, 2002).

The notation based on relative abundances can be used to express the absolute isotope ratio of O_2 for products ($^{i}R_p$) and for substrates ($^{i}R_s$) involved in a momentary process (i.e. photosynthesis, respiration). The relationship between these terms is given by the isotope fractionation factor α as:

$$\alpha^{i}\mathrm{O} = \frac{^{i}R_p}{^{i}R_s} \qquad (1.9)$$

where, $^{i}R_p$ and $^{i}R_{sa}$ are the relative abundances of the sample with respect to a reference for the products (p) and substrates (s) in a specific process (e.g. ($^{i}R_s$ / $^{i}R_p$) = [c(^{i}O)/c(^{16}O)]$_s$ / [c(^{i}O)/c(^{16}O)]$_p$). The superscript *i* corresponds to the masses 17 or 18. Therefore, the factor α can be used to describe the overall fractionation process of several isotope exchange reactions.

If, $\alpha^{17}\mathrm{O}= {}^{17}R_p$ / $^{17}R_s$ and $\alpha^{18}\mathrm{O} = {}^{18}R_p$ / $^{18}R_s$, the relationship between fractionation factors involved in a specific process is given by:

$$\alpha^{17}\mathrm{O} = {}^{17}\Delta \times (\alpha^{18}\mathrm{O})^{\lambda} \qquad (1.10)$$

The correlation between fractionation factors therefore is given by the $^{17}\Delta$ with a slope (or isotope exponent) λ. The definition of $^{17}\Delta$ is given in detail in the section below.

1.10.2 Definition of ^{17}O anomaly ($^{17}\Delta$).

Early investigations in laboratory experiments, found that the process in which ozone is formed from molecular oxygen, conforms to a ‘mass-independent’ isotopic fractionation (MIF) (Thiemens and Heidenreich III, 1983; Miller, 2002). In the stratosphere, this process is characterized by the photochemical reaction to form ozone (O_3) from molecular O_2, induced by UV solar radiation at wavelengths below 315 nm.

This reaction fractionates oxygen isotopes in a mass-independent way with about equal ^{17}O and ^{18}O enrichments relative to ^{16}O, clearly different to the ratio for the mass dependent processes (e.g. Thiemens and Heidenreich III, 1983; Thiemens, 2001) driving an anomalously depleted atmospheric O_2 in $\delta^{17}O$ abundance compared to $\delta^{18}O$.

The term MIF is used to refer to any deviation of the ^{17}O enrichment from about half the ^{18}O enrichment, or to the MDF processes. As was discussed by Kaiser *et al*. (2004) although the ^{17}O and ^{18}O fractionation factors are clearly different, and therefore do depend on the isotope involved in the reaction, this definition must be identified preferably as 'oxygen isotope anomaly' or a 'non-mass-dependent' isotope fractionation (Thiemens and Heidenreich III, 1983).

As for the MIF process, the fractionation of oxygen in the stratosphere is such that $\delta^{17}O$ of O_2 decreases by a factor of 1.7±0.03 relative to $\delta^{18}O$, rather than a factor between 0.5 and 0.53 for MDF processes. Thus, in the stratospheric formation of oxygen a faster transfer of ^{17}O than ^{18}O occurs into CO_2 and establishes a reference value throughout the lower and middle stratosphere (Lämmerzahl *et al.*, 2002).

Ultraviolet photolysis of O_3 in the stratosphere generates an oxygen atom in an electronically excited state (equation 1.13), O (^1D), which can undergo isotope exchange with CO_2 (equation 1.14); this can be expressed in the following sequence of reactions:

$$O_2 + h\nu \rightarrow 2O \quad (1.11)$$

$$O + O_2 \rightarrow O_3 \quad (1.12)$$

$$O_3 + h\nu \rightarrow O(^1D) + O_2 \quad (1.13)$$

$$O(^1D) + CO_2 \rightarrow CO_3^* \quad (1.14)$$

$$CO_3^* \rightarrow CO_2 + O(3P) \quad (1.15)$$

$$O + O \rightarrow O_2 \quad (1.16)$$

As shown in the previous series of reactions, stratospheric isotopic fractionation of O_3 is based on the exchange of the oxygen atom between molecular O_2 and CO_2. Heavier isotopes are transferred to CO_2, increasing the abundance of $\delta^{17}O$ compared to $\delta^{18}O$. On the other hand, the $\delta^{17}O$ of O_2 decreases by more than 0.5 times the $\delta^{18}O$ decrease.

The formation rate of anomalous O_2 is determined by the amount of O_3 and CO_2 in the stratosphere and by the rate of O_2 photolysis. The fractionation process in the isotope transfer must have a temperature dependence to keep a constant relationship between ^{17}O and ^{18}O in the stratospheric CO_2 (Lämmerzahl *et al.*, 2002). The main source of stratospheric oxygen for the MIF is the ozone and atomic oxygen (^1D) being the ultimate source for the stratospheric O_2 reservoir. Thus, the O_2 reservoir in the air becomes anomalously depleted as CO_2 becomes anomalously enriched (Luz *et al.*, 1999).

Anomalous O_2 and CO_2 are transferred from the stratosphere to the troposphere and consequently to the surface ocean. The $^{17}\Delta$ remains in the atmospheric O_2 since the anomalous CO_2 loses this characteristic at the Earth's surface by isotope exchange. The CO_2 is hydrated, thus the isotope exchange is made with liquid water in leaves and in the ocean. The anomaly in the atmospheric O_2 also becomes more important considering the concentration of O_2 compared to the one of CO_2 (210,000 ppmv and 386 ppmv, respectively) (Blunier *et al.*, 2002). The CO_2 concentration given here corresponds to the annual global average for 2009 according to CO_2 monitoring by the Earth System Research Laboratory at the Global Monitoring Division, NOAA (*Dr. Pieter Tans, www.esrl.noaa.gov/gmd/ccgg/trends/)*.

An oxygen molecule cycles through the stratosphere nominally ~24 times before it is consumed by respiration. This number is equal to the ratio of the turnover time or residence time of O_2 in air with respect to biology (~1200 years) to the time required for the global atmosphere to cycle through the stratosphere (~50 years) (Bender *et al.*, 1994a; Luz *et al.*, 1999; Blunier *et al.*, 2002; Sarma *et al.*, 2006a). Therefore, it is enough time for the $^{17}\Delta$ in atmospheric oxygen to be transferred to the surface ocean via air-sea gas exchange.

The way to calculate $^{17}\Delta$ has improved over time as a result of more detailed studies in specific processes in order to identify variations and to improve the limits of detection. To quantify the $^{17}\Delta$, it is necessary to measure the excess of $\delta^{17}O$ using atmospheric O_2 as reference, considering a given $\delta^{18}O$ of O_2 produced solely by biological production and consumption (Luz *et al.*, 1999; Luz and Barkan, 2005).

In 2002, Miller referred to the ^{17}O, expressed by "$\Delta^{17}O$", as an indirect measurement of the ^{17}O excess, or deficit, in a sample with respect to a given mass-dependent reference fractionation line on the three isotope plot with slope λ. This was a general concept for a range of λ and sample δ-values and with dependence on the isotopic composition to different reference materials.

The $\Delta^{17}O$ in logarithmic expression according to Miller (2002) is given by:

$$\ln(1+\Delta^{17}O) = \ln(1+\delta^{17}O) - \lambda \ln(1+\delta^{18}O) \qquad (1.17)$$

Later on, the term "$^{17}\Delta$" for the ^{17}O anomaly was chosen by Luz and Barkan (2005) to represent the logarithmic expression of the $\Delta^{17}O$ ($\ln(1+\Delta^{17}O)$) as defined previously, thus:

$$^{17}\Delta = \ln(1+\delta^{17}O) - \lambda \ln(1+\delta^{18}O) \qquad (1.18)$$

The ^{17}O anomaly according to Luz and Barkan is the line intercept with the vertical axis in the plot $\ln(\delta^{17}O + 1)$ vs. $\ln(\delta^{18}O + 1)$, being an indirect measure of excess or deficit of ^{17}O in a sample with respect to the reference.

The magnitude of the $^{17}\Delta$ values calculated with equation 1.18 is very small, thus the resulting value must be multiplied times 10^6, which represents "per meg" units. After a careful revision made by Kaiser *et al.* (2004) and Miller (2002) of previous $^{17}\Delta$ definitions reported by several authors (Cliff and Thiemens, 1997; Li and Meijer, 1998; Miller, 2002; Assonov and Brenninkmeijer, 2003; McLinden *et al.*, 2003) and laboratory experiments the latter is the preferred definition chosen for the quantification of oxygen isotope anomalies.

Miller and Kaiser *et al*. pointed out the difference in the consideration of the logarithmic ^{17}O non-logarithmic expression. As a conclusion, $^{17}\Delta$ is very closely approximated to $\ln(1 + \Delta^{17}O)$ for values $^{17}\Delta << 1$, therefore any distinction between $^{17}\Delta$ and $\Delta^{17}O$ only reaches the limit of detection (~6 per meg) for $^{17}\Delta > 3400$ per meg, which is an order of magnitude greater than the ^{17}O anomaly associated with the processes of interest in the marine and atmospheric isotopic fractionation of oxygen (i.e. photosynthesis, respiration and stratospheric chemistry).

Finally, Miller suggested that using the logarithmic notation to plot the relative abundance of ^{17}O and ^{18}O, avoids the dependence of the λ value over the isotopic composition of the reference material. In the $\Delta^{17}O$ the three isotope exponent λ, expresses the ratio of the partition of the triple oxygen isotopes in a reaction; thus, λ represents the slope obtained from the trend line of the plot of the relative abundance of $\ln(1+\delta^{17}O)$ vs. $\ln(1+\delta^{18}O)$ generated by mass dependent fractionation, with the ordinates representing the ^{17}O anomaly. The fractionation slope λ is not equal to a single value. It corresponds to the slope of the characteristic kinetics of the isotope fractionation process which it comes from, thus every isotopic fractionation process in the environment will have a particular λ value (Miller, 2002; Kaiser *et al.*, 2004).

For the biological production and consumption of O_2 in the environment, a wide range of $\delta^{17}O$ and $\delta^{18}O$ values have been observed from laboratory observations. As a result of plotting one against the other, various experiments had suggested different values for the reference slope λ, depending on the main mass dependant isotopic fractionation process to be used as reference for the $^{17}\Delta$ estimation.

In MDF processes, the λ values are within a range of 0.5 and 0.53 defining the variety of slopes for the different kinetic isotope fractionation lines (Kaiser et al., 2004; Luz and Barkan, 2005). In 2003, Angert *et al.* suggested a value of λ equal to 0.516, associated with ordinary dark respiration (cytochrome oxidase pathway) as the dominant form of oxygen consumption by biological processes. The slope for respiration via the alternative pathway is 0.514 and for photorespiration is ~0.506 (Angert *et al.*, 2003).

Respiration is the main MDF process of atmospheric O_2 (Blunier *et al.*, 2002). The lighter oxygen isotope, ^{16}O, is consumed preferentially, increasing both $\delta^{18}O$ and $\delta^{17}O$ in a mass-dependent way. Since respiration does not cause $^{17}\Delta$ to change (Reuer *et al.*, 2007a) the fractionation line of the isotopic abundance during this process is preferred as a reference to evaluate the deviation from MDF (Luz *et al.*, 1999; Barkan and Luz, 2003; Luz and Barkan, 2005).

In order to understand in detail the role of the respiration process in the alteration of the air O_2 isotopic abundance, the "*Dole effect*" must be defined. In the aquatic systems, the fact that the O_2 in the ocean water is depleted in $\delta^{18}O$ compared with atmospheric O_2 is known as the *"Dole effect"* (Dole and Jenks, 1944). This is mainly attributed to the isotopic composition of O_2 produced by marine and terrestrial photosynthesis, and the discrimination against ^{18}O during respiration. The discrimination increases $\delta^{18}O$ in the remaining oxygen by ~18 – 20 ‰ compared with seawater O_2 (Bender *et al.*, 1994b; Blunier *et al.*, 2002; Miller, 2002). The origin of the Dole effect remains uncertain; recent estimates explain a value between +20.8 and +23.5 ‰ of $\delta^{18}O$ in excess in the air O_2 compared with the seawater O_2 with respect of SMOW (Bender *et al.*, 1994b). To estimate the Dole effect, the uncertainties due to underestimations of the leaf water enrichment (increase in ^{18}O due to evapotranspiration of the lighter isotope in leaves of terrestrial plants) and alternative respiration pathway (i.e. respiration by the alternative oxidase pathway) must be considered (Bender *et al.*, 1994b; Angert *et al.*, 2003).

In 2005, Luz and Barkan suggested 0.5179±0.0006 as an optimal and universal value to characterize the kinetic respiratory slope λ. This value represents the main O_2 consumers (i.e. bacteria and other microplanktonic organisms) in aquatic systems, characterizing both dark and light respiratory (Mehler reaction and photorespiration) fractionations. The experiments of Luz and Barkan showed that the value of λ is independent of the temperature in the range of temperatures relevant for most living organisms (17 to 37 ºC) and that the triple isotope fractionations under light and dark conditions are identical within the experimental error.

In the present work, the preferred value for λ is 0.5179 following Luz and Barkan (2005); this is to assure a high precision determination of $^{17}\Delta$ in per meg from the $\delta^{17}O$ and $\delta^{18}O$ in seawater samples.

1.10.3 Standardization for O_2/Ar and oxygen isotopes measurements in natural waters.

In contrast to λ, the magnitude of $^{17}\Delta$ depends not only on the biological and photochemical processes, but also on the arbitrary selected reference material (e.g. atmospheric O_2 or VSMOW) and in the value of the reference slope λ (Luz and Barkan, 2005).

In natural waters, atmospheric O_2 is the preferred standard as reference for the estimation of O_2/Ar ratios and triple oxygen isotopes. The selection of this standard against the VSMOW is due to:

1- Its isotopic composition is close to the previous observed composition in dissolved O_2 in most natural O_2 samples; while VSMOW is about 20 ‰ depleted in ^{18}O with respect to most air samples.
2- The method of preparation of oxygen from VSMOW may cause some isotopic fractionation with a variable and unknown relationship between the three oxygen isotopes in VSMOW to atmospheric O_2.
3- Atmospheric oxygen is easily obtained without any fractionation due to the preparation process (Luz et al., 1999; Barkan and Luz, 2003; Luz and Barkan, 2005).

1.10.4 Range of values for $^{17}\Delta$ in natural aquatic systems.

The characteristic isotopic signature of the biologic mass dependent and independent stratospheric processes, as given by the $^{17}\Delta$ in dissolved O_2, is useful for the determination of the rate of photosynthesis and respiration in aquatic systems. For this, it is necessary to quantify the magnitude of the deviation of O_2 that would have been produced during the MDF process in the absence of stratospheric chemistry (Bender *et al.*, 1994a; Luz and Barkan, 2000; Blunier *et al.*, 2002).

The range of values of $^{17}\Delta$ for dissolved oxygen in the mixed layer of aquatic systems is between 0 to +249 per meg. The maximum value of $^{17}\Delta$ for seawater and O_2 produced by photosynthesis ($^{17}\Delta_{max}$) is +249 ± 15 per meg, measured against air O_2 as reference and considering the respiratory slope λ as 0.5179 (Luz and Barkan, 2000; Hendricks *et al.*, 2004; Luz and Barkan, 2005; Sarma *et al.*, 2006a; Reuer *et al.*, 2007a). Marine photosynthesis produces O_2 that has the same isotopic composition as seawater ($\delta^{18}O$ = −22.96 ‰). Photosynthesis converts oxygen of H_2O to O_2 with a slight O_2 fractionation (about ±0.3 ‰); however, such small values will not affect considerably the $^{17}\Delta$, leaving the resulting isotopic composition of photosynthetic O_2 very close to that of the water used in this process (Guy *et al.*, 1993; Luz and Barkan, 2000; Miller, 2002; Helman *et al.*, 2005); thus, it is assumed that there is essentially no isotopic fractionation in photosynthesis. Experiments carried out by Luz and Barkan in 2005, confirmed that the $^{17}\Delta$ of photosynthetic O_2 is identical to that of water within the experimental error.

Biological steady state between photosynthesis and respiration can be achieved if $\delta^{18}O$ of O_2 produced by photosynthesis equals $\delta^{18}O$ of O_2 consumed by respiration. Due to the O_2 from the stratospheric fractionation is enriched in $\delta^{18}O$, the stratospheric exchange reaction will tend to equal the $\delta^{18}O$ (Hendricks et al., 2004; Blunier et al., 2002; Luz and Barkan, 2005). However, it has been already discussed that respiration does not cause $^{17}\Delta$ to change.

By definition, the $^{17}\Delta$ of atmospheric O_2 ($^{17}\Delta_{air}$) is 0 per meg. The value of dissolved O_2 in seawater at STP conditions and equilibrium solubility ($^{17}\Delta_{eq}$) has led to controversy since various authors have found a range of values at room temperature. For mean ± 1 standard error, the $^{17}\Delta_{eq}$ values reported by other authors have been: 18 ± 2 per meg (Juranek and Quay, 2005; Sarma *et al.*, 2006b); 8 ± 2 per meg (Reuer *et al.*, 2007a); for mean ± 1 standard deviation: 16 ± 2 per meg (Luz and Barkan, 2000). Recently, Luz and Barkan (2009) suggested a linear fit for $^{17}\Delta_{eq}$ considering the seawater *in situ* temperature (θ in °C): $^{17}\Delta_{eq} = 0.6 \times \theta + 1.8$; where $^{17}\Delta_{eq}$ is given in per meg (Luz and Barkan, 2009).

The difference between $^{17}\Delta_{eq}$ with respect to the reference value $^{17}\Delta_{air}$ is due to the processes occurring when O_2 is dissolved in the water (Luz and Barkan, 2000).

In the next schematic (Figure 1.8), the relationship between $\delta^{17}O$ and $\delta^{18}O$ in VSMOW is used to show the interactions between photosynthetic and atmospheric oxygen in aquatic systems and how this is balanced by air-sea exchange. It is assumed that the production of oxygen from marine photosynthesis is the dominant source of this gas and constitutes the primary supply of atmospheric oxygen. Biological reactions dominate the turnover of O_2 in the mixed layer and play a key role in the isotopic composition of dissolved oxygen (Luz *et al.*, 1999; Luz and Barkan, 2000; Blunier *et al.*, 2002; Miller, 2002). As more O_2 with a biological isotopic signature is produced by photosynthesis in the mixed layer, the anomaly introduced from the atmospheric O_2 is removed, until reaching the maximum value for $^{17}\Delta$ ($^{17}\Delta_{max}$ = +249 per meg).

The effect of gas exchange is always to push O_2 towards equilibrium with the atmosphere. Air-sea gas exchange introduces O_2 from the tropospheric reservoir which contains the ^{17}O anomaly signature (^{17}O depleted with respect to $\delta^{18}O$ in comparison to the O_2 produced by photosynthesis and from the water molecule). By bringing more atmospheric O_2 into the mixed layer, the $^{17}\Delta$ will tend to decrease until reaching the equilibrium value ($^{17}\Delta_{eq}$) depending on the temperature of the seawater (Luz and Barkan, 2000; Luz and Barkan, 2009). In a global perspective, the estimation of $^{17}\Delta$ is a proxy to analyze at temporal and spatial macro-scales, the changes of global photosynthesis, which can be related to the levels of the concentration of CO_2 in the ocean.

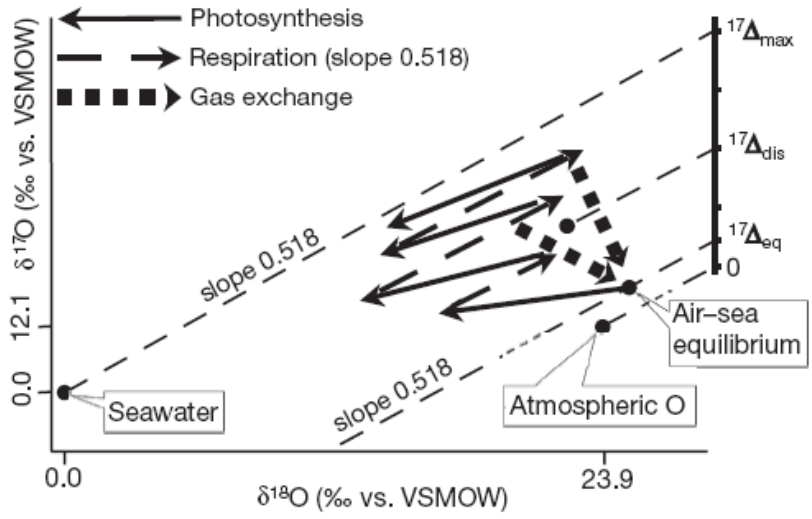

Figure 1.8 – Schematic illustration of the relationship between $\delta^{17}O$ and $\delta^{18}O$ of air O_2 vs. for VSMOW (‰) (Barkan and Luz, 2005). The values of $^{17}\Delta$ for dissolved oxygen ($^{17}\Delta_{dis}$ in the figure and $^{17}\Delta$ in the text; right axis in per meg) follow the line with slope 0.518 (λ) and depend on the rate of oxygen produced by photosynthesis and the oxygen entrained from the atmosphere. The $^{17}\Delta$ of atmospheric air is 0 per meg. As photosynthesis adds O_2 (full-line arrows) the $\delta^{18}O$ decreases with a rise in $^{17}\Delta$ towards +249 per meg. As gas exchange delivers atmospheric O_2 (dotted-line arrow) the $^{17}\Delta$ will decrease towards the value in equilibrium ($^{17}\Delta_{eq}$). Respiration forces O_2 to decrease (dashed-line arrow) with an increase in $\delta^{18}O$ of the dissolved water and $^{17}\Delta$ remains unchanged following the same line with slope λ (Luz and Barkan, 2009).

In 2000, Luz and Barkan showed that the relative rate of photosynthesis (as given by G) can be calculated from $^{17}\Delta_{max}$, $^{17}\Delta_{eq}$ and the magnitude of the measured $^{17}\Delta$ in dissolved oxygen, considering a steady-state mixed layer, according to:

$$G = k_w \times c_{eq}(O_2) \times \left[\frac{^{17}\Delta - {}^{17}\Delta_{eq}}{^{17}\Delta_{max} - {}^{17}\Delta} \right] \qquad (1.19)$$

G equals the total O_2 production from photosynthesis in the mixed layer, also produced over the residence time of O_2 in the mixed layer. Finally, the ratio of N over G is equivalent to the "f ratio" (Eppley and Peterson, 1979) in terms of oxygen ($f(O_2)$) where lower values indicate that most of the oxygen being produced by photosynthesis in the mixed layer was consumed by respiration within the same range of depth (Hendricks *et al.*, 2004).

Chapter 2

Methods

2.1 Field work

In this chapter, I present the method followed to estimate marine biological productivity from dissolved oxygen measurements. During two oceanographic research cruises, dissolved oxygen concentrations ($c(O_2)$) were measured by an oxygen/temperature optode (Model 3835, *Aanderaa* Instruments AS, Bergen, Norway) in the ship's scientific underway seawater supply (USW). From the same source of water, O_2/Ar ratios were measured continuously by Membrane Inlet Mass Spectrometry (MIMS).

The continuous measurements were calibrated by discrete samples taken from rosette samples and from the USW. Discrete samples were also used for the quantification of $^{17}O/^{16}O$ and $^{18}O/^{16}O$ by Isotope Ratio Mass Spectrometry (IRMS) in the university laboratory.

The method used here has been thoroughly described previously in various works (Craig and Hayward, 1987; Luz *et al.*, 1999; Luz and Barkan, 2000; Hendricks *et al.*, 2004; Kaiser *et al.*, 2005; Reuer *et al.*, 2007a). With the aim of improving the efficiency and to test the method used here in different regions of the world's oceans, various authors have been making improvements for different applications (Tortell, 2005a; Sarma *et al.*, 2006b; Cassar *et al.*, 2007; Sarma *et al.*, 2008; Luz and Barkan, 2009; Juranek and Quay, 2010) since it was first tested.

Here, I describe in detail the shipboard set up used for continuous measurements in polar waters during extensive oceanographic cruises.

2.1.1 Oceanographic cruises.

The following table lists (Table 2.1) the two oceanographic cruises that are the subject of this thesis. Both were done during the austral summer of 2007 in the Pacific sector of the Southern Ocean.

Auxiliary physical variables for each cruise were also collected and analyzed. Details of the shipboard sampling system, laboratory work, data analysis and calibration are explained in the following sections of this chapter.

Table 2.1 – List of oceanographic campaigns sampled for marine productivity estimates.

Cruise	*Project*	*Principal investigator (affiliation)*	*Research ship (acronym)*	*Area of study and dates*
JR158	ADELIE (Antarctic Drifter Experiment: Links to Isobaths and Ecosystems)	Karen Heywood (University of East Anglia)	*RRS James Clark Ross* (JCR)	Drake Passage and Weddell sea; February 2007
JR165	ACES-FOCAS (Antarctic Climate and the Earth System - Forcings from the Oceans, Clouds, Atmosphere and Sea-ice)	Deborah Shoosmith (British Antarctic Survey)		Drake Passage and Bellingshausen sea; February to April, 2007

2.1.2 Rosette sampling.

During the cruise JR158, a stainless steel frame (*SBE32 24* way rosette pylon) equipped with 8 10-l Niskin bottles (*General oceanic* 1010) and a CTD (*Sea-Bird 9/11 plus*) was deployed at 20 stations (i.e. 20 CTD casts). The CTD had two temperature, pressure and conductivity sensors. The rosette was also equipped with other sensors (i.e. temperature, oxygen, fluorometer) and an ADCP (Acoustic Doppler Conductivity Profiler). Details of the calibration by manufacturer and general configuration can be found in the corresponding cruise report (http://www.bodc.ac.uk/data/information_and_inventories/cruise_inventory/report/jr158.pdf).

Cruise JR165 was subsequent to JR158 and the same CTD configuration was used for both cruises. For cruise JR165 the rosette was prepared with 12 10-l Niskin bottles for the collection of water samples; details of sensors used and configuration are found in the corresponding cruise report (JR165 cruise report; D. Shoosmith, *in preparation*).

2.1.3 Underway Surface Seawater Sampling System (USW-SS)

A schematic design of the USW sampling system (USW-SS) for O_2/Ar and $c(O_2)$ is shown in Figure 2.1. The USW-SS is divided into three main components that correspond to outlets of underway seawater for different sampling purposes. Referencing in parenthesis to the numbers in figure 1: free USW outflow for discrete sample collection (1), O_2/Ar sampling outlet (2) and $c(O_2)$ sampling outlet (3).

Two types of discrete samples were collected from outlet 1: 1) for quantification of $c(O_2)$ by Winkler titration (section 2.3) and 2) for quantification of O_2/Ar and triple O_2 isotopes by IRMS (section 2.6).

The system was connected mainly by PVC tubing (*Tygon*®) of different diameters from the USW outlet tap. The tubing was covered, as much as possible, with insulating foam to avoid warming of the water flow on its transit from the tap to the degassing membrane.

With PVC tubing of the same characteristics, outlets 2 and 3 were attached to the corresponding analytical equipment (see below). Therefore, as outlet 1 was a free flow it was also used to regulate the water flow due to instabilities in the ship's seawater intake.

From outlet 3 of the sampling system, the USW was directed into a 500 ml dark plastic open bucket (4) where an *Aanderaa* optode 3835 (5) was introduced. The optode is an optical sensor based on dynamic fluorescence quenching; therefore, while operating it must not be exposed to direct light. Care was taken to avoid bubbles from turbulent flow. Unlike electrochemical oxygen measurements, optodes do not consume oxygen; hence, the method is not flow sensitive and can be used both in water and air. The oxygen response of an optode is exponential (i.e. highest sensitivity at low concentrations). The manufacturer-stated resolution is <1 μmol l^{-1}

with an accuracy better than 8 μmol l^{-1} or 5 %, whichever is greater. The e-folding response time of an optode to O_2 changes is < 25 s. The maximum sampling rate stated by the manufacturer is 10 Hz, however in the present study a data point was recorded every 10 s (0.1 Hz). A sufficient flow through the open buckets (components 4 in Figure 2.1) must be maintained in order to ensure a constant replacement of water during the acquisition. A detailed description of the optode sensor, data acquisition and calibration are shown in section 2.5 below.

From outlet 2, the USW flow was directed through to a closed 50 μm filter (6) used to remove bigger particles that may clog the membrane. The outflow from the 50 μm filter was ≈600 ml/min and directed to an open bucket (7) in order to remove macroscopic bubbles and avoid pressure surges. The water in the bucket was continuously pumped using a gear pump (*Micropump*) (9), through a 4-port 2-position valve (*Valco*) (8) to a membrane chamber (15). This interface consisted of a *Teflon AF®* membrane (*Random Technologies*) mounted on the inside of a PVC membrane chamber (hereinafter referred as to "*membrane box*"). The inner diameter of the degassing membrane is 600 μm and the length is 10 cm. The gear pump was used to maintain a constant water flow from the inlet through the membrane by regulating the frequency of the rotor.

The membrane box and PVC tubing were submerged in a water bath controlled at constant temperature (0 °C) (14). This latter was in order to eliminate the O_2/Ar variations in the water flow due to changes in temperature, water vapour pressure effects and also to avoid the degasification of water before entering the membrane.

The membrane was held under vacuum and connected to a quadrupole mass spectrometer (QMS, *Pfeiffer Vacuum Prisma*) (16), using a safety valve to protect the QMS from membrane failure and variations in pressure inside the system. The MS was equipped with two detectors: channeltron and faraday cup.

The outflow from the membrane box was restricted by a needle valve (17) to provide back pressure in the flow and to avoid bubble formation inside the membrane box that can cause signal instabilities recorded by the MS. This step was necessary in order to eliminate bubbles trapped in the system. A flow meter (18) was located in

the outflow tubing (19) in order to measure the water outflow rate. The flow rate during the JR158 was 75 ml/min and during the cruise JR165 was about 30 ml/min.

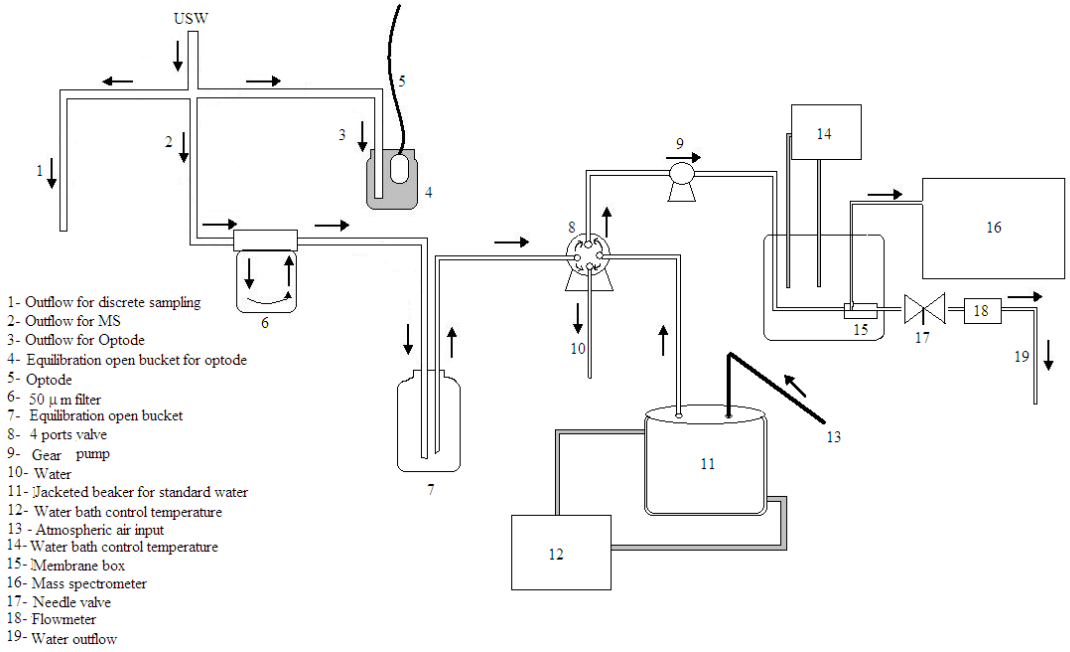

Figure 2.1 – Schematic diagram showing the main components of the on-board continuous and discrete Underway Surface Seawater sampling system (USW-SS) for O_2 and O_2/Ar quantification. The connections between the components are tubing of ¼ ” of PVC (*Tygon*®).

The resolution of the continuous data for the MIMS was 6 s, equivalent to one cycle of measurements. The ion intensities and derived signals of interest, including O_2/Ar, were recorded and stored on a daily basis. The complete list of signals recorded by MIMS during both cruises is shown in table 2.2. The e-folding response time for the MIMS was found to be on average 2 min.

The average spatial sampling resolution (at a ship’s speed of 10 kn) for the acquisition of MIMS data corresponded to 300 m. In the case of the optode data was about 100 m.

As part of the USW-SS, air-equilibrated seawater was prepared as standard (hereinafter referred to as “*equilibrated water*”) to verify the performance of the MS during the period of analysis. Seawater previously filtered through a 0.2 µm cellulose acetate filter, was kept under constant bubbling with marine air and stirring in a 1.5 l jacketed glass beaker (11). The air was drawn with a diaphragm pump through a line (13) located at the top of the main mast of the ship.

Table 2.2 – Ion intensities and composite signals of interest recorded by MIMS for the continuous on board analysis of USW.

Compound/ Element	*m/z (intensity)*
H_2O	18
N_2	28
^{15}N	29
O_2	32
Ar	40
CO_2	44
$^{13}CO_2$	45
CO^{18}_2	46
Derived signals	
O_2/Ar	
O_2/N_2	
N_2/Ar	
$^{14}N^{15}N$ / ^{14}N	
$^{13}CO_2/^{12}CO_2$	
Air	
CO_2/Air	
H_2O/Air	

The water temperature in the beaker was controlled with a second water bath (12). The *Valco* valve mentioned above (8) was used to select manually the flow of water to be delivered to the membrane box, which are the flow from the USW (sample) or from the equilibrated seawater beaker (standard). The total volume of the jacketed beaker was enough to pump approximately 15 min of equilibrated water through the membrane box. A stable signal was achieved within 2 min from the pump switching (equivalent to the MIMS response time). Regular intervals of equilibrated waters were run during the data collection. One equilibrated water run was done per 24 h of cruise as long as the MS and USW were working. More details of the MIMS data collection and calibration are presented in section 2.7.

The next Figure is a photpgraph showing the main components of the shipboard USW-SS with the MIMS method. The picture corresponds to the system on board the *B/O Hespérides* during the ESASSI oceanographic cruise in January 2008; a subsequent campaign of the cruises that are subject of this thesis.

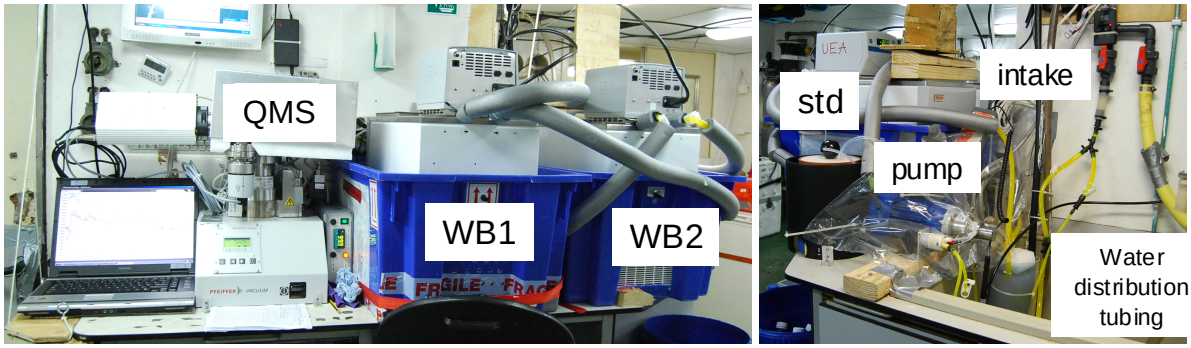

Figure 2.2 – Main components of the MIMS method for shipboard dissolved gas ratio measurements. From left to right: computer to record the data, quadrupole mass spectrometer (QMS), water baths with controlled temperature (WB1 and WB2) for water flow tubing and membrane box; jacketed beaker for equilibrated water (std); gear pump to deliver the flow of water through the system (pump); tap of source of intake water (intake) and yellow PVC tubing are the main distribution lines of water (Water distribution tubing). ESASSI cruise *B/O Hespérides*, January 2008.

2.1.4 Surface water flow perturbations.

The entrance of bubbles is the main cause of signal instabilities during sampling. Therefore, the quality of the recorded measurements depends strongly on the physical design of the ship's intake and pumping system. In section 2.8, the effect of the USW intake system on the $c(O_2)$ and O_2/Ar ratio measurements on the JCR are discussed.

The perturbations causing noise in the continuous signals recorded, both from the MIMS and optode, were due to two main reasons:

1) Perturbations in the continuous water inflow due to entrainment of bubbles in the intake system by:
   - Rough seas causing a turbulent inflow of seawater, this event is common during the presence of high wind conditions,
   - Intake design, enhancing a turbulent flow of water inside the pipes,
   - Probe height variations, manually performed according to navigation conditions (surrounding ice, turbulent surface water column, etc.),
   - The turnover of the intake sieves to trap coarse particles. The intake of the JCR was equipped with two sieves: pre-sieve of 5 mm mesh and a post-sieve of 2 mm mesh. The purpose of these sieves is to remove coarse particles before the water is delivered by the pump through the uncontaminated system. This action was performed on average once a day.

- As a result of the sieves turnover, perturbations in the water flow can cause a turbulent flow.
- Unexpected events like pieces of ice trapped in the intake,
- Variations in the flow rate due to intake's pump malfunctioning,
- Switching on and off the intake flow.

The entrance of bubbles in the intake system due to the previous events can not be controlled easily, or at all, during continuous data acquisition on an oceanographic campaign. These events are identified and recorded on board to be taken into account during data analysis, by discrimination of "good" and "bad" periods of data. For this purpose, a diary containing the observed events was kept at all times.

2) Local perturbations in the USW-SS

Each set of continuous data from the optode and MIMS also presented independent perturbations due to particular problems in the analytical equipment or to malfunction in some of the components of the USW-SS.

The optode component was more stable than the MIMS. The instabilities recorded in the optode continuous data were mainly due to the perturbations mentioned above in the intake system.

For the MIMS data collection, the main local perturbations were:

- noise or spikes in the continuous signal due to membrane behaviour during degasification (i.e. clogging, noise generated during the degasification step mainly due to alterations in the laminar flow),
- air injection into the membrane instead of water inflow due to leaks in the system,

These instabilities in the signal were also recorded in the diary and removed during the data analysis.

2.2 Auxiliary variables.

Auxiliary variables were also acquired during the cruises and used for the analysis, those are: sea surface temperature (SST), sea surface salinity (S), navigation data (longitude and latitude), wind speed (u) and direction, barometric pressure (P) and air temperature (T_{air}). The data processing for each set of complementary variables after acquisition was carried out by individuals from the different research groups

involved in the oceanographic campaigns. Details can be found in the corresponding cruise reports (section 2.1.2 for reference). All data analysis was done in MATLAB. The acquisition time for each group of data was variable. The optode data was collected every 10 s while each data point in the MIMS data was recorded every 6 s.

The time interval for the navigation, meteorological, SST and *S* varied from 1 s to 1 min. To facilitate the data analysis, the complementary variables, together with the optode and MIMS continuous data, were merged into a matrix with a common time base and a grid with a resolution of 10 s.

Periods of time considered as "bad" for the optode or MIMS data were replaced by the suffix "NaN" (Not a Number). The list of variables included in the merged matrix for each oceanographic campaign is shown in table 2.3. Details of each variable and a brief description for calibration are described in the following sections.

Table 2.3 –Working continuous variables.

	Symbol	*Units*		*Symbol*	*Units*
Optode			**MIMS**		
Dphase	ϕ	degrees	Cycle		1
Temperature	θ_{opt}	°C	Oxygen	O_2	Å
Oxygen	$c(O_2)$	μmol kg^{-1}	Argon	Ar	Å
Oxygen supersaturation	ΔO_2	%	Internal pressure	P_{int}	mbar
			O_2/Ar (Channeltron)	O_2/Ar	1
			O_2/Ar (Faraday Cup)	O_2/Ar	1
Navigation			Air	Air	mbar
Latitude	Lat	degrees	Water/Air	H_2O/Air	1
Longitude	Lon	degrees			
			SST sensor		
Meteorological			Sea surface temperature	θ_{int}	°C
True wind speed	u	m s^{-1}			
True wind direction	τ	degrees	**Thermosalinograph (TSG)**		
Atmospheric pressure	P	mbar	Temperature	θ_{TSG}	°C
Air temperature	T_{air}	°C	Sea surface salinity	S	1

2.2.1 Sea surface temperature (SST)

Three sets of continuous SST were obtained by the end of each cruise:

1) Optode continuous temperature (θ_{opt}), recorded from the USW along with the $c(O_2)$ data,

2) Sea surface temperature (θ_{int}) from the sensor located in the bow of the ship in the intake of the USW (called "oceanlogger"), and

3) Temperature from the thermosalinograph sensor (θ_{TSG})

The variable SST is used here as the generic term for the sea surface temperature; this also corresponds to the final calibrated signal (see below) used as auxiliary variable for the productivity estimates.

To evaluate the signal stability from the three different temperature measurements, offsets due to warming in the intake pipes and time-delays were identified and corrected.

a) Response time of signal stabilization after periods of USW flow restoration.

In the case of the JCR, the response time of θ_{int} to reach a stable signal, after an event of flow restoration, was about 1 h. Figure 2.3, shows an example of the typical oceanlogger signals from the variables (i.e. water flow, θ_{int}, conductivity, $S - 32$ and θ_{TSG}) measured for a period of 7 hr after water flow restoration. The stabilization time for conductivity, water flow and salinity signals was about 6 min (0.1 h), while it is evident that for θ_{int} and θ_{TSG}, the stabilization time for the signal was about 1 h after flow restoration at time 0.

The observed lag is probably due to the lack of insulation of pumps in some sections of the intake pipes, causing a slow thermal response. To eliminate the effect of different stabilization times on the signals, we removed all data for the periods until one hour after restoration of the intake water flow.

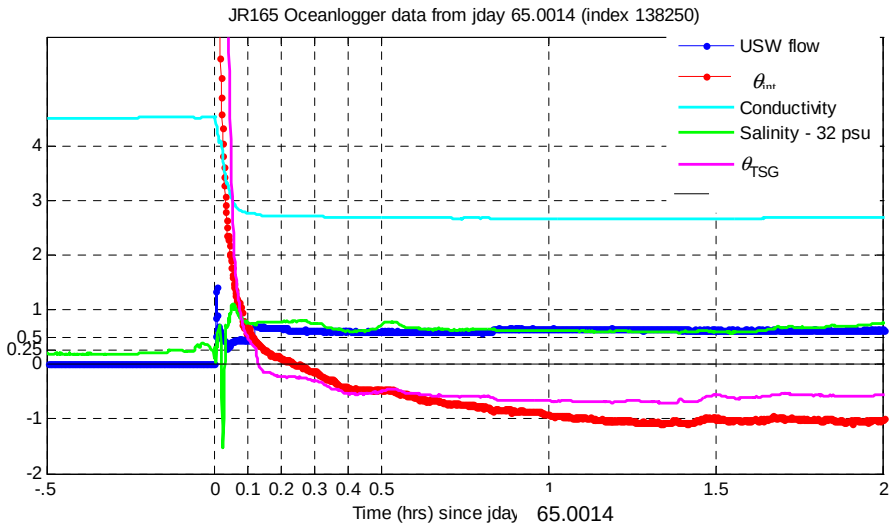

Figure 2.3 – Typical oceanlogger signals for Julian day 65.0014 showing the delay time after USW flow restoration: blue, USW flow; red, θ_{int}; cyan, conductivity; green, salinity – 32 and magenta, θ_{TSG}.

b) Temporal stability of continuous temperature signals.

To evaluate the stability over time of the temperature sensors, I compared the temperature signals from the three sensors during Julian days 57 to 98 (26 February to 8 April 2007, respectively) on cruise JR165. The difference between data sets was calculated (i.e. $\theta_{TSG} - \theta_{opt}$; $\theta_{int} - \theta_{opt}$ and $\theta_{TSG} - \theta_{int}$) in order to observe the stability between the signals over time.

Considering the location of the three temperature sensors, the θ_{int} was expected to be the lowest temperature recorded (sensor located at the bow of the ship), followed by similar temperatures from θ_{opt} and θ_{TSG} for being located in the deck level of the ship. Despite the seawater temperature variations, an offset of temperature between signals is expected.

As can be observed in the next figure, at the beginning of the period at around Julian day 56.5, the relationship between the temperature signals was: $\theta_{TSG} > \theta_{opt} > \theta_{int}$. Over a period of 42 days there is a constant increase in the θ_{int} with respect to θ_{opt} (i.e. $\theta_{int} - \theta_{opt}$) of about 0.6 ºC (from an average of −0.3 ºC to 0.3 ºC).

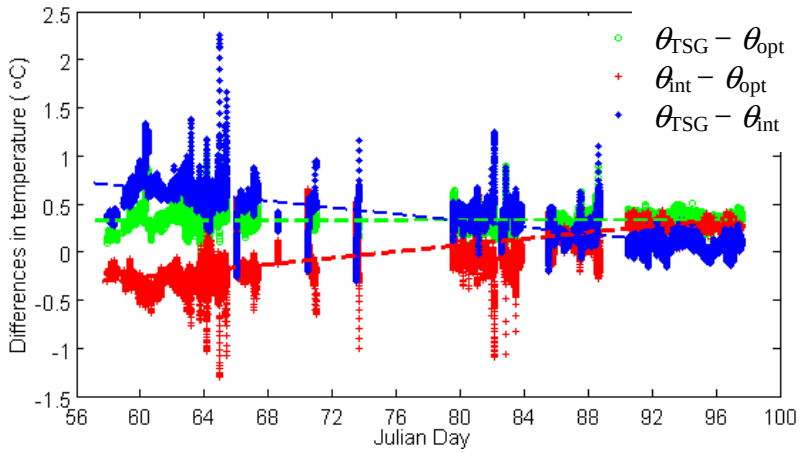

Figure 2.4 – Differences (symbols) and linear relation (dashed lines) between three continuous sea surface water temperatures from sensors recorded over 42 days in Drake Passage and Bellingshausen Sea (JR165 cruise) at JCR: green circles, $\theta_{TSG} - \theta_{opt}$; red crosses, $\theta_{int} - \theta_{opt}$ and blue dots, $\theta_{TSG} - \theta_{int}$. Missing data (i.e. from Julian day 74 to 79) represent periods of time when the intake system was switched off.

The same behaviour can be observed for the ($\theta_{TSG} - \theta_{int}$) signal, showing a constant decrease of about 0.7 ºC from the beginning to the end of the period evaluated. On the contrary, a constant offset of about 0.3 ºC, was observed for ($\theta_{TSG} - \theta_{opt}$).

From previous observations, the θ_{int} sensor showed to be unstable over the time. The changes in temperature from the intake sensor with an apparent memory effect could be due to a fault or drift in electronics over time during the JR165 cruise. This difference was not registered in the cruise JR158 that occurred previous to the cruise JR165.

The θ_{opt} signal showed to be more stable over the time with respect to θ_{int} and θ_{TSG} registered a higher warming effect in the surface water due to its transport in the intake pipes. Thus, the preferred signal to represent the sea surface temperature (SST) in both cruises is θ_{opt}.

The temperature given by optodes is based on measurements of a thermistor. The temperature equilibration in the optodes can have a long time response (30 s stated by the manufacturer) due to the titanium housing of the whole sensor that can act as an insulator to temperature changes. If the time response is constant over time and the lack of effect due to pressure changes in the sensor (this is true as measurements are only done in surface waters) then a constant offset of θ_{opt} against the true

temperature might be encountered. However, this time response might be critical for steep temperature gradients.

To corroborate the stability of θ_{opt} over time, a comparison against the surface temperature (θ_{CTD}) as given by the high precision temperature sensor SBE35 (*Sea-Bird Electronics, Inc.*) was done. The SBE35 sensor was mounted in the CTD rosette (θ_{CTD}) and these values were used to calibrate θ_{opt}. Calibration and specifications of the sensor for both cruises are provided in the JR158 cruise report.

c) θ_{opt} *calibration against* θ_{CTD} *from SBE35-CTD temperature sensor.*

To correct the θ_{opt} due to a warming effect from the intake to the USW-SS, a comparison between θ_{opt} and θ_{CTD} (as measured by the SBE35-CTD) was done. The values for θ_{CTD} were recorded at the time the surface Niskin bottle was fired.

Since θ_{CTD} was available only for the CTD stations, the continuous θ_{opt} (which included sections where no CTD stations were available) was corrected by removing the average temperature offset between θ_{opt} minus θ_{CTD} for the times in common.

The time at which the Niskin bottle of the surface depth was fired (i.e. time at which θ_{CTD} was recorded, t_{surf}) was matched up with the time corresponding to the θ_{opt} signal. From this reference time (t_{opt}) an average of θ_{opt} for two minutes, corresponding to $t_{opt} \pm 1$ min, was extracted to represent the temperature from the optode recorded when the SBE35 sensor recorded the surface data in the CTD (Figure 2.5).

In Figure 2.5, the error bars represent the mean standard deviation for the two minutes averages of θ_{opt} data (total average of 0.0087 ºC). The low variability within a period of two minutes from the optode temperature was expected since it corresponded to periods when the ship was on station.

The temperature measurements from the optode and CTD sensor were in good agreement. A systematic mean offset between θ_{opt} and θ_{CTD} for the JCR was 0.65 ºC ($\theta_{opt} - \theta_{CTD}$) (Figure 2.6). This offset was removed from θ_{opt} to obtain a continuous record of calibrated sea surface temperature (SST).

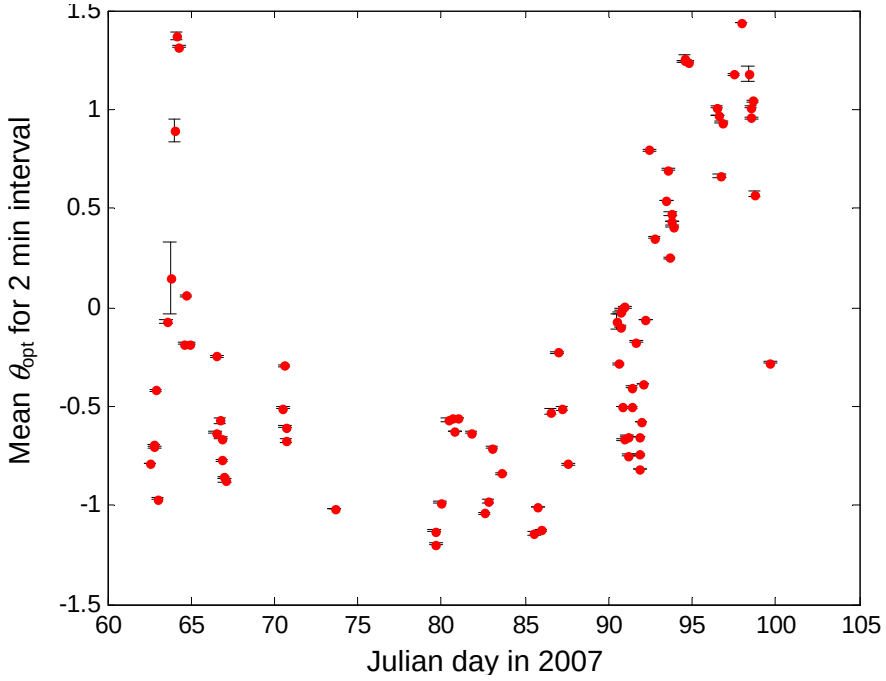

Figure 2.5 – Mean θ_{opt} for a period of two minutes at the firing time of surface Niskin bottles (times when SBE35 for θ_{CTD} was recorded). Error bars show $\pm 1\sigma$ of the two minutes-θ_{opt}.

Some of this offset might be due to the thermistor of the optode with a poor accuracy. However, most of it should be due to the warming effect of the sea surface water by its flow trough the intake pipes to the USW-SS system.

In the *RRS James Clark Ross* the USW-SS was installed in the chemistry lab located at deck level. The intake of the USW is located at the bow of the ship at a nominal depth of 6 m. The approximate time delay from the intake of the uncontaminated seawater supply to the main laboratory forward outlet is 2 min, after travelling through the pipes over a distance of 72.5 m from the sea surface (*personal communication S. Wright, Deck engineer on duty for JR165*). Thus, the effect of the 2 min delay from the intake to the USW-SS might explain most of the observed warming effect in the surface seawater.

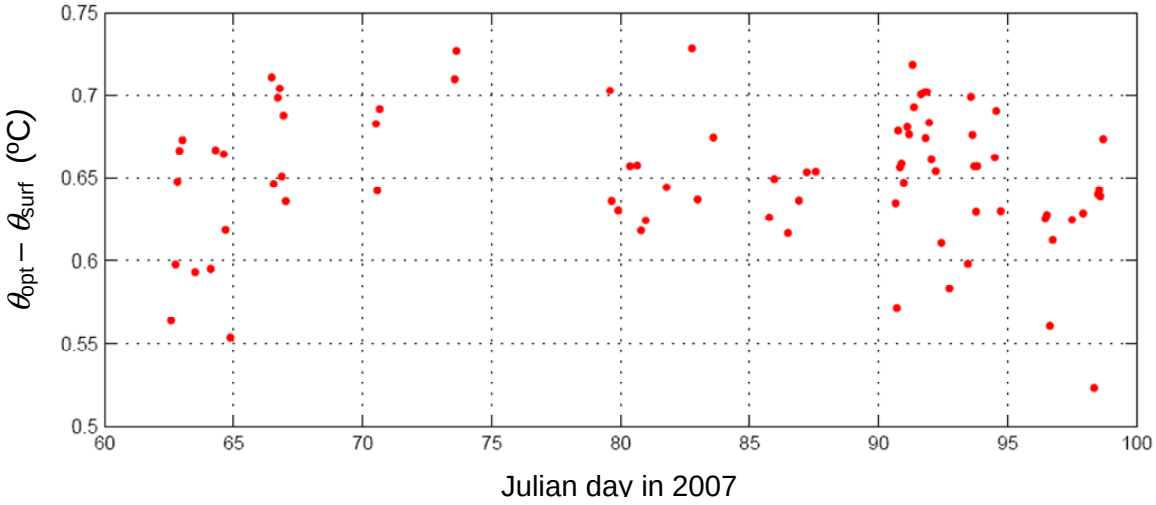

Figure 2.6 – Difference over time between the average two minutes-θ_{opt} minus the corresponding θ_{CTD} for SST calibration.

2.2.2 Sea surface salinity (*S*)

Discrete seawater samples from the USW flow directed to the TSG were collected once or twice a day. The samples were analyzed on board with a salinometer (*Guildline Autosal 8400B*) located in a controlled ambient temperature lab (at constant 22-23 ºC). The samples during both cruises were processed according to WOCE (World Ocean Circulation Experiment) standards and protocols. The salinity results for discrete samples (S_{disc}) were used to calibrate the continuous TSG signal (S_{TSG}).

For JR158 the signal was calibrated on board by Adrian Matthews (University of East Anglia), details can be found in the corresponding cruise report. For this cruise, A. Matthews reported a consistent and systematic difference with the TSG salinity values being an average of 0.026 below the discrete values obtained from the salinometer.

For the cruise JR165, I performed the calibration of the TSG data. After comparing the results from the discrete samples analyzed on board in the salinometer (performed by various members of the cruise party), a consistent difference of 0.0337 was observed between discrete samples and TSG data (Figure 2.7). The final calibrated *S* was obtained by removing this offset from the raw TSG signal.

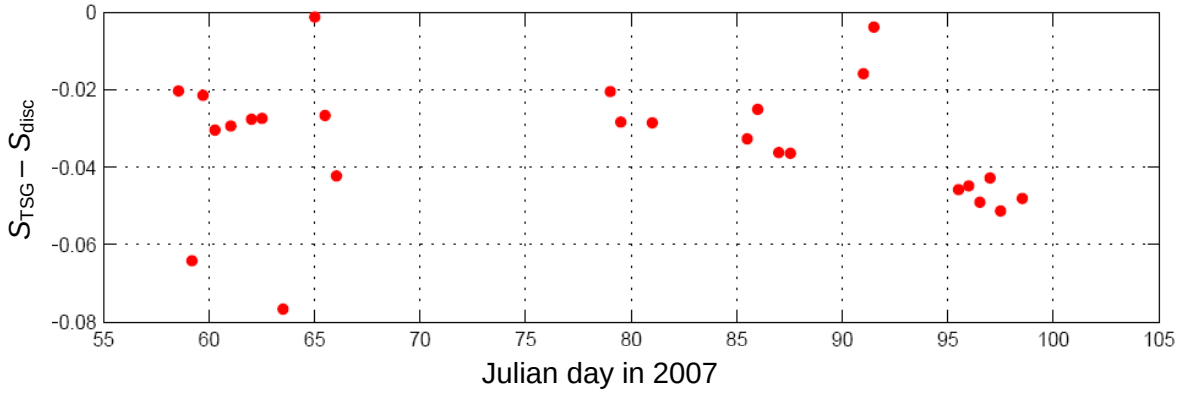

Figure 2.7 – Difference over time between the continuous TSG salinity (S_{TSG}) minus salinity from discrete samples (S_{disc}) analyzed with the shipboard salinometer for cruise JR165.

2.2.3 Atmospheric pressure (*P*).

Atmospheric pressure measured by the barometer of the meteorological station on board, was corrected by the height of the barometer location above the sea surface. This correction was performed by applying the "*Barometric law*".

The atmospheric pressure at the barometric height (*P* in mbar) is a function of the density of a gas, in this case air (ρ_{air} in kg m^{-3}) and is given by:

$$P = \frac{\rho_{air} R T_{air}}{M_m} \qquad (2.1)$$

where *R* is the ideal gas constant (8.3145 JK^{-1} mol^{-1}), T_{air} is the absolute air temperature in degrees K and M_m is the mean molecular mass of air (0.028966 kg mol^{-1}).

The term *P* can also be expressed in terms of the pressure at the sea surface (P_0) by:

$$P = P_0 e^{-\frac{h}{H}} \qquad (2.2)$$

where *h* (m) is the altitude of the barometer with respect to the mean sea surface level. The exponential scale height (*H*) is the change in height required to achieve a pressure drop of a factor of 1/*e* and is expressed by:

$$H = \frac{RT_{\text{air}}}{gM_{\text{m}}} \qquad (2.3)$$

Thus P_0 can be derived from equation 2.2 (Brimblecombe, 1996). The T_{air} must be also extracted from the records of continuous values from the meteorological station.

For both cruises, the pressure correction led to an average increase of 1.5 % of the measured barometric pressure. For the cruise JR158, the pressure correction was done by A. Matthews (see corresponding cruise report), while for cruise JR165 this correction was performed on board by M. Brandon (The Open University, UK).

2.2.4 Wind speed. (u)

Correction of measured ship's wind speed relative to sea surface.

Wind speed was recorded by an anemometer located in the main mast of the JCR. This wind speed is assumed to be relative to the ship-motion; therefore a correction to convert the speed relative to ground is needed.

The convention in the JCR data is that the underway wind direction (τ) is the direction the wind is blowing from. The true wind direction relative to ground (τ_{true}) is obtained by adding τ to gyrocompass heading (γ) and then converted to the direction the wind is blowing to. Underway wind speeds and true directions are broken into east (υ) and north (ν) velocity components. The ship's velocity (U_{ship}) is derived from a fixed position; this speed and angle are converted to the ship's east and north velocities (υ_{ship} and ν_{ship}, respectively). These are interpolated to the same timestamps as the underway data. East and north components of true wind are derived by adding the east and north components of ship's velocity and wind velocity. Finally, these are converted back to true wind speed and direction relative to ground (τ_{true}), with the latter forced to lie in a range from 0 to 360 degrees.

Since the anemometer of the JCR was located at 15.9 m above sea level (h) (Yelland *et al.*, 2002), the ship's wind speeds were then corrected to 10 m above sea level for thermal stability effects (Johnson, 1999) according to the following power expression:

$$\frac{u_{10}}{u_z} = \left(\frac{10}{z}\right)^n \qquad (2.4)$$

Where u_{10} is the wind speed at 10 m above sea level, u_z is the wind speed at an elevation z and n is the exponential corresponding to the different sea wave age as an indicator of the sea roughness (the younger the waves, the higher the sea roughness and the higher the value for *n*). The u_{10} obtained from this equation has an error of 3 % for a range of elevations at which wind speed was originally measured of $5 \leq z < 60$ m. This correction was performed by A. Matthews for cruise JR158 and by M. Brandon for cruise JR165.

2.2.5 Weighted mean gas transfer coefficient (k_w)

The calculation of the gas transfer coefficient, *k*, was following the quadratic fit proposed by Sweeney *et al*. (2007) (see Chapter 1, section 1.6 for details). The value of *k* represents the transfer of gas as given by the current wind speed at the sampling day. However, the O_2 contained in the mixed layer is the result of the processes that occurred a few weeks prior to the sampling time; furthermore, the biological O_2 concentration as estimated during the cruises represents the integrated O_2 production according to the gas equilibration time in the mixed layer under the influence of the wind speed. Thus, in order to take into account the residence time of the O_2 associated with the history of the wind speed variability over a specific mixed layer thickness (z_{mix}), a weighted gas transfer coefficient (k_w) is calculated. For this, a weighting technique proposed by Reuer *et al*. (2007) is used.

To account for the historical wind speed over a specific time period previous to the sampling day, we must rely on products that forecast the global wind speed. Various wind speeds from publicly available products (u_{10_prod}) were evaluated for their accuracy compared to the ship's wind speeds (u_{10_ship}) at the same sampling time. The wind speed products are standardized to 10 m height and provide a global forecast of u_{10} for different time resolutions (i.e. 6 h, 24 h). Here, 60 days are considered as the historical time frame to account for the wind speeds before the sampling day. This time proved to be sufficient to ventilate the typical thickness of mixed layers encountered in the areas of study.

Three wind data products were evaluated: ECMWF (European Centre for Medium Range Weather Forecast) 6 h resolution, NCEP (National Center for Environmental Prediction) 10 m wind speed at 6 and 24 h resolution and QSCAT (QuikSCAT) wind speed representing the mean of daily (24 h) observations.

The results of this comparison are shown in Figure 2.8. Based on the root mean squared of the difference between the compared wind speeds ($s(\Delta u)$ in m s^{-1}), the ECMWF at 6 h resolution shows the best agreement ($s(\Delta u)$ = 2.5 m s^{-1}) with u_{10_ship} compared with the other wind products. Therefore, data from ECMWF was used for the calculations of the weighed gas transfer coefficient (k_w) in this study.

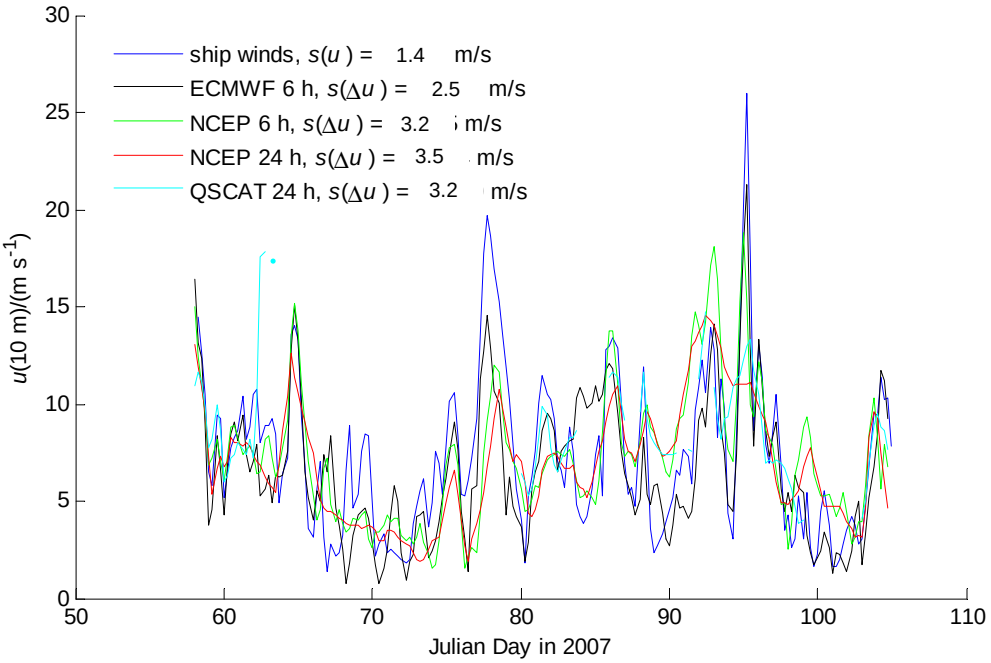

Figure 2.8 – Comparisons between ship's wind speeds (u_{10_ship}) and wind speed from products (u_{10_prod}): ECMWF, QSCAT and NCEP at different time resolutions for the sampling day. The corresponding $s(\Delta u)$ represents the root mean squared of the difference between wind speeds from products and ship's measurements in m s^{-1}. The figure includes the period of time for the JR165 cruise.

2.3 Dissolved oxygen by Winkler titration.

In order to calibrate the continuous $c(O_2)$ acquired by the optode, the dissolved O_2 in discrete samples collected from the USW ($c_{sa}(O_2)$) was quantified by Winkler titration. The Winkler titrations are traditionally preferred since they offer a reliable and accurate shipboard work with high precision results (about 0.1 %).

Besides discrete sample collection from USW, samples from Niskin bottles at selected depths (including surface) from the sampling rosette were collected in order to calibrate the CTD-O_2 sensor.

2.3.1 Sampling procedure and quantification of $c(O_2)$ in seawater by Winkler titration.

A volume of about 150 ml of seawater was collected in BOD glass flasks from the USW-SS outlet for discrete samples collection at an approximate frequency of sampling from 4 to 6 h, depending on the ship speed. In the case of discrete samples from the Niskin bottles, selected stations and depths were sampled for the calibration of the CTD-O_2 following the same procedure (section 2.4).

The $c_{sa}(O_2)$ were obtained by whole-bottle Winkler titration in seawater (Carpenter, 1965), following World Ocean Circulation Experiment (WOCE) procedure (Culberson, 1991; Dickson, 1996). The endpoint was identified photometrically.
The calibration was performed with a standard solution of potassium iodate (KIO_3 analytical standard; Fluka, *Sigma-Aldrich*) at 2.339 mmol l^{-1} gravimetrically prepared before the cruise. A thiosulphate ($Na_2S_2O_3$) solution at 0.2 mol dm^{-3} was used as titration reagent and was standardized by iodometry against the KIO_3 standard solution.

For selected stations, surface water from Niskin bottles was collected in order to compare the O_2 concentration from the USW to results from near-surface Niskin bottles. This approach was performed to identify any O_2 concentration changes in the pipes of the intake systems due to warming and outgassing or biological activity (Kaiser *et al.*, 2005). The results from these comparisons are shown in section 2.8.

2.3.2 Corrections to the measurements of dissolved oxygen by Winkler titration.

A total of 174 discrete samples were collected during JR158 and 469 during JR165, over 46 days, for analysis by Winkler titration. From those, 84 samples for JR158 and 186 samples for JR165 (including duplicates) were taken from the USW. The remaining samples were for the calibration of the CTD-O_2 sensor, corresponding to samples at different depths with some duplicates distributed in the sampling stations. The difference in the oxygen concentration for each duplicate gives the precision of the sampling technique and titration procedure. According to the WOCE procedure for Winkler titrations (Culberson, 1991; Dickson, 1996), the analytical precision ($\pm 1\sigma$) to ensure an adequate precision of the data obtained must be 0.5 μmol kg^{-1}. In the case of the JR158 campaign the average standard deviation of a duplicate analysis was 0.26 μmol kg^{-1} (n = 28) on average. For JR165, this value was 0.29 μmol kg^{-1} (n = 76).

For the USW samples, the temperature given by the *Aanderaa* optode (θ_{opt}) was used as the temperature of the sample. For the discrete samples taken from Niskin bottles, the temperature of the sample was the one recorded by the CTD temperature sensor (θ_{surf}).

a) Titration blank

A reagent blank was determined in order to quantify the presence of redox species apart from oxygen in the reagents which can behave equivalently to oxygen in the analysis (Dickson, 1996).

$$V_{blank} = V_1 - V_2 \qquad (2.5)$$

V_{blank} in ml, is the volume difference between the volumes V_1 and V_2; these represent the $S_2O_3^{2-}$ used to titrate the first and second aliquots of KIO_3, respectively. The reagent blank with distilled water for JR158 campaign accounted for 0.0019±0.0003 ml (n = 4) and 0.0009±0.0006 ml (n = 6) for JR165.

However, other redox species besides O_2 can be present in the sample, causing interferences in the final O_2 analysis due to their similar behaviour during the reaction. These species can be typically measured in a blank prepared with an aliquot

of seawater. Reagent blanks with seawater for the present study showed an average value of 0.0035±0.0002 ml (n = 5) and 0.0023±0.0018 ml (n = 12) for the JR158 and JR165 campaigns, respectively.

For all the USW and Niskin seawater samples in JR165 (including duplicates), an average 0.5±0.02 μmol kg^{-1} (n=469, corresponding to 283 from Niskin bottles and 186 from the underway system) higher $c_{sa}(O_2)$ was observed using blanks with distilled water versus the oxygen concentration using seawater blanks. Although this difference can be considerable, the seawater blanks have been suggested not to be constant (Culberson, 1991; Wong and Li, 2009).

According to Culberson (1991), the blanks with seawater tend to vary with depth and position, therefore in order to use them to correct the $c_{sa}(O_2)$, they should be determined at each depth where oxygen samples are taken, being in the end an unfeasible technique. To correct the O_2 concentration measurements for the present study, we used the distilled water blanks following the WOCE procedure.

b) Air buoyancy correction

The volume of the Winkler flasks (V_{20}, in ml) at calibration temperature (θ_{20} = 20 ºC) must be measured by mass difference of empty and full flask using distilled water (Culberson, 1991).

$$V_{20} = m_w \, f_{buoy} / \rho_{fw} \qquad (2.6)$$

f_{buoy} (dimensionless) represents the **air buoyancy correction** which can be measured, according to Culberson (1991), as the quotient of the mass of water in air (m_w, expressed in kg) contained or delivered to the density of pure water ($\rho_{fw} \approx 1000$ kg m^{-3}) at θ_{20}. Considering that the weight of objects in air is less than that in vacuum, the buoyancy correction must be applied to the weight of pure water contained or delivered by volumetric glassware, this correction is given by:

$$f_{buoy} = \frac{(1-\rho_{air})/\rho_{weights}}{(1-\rho_{air})/\rho_{fw}} \qquad (2.7)$$

where ρ_{air} is the density of air at the temperature and pressure during the weighing process (≈1.2 kg m^{-3} at 20 ºC) and $\rho_{weights}$ is the density of the weights used for balance calibration (≈8000 kg m^{-3} for stainless steel). For weighing temperatures between 10 and 30 ºC, the buoyancy factor can be approximated as 1.00105, resulting in an error of less than 0.1 % due to the buoyancy correction.

c) Thermal glass expansion correction

In order to correct for the **thermal glass expansion** (or contraction) due to differences of the seawater temperature at sampling and calibration, V_{20} was corrected for each sample using the following equation (Culberson, 1991).

$$V_{flask} = V_{20}\left[1+\alpha_V(\theta_{sa}-\theta_{20})\right] \quad (2.8)$$

where, V_{flask} is the final volume of the Winkler flasks (in ml) at the temperature of the sample θ_{sa} (in ºC, which corresponds to θ_{opt} for USW and θ_{surf} for CTD samples) during the pickling time. The factor α_V is the cubical coefficient of thermal expansion for a particular glass. For borosilicate glass, this factor is approximately 1×10^{-5}.

On average, the thermal expansion correction accounted for 0.019 % increase in the final V_{flask}, equivalent to a range of volumes from 0.005 to 0.032 ml. In terms of O_2 concentration, this correction accounted for −0.07 to 0.09 µmol kg^{-1} to the final concentration for a corresponding range of seawater temperatures from −1.8 to 16.4 ºC, respectively.

d) Concentration of the titrant ($Na_2S_2O_2$)

After an average of 21 Winkler samples measured (called a “session”) the concentration of the solution of sodium thiosulfate ($Na_2S_2O_2$) used as titrant was measured by titration of 6 aliquots of a standard solution of KIO_3 of known concentration. A confirmation of the $Na_2S_2O_2$ concentration at the beginning of the analysis of each session helped to identify any problems in the analytical equipment. The average $Na_2S_2O_2$ concentration over several sessions (see Table 2.4 below) was used for the final calculation for the O_2 concentration on each discrete seawater sample ($c_{sa}(O_2)$).

e) $c(O_2)$ in a seawater sample by Winkler titration

The $c_{sa}(O_2)$ (μmol kg^{-1}) for discrete samples collected from USW and from the CTD, was calculated following:

$$c_{sa}(O_2) = \frac{(V_{thio} - V_{blank}) \times c(Na_2S_2O_3) / 4\,\text{mol} - 0.076\,\mu\text{mol}}{(V_{flask} - 2) / \rho_{sw}} \qquad (2.9)$$

where, V_{thio} is the volume in ml of titrant ($Na_2S_2O_3$) needed to titrate the sample and ρ_{sw} is the density of the seawater (kg dm^{-3}) at the temperature and salinity of the sample (θ_{sa} and S_{sa}, respectively).

The $c(Na_2S_2O_3)$ is divided by 4 mol, considering that 1 mol of O_2 reacts with 4 mol of $Na_2S_2O_3$. The factor 0.076 μmol corrects for the O_2 content of the pickling reagents (1 ml $MnCl_2$ and 1 ml NaOH/NaI at about 25 ºC) introduced to the sample (Dickson, 1996).

The term (V_{flask} − 2) in the denominator of the previous equation represents the volume of seawater in the flask that was pickled, which is corrected by 2 ml representing the volume of sample displaced by the 2 ml of pickling reagents. In order to obtain the mass of seawater, this term is divided by the density of seawater (ρ_{sw} in kg dm^{-3}) calculated at the temperature and salinity of the sample (θ_{sa} and S_{sa}, respectively). The θ_{sa} and S_{sa} values were extracted from the continuous SST and *S* calibrated signals respectively, at the corresponding sampling time (t_{sa}).

For convention, the variable $c_{sa}(O_2)$ refers to the O_2 concentration from discrete samples collected from the USW and $c_{CTD}(O_2)$ for discrete samples collected from the Niskin bottle only from the depth near the surface.

2.4 Calibration of CTD-O_2 sensor.

For the cruise JR158, the calibration of the CTD-O_2 sensor was performed by *J. Screen* (see cruise report) from Winkler titration of discrete samples that J. Kaiser and myself have analyzed on board during the same cruise.

In the case of the cruise JR165, besides the analysis of discrete samples, I did the calibration of the CTD-O_2. For this cruise, the CTD was equipped with two *Sea-bird* SBE43 oxygen sensors (referred to as “oxy1” and “oxy2” hereinafter).

In order to calibrate the oxygen sensors, a total of 68 stations (corresponding to 27 % of the total 253 CTD casts) were sampled at selected depths for each profile. A total of 283 discrete samples (including duplicates) were collected from Niskin bottles into Winkler flasks and analyzed by whole-bottle Winkler titration following the same procedure for the USW samples (section 2.3).

Two $Na_2S_2O_3$ solutions and five KIO_3 standards were used due to the need of its replacement when one was finished. Also a new set of oxygen-fixation chemicals was used from the 8th of March (Julian Day 67). The calibrations of the $Na_2S_2O_3$ and KIO_3 were done immediately after their replacement and before the samples analysis. To evaluate the stability of the $Na_2S_2O_3$ solution, several other calibrations were performed alternating the samples analysis.

In Table 2.4 the results from the different calibration sessions during the cruise are shown. A total of sixteen independent calibrations were performed each of them corresponding to the different $Na_2S_2O_3$ and KIO_3 solutions used (columns 6 and 7). Three final groups were used to calibrate the CTD stations. The last column of Table 2.4 shows the group of CTD stations affected by each independent calibration. The typical standard deviation of a duplicate analysis for the samples from Niskin bottles was 0.05 μmol kg^{-1} (0.003 ml l^{-1}), based on 34 duplicate samples (12 % of all sampled Niskin bottles).

The up-cast O_2 profiles were calibrated by linear regression obtained from the comparison between the O_2 concentrations in discrete samples against the O_2 concentration as given by the CTD-O_2 sensor.

Table 2.4 – Results for the calibration of $c(O_2)$ in seawater samples from USW and Niskin bottles during cruise JR165. Shadows are used to identify the three groups of calibrations according to the $Na_2S_2O_3$ and KIO_3 solutions used during the cruise.

Date	*Session #*	*Blank (distilled water) (ml)*	*$Na_2S_2O_3$ vol. (ml)*	*$Na_2S_2O_3$ concentration (M)*	*$Na_2S_2O_3$ solution #*	*KIO_3 std. solution #*	*CTD stations*
02/03/2007	2		0.6668	0.2003	1	2	1 to 89
04/03/2007	4	0.0006			1	2	
06/03/2007	5	0.0005			1	2	
08/03/2007	6	0.0014			1	2	
12/03/2007	9	0.0009	0.6679	0.1999	1	2	
12/03/2007	9	0.0009	0.6631	0.2015	1	3	90 to 154
20/03/2007	11	0.0010	0.6636	0.2012	1	3	
23/03/2007	13		0.6964	0.2019	1	4	
24/03/2007	14		0.6971	0.2017	1	4	
27/03/2007	15		0.6986	0.2014	1	4	
29/03/2007	16	0.0009	0.7013	0.2004	2	4	155 to 253
31/03/2007	17		0.7025	0.2005	2	4	
02/04/2007	18	0.0009	0.7018	0.2005	2	4	
06/04/2007	20		0.7036	0.1999	2	4	
08/04/2007	21		0.7001	0.2010	2	5	
15/04/2007	22		0.7003	0.2007	2	5	

First, the oxygen values given during the up-cast by oxy1 and oxy2 sensors were compared. In Figure 2.9 the differences between the O_2 concentrations from Winkler analysis is shown for the corresponding sample minus the values given by the CTD-O_2 sensors. The oxygen concentration provided by the CTD sensors is expressed in ml l^{-1}, and in the following results are presented in these units. Since for the present work the preferred units are μmol kg^{-1} it is important to express the conversion between units. The concentration of oxygen in ml l^{-1} is divided by the density of the seawater (ρ_{sw} in kg m^{-3}) and multiplied times 44.656 μmol ml^{-1}; the latter is obtained from the ratio between the density of oxygen (ρ_{O2} = 1.429 g l^{-1}) over the molar mass of O_2 (32 g), thus: 1 ml O_2 l^{-1} = 1 μmol O_2 kg^{-1} × (ρ_{O2} / molar mass of O_2) / ρ_{sw}.

As observed in Figure 2.9, the oxygen concentration given by the sensor oxy1 was less consistent over the cruise time. A clear increase of about 0.5 ml l^{-1} (21.8 μmol kg^{-1}) in all the readings was observed after station 85, this is possibly due to instabilities in the oxygen sensor 1.

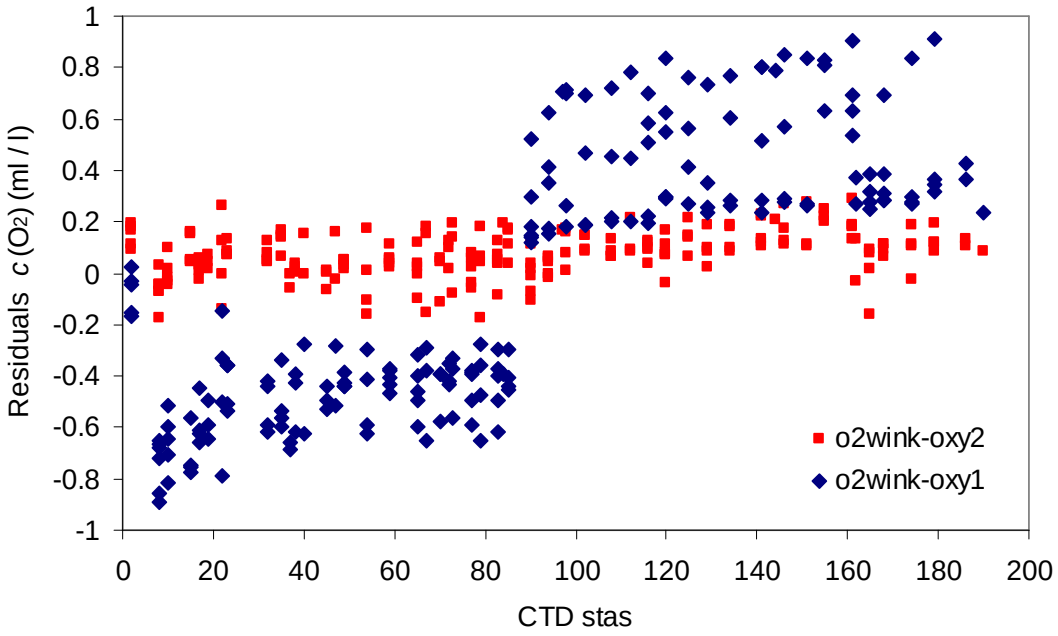

Figure 2.9 – Mean residuals between oxygen concentrations from Winkler method in seawater at selected depths minus the corresponding value from the CTD oxygen sensors; diamonds are the difference with data from sensor oxy1 and squares are the difference with data from sensor oxy2.

Before calibration, a constant mean residual of (0.08 ± 0.09) ml l^{-1} (3.5 ± 3.9 µmol kg^{-1}) was observed between O_2 concentration from Winkler titration minus the concentration given by the oxy2 sensor. Based on the previous observation, only the data given by the sensor oxy2 were calibrated.

Figure 2.10 shows the linear regression fit (r^2 = 0.997) for the sensor calibration after comparison against the corresponding oxygen concentration from Winkler analysis ($c(O_2)$ from oxy2 = 0.996 × $c(O_2)$ from Winkler − 0.050; for the concentration in ml l^{-1}). This equation was applied to the CTD-O_2 up cast profiles as given by oxy2 sensor for calibration.

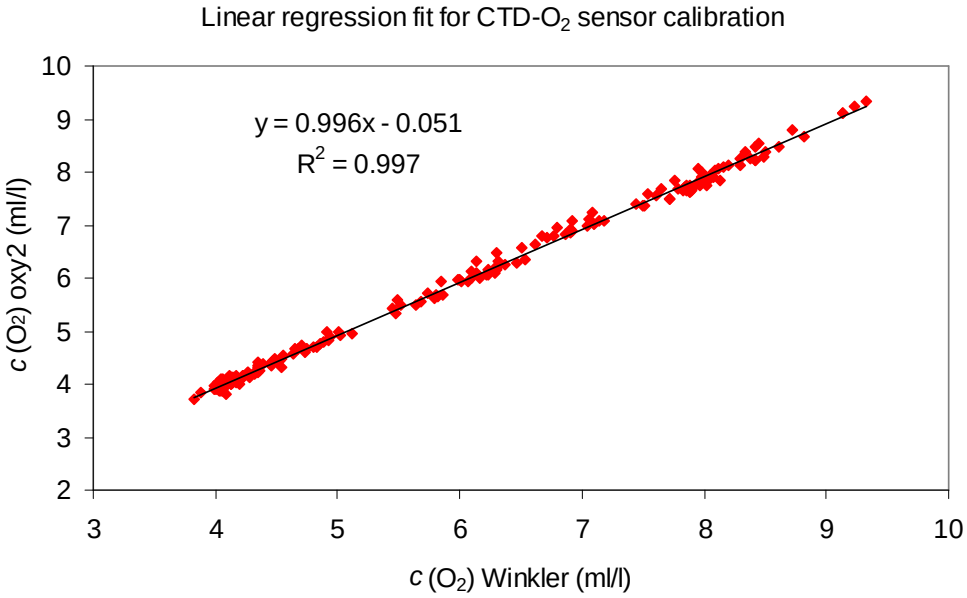

Figure 2.10 – Linear regression fit and equation for calibration of CTD-O_2 sensor in cruise JR165. Error bars of the duplicate analyses are shown however those are smaller than the marker size.

2.5 Calibration of $c(O_2)$ from *Aanderaa* oxygen optode 3835.

At a fixed resolution of 10 s the output data measured with the *Aanderaa* oxygen/temperature optode sensor (Model 3835) from the USW flow was recorded on a daily basis. The useful output variables were: date, time, temperature and DPhase (ϕ).

The optode is an optical sensor that provides an internally calculated phase value (ϕ in degrees) to estimate the concentration of oxygen. It is based on a dynamic fluorescence quenching on which the molecule of oxygen has influence over the fluorescence of luminophore (platinum porphyrine) in a sensing foil. As a blue light is emitted (505 nm), the luminophore is excited to pass onto a relaxation state liberating photons; the expression of this state is a red fluorescence light. However, the energy can also be transferred to a molecule (i.e. oxygen) and the emission of the red fluorescence light is restricted (or quenched). The restricted intensity of the red light is proportional to the number of molecules restricting it, in this case, equivalent to the amount of molecules of oxygen in the seawater (Körtzinger *et al.*, 2005).

From the fluorescence quenching, the optode first gets continuous measurements of a raw (i.e. uncalibrated) phase (ϕ_{raw}). Thus, ϕ_{raw} represents the difference between the

phase obtained due to the excitation of the luminophore with the blue light (ϕ_{blue} or BPhase) minus the phase obtained from the red light after relaxation (ϕ_{red} or RPhase). The internally calculated phase (ϕ in degrees) is obtained from a 3rd degree polynomial (equation below) of ϕ_{raw}.

$$\phi = a + b\phi_{raw} + c{\phi_{raw}}^2 + d{\phi_{raw}}^3 \qquad (2.10)$$

Coefficients *a*, *b*, *c* and *d* from the polynomial above are values stored in the optode after its calibration. Coefficients *a* and *b* are determined previously in the laboratory from a two point calibration of water with zero oxygen against water saturated with air; coefficients *c* and *d* are set to zero. Thus, the ϕ value is a linear function of ϕ_{raw} leaving the above polynomial onto a 1st degree equation.

The internal software of the optode calculates a raw concentration of oxygen ($c_{raw}(O_2)$), however the quenching of fluorescence is not enough to estimate the actual amount of dissolved oxygen. Instead, the optode provides measurements of the fluorescence lifetime of the excitation light expressed as a phase (dimensionless) values (or raw phase).

The $c_{raw}(O_2)$ given by the optode is based on ϕ and a set of coefficients (C_0 to C_4, stored by the manufacturer) with a specific internal calibration function given by a 4th degree polynomial:

$$c_{raw}(O_2) = C_0 + C_1\phi + C_2\phi^2 + C_3\phi^3 + C_4\phi^4 \qquad (2.11)$$

The coefficients C_0 to C_4, are temperature dependent coefficients using θ_{opt} (in ºC) and are calculated as:

$$C_x = C_{x0} + C_{x1}\theta_{opt} + C_{x2}{\theta_{opt}}^2 + C_{x3}{\theta_{opt}}^3 \qquad (2.12)$$

The subindice *x* represents the numbers 0 to 4 for the corresponding coefficients C_0 to C_4. θ_{opt} is obtained from the internal thermostat measurements and is calculated internally using a similar polynomial with specific coefficients as well. Since the optode sensor's foil is only permeable to gas and not water, the optode can not sense the effect of salt dissolved in seawater, hence the optode always measures as if

immersed in fresh water. Post compensation due to salinity effects must be performed for the final $c(O_2)$ calculation.

2.5.1 Calibration of ϕ from $c_{sa}(O_2)$ values.

The calibration of the $c(O_2)$ from the optode readings is calculated by using a new phase calibrated (ϕ_{cal}) from the ϕ data. The steps to complete this calibration are shown in the next figure. According to Figure 2.11:

Step 1 – Look up at the corresponding time (t_{sa}) the discrete calibration samples were taken (i.e. for Winkler titration from the USW), the DPhase for each sample (ϕ_{sa}) and temperature (θ_{sa}) from the continuous data set given by the optode (ϕ and θ_{opt}),

Step 2 – Look up the salinity (S_{sa}) and temperature calibrated (θ_{cal}) from the *S* and SST record at the corresponding t_{sa},

Step 3 – A DPhase solved (ϕ_{sol}) is derived from the following polynomial as a function of the $c_{sa}(O_2)$ for each discrete sample (measured by Winkler titration) and their corresponding θ_{cal}, θ_{sa} and S_{sa}.

$$c_{sa}(O_2)^* = P_{u0} + P_{u1}\phi_{sol} + P_{u2}\phi_{sol}^{\ 2} + P_{u3}\phi_{sol}^{\ 3} + P_{u4}\phi_{sol}^{\ 4} \qquad (2.13)$$

The term $c_{sa}(O_2)^*$ corresponds to the $c_{sa}(O_2)$ corrected by the concentration of oxygen at equilibrium with the atmosphere ($c_{eq}(O_2)$) from θ_{cal} in seawater (S_{sa}) and in freshwater (Benson and Krause, 1984; Garcia and Gordon, 1992) and by the density of the seawater and freshwater (ρ_{sw} and ρ_{fw}, respectively). This correction, improves the deviation of the gas saturation concentration, particularly at low and high temperatures and salinities (Garcia and Gordon, 1992).

In equation 2.13 the coefficients P_{u0} to P_{u4} represent P_{u*} in the polynomial:

$$P_{u*} = A_n + B_n\theta_{sa} + C_n\theta_{sa}^{\ 2} + D_n\theta_{sa}^{\ 3} \qquad (2.14)$$

The subscript "n" represents the coefficients 0 to 4 for *A*, *B*, *C* and *D*; thus a total of 20 coefficients stored for each particular optode are used for the phase calibration,

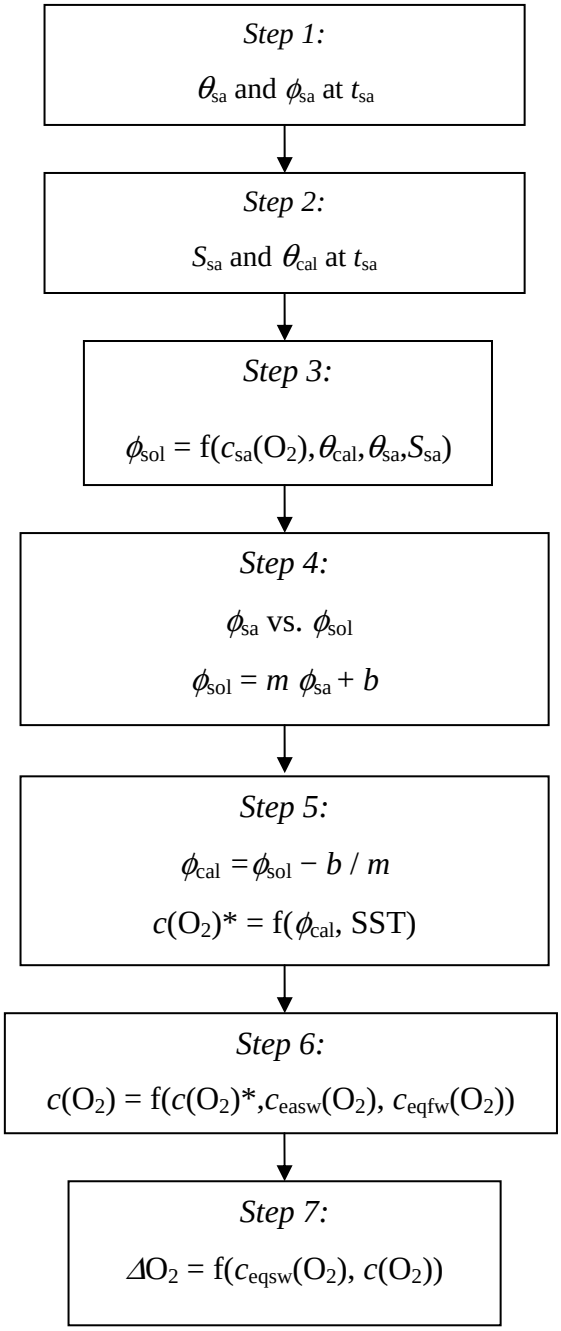

Figure 2.11 – Flow diagram for the calibration of the continuous optode data for $c(O_2)$ in USW.

Step 4 – A secondary calibration function is calculated from a least square fit of ϕ_{sa} vs. ϕ_{sol}. In the JR165 cruise, from the 186 samples collected from the underway for the optode calibration, 36 samples were removed considered as outliers due to possible entrainment of bubbles in the sample originally trapped in the pipes of the intake or introduced by the operator during the sampling procedure. In the Figure

2.12 is shown the relationship between ϕ_{sa} versus ϕ_{sol} for the USW samples analysed for the JR165 cruise is shown.

Step 5 – The continuous oxygen concentration from the continuous USW measurements is calculated by replacing the recorded ϕ in the linear equation from ϕ_{sol} vs. ϕ_{sa} (ϕ_{sol} = 0.925 ϕ_{sa} + 1.187). The Figure 2.12 shows this regression only for cruise JR165.

Thus, a calibrated phase (ϕ_{cal}) is obtained and is used in equation 2.13 that is now expressed as:

$$c(O_2)^* = P_{u0} + P_{u1}\phi_{cal} + P_{u2}\phi_{cal}^{\ 2} + P_{u3}\phi_{cal}^{\ 3} + P_{u4}\phi_{cal}^{\ 4} \qquad (2.15)$$

For the calculation of the coefficients P_{u*} (following equation 2.14), the continuous calibrated sea surface temperature (SST) is used instead of θ_{sa}. The term $c(O_2)^*$ corresponds to the concentration of dissolved oxygen with no salinity effect.

Step 6 – To obtain the final continuous dissolved oxygen concentration in the sea surface, the $c(O_2)^*$ is corrected by the salinity effect. For this, the continuous O_2 concentration at saturation is calculated at the *in situ* conditions in the surface mixed layer and for freshwater ($c_{eqsw}(O_2)$ and $c_{eqfw}(O_2)$, respectively) using SST, S and P_0 (Benson and Krause, 1984; Garcia and Gordon, 1992). The correction by the water vapour of seawater was performed according to Green and Carrit, 1967 .

Step 7 – Finally, the O_2 supersaturation (ΔO_2 in %) with respect to the oxygen concentration at saturation for the continuous record is calculated following equation 1.4 in chapter 1. For cruise JR165, the mean difference between the ΔO_2 for the continuous optode data and Winkler measurements was (0.0 ± 0.6) %.

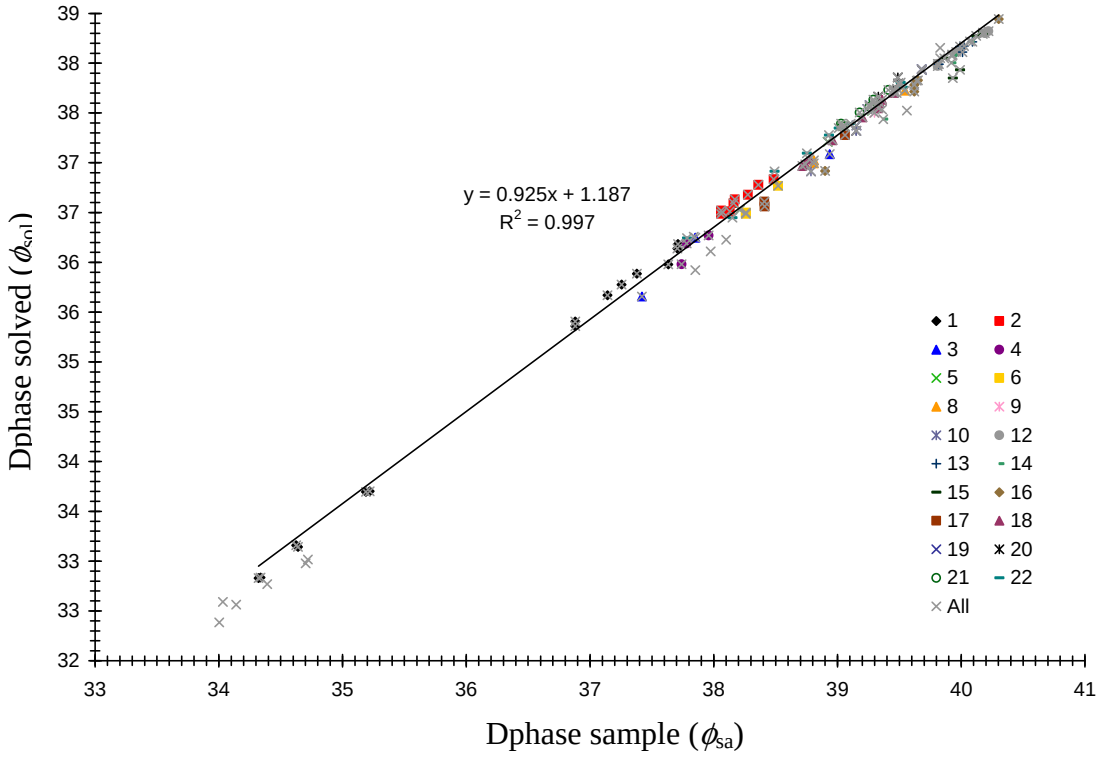

Figure 2.12 – DPhase for each underway seawater sample (ϕ_{sa}) as given by the optode versus the corresponding DPhase solved (ϕ_{sol}) used for calibration of dissolved oxygen from an optode in cruise JR165. The different markers indicate the 22 subsessions of Winkler analysis during the cruise. Data indicated by crosses are all the values before elimination of outliers.

To evaluate the precision of the optode calibration and the possibility of a drift on the sensor, the difference between the results from Winkler titration ($c_{sa}(O_2)$) and the corresponding oxygen concentration from the continuous signal at the time t_{sa} was calculated for both cruises.

In cruise JR158, from 84 samples collected from the USW for Winkler titration, only 46 comparisons were done. For the remaining 38 samples there was no available data from the continuous $c(O_2)$ record at the corresponding sampling time to compare with; 17 out of 46 were considered as outliers for having a considerably higher difference in concentrations (±2 µmol kg^{-1}) indicating a possible contamination with air in the sample during collection or a drift from the optode sensor. For the final 29 comparisons, the mean difference between ($c_{sa}(O_2)$ − $c(O_2)$ at t_{sa}) corresponds to (−0.1 ± 0.5) µmol kg^{-1} with an overall precision for the optode calibration of 1.6 %.

In cruise JR165, 36 outliers were removed after the calibration of ϕ (Figure 2.12). For the remaining 150 samples only 67 had duplicates. Averaging the results from the duplicate samples the mean of ($c_{sa}(O_2)$ − $c(O_2)$ at t_{sa}) is (0.03 ± 0.57) µmol kg^{-1} (n = 57) (Figure 2.13); 4 outliers were removed due to a high oxygen content in the $c_{sa}(O_2)$ (> 2 µmol kg^{-1}) indicating a possible contamination with air in the sample during collection. For 22 samples there was no data from the $c(O_2)$ record due to noise in the continuous record). The mean residual for the calibration was (0.0 ± 0.1) %. The precision for this calibration corresponded to 1 %.

Since no clear drift from the optode signal was observed in the Figure 2.13, and during the evaluation of data from the cruise JR158, the stability of the optode sensor over the time can be assured and a single step for calibration for each cruise of the corresponding continuous data was done.

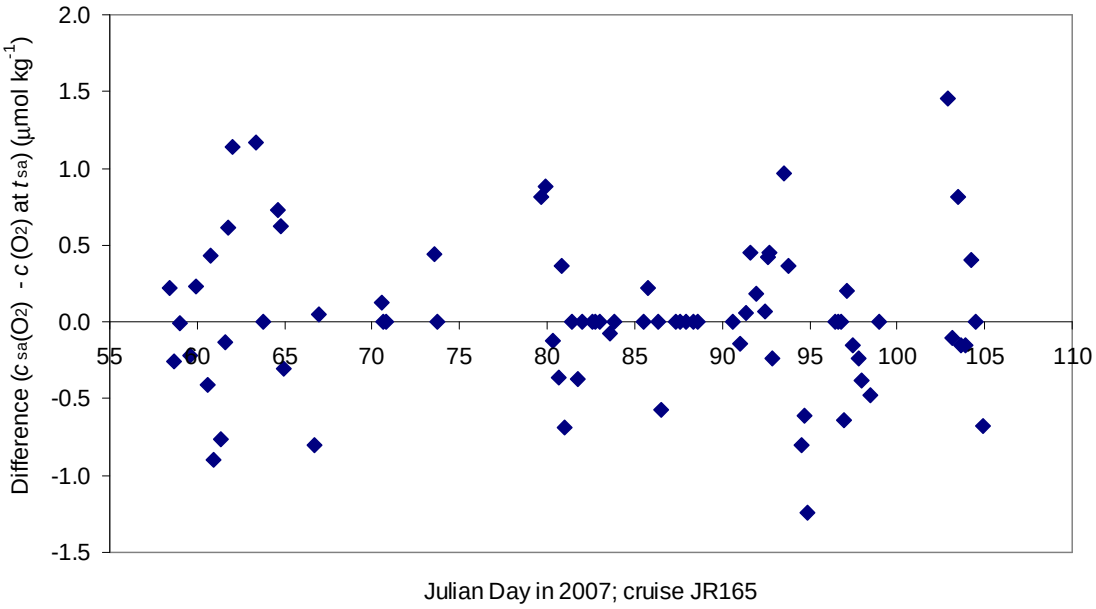

Figure 2.13 – Difference between ($c_{sa}(O_2)$ − $c(O_2)$ at t_{sa}) for cruise JR165.

2.5.2 Air-to-sea oxygen flux (F_g) from ΔO_2.

The ΔO_2 together with a weighted gas transfer coefficient (k_w, section 1.6; chapter1) are used to estimate the flux of oxygen through the air-sea interface (F_g) following equation 1.2 (section 1.7; chapter 1).

2.6 O_2/Ar ratios and triple oxygen isotopes by IRMS.

2.6.1 Sampling procedure.

Discrete samples for O_2/Ar were collected from the free running seawater outlet in the USW-SS (Figure 2.1, outlet 1) for the calibration of the MIMS data. The same sample was also used to measure the isotopic abundance of the dissolved oxygen. Only 7 samples between the two cruises were also collected from Niskin bottles (mainly from the surface sample) for the O_2/Ar and isotope quantification.

Seawater samples were collected into 350 ml glass bottles (referred to as "evacuated bottles" hereinafter) with compression o-ring valves (*Glass expansion*) previously rinsed, dried and air evacuated to less than $<10^{-3}$ mbar. As part of the evacuated bottle preparation, a volume of 100 μl of saturated $HgCl_2$ solution was added to avoid biological activity during storage until further analysis (Kirkwood, 1992; Quay *et al.*, 1993; Emerson *et al.*, 1995; Kaiser *et al.*, 2005). The preparation of the evacuated bottles was done in the stable isotope laboratory at UEA before the oceanographic campaigns. The o-rings of the high-vacuum stopcocks were lubricated with high-vacuum inert grease prior to vacuum evacuation. The volume of the bottles was calibrated by the difference between the weights of the full bottle with water minus the weight of the empty bottle.

About 250 ml of the seawater sample was drawn into each evacuated bottle through the valve side arm with care to not introduce air. After closing the valve, the arm was filled with water to create a water-seal, retained in place by covering the end of the arm with flexible plastic caps.

The discrete samples in evacuated bottles were collected approximately every 6 h during each cruise, as long as the USW was on. The bottles were stored at room temperature until further analysis after being shipped to UEA.

As discussed in section 2.3.1, simultaneous samples were taken to compare O_2 concentrations in USW and surface Niskin bottles, as a way to evaluate the effect of the intake system over the seawater in the USW. The same approach was used for evacuated bottle samples and O_2/Ar ratios. Results are discussed in section 2.8.

2.6.2 Quantification of O_2/Ar ratio and triple oxygen isotopes (^{16}O, ^{17}O and ^{18}O).

The samples in evacuated bottles from the JCR cruises were all analyzed in Michael Bender's laboratory at Princeton University (PU). The extraction line (see Figure 2.14) was the same as the one used by Reuer *et al*. (2007a) with minimal modifications. The sample analysis was performed during June and July 2007; two to three months after the samples were collected. The analysis was done according to the sampling chronological order (i.e. first JR158 samples, then JR165 samples).

In 2002, Luz *et al.* reported that keeping the bottles with the water lock, the storage time between collection and analysis could be several months without deteriorating (Luz *et al.*, 2002). Reuer *et al.* (2007a), made a more complete evaluation of this. In order to evaluate the effect of the gas permeation and sample contamination by using Viton o-rings (the same as the ones used in this study), the authors concluded that based on a sample volume (250 m) of Subantarctic type waters (i.e. at 10 ºC and 34.5 of salinity) the O_2/Ar measurements have an associated error of 0.1 % for samples stored and analyzed 6 months later. An error of 0.16 % was found for samples stored for a year. In the case of the isotopic composition of oxygen, the authors concluded there is no fractionation effect associated with the o-ring during storage. Thus, from these results the samples subject of this research might not have suffered from this effect either.

After headspace equilibration of the samples, reached during the period of transport and storage, ~99 % of the water phase in the evacuated bottles was drawn out of the bottle under vacuum. The bottle was then connected to an automated extraction line in order to quantitatively separate the gases of interest (O_2 and Ar) from N_2, CO_2 and H_2O, and leave the samples ready for mass spectrometric analysis. The system was developed and described first by Luz *et al.*, (1999) followed by modifications by various authors (i.e. Blunier *et al.*, 2002; Barkan and Luz, 2003; Hendricks *et al.*, 2004; Reuer *et al.*, 2007a).

The main steps in the extraction line are shown in the Figure 2.14 followed by their corresponding description.

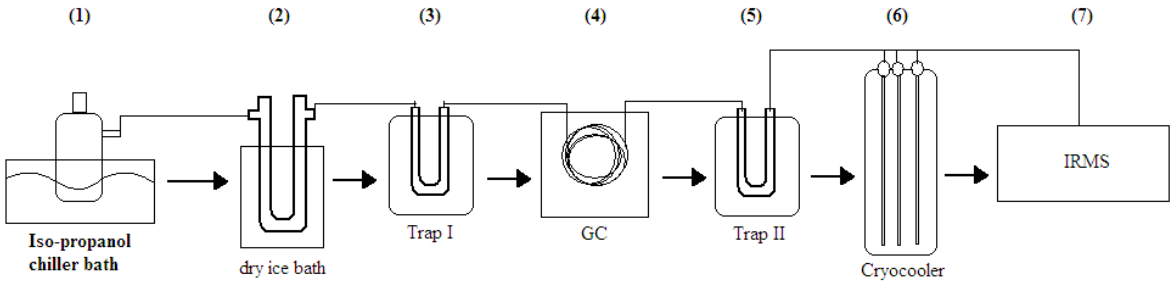

Figure 2.14 – Schematic representation of the extraction line used to remove N_2, CO_2 and H_2O from the headspace of seawater samples as preparation for the IRMS analysis.

In order to freeze most of the H_2O contained in the bottle (as liquid and vapour phase), the evacuated bottles containing the sample headspace were immersed in a chiller bath with iso-propanol at −70 ºC (1) for about 30 min. The chiller bath was connected to the extraction line which was kept under vacuum at all times (~10^{-4} mbar). The system at PU allowed the automated extraction by groups of five samples and one aliquot of compressed dry air (Cair). The latter was admitted to the extraction line to be analyzed in the same way as the headspace from the seawater samples. The Cair aliquot was used as the reference sample.

The valves of each bottle were opened in order to expand the gas mixture into a glass spiral-trap (2) immersed in a dewar with iso-propanol cooled with dry ice to reach −78 ºC; this step was in order to remove the remaining water vapour after the first chilling step. After this process, the dry gas mixture was condensed on coarse (2 mm diameter) type 5Å mol sieve (3, Trap I) held at liquid nitrogen temperature (−196 ºC or 77 K).

The sample was then passed through a chromatographic column (4), (mol sieve 5 Å, 4 m, 1/8” outer diameter, 60/80 mesh) held at 40 ºC. Helium grade 5.0 was used as a carrier gas at a constant flow of 13 ml min^{-1}, the latter was cleaned of contaminants by passing it through a mol sieve trap cooled by liquid nitrogen before entering the chromatographic column (Barkan and Luz, 2003; Reuer *et al.*, 2007a).

The preparatory chromatography removes N_2 and CO_2, retaining only O_2 and Ar on a second mol sieve trap (5, Trap II) of 5 Å and 45/60 mesh. The carrier gas was pumped away while keeping the trap at 77 K with liquid N_2. Finally, the O_2 and Ar mixture was transferred to stainless steel tubes (6) cooled to < 20 K with a He cryocooler.

Each run of the extraction line was enough for five seawater samples plus the dry Cair aliquot as reference standard per set of samples. The time required for the preparation through the extraction line was 46 min/sample (~4.5 h per set of six samples). The cryocooler containing the purified O_2 and Ar mixtures was then connected to an IRMS. Before the analysis of the samples, the cryocooler was warmed to 300 K for 4 h as equilibration time to minimize adsorption effects in the walls of the stainless-steel tubes.

The same procedure was applied to air-equilibrated water samples (Eqwat hereinafter) prepared in the laboratory. Since no replicates of the seawater samples were collected, the results from the Eqwat samples were used to verify the reproducibility and performance of the extraction line and mass spectrometer. The equilibrated water samples were prepared as follows: a 3 l beaker of distilled water was spiked with 1 ml of saturated $HgCl_2$ solution and left under continuous stirring for at least 24 h to reach equilibrium with the atmosphere. Sets of subsamples were drawn into previously prepared evacuated bottles as for the seawater samples.

The O_2 and Ar gas mixture from seawater samples, Cair and Eqwat were analyzed for O_2/Ar and $\delta^{17}O$ and $\delta^{18}O$ values (relative $^{17}O/^{16}O$ and $^{18}O/^{16}O$ isotope ratio differences) by a dual inlet mass spectrometer system (*Thermo Finnigan* MAT 252). Simultaneous measurements of the ion beams *m/z* 32, 33 and 34 were made to determine the $\delta^{17}O$ and $\delta^{18}O$ values of the O_2 using a multi-collector. Afterwards, the O_2/Ar ratios were measured by a series of single measurements for the ion beam intensities of $^{16}O_2$ and ^{40}Ar on a single collector (peak jumping); all measurements were made relative to a gas mixture working reference (see below). Also, N_2 (*m/z* 28) was measured to either indicate incomplete gas separation by the preparatory GC or air contamination during the process. The identification of N_2 was used to correct for interference with the O_2 isotope measurements (Barkan and Luz, 2003).

The working reference was a pressurized mixture of Ar (4.23 %) and O_2; similar to the ratio of these two gases in air (20.942 % O_2 and 0.934 % Ar).

Each mass spectrometric measurement consisted of three separate runs during which the ratio of sample to working reference was determined 24 times (cycles) to achieve high precision in the δ-values. Therefore, the reported δ-values are averages of the results from the three runs.

Aliquots of the sample and working reference gas were balanced by measuring the voltage of mass 32 in the bellows before each of the three runs; this procedure is useful to decrease the analytical error due to pressure imbalance between the sample and standard side in the MS. The efficiency of the sample preparation in the extraction line and analysis in the mass spectrometer is given by the analyzed aliquots of dry compressed air. For 22 aliquots of Cair measured during the entire period of time of analysis (for all samples from JR158 and JR165), the 1σ standard deviation of the mean was ±0.006 ‰ (δ^{17}O), ±0.010 ‰ (δ^{18}O), ±0.1 % (O_2/Ar) and ±7.7 per meg ($^{17}\Delta$).

Each block of 24 measurements (each done 3 times) took ~2 h. This permitted the analysis of six samples (five seawater samples and one Cair aliquot) per day. The average ±1σ output voltage for the *m/z* 32 ion beam for the standard (ST) side and the sample (SA) side in IRMS for the zero readings, seawater samples, equilibrated water samples and compressed air aliquots is 3.017±0.152 V and 3.006±0.202 V, respectively. The mean of the absolute imbalance between both bellows was 0.0005 V using a range of manually fixed voltage. See section 2.9 for further details of the data corrections and bellows imbalance results.

2.6.3 Corrections to the measurements of O_2/Ar ratios.

a) Normalization of δ-values against atmospheric air for c(O_2/Ar).

The measurements of O_2/Ar ratios in the evacuated bottles by IRMS were done from the ion current converted to voltage (*U*) for both masses (*m/z* 32 and 40), and represented as standard δ-notation following:

$$\delta_{\mathrm{sa/ref}}(\mathrm{O_2/Ar}) = \frac{(U_{32}/U_{40})_{\mathrm{sa}}}{(U_{32}/U_{40})_{\mathrm{ref}}} - 1 \qquad (2.16)$$

where, U_{32} and U_{40} represent the voltage of the ion beam intensities for *m/z* 32 and 40, respectively. The subindice "sa" indicates the corresponding ratio for Cair aliquots and seawater samples, while "ref" is the ratio for the working reference. Thus, this is referring to $\delta_{\mathrm{sa/ref}}(O_2/Ar)$ and $\delta_{\mathrm{cair/ref}}(O_2/Ar)$, respectively.

The O_2/Ar ratios for air-equilibrated water ($(O_2/Ar)_{Eqwat}$) and working reference ($(O_2/Ar)_{ref}$) were also measured to verify the performance of the mass spectrometer and efficiency of the method. The preferred reference for O_2/Ar ratios is atmospheric air. The composition of atmospheric air is well known; thus, atmospheric air is considered as a globally constant reference for the analysis of triple oxygen isotopes (Barkan and Luz, 2003). Therefore, the dry Cair aliquots analyzed at the same time as the set of samples is the reference for the seawater samples results. The relative O_2/Ar ratio difference of the samples with respect to air was computed from the mass spectrometer measurements as follows:

$$\delta_{\mathrm{sa/Cair}}(\mathrm{O_2/Ar}) = \frac{\delta_{\mathrm{sa/ref}}(\mathrm{O_2/Ar}) - \delta_{\mathrm{Cair/ref}}(\mathrm{O_2/Ar})}{1 + \delta_{\mathrm{Cair/ref}}(\mathrm{O_2/Ar})} \qquad (2.17)$$

A total of 40 measurements of Cair were evenly distributed during sample analysis (34 days). 18 out of 40 were useless due to several problems with equipment and power cuts during the analysis, during these periods also some seawater samples were lost. The median value for $\delta_{\mathrm{Cair/ref}}(O_2/Ar)$ values for the remaining 22 samples was −8.8±1.1 ‰. This value was used in the equation above as a constant value to correct for all the discrete samples.

As was discussed by Hendricks *et al.* (2004), due to the quantification of $^{16}O_2$ and ^{40}Ar as peak jump on a single collector in the mass spectrometer, no measure of internal precision accounted for the O_2/Ar measurements. As discussed before, the Equwat samples are used to verify the reproducibility and performance of the method and sample analysis due to the lack of sample duplicates.

b) *Correction by solubility.*

In order to calculate the O_2/Ar ratio for the discrete seawater samples ($(O_2/Ar)_{sa}$), including samples from USW and from Niskin bottles), the Cair reference in the δ-value of the gas ratio for each sample was removed by applying the equation below. The O_2/Ar ratio in air was taken as 22.42 (with a percentage abundance of O_2 for atmospheric air as 20.942 % and for Ar, 0.934 % (Glueckauf, 1951).

$$(O_2/Ar)_{sa}^{*} = \left[1 + \delta_{sa/Cair}(O_2/Ar)\right] \times (O_2/Ar)_{Cair} \qquad (2.18)$$

The term $(O_2/Ar)_{sa}^{*}$, implies a partial result for the O_2/Ar ratios. Due to the distribution of gases between the headspace and water in the sampling bottles at room temperature (θ = 21 ºC) during the equilibration, a solubility correction was applied considering the volume ratio of water to headspace and the solubility of each gas at the temperature of analysis (Luz and Barkan, 2002; Luz *et al.*, 2002), following:

$$(O_2/Ar)_{sa} = Q \times (O_2/Ar)_{sa}^{*} \qquad (2.19)$$

The factor Q is determined from the volume ratio of water to headspace ($\varepsilon = V_{sw}/V_g$, where V_{sw} and V_g are the volumes of the seawater and headspace phase for each sample, respectively) corrected by the solubility of O_2 and Ar at 21 ºC, using:

$$Q = \frac{1 + \alpha(O_2)\,\varepsilon}{1 + \alpha(Ar)\varepsilon} \qquad (2.20)$$

The term α is the Ostwald solubility coefficient for each gas, which accounts for the volume of dissolved gas per volume of water at the measurement conditions (21 ºC and salinity of 33 for seawater samples). The solubility correction for the O_2/Ar ratios in the seawater samples accounted for 5.5±0.2 % (n=108) of the ratio for the corrected final value ($(O_2/Ar)_{sa}$).

A total of 11 air-equilibrated samples were measured together with the seawater samples showing an average of 20.437±0.040 in the O_2/Ar with a precision of 0.195 % equivalent to the overall precision of the method.

The ratio values obtained here are in good agreement with Hamme and Emerson (2004). After a repetitive analysis of 14 air-equilibrated water samples, the authors found an average O_2/Ar ratio of 20.399 ± 0.010; however the precision observed by the authors (± 0.048 %) (Hamme and Emerson, 2004) was about 4 times better than the precision found in this study. This is due to the differences in the method applied to measure these values.

2.7 Calibration of continuous O_2/Ar ratios from MIMS.

The continuous underway O_2/Ar ratios were calibrated by linear regression against the O_2/Ar ratios from the discrete seawater samples ($(O_2/Ar)_{sa}$). After interpolation of the working MIMS variables (Table 2.3) and creation of the 10 s resolution grid, elimination of water flow perturbations and measurements from the jacketed beaker from the continuous data, the USW-MIMS O_2/Ar values were calibrated using the results from the discrete samples; 1 min-averages of the O_2/Ar ratio from the continuous data were extracted at the collection time of the discrete samples in the evacuated bottles (t_{evbot}). A least squares fit was obteined between $(O_2/Ar)_{sa}$ and O_2/Ar at time t_{evbot}.

Samples from the Niskin bottles were excluded of the O_2/Ar calibration. A total of 90 discrete samples in evacuated bottles were collected from the USW and surface Niskin bottles for the cruises JR158 and JR165; 14 samples corresponded to the JR158 cruise but 4 samples were removed due to air-contamination during the sampling procedure. The remaining 76 samples corresponded to the JR165 cruise; 6 samples out of the 76 were collected from Niskin bottles, therefore were not considered for the calibration equation fit.

An independent linear fit was performed for each cruise; however, some criteria were considered within each cruise to construct secondary linear fit equations, grouping the discrete samples based on: the usage of a particular degassing membrane, rate of water flow through the degassing membrane and gear pump speed. For JR158, 6 discrete samples were used for the calibration process (Julian days 43.5 to 47.8). During that time a longer degassing membrane was used, the coefficient of determination (r^2) for this fit corresponded to 0.97. The O_2/Ar ratios given by the

MIMS data were on average 1.46±0.47 higher than the O_2/Ar values from the discrete samples.

After Julian day 47.8 the membrane box mentioned in section 2.1.3 was used. For this calibration, 4 discrete samples were used to construct the linear fit (r^2 = 0.99) (plot not shown). A better agreement between the results from the membrane box and the ones from the discrete sample analysis was observed. The MIMS data using a membrane box were 0.27±0.03 higher than the O_2/Ar values from the discrete samples.

During cruise JR165 only the membrane box was used. A total of 70 samples from USW samples were selected to be used for the continuous signal calibration, however only for 54 samples an O_2/Ar at t_{evbot} was available from the continuous record.

The overall calibration for the continuous O_2/Ar data for cruise JR165 was split into seven groups (i.e. seven linear equation fits), where each corresponded to a different gear pump speed translated to a different water flow used to feed the membrane (Figure 2.15). The average coefficient of determination for the seven linear fits accounted for 0.96. The mean residual after calibration corresponded to (0.0 ± 0.4) %.

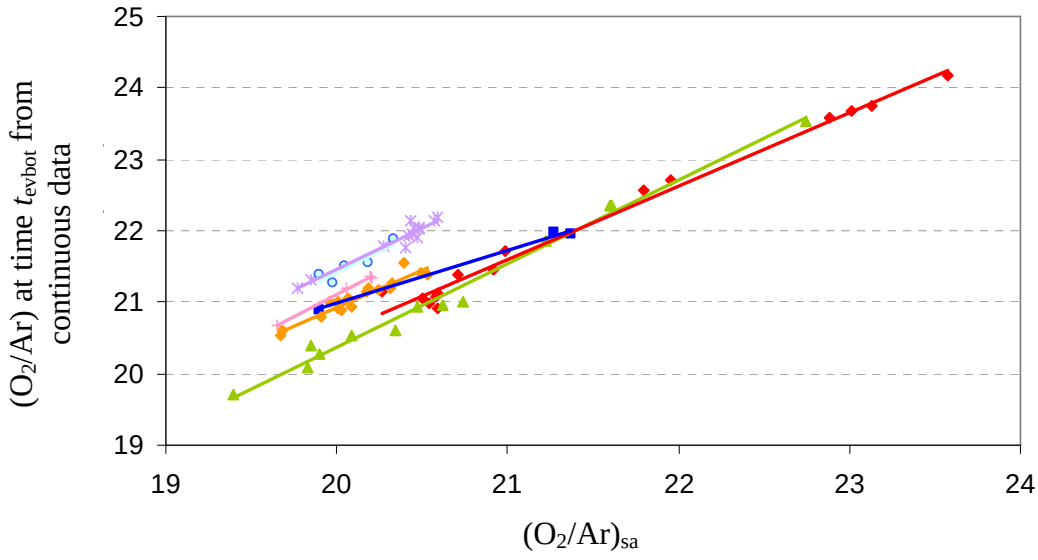

Figure 2.15 – Seven linear regression fits for the calibration of O_2/Ar from MIMS data recorded during cruise JR165.

2.7.1 Biological O_2 flux (F_{bio}) from $\Delta O_2/Ar$ estimates.

The biological contribution to the O_2 saturation can be estimated by comparing the measured O_2/Ar ratio with the ratio at saturation with the atmosphere ($(O_2/Ar)_{eq}$) (Craig and Hayward, 1987). Thus, the calculation of the biological O_2 supersaturation ($\Delta O_2/Ar$) (equation 1.5 of chapter 1; section 1.7) is given by the ratio between the measured O_2/Ar ratio in the surface seawater and $(O_2/Ar)_{eq}$. The latter is the saturation concentration ratio ($c_{eq}(O_2)$ / $c_{eq}(Ar)$) determined from the solubility equations for O_2, (Benson and Krause, 1984; Garcia and Gordon, 1992; Garcia and Gordon, 1993) and for Ar (Hamme and Emerson, 2004) as a function of the corresponding *in situ* temperature, salinity and pressure (SST, S and P_o, respectively). The biological O_2 supersaturation was also calculated for the discrete samples ($\Delta_{sa}(O_2/Ar)$).

From the $\Delta O_2/Ar$, $c_{eq}(O_2)$ and the appropriate weighted gas transfer coefficient (k_w) (Sweeney *et al.*, 2007; Reuer *et al.*, 2007a) it is possible to estimate the rate of biological O_2 production, here referred as to biological O_2 flux (F_{bio} in mmol m^{-2} d^{-1}), integrated over the mixed layer. F_{bio} is calculated following the equation 1.5 in section 1.8 (chapter 1).

2.8 Comparison between discrete CTD and USW samples for ΔO_2 and $\Delta(O_2/Ar)$: an evaluation of the effect of the intake pipes

As discussed in section 2.2.1, the time delay of the water flowing through the intake pipes by 2 min, was the main cause of the warming of 0.65 ºC in the surface water. The warming effect can potentially affect the O_2 content in surface waters, adsorption in the walls of the intake pipes or by degasification or by consumption of O_2 (respiration) by biological activity (if any).

In order to identify any potential effect in the dissolved O_2 concentration due to the pipes of the intake system, a comparison of results of $c(O_2)$ and O_2/Ar between discrete samples collected parallel from the surface Niskin and from the USW was done.

From this comparison, is also possible to identify the entrance of bubbles into the system, leading to an apparent excess of dissolved O_2 in the seawater when compared to the O_2 concentration in the sample from the surface Niskin.

2.8.1 Comparison between $\Delta_{sa}O_2$ and $\Delta_{CTD}(O_2)$ in discrete samples.

For JR158, a total of 16 out of 20 CTD stations were simultaneously sampled from the surface Niskin and USW to compare their O_2 content. The comparison was made in terms of the O_2 supersaturation for both sources ($\Delta_{CTD}(O_2)$ and $\Delta_{sa}O_2$, respectively).

The absolute of the mean difference in ΔO_2 ($\Delta_{diff}(O_2) = |\Delta_{sa}(O_2) - \Delta_{CTD}(O_2)|$) was 0.3±0.2 %. Considering a $c_{eq}(O_2)$ equivalent to 351.9 µmol kg^{-1} at 0 ºC and salinity of 33.5 in the surface ocean (1013 mbar) (Benson and Krause, 1984; Garcia and Gordon, 1992) the $\Delta_{diff}(O_2)$ during cruise JR158 was equivalent to 1.0±0.7 µmol kg^{-1} in terms of $c(O_2)$. This comparison suggests a higher O_2 content in the water from the USW than in the one from the surface Niskin (independently if they are super or undersaturated with respect to the O_2 value at saturation) (Figure 2.16).

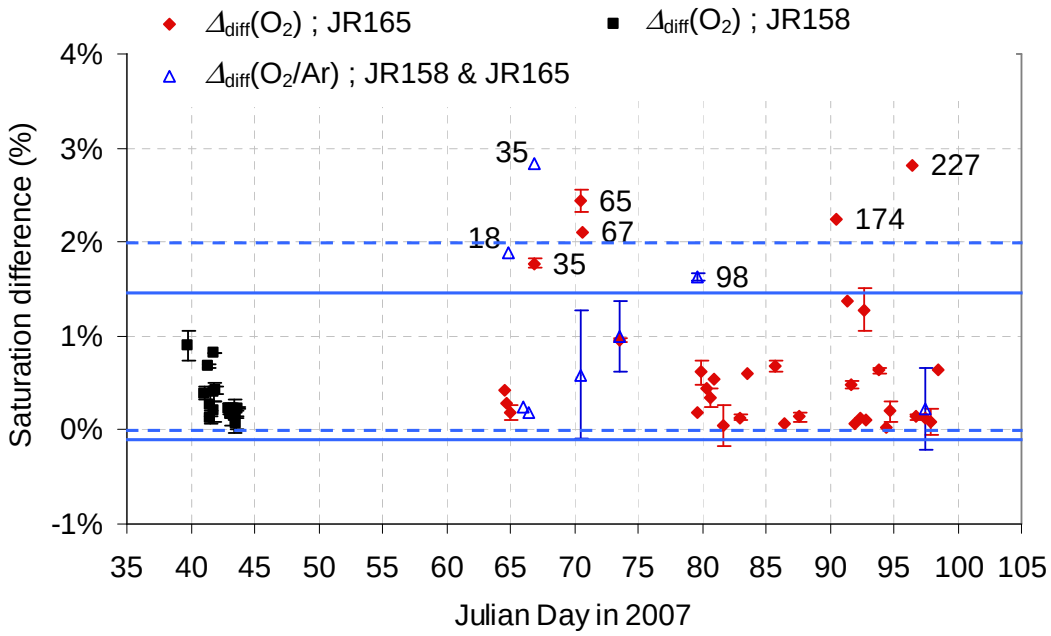

Figure 2.16 – Difference between $\Delta_{sa}(O_2)$ minus $\Delta_{CTD}(O_2)$ ($\Delta_{diff}(O_2)$ in %) for: JR158 (squares) and JR165 (diamonds). Error bars show ±1σ from the mean ΔO_2 for USW duplicate samples. Only three samples from the CTD Niskin bottle during cruise JR158 had duplicate analysis, while none during the cruise JR165. Empty triangles represent the difference between $\Delta_{sa}(O_2/Ar)$ minus $\Delta_{CTD}(O_2/Ar)$ for JR158 and JR165 ($\Delta_{diff}(O_2/Ar)$ in %); error bars show ±1σ between pairs of samples comparisons. Upper and lower limits of the mean ±1σ is represented for JR165 (full horizontal lines) and for all the $\Delta O_2/Ar$ comparisons (dashed horizontal lines).

The analytical precision of the Winkler titrations during JR158 was 0.26 μmol kg^{-1}; thus, the difference in O_2 concentration between samples is off the range of the precision and some effect might have happened in the intake pipes to increase slightly the O_2 concentration. Unfortunately, the comparisons are not enough in number to go further on this explanation. More data for a reliable comparison is needed. Considering the relatively small difference in concentration between both water sources, no further correction due to the influence of the pipes of the intake system was done for the data of cruise JR158.

For JR165, a total of 34 comparisons between $\Delta_{sa}(O_2)$ and $\Delta_{CTD}(O_2)$ were made. A mean $\Delta_{diff}(O_2)$ of 0.7±0.8 % was identified. The $c_{diff}(O_2)$ corresponded to 2.4±2.8 μmol kg^{-1} suggesting, as in the JR158 cruise, higher amount of O_2 in the USW samples than in the CTD samples (Figure 2.16). Five of the comparisons showed a difference higher than the mean $+1\sigma$ (1.4 %) (stations 35, 65, 67, 174 and 227) resulting in less O_2 in the CTD sample than in the USW by as much as 2.3±0.4 % (8.0±1.4 μmol kg^{-1}).

To evaluate the situation for each station, the data of the optode was investigated at the time of collection of discrete samples. For station 67, the signal for $c(O_2)$ provided by the optode at the time of samples collection was very noisy, indicating bubbles created by turbulence into the intake system due to heavy seas.

The design of the intake system is a key factor to successfully obtain continuous gas measurements from surface water. At the JCR, the design consists of a pipe with three positions: 1) up, 0.5 m above the keel, 2) mid, in line with the keel, and 3) down, where the pipe extends 0.3 m below the keel. The internal pipe diameter of the intake is 125 mm. The surface seawater is delivered through the intake by two pumps alternating their pumping period every 12 hr; each pump has an average flow rate of 7400 l h^{-1}. As explained in section 2.1.4, two sieves are used (prior to the pumping system) to avoid the entrance of large particles (> 5 mm) that could clog or damage the system. During heavy seas, presence of ice floes and/or at ship speeds >12 kn the intake pump is turned off or remains in mid position in the best case. The down position of the intake showed to be the best for continuous measurements of dissolved gases from the USW, improving the data quality significantly by avoiding

the entrance of a large amount of bubbles into the pipes. During the occupation of station 67, the JCR deck engineer changed the intake to upward position to avoid the pipe to brake due to possible crash with waves. As a result in our oxygen measurements, an apparent higher ΔO_2 was identified when comparing with its similar from the Niskin surface bottle, by as much as 2.1 % (7.3 μmol kg^{-1}). For the remaining four comparisons for stations 35, 65, 174 and 227 during JR165, no noise generated by entrainment of bubbles was detected in the optode signal. For this group of stations, the $\Delta_{sa}(O_2)$ was on average 2.3±0.4 % (8.0±1.4 μmol kg^{-1}) higher than the $\Delta_{CTD}(O_2)$.

The change in O_2 solubility in seawater (33.5) at atmospheric pressure (1013 mbar) is about 2.37 % due to a change by 1 ºC of temperature in the water (Benson and Krause, 1984; Garcia and Gordon, 1992). For the previous comparisons it is important to take into account the following assumptions: 1) all the USW were under the same warming effect of 0.65 ºC, 2) the change in the gas solubility is slower than the change in the water temperature and 3) as the temperature of the water increases the O_2 concentration will decrease; thus, the differential O_2 saturation between USW and CTD samples must be due to other reasons than a warming effect by the intake pipes. Unfortunately, the comparisons were not enough in number to explain the observed differences.

Consideration should be made to the low temperature of seawater which can have an important effect to the solubility response of O_2 in comparison to the change of temperature. The latter might happen at a faster rate than the former; however, the change in oxygen solubility is not linear. The rate of change in the oxygen content is slower as the temperature of the water increases. At constant salinity (33.5) and at atmospheric pressure (1013 mbar) the dissolved oxygen concentration on average decreases 8.8 μmol kg^{-1} per 1 ºC of change in the water; this is true for a range of cold waters (−1 to 3 ºC). On the other hand, as the water is warmer (4 to 10 ºC) the O_2 content decreases by 6.9 μmol kg^{-1} under the same conditions of salinity and pressure (Figure 2.17). Thus, the warming effect identified in the intake pipes is expected to cause a decrease in oxygen concentration of the surface water rather than the observed decrease in comparison to water from the Niskin bottles.

If the effect of the intake pipes over the surface water is not clear (or possible to explain from the few comparisons made above) to explain an apparent "production" of oxygen in the surface, we could think of a degassing effect on the water sample into the Niskin bottle. This could be possible if one of the following conditions, or a combination between them, is true: 1) the closing system of the Niskin bottle was not working properly, 2) the water sample was not the first one to be collected from the Niskin bottle, thus contamination by air could entrain or 3) a delay of several minutes between the sample collection from the USW and Niskin bottle, leaving the water into the Niskin bottle for a long time.

For condition 1, during both oceanographic campaigns some Niskin bottles did not close properly during firing; however they were identified on time to avoid sampling water from them.

For condition 2, the samples for O_2 analysis during both cruises were the first ones to be collected from the Niskin bottles immediately after the rosette was brought back to the deck. Therefore, neither of the factors 1 and 2 would account for the observed $c_{sa}(O_2) > c_{CTD}(O_2)$.

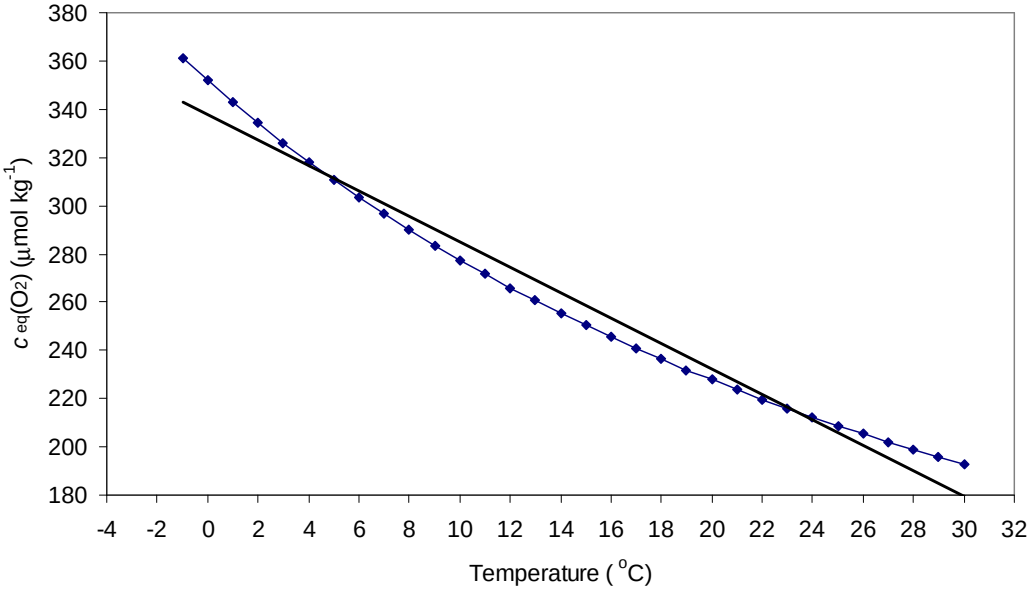

Figure 2.17 – Non-linearity of the concentration of dissolved O_2 ($c_{eq}(O_2)$) over a range of temperatures between −1 to 30 ºC for seawater (constant salinity of 33.5) at atmospheric pressure (1013 mbar). The calculations of solubility were based on Benson and Krause (1984) and Garcia and Gordon (1992 and 1993) equations.

For condition 3, this is also unlikely to happen due to the degassing of the seawater contained in the Niskin bottle can be a slow process if the latter is working correctly. In any case, an evaluation of the difference in collection times for both USW and Niskin bottle is made next.

To evaluate the time difference between sample collections the USW sample collection time was registered during the cruise. Although the real collection time of the sample from the Niskin bottle was not registered, the firing time of the surface Niskin bottle was used instead. For all the 34 comparisons, an average difference between collection times (sampling time delay) of the USW sample and the surface Niskin bottle firing is 2.7±2.4 min (Figure 2.18).

For 31 samples, the USW sample was collected before the Niskin bottle, intending to collect the USW sample at around the same time when the Niskin bottle was fired. The time delay between sample collection is an indication of the probability to collect the same water mass. As can be observed for the stations of interest, it took about 2 min between the USW sample collection and the surface Niskin bottle was fired, therefore we can conclude that the same water mass was sampled and the differences in the O_2 saturation is not due to a delay between samples collection.

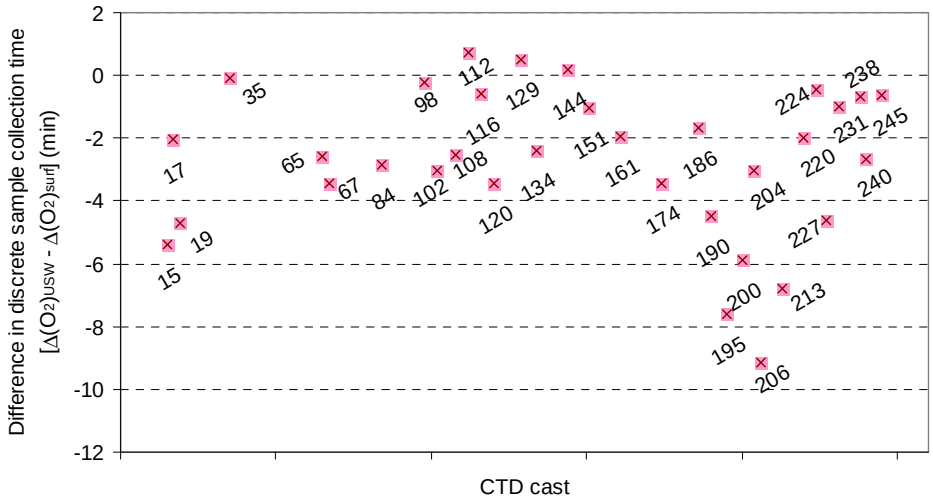

Figure 2.18 – Sampling time delay (min) between $\Delta_{sa}(O_2)$ and $\Delta_{CTD}(O_2)$. Negative values indicate the time in min the USW discrete sample was collected before the firing time of the surface Niskin bottle.

Thus, in view of no clear explanation for the $c_{sa}(O_2) > c_{CTD}(O_2)$, stations 35, 65, 174 and 227 were not considered for the calibration purposes. If removed the offsets from the differences in the stations discussed above, the remaining $\Delta_{diff}(O_2)$ for the rest of the stations showed a mean value of 0.4±0.4 % (1.4±1.4 μmol kg^{-1}, n=28) of O_2 higher in the USW sample than in the surface Niskin. This result is in close agreement with the observations during the cruise JR158 (0.3±0.2 %).

After this evaluation, the comparison between $c_{sa}(O_2)$ and $c_{CTD}(O_2)$ leaves no clear explanation for the apparent "autotrophy" in the intake pipes or "heterotrophy" in the Niskin bottles. Furthermore, the intake system in the JCR does not cause a significant degassing of the surface seawater, either by a warming effect or gas adsorption.

From the few comparisons made and considering the analytical precision for the Winkler titrations during the cruise JR165 (0.29 μmol kg^{-1}), approximately 0.14 % (0.5 μmol kg^{-1}) of the total O_2 concentration can be attributed mostly to analytical error by the introduction of bubbles during the USW sampling into the Winkler flask.

Recent efforts by other authors have been made in order to evaluate the effect of the intake pipes over the surface water for dissolved gas studies (Juranek *et al.*, 2010). However most of the few evaluations made so far resolve a loss of oxygen (up to 2 %) in the intake pipes and no previous study of this nature has been done for the JCR. For this study, the unclear comparisons were removed from the calibration of continuous data.

2.8.2 Comparison between $\Delta_{sa}(O_2/Ar)$ and $\Delta_{CTD}(O_2/Ar)$ in discrete samples.

A total of 5 comparisons (stations 2, 65, 84, 98 and 238) between the $\Delta O_2/Ar$ discrete results from USW ($\Delta_{sa}(O_2/Ar)$) and surface Niskin bottles ($\Delta_{CTD}(O_2/Ar)$) for both JR158 and JR165 cruises, were performed (average difference 1.3 ± 3.5 %; n=4, station 2 not included).

However, in order to have more observations the $\Delta_{CTD}(O_2/Ar)$ were compared to the corresponding $\Delta O_2/Ar$ from the continuous MIMS data at the Niskin bottles sampling time (firing time, t_{firing}). A few more comparisons were possible (8 in total) with stations 18, 23, 29 and 35 added to the list of comparisons. A mean $\Delta O_2/Ar$

difference ($\Delta_{diff}(O_2/Ar)$ = $\Delta(O_2/Ar)$ at t_{firing} − $\Delta_{CTD}(O_2/Ar)$) of 1.1 ± 1.0 % was observed (Figure 2.16). In agreement to the $c(O_2)$ comparisons, the O_2/Ar saturation was on average higher in the USW than in the CTD samples.

The ΔO_2/Ar comparisons are not intended to identify a degassing process in the intake pipes due to both Ar and O_2 are expected to degas at the same rate if both remain under the same saturation levels with respect to the atmosphere. On the other hand, these comparisons would only allow to confirm (or reject) our explanation of the presence of bubbles causing artefacts in the O_2-USW data.

Stations 35, 65, 84, 98 and 238 were also compared for $c(O_2)$ discrete samples. Station 65 did not show high $\Delta_{diff}(O_2/Ar)$ as in $\Delta_{diff}(O_2)$ (0.59 % and 2.44 %, respectively), despite it was collected nearly 18 min before the Niskin bottle was fired (Figure 2.19). Therefore, the introduction of bubbles while sampling the discrete USW for $c(O_2)$ analysis is supported.

In an analysis for the delay on time between discrete sample collection, the average time was 4.6 min for the USW samples collected before the surface Niskin was fired. The ship was still on station during that period of time, therefore the observed $\Delta(O_2/Ar)$ at t_{firing} > $\Delta_{CTD}(O_2/Ar)$ apparently is not due to the introduction of bubbles during ship movement (Figure 2.19).

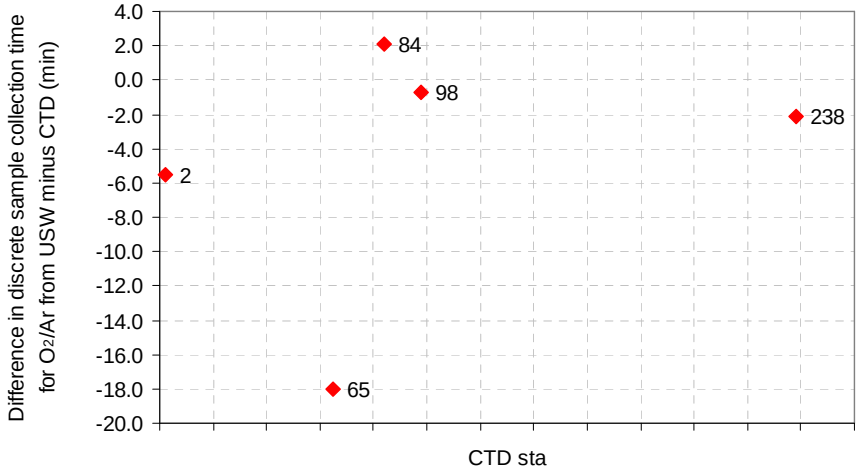

Figure 2.19 – Sampling time delay (min) between $\Delta_{sa}(O_2/Ar)$ and $\Delta_{CTD}(O_2/Ar)$. Negative values indicate the time in minutes that the USW discrete sample was collected before the firing time of the surface Niskin bottle.

Station 35 showed for both comparisons in O_2 and O_2/Ar saturations, high values in the USW samples (1.8 % and 2.8 %, respectively) indicating that, as provided solely by the O_2 data, during this station a possible entrance of bubbles in the intake system during the sampling time was likely to happen. In the case of stations 18, 65, 84, 98 and 238 no clear explanation can be drawn regarding the higher ΔO_2/Ar observed in the continuous USW (0.8 ± 0.7 % on average). The $\Delta_{diff}(O_2/Ar)$ is in the range of the mean ± 1σ; however, more comparisons are needed in order to draw conclusive observations.

In summary, the USW discrete samples showed in average 0.4 % to 0.8 % higher saturation for O_2 and O_2/Ar analysis respectively, than in the discrete samples from the surface Niskin. These differences are in both cases higher than the precision reached by the Winkler titrations (0.1 %) and during the O_2/Ar measurements (0.1 – 0.2 %). Some of this difference could be due to analytical error by the introduction of bubbles during the sampling procedure. However, the low number of comparisons for both O_2 and O_2/Ar determinations might have not been enough to evaluate the contribution of the intake pipes of the JCR or analytical errors. For the calibration procedure in both cruises, the non-explicable comparisons were removed and no further corrections to the O_2 and O_2/Ar data were done.

2.9 Corrections to the triple O_2 isotopes for $^{17}\Delta$ calculations.

From the measurements of $^{17}O/^{16}O$ and $^{18}O/^{16}O$ in the headspace of seawater samples, the isotopic abundance can be expressed in δ-notation (in parts per mille, ‰) following:

$$\delta^i O = R_{sa}(^iO/^{16}O)/R_{ref}(^iO/^{16}O) - 1 \qquad (2.21)$$

where, i is equal to 17 or 18 (i.e. $\delta^{17}O$ and $\delta^{18}O$). The relative abundance of $^{17}O/^{16}O$ and $^{18}O/^{16}O$ for the seawater samples (sa) was measured against the same working reference (ref) used for O_2/Ar ratios. However, as in the case of the $c(O_2/Ar)$ ratios, the preferred working reference is atmospheric air; thus, a normalization against atmospheric air is needed.

2.9 Corrections to the triple O_2 isotopes for $^{17}\Delta$ calculations

The $^{17}\Delta$ calculation, as explained in Chapter 1 (equation 1.18, section 1.10.2) was performed according to the following equation:

$$^{17}\Delta = \ln(1+\delta^{17}\mathrm{O}) - \lambda \ln(1+\delta^{18}\mathrm{O}) \qquad (2.22)$$

The coefficient λ represents the reference mass-dependent fractionation slope for the kinetic respiratory process (consumption by respiration of O_2 produced by photosynthesis) in aquatic systems corresponding to 0.5179 (Luz and Barkan, 2005). The measurement of δ-values can vary due to interactions between the gas species in the sample, such as CO_2 and N_2. Interactions in the IRMS ion source might occur; therefore separation of gases such as Ar from N_2 are important before the isotopic measurements are performed (Barkan and Luz, 2003). However, some interactions might still occur and corrections to the final δ-values are needed before the final $^{17}\Delta$ calculation. The following corrections were performed in the subsequent order: 1) pressure imbalance in the sample and standard side bellows of the MS, 2) N_2 interaction, 3) Ar interaction and finally, 4) the normalization to atmospheric air as reference.

For δ^{17}O and δ^{18}O, the solubility correction was not performed as in the O_2/Ar ratios (section 2.6.3). This correction only accounts for about 0.2 per meg, being a negligible value for the overall quantification (J. Kaiser, *personal communication*).

2.9.1 Pressure imbalance correction.

For MAT-*Finnigan* MS with dual inlet system, the design for the isotope ratio determination consists of the balance of pressures between the sample and standard side bellows in order to reach equal voltage. The MS switches between the two inlets in each run, sending gas from one inlet to the ionization source and gas from the other inlet to waste. Balance between the expansion of the sample and standard bellow must be reached according to the aliquots expected to be used.

Since the reference gas has a different composition than the gas from samples, differences in the ionization efficiencies of the two gas mixtures could cause different voltage measured values due to imbalance in the bellows. Therefore, the measured isotope ratio depends on the adjustment of the sample and standard

voltages before the MS analysis. The adjustment is performed in the most abundant *m/z* of interest, which is in this case, 32. The adjustment is done automatically; however, measurements are sensitive to any imbalance.

The pressure imbalance for the analysis of the JR158 and JR165 samples was corroborated at the end of the sample analyses. A total of 5 zero enrichment measurements were done by a manual voltage variation of ±0.05 V to the *m/z* 32 fixed value (2.99 V) in the sample side bellow. A total of five steps on the voltage variation (i.e. every 0.025 V) were performed in order to generate a pressure imbalance between the sample and reference side bellows of the IRMS. On average, the difference between the output voltages from the sample side minus the fixed reference side was 0.007±0.048 V. The median (±1σ) of the change in δ^{17}O was 0.005±0.017 ‰ and for δ^{18}O −0.003±0.008 ‰ (Figure 2.20). This change was negligible and no further corrections were done due to bellows imbalance for the results of the seawater samples.

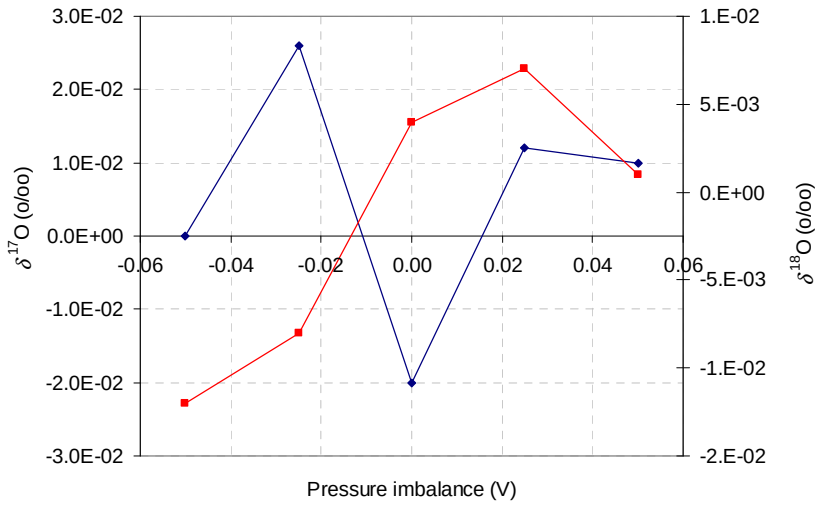

Figure 2.20 – Variations in the pressure imbalance (−0.05 to 0.05 V; in steps of 0.025 V) of the sample and reference side bellow for δ^{17}O (blue line) and δ^{18}O measurements (red line) (‰).

2.9.2 Corrections by N_2 interactions.

Since N_2 is the main constituent of the atmospheric air; as discussed previously, it was removed by gas chromatography from the headspace in order to avoid interactions with the gases of interest (O_2 and Ar).

Traces of N_2 due to an inefficient separation through the chromatographic column during the sample preparation, or contamination of the sample, can lead to interactions in the ion source affecting the final O_2 δ-values. To correct for the presence of N_2 traces, the N_2/O_2 ratio was calculated for each sample and multiplied by a previously estimated N_2 slope for $\delta^{17}O$ and $\delta^{18}O$ respectively.

The N_2 slope was calculated after all the sample analyses. A series of gas mixtures with different N_2 content (variations of N_2 content in the working reference), were injected in the sample side bellow of the MS. The isotopic abundance of ^{17}O and ^{18}O after N_2/O_2 variations was measured for each mixture. These results were plotted against the $\delta(N_2/O_2)$ (‰) values from *m/z* 28 and 32, calculated by the following equation:

$$\delta(N_2/O_2) = \frac{(U_{28}/U_{32})_{sa}}{(U_{28}/U_{32})_{ref}} - 1 \qquad (2.23)$$

where U_{28} represent the voltage of the ion beam intensities for *m/z* 28 in the sample side (sa) and standard side (ref). Next figure (Figure 2.21) shows the N_2 slopes obtained from the linear relationship between $\delta^{17}O$ and $\delta^{18}O$ versus $\delta(N_2/O_2)$, obtained by increasing up to 3 times the N_2 concentration in the working reference (sample side) measured against the original concentration (standard side). Each reading was performed in triplicate.

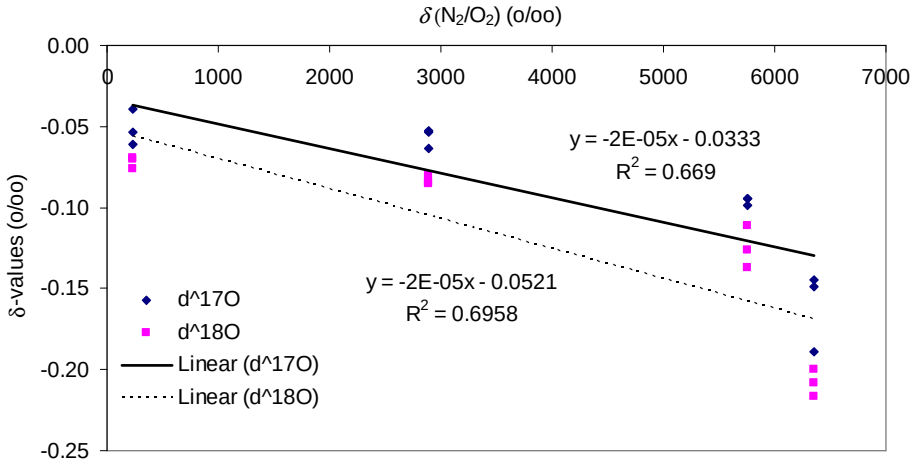

Figure 2.21 – N_2 slope for $\delta^{17}O$ and $\delta^{18}O$ using four different concentrations of working reference measured in triplicate.

The N_2 slope for $\delta^{17}O$ (N_2^{d17O}) corresponds to -1.5×10^{-5}; while for $\delta^{18}O$ (N_2^{d18O}) is -1.8×10^{-5}. The factors (in ‰) for the N_2 correction in the $\delta^{17}O$ and $\delta^{18}O$ ($N_2\_\delta^{i}O$), were calculated according to (i = 17, 18):

$$N_2\_\delta^{i}O = \left(\frac{(U_{28}/U_{32})_{sa}}{(U_{28}/U_{32})_{ref}} - 1 \right) \times N_2^{dio} \qquad (2.24)$$

All discrete seawater samples, air-equilibrated water samples and compressed air aliquots were corrected by this factor. It is assumed that the ratios from the reference do not change over time due to changes in ionization efficiencies.

On average, the N_2 correction for the seawater samples accounted for 0.0105 ‰ for the $\delta^{17}O$ values, while for the $\delta^{18}O$ values corresponds to 0.0089 ‰.

2.9.3 Corrections by Ar interactions.

As was described before, Ar was not separated from the main gas mixture in order to quantify the O_2 and Ar abundance. However, $\delta^{17}O$ and $\delta^{18}O$ depend on variations in the Ar/O_2 ratio (Barkan and Luz, 2003).

In terms of the oxygen isotopes determination, a small Ar interference in the ion source of the IRMS can occur. Corrections over the δ-values (previously corrected by N_2 interferences) were performed. An Ar slope was calculated (following the same procedure as for the N_2 slope described above), by using the Ar/O_2 ratios.

$$\delta(Ar/O_2) = \frac{(U40/U32)_{sa}}{(U40/U32)_{ref}} - 1 \qquad (2.25)$$

Next figure (Figure 2.22) shows the Ar slope obtained from the linear relationship between $\delta^{17}O$ and $\delta^{18}O$ versus $\delta(Ar/O_2)$, obtained by increasing up to 3 times the Ar concentration in the working reference (sample side) measured against the original concentration (standard side). Each reading was performed in triplicate.

The Ar slope for $\delta^{17}O$ (Ar^{d17O}) corresponds to -3.4×10^{-5}; while for $\delta^{18}O$ (Ar^{d18O}) is -9.6×10^{-5}. The factors (in ‰) for the Ar correction in the $\delta^{17}O$ and $\delta^{18}O$ ($Ar\_\delta^{i}O$), were calculated according to (i = 17, 18):

$$\mathrm{Ar}\_\delta^{i}\mathrm{O} = \left(\frac{(U_{40}/U_{32})_{\mathrm{sa}}}{(U40/U_{32})_{\mathrm{ref}}} - 1 \right) \times \mathrm{Ar}^{\mathrm{dio}} \qquad (2.26)$$

Both N_2 and Ar correction factors ($N_2\_\delta^{i}O$ and $Ar\_\delta^{i}O$) due to interferences were removed from the measured $\delta^{17}O$ and $\delta^{18}O$. The overall correction due to N_2 and Ar accounted for 0.0085 ‰ and 0.0098 ‰ of the $\delta^{17}O$ and $\delta^{18}O$ values, respectively.

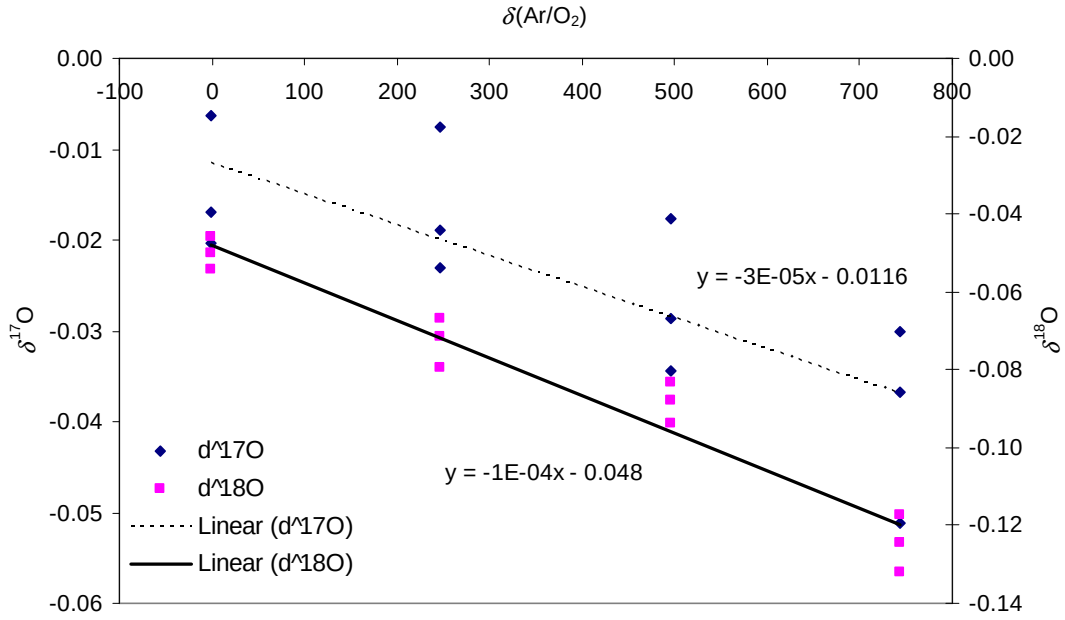

Figure 2.22 – Ar slope for $\delta^{17}O$ and $\delta^{18}O$ using four different concentrations of working reference measured in triplicate.

2.9.4 Normalization of δ-values against atmospheric air.

As was done for the O_2/Ar analysis, the $\delta^{17}O$ and $\delta^{18}O$ were normalized to atmospheric air as reference since the isotopic abundances for atmospheric air are well known and are 23.88 ‰ and 12.08 ‰, for $\delta^{18}O$ and $\delta^{17}O$ respectively, both with respect to VSMOW (Barkan and Luz, 2003; Luz and Barkan, 2005).

The dry Cair aliquots analyzed at the same time as the set of samples were used as the reference for the seawater sample results. To express the δ-values for the seawater samples with respect to atmospheric air, the following equation was used for both $\delta^{17}O$ and $\delta^{18}O$ ($\delta_{\mathrm{sa/ref}}{}^{*}O$) after correction for N_2 and Ar interferences (i = 17, 18):

$$\delta_{sa/cair}{}^{i}O = \frac{\delta_{sa/ref}{}^{i}O - \delta_{cair/ref}{}^{i}O}{1 + \delta_{cair/ref}{}^{i}O} \quad (2.27)$$

The median of the Cair δ-values referenced to the working reference was 0.37±0.01 ‰ for $\delta_{cair/ref}{}^{17}O$ and 0.77±0.01 ‰ for $\delta_{cair/ref}{}^{18}O$. Both values were also corrected for N_2 and Ar interferences.

The final δ-values, after correction by the last equation, were used for the $^{17}\Delta$ calculation. In the case of the $^{17}\Delta$ for Cair corresponded to 0.45±7.59 per meg (16.9 % standard error).

2.9.5 Air-equilibrated water measurements.

In order to check the reproducibility and performance of the extraction line and the MS analysis, a total of 11 air-equilibrated water samples were measured together with the seawater samples. The mean δ-values (after correction for N_2 and Ar interferences and normalization against atmospheric air) are 0.33±0.01 ‰ for $\delta^{17}O$ and 0.61±0.017 ‰ for $\delta^{18}O$.

In terms of δ-values the standard error of the mean values in our measurements for the air-equilibrated water were 0.5 ‰ for $\delta O_2/Ar$, 0.003 ‰ for $\delta^{17}O$, 0.005 ‰ for $\delta^{18}O$ and 2.7 per meg for $^{17}\Delta$, all referenced to atmospheric air.

The error is higher for the $\delta^{18}O$ and $\delta^{17}O$ values than $^{17}\Delta$, this has been discussed before by Hendricks *et al*., 2004 and Reuer *et al*., 2007, and it is mainly due to the mass dependant fractionation that occurs during sample processing and analysis in the mass spectrometer. The mean±1σ for the $^{17}\Delta$ in the air-equilibrated water was 20±9 per meg (uncertainty of 45 %).

2.9.6 Zero enrichment measurements.

A total of 55 zero enrichment measurements were performed during the sample analysis. This consisted of the analysis of the working reference against the working reference itself. This analysis is merely an indication of the MS performance (precision). Two sets of zeros analysis were performed at the beginning of each set of samples. The average results for $\delta^{17}O$ and $\delta^{18}O$ values (corrected for N_2 and Ar

interferences) with respect to the same working reference corresponded to −0.003±0.009 ‰ and −0.004±0.010 ‰, respectively. After the corresponding normalization to atmospheric air, the $\delta^{17}O$ and $\delta^{18}O$ corresponded to 0.70±0.01 ‰ and 1.376±0.017 ‰, respectively.

The estimated $^{17}\Delta$ from the corrected δ-values for the reference is 23.9±6.8 per meg. A high variability of the measurements of the reference was observed (standard error 29 %) indicating instability over time. However, for this reason the samples were referenced instead to atmospheric air.

The overall precision from the isotopic abundance of dissolved oxygen in seawater from JR158 and JR165 cruises corresponded to: 0.5 ‰ for δO_2/Ar, 0.003 ‰ for $\delta^{17}O$, 0.005 ‰ for $\delta^{18}O$ and 2.7 per meg for $^{17}\Delta$, all corresponding to the air-equilibrated water analysis.

2.9.7 Gross O_2 production (G) estimates from $^{17}\Delta$.

The gross O_2 production (G, in mmol m^{-2} d^{-1}) integrated in the mixed layer is estimated from the ^{17}O anomaly of dissolved O_2 ($^{17}\Delta$) measured from discrete seawater water samples, $^{17}\Delta_{max}$, $^{17}\Delta_{eq}$, k_w and $c_{eq}(O_2)$ according to equation 1.19 (section 1.10.4 in chapter 1).

The values for $^{17}\Delta_{eq}$ in this study were calculated according to the seawater *in situ* temperature (θ in °C) (Luz and Barkan, 2009). The $^{17}\Delta_{eq}$ values are from 1.4 to 6 per meg considering the range of temperatures in the area of study (i.e. −0.6 °C in the Bellingshausen Sea to 7 °C for the northern part of the Drake Passage).

2.10 Derived Ar supersaturation (ΔAr) and concentration (c(Ar)).

Since Ar is only affected by physical processes, the estimation of Ar supersaturation will provide an indication of the physical mechanisms present at the sampling time (i.e. bubble injection, mixed layer warming, atmospheric pressure variation or vertical and horizontal fluxes).

The Ar supersaturation (ΔAr) was derived from the $\Delta O_2/Ar$ and ΔO_2 previously measured, by substituting in the following equation:

$$\Delta \mathrm{Ar} = \frac{\Delta \mathrm{O}_2 - \Delta \mathrm{O}_2/\mathrm{Ar}}{1 + \Delta \mathrm{O}_2/\mathrm{Ar}} \tag{2.28}$$

For discrete samples (Δ_{sa}(Ar)) the corresponding $\Delta_{sa}(O_2/Ar)$ and $\Delta_{sa}(O_2)$ were used. Common sampling times for O_2 estimation by Winkler method and O_2/Ar discrete analysis were used.

The continuous Ar concentration (c(Ar), and c_{sa}(Ar) for discrete samples in the mixed layer was derived from the definition of ΔAr:

$$\Delta \mathrm{Ar} = \frac{c(\mathrm{Ar})}{c_{\mathrm{sat}}(\mathrm{Ar})} - 1 \tag{2.29}$$

Chapter 3

Determination of mixed layer depth from dissolved oxygen in the Bellingshausen Sea, Southern Ocean

3.1 Abstract.

In order to improve the definition of mixed layer depth (MLD) for dissolved gas studies, a threshold criterion for summer MLD based on dissolved oxygen concentrations (MLD-O_2) suitable for the coastal areas of the Southern Ocean (SO), is proposed here.

Defining MLD in the SO solely based on temperature and density is challenging, particularly in the coastal region. The sea-ice dynamics, pronounced haloclines, horizontal mixing and upwelling can create steeper gradients between the thermocline or pycnocline and the vertical distribution of oxygen are typical features in the coastal SO. The MLD-O_2 reflects best the influence of biological and physical processes in the upper water column of the coastal SO as a result of historical surface forcing from the atmosphere and the sea-ice melting process.

After objective analysis by computing algorithms (and further visual inspection) of 251 oxygen profiles distributed in the Bellingshausen Sea, a limit for summer MLD was chosen as the depth at which the absolute difference in the concentration of O_2 is higher by 0.5 %, referenced to the O_2 concentration at the near-surface reference depth (11 dbar). To validate the MLD-O_2 criterion, typical MLD threshold criteria based on potential temperature ($\Delta\theta$ = 0.2 and 0.5 ºC) and density ($\Delta\sigma_\theta$ = 0.03 and 0.125 kg m^{-3}) were applied to the same CTD profiles and compared with the MLD-O_2 values. Comparisons to published MLD climatologies (Monterey and Levitus, 1997; Kara *et al*., 2003 and de Boyer Montégut *et al*., 2004) and non-climatological data sets (World Ocean Atlas, 2005) were also performed. MLD-O_2 closely follows MLD based on the $\Delta\sigma_\theta$ = 0.03 kg m^{-3} criteria. In the absence of oxygen profiles (or CTD stations at all), it is recommended to use the $\Delta\sigma_\theta$ = 0.03 kg m^{-3} criterion or the published monthly climatology by de Boyer Montégut *et al*., 2004 defined after the same σ_θ criterion.

3.2 Introduction.

The mixed layer depth (MLD) delimits the surface waters under atmospheric influence (exchange of momentum, heat, moisture and gases) (Dong *et al.*, 2008) from the thermocline and deeper waters. As a general concept, the mixed layer (ML) is the portion of the upper water column where the water properties and solute concentrations are vertically and horizontally homogeneous (Brainerd and Gregg, 1995; Lukas and Lindstrom, 1999). The interaction between the ML and waters below determines the ventilation of the ocean interior and influences the large-scale circulation (Le Quéré *et al.*, 2003; Cisewski *et al.*, 2008).

A proper representation of MLD in the Southern Ocean (SO) is needed since it is considered a significant region for the global ocean-atmosphere carbon balance, which has a large impact on oceanic CO_2 uptake (Sarmiento and Le Quéré, 1996; Sarmiento *et al.*, 1998). In particular, Antarctic shelf waters act as a strong sink for CO_2 due to high biological productivity and ventilation of deep waters (Arrigo *et al.*, 2008).

Due to the lack of physical barriers of the eastward flowing Antarctic Circumpolar Current, a strong link exists between the atmosphere and the surface Southern Ocean. Therefore, biogeochemical and physical processes in this region experience similar seasonal cycles (Rintoul and Trull, 2001); due to this, the SO is an ideal oceanic region to investigate how physical forcing influences the marine ecosystem (Smith *et al.*, 2008a). Several efforts to define MLD in the SO have been made during the last two decades. For this, the previously proposed criteria are based on physical properties (i.e. potential temperature or density) (Gordon and Huber, 1990; Rintoul and Trull, 2001; Verdy *et al.*, 2007; Cisewski *et al.*, 2008; Dong *et al.*, 2008).

In high latitudes and coastal areas, the shelf bathymetry and sea-ice dynamics (advance, duration, extent and retreat) are important factors affecting the ML (Ducklow *et al.*, 2006; Williams *et al.*, 2008). In these regions, little temperature stratification occurs, and the vertical distribution of density is dominated by changes in salinity (de Boyer Montégut *et al.*, 2004; Dong *et al.*, 2008) caused by the ice-melting signal.

Due to differential stratification processes, horizontal gradients and mixing between temperature and salinity in the coastal SO, other water column structures can also

develop, (e.g. temperature inversions, barrier layers and density-compensated profiles) (Rintoul and Trull, 2001; de Boyer Montégut *et al.*, 2004). Therefore, it is challenging to find an adequate criterion for MLD definition in the coastal SO.

MLD is a dynamic property that depends on changes in surface fluxes on daily, seasonal or interannual time scales (de Boyer Montégut *et al.*, 2004; Cisewski *et al.*, 2008). Several authors have investigated MLD variability associated with the seasonality of sea ice (Vernet *et al.*, 2008; Williams *et al.*, 2008; Smith *et al.*, 2008a), the amount of solar radiation to regulate phytoplankton biomass (Garibotti *et al.*, 2005) and the vertical distribution of chlorophyll *a*.

Vertical convection, turbulent mixing and overturning of surface waters are driven by heat loss from the ocean, buoyancy changes and wind stress (Brainerd and Gregg, 1995; Kara *et al.*, 2003; de Boyer Montégut *et al.*, 2004; Cisewski *et al.*, 2008). These processes homogenize temperature, salinity, concentrations of tracers (including gases) and the distribution of plankton. As a consequence, the supply of nutrients (Cisewski *et al.*, 2005) and light availability regulate the development of phytoplankton blooms, the length of the growing season and overall primary productivity of the upper water column (Boyd *et al.*, 1995; Rintoul and Trull, 2001; Hense *et al.*, 2003; Le Quéré *et al.*, 2003; Vernet *et al.*, 2008).

During late spring in the sea-ice zone (SIZ) of the West Antarctic Peninsula (WAP), the melting ice-shelves produce a surface layer of freshwater. This layer is generally supersaturated or at equilibrium with respect to O_2 concentrations and rich in iron (Hopkinson *et al.*, 2007). In these areas, the water column stability is a controlling factor for the success of phytoplankton communities (Vernet *et al.*, 2008). The freshwater input stabilizes the upper water column by forming shallow mixed layers during summer, with enhanced light and macro nutrient availability and consequent increase in the coastal marine productivity in a well stratified water column (Smith *et al.*, 2000; Hopkinson *et al.*, 2007).

By early autumn, sea-ice starts to re-form. As a result, brine rejection in the coastal area leads to cold and denser water in the surface that rapidly sinks, following the coastal topography, to form Antarctic Bottom Water (AABW).

The intensification of vertical convection ventilates the deep waters and causes a deepening of the MLD (Boyd *et al.*, 1995; Watson and Naveira, 2006; Verdy *et al.*, 2007; Dong *et al.*, 2008). During that process, surface waters may become depleted in macro-nutrients and understaturated in O_2 as a result of mixing with deep and low oxygenated waters. In addition, the presence of temperature inversions below the mixed layer can lead to entrainment of warmer water. This process can also imply the destruction of barrier layers if present. These processes are important to take into account for gas exchange studies, particularly in the coast of the Antarctic continent.

The definition of the MLD is arbitrary (de Boyer Montégut *et al.*, 2004); it depends on the choice of the tracer, its temporal variability and resolution. Ideally, the chosen MLD criterion must best characterize the processes of interest in the upper water column (e.g. air-sea gas exchange, heat balance). Definitions of the MLD can be classified into two groups of criteria (de Boyer Montégut *et al.*, 2004; Cisewski *et al.*, 2008; Dong *et al.*, 2008): a) difference criterion, where MLD is defined as the depth where the oceanic property had changed by a certain amount from a reference value (Levitus, 1992); and b) gradient-based criterion, where MLD is defined as the depth where the vertical gradient of the property reaches a threshold value (Lukas and Lindstrom, 1999).

Previous comparisons between gradient and difference-based criteria, suggested that the latter provides a more dependable MLD (Brainerd and Gregg, 1995; Cisewski *et al.*, 2008). This is because the gradient-based criteria require well-resolved profiles. Based on ARGO float density profiles, Dong *et al*. (2008) concluded that the presence of anomalous spikes and perturbations within the well-mixed layer can lead to false shallow MLD values, with differences as much as 100 m when using a gradient-based criterion compared to the difference-based criterion. This is due to the limited resolution and noise of the sensor used to measure the water property. A difference-based criterion also performs better in regions with temperature inversions or weak upper water column stratification.

Here is presented a difference-based criterion using dissolved O_2 concentrations suitable for MLD definition (MLD-O_2) in the coastal waters of the SO. MLD values are obtained through visual inspection of vertical O_2 profiles in the Bellingshausen Sea (BS). Dissolved oxygen ($c(O_2)$) in the water column is influenced by both

biological and physical processes (e.g. vertical mixing, horizontal advection, air-sea exchange of bubbles and heat). Historically, O_2 has been used as a useful tracer for water masses, biological activity and air-sea interaction (e.g. Reuer *et al.*, 2007a; Jenkins and Jacobs, 2008; Körtzinger *et al.*, 2008).

In the upper water column, dissolved oxygen adjusts rapidly to the atmospheric equilibrium concentration on timescales of about one month (Verdy *et al.*, 2007). It is also influenced by interaction with the upper thermocline through advection and turbulence, biological processes and heat exchange.

The seasonal trends of surface heating and cooling and biological O_2 production lead to a correlation between heat flux anomalies and air-sea oxygen flux (Garcia and Keeling, 2001). During the last decade, a decrease of dissolved O_2 in the surface ocean has been tentatively attributed to climate change (Keeling and Garcia, 2002; Garcia *et al.*, 2005b; Stramma *et al.*, 2008). A warming of surface waters will cause stronger stratification and a general decrease of surface O_2 concentrations, reducing ventilation by decreasing the O_2 transported to deeper waters. The response of O_2 solubility to changes in temperature and salinity is not linear and immediate. Therefore, a MLD defined solely on potential density does not describe fully the properties of the water column, particularly in terms of dissolved oxygen.

An oxygen-based MLD allows calculation of O_2 budgets in the upper ocean better than the MLD solely based on temperature or density. Therefore, a suitable MLD will improve the understanding of the atmosphere-ocean coupled system and marine biogeochemical cycles (Brainerd and Gregg, 1995; Lukas and Lindstrom, 1999; Cisewski *et al.*, 2008).

3.2.1 Criteria to define MLD in published climatologies.

Various global mixed layer depth climatologies with different criteria have been published. Below, the most widely used criteria are mentioned.

In 1997, Monterey and Levitus (**ML97**) published a monthly averaged global climatology based on vertically averaged and interpolated profiles from World Ocean Atlas 1994 data (WOA94) with a spatial resolution of $1^o \times 1^o$ and temporal scale from 1990 to 1992. ML97 climatology proposes two different criteria for MLD:

based on a fixed density ($\Delta\sigma_\theta$ = 0.125 kg m^{-3}) and fixed temperature ($\Delta\theta$ = 0.5 ºC), both with respect to the surface value (Monterey and Levitus, 1997).

In an effort to improve the ML97 climatology, Kara *et al*., (2003; **K03**) proposed in 2000 and 2003 a global MLD climatology based on a density difference criterion, able to represent the depth of the *turbulent mixing layer* (TML) by using a convective mixing scheme (which removes instabilities from the density profiles).

The TML is the active region of the mixed layer directly affected by the wind shear, lateral advection, vertical transport and turbulence during the day; therefore is where the surface flows of water are actively mixed (Brainerd and Gregg, 1995) within diurnal timescales (< 24 hr). This region is located generally within the top 10 m and has a greater vertical uniformity than the integrated mixed layer (de Boyer Montégut *et al.*, 2004). The TML therefore acts as a boundary where the direct atmospheric influence occurs (i.e. air-sea gas fluxes and heat balance) and is generally limited by the diurnal thermocline. The layer below remains stratified and does not interact actively with the atmosphere until the nighttime processes of overturning and convective mixing integrates the mixing layer properties (e.g. gases, heat and phytoplankton) to form the mixed layer.

The mixing layer can be best identified by turbulence sensors such as microstructure profilers (Brainerd and Gregg, 1995; Cisewski *et al.*, 2005). However, K03 suggested a variable density criterion based on a fixed temperature difference ($\Delta\theta$ = 0.8 ºC) to represent the mixing layer processes. The K03 global climatology uses the same WOA94 data and spatial resolution as ML97.

Both ML97 and K03 temperature criteria have been widely applied for areas where sharp temperature stratification is present in the upper water column. The larger temperature difference of the K03 criterion produces deeper MLDs than those of ML97. Furthermore, the wide and irregular vertical resolution on the profiles (0, 10, 20, 30, 50, 75, 100, 125, 150 m, every 50 m to 300 m, and then every 100 m to a depth of 1000 m) and the scarcity of temperature and salinity profiles in the Southern Ocean (Kara *et al.*, 2003), are some of the main constraints to define MLD in this region from K03 (and ML97) climatology.

The most recent climatology was published by de Boyer Montégut *et al*., (2004, **BM04**) consisting of a monthly field with a spatial resolution of 2º × 2º. It is the result of the inspection of more than 4.5 million individual profiles globally distributed from the World Ocean Circulation Experiment (WOCE) and the National Oceanographic Center (NODC) with a temporal coverage from 1941 to 2002. It includes profiles from MBT (Mechanical BathyThermograph), XBT (eXpandable BathyThermograph), CTD and PFL (Profiling FLoats), providing a wide range of vertical resolutions from CTD (2.3 m) to XBT (19.5 m). With these observations, the identification of vertical structures such as barrier layers and temperature inversions was possible. The threshold criteria proposed by BM04 is 0.2 ºC for θ and 0.03 kg m^{-3} for σ_θ, taking as a reference the 10 m value in both cases. The MLD field in BM04 represents the global ocean MLD seasonal variability with a minimum mixing timescale of a day (de Boyer Montégut *et al.*, 2004).

The updated version of the BM04 climatology (hereinafter referred to as **BM04b**) was made public (http://www.locean-ipsl.upmc.fr/~cdblod/mld.html) and includes Argo float density profiles. The temporal coverage includes data from 1961 to September 2008, whereas the spatial resolution and both criteria for density and temperature remain the same as in BM04. The MLD from the ML97 and BM04 (and BM04b) global climatologies have been widely used for the determination of this parameter based on conservative properties over a minimum spatial scale of one squared degree in latitude and longitude. However, the data coverage in the Southern Ocean (particularly in the ML97) remains poor south of 30º S and the identification of MLD in the Antarctic coastal zone is scarce.

MLD definitions using numerical algorithms based on optical or hydrographical data have been recently proposed (Zawada *et al.*, 2005; Swain *et al.*, 2006; Vernet *et al.*, 2008; Holte and Talley, 2009) due to their potential ability to rapidly determine MLD over large regions. However, these methods have limitations involving: laborious work with complex methods (i.e. curvature method (Lorbacher *et al.*, 2006); split and merge method (Thomson and Fine, 2003)), most of the variables for these algorithms (e.g. beam transmissometer measurements) are not generally available for the SO and during all seasons (Zawada *et al.*, 2005), or the usage of complex models (i.e. ocean general circulation model,(Noh and Lee, 2008).

Recently, Holte and Talley (2009) have proposed a new algorithm for MLD identification of individual profiles using temperature and salinity data. However, geographical and temporal limitations, as well as poor accuracy from the algorithm MLD when compared with direct visual profile inspections are generally encountered (Holte and Talley, 2009).

In order to identify barrier layers (BL), recently, de Boyer Montégut *et al*., (2007) published a 2º × 2º resolution BL global climatology based on about 500,000 globally distributed salinity and temperature profiles from NODC, WOCE and ARGO covering 37 years (1965-2002) (de Boyer Montégut *et al.*, 2007) (see Table 3.1 for more details).

Table 3.1 – MLD climatologies and non-climatological data sets used in the present work to compare with the MLD extracted from vertical O_2 profiles.

Author/ID	*Description*	*Source data and temporal coverage*	*Profiles*	*Resolution*	*Criterion*	*Reference depth*
Monterey and Levitus, 1997 (ML97)	MLD global climatology	WOA[2] (1990-1992)	Averaged and interpolated	1º×1º monthly mean	$\Delta\sigma_\theta = 0.125$ kg m^{-3} $\Delta\theta = 0.5$ ºC	Surface
Kara, 2003 (K03)	MLD global climatology	WOA[2] (1990-1992)	Averaged and interpolated	1º×1º monthly mean	$\Delta\sigma_\theta = \sigma_\theta(\theta+\Delta\theta,S,P) - \sigma_\theta(\theta,S,P)$; $\Delta\theta = 0.8$ ºC (after statistical comparison with Ocean Weather Station data)	Surface
de Boyer Montégut *et al*., 2004 (BM04)	MLD global climatology	NODC[3]/WOCE[4] (1941-2002)	Individual	2º×2º monthly mean	$\Delta\sigma_\theta = 0.03$ kg m^{-3} $\Delta\theta = 0.2$ ºC	10 m
LOCEAN-IPSL[1], 2008 (BM04b)	MLD global climatology	NODC[3]/WOCE[4]/ Argo (1941-2008)	Individual	2º×2º monthly mean	$\Delta\sigma_\theta = 0.03$ kg m^{-3} (after individual inspection of ≈9×10^6 profiles)	10 m
Dong *et al*., 2008 (D08)	MLD SO climatology	Argo (2001-2006)	Individual float profiles	1º×1º monthly mean	$\Delta\sigma_\theta = 0.03$ kg m^{-3} (following BM04)	Near surface to 20 m
WOA, 2005 (WOA05-σ_θ)	T and S (σ_θ constructed) global historical data set	WOA[2] (1965-2005)	Averaged and interpolated	1º×1º	$\Delta\sigma_\theta = 0.03$ kg m^{-3}	10 m
WOA, 2005 (WOA05-O_2)	O_2 global historical data set	WOA[2] (1965-2005)	Averaged and interpolated	1º×1º	$\Delta c(O_2) = 0.5\%$	10 m

[1] Laboratoire d'Océanographie et de Climatologie par l'Expérimentation et l'Analyse Numérique- Institut Pierre Simon Laplace.
[2] World Ocean Atlas
[3] National Oceanographic Data Center
[4] World Ocean Circulation Experiment

A noticeable increase in the data coverage for the SO region was provided by the Argo database; the latter is an important contribution to climatologies for that region. A barrier layer (BL) is formed when the salinity and temperature distributions in the water column are such that the halocline is shallower than the thermocline. BL have been observed in different regions of the world's ocean, particularly in the surface waters of the SO (Lukas and Lindstrom, 1999).

3.2.2 Previous MLD definitions and climatologies in the SO.

In 1982, Reid suggested that the seasonal variability of the O_2 saturation ($c_{eq}(O_2)$) in the upper water as a proxy for detection of the winter MLD in the North Pacific subtropical gyre as a result of the overturning process (Reid, 1982). A suitable criterion, modified by Talley (1999), was suggested to be 95 % of the surface saturation concentration for the winter mixed layer depth ($c_{eq}(O_2) < 95$ %). With this criterion, it was possible to identify the worldwide deepest mixed layers and the presence of the Subantarctic Mode Waters (SAMW) as a precursor of intermediate water formations. Results from a recently published algorithm (Holte and Talley, 2009) to find deep MLD were compared with the MLD defined by O_2 saturation finding approximately the same depth range using data from WOA, 2005 and Argo profiles. A consistent deep mixed layer region north of the Subantarctic Front was identified by both methods. The O_2 saturation criterion was therefore suitable for identification of deep mixed layers (Talley, 1999; Hanawa and Talley, 2001; Dong *et al.*, 2008) reflecting roughly the integration of monthly timescale processes of water mass convection and overturning. However, this criterion is not suitable for the detection of shallow MLD and ML dynamics, particularly in the coastal SO where surface cold waters are normally in equilibrium or slightly undersaturated in O_2 during most part of the year (Garcia and Keeling, 2001).

Dong *et al.*, (2008) published a monthly MLD climatology exclusively for the Southern Ocean region (30º to 65º S and 0º to 360º E) based on σ_θ derived from temperature, salinity and pressure from Argo float profiles. The criterion to define the MLD was the same as BM04 (fixed difference criterion, $\Delta\sigma_\theta = 0.03$ kg m^{-3}). By an objectively mapping methodology about 42,000 individual profiles in the SO region were integrated.

The MLD-Argo climatology provides a new insight for seasonal MLD investigations in a region where the lack of data during austral winter from direct observations from research ships is considerable. However, the latitudinal limits for the MLD-Argo do not reach the BS region (66º - 74º S and 65º- 95º W).

Argo floats with O_2 sensors have been launched since 2007. Few floats with these characteristics can currently be found in the SO region. However, these floats are only launched in deep waters and the coarse vertical resolution that the Argo profiles provide (~10.5 m) are important limitations for detection of the shallow summer MLDs in the coastal region of the SO from this data source.

To validate the MLD criterion from the vertical oxygen distribution proposed here (MLD-O_2), the MLD obtained from the O_2 distribution is plotted against the MLD obtained in the same BS profiles after applying the temperature and density criteria proposed in the public climatologies. Finally, a comparison of the observed MLD-O_2 to those directly given by the ML97, K03 and BM04b climatologies for the same location and time of the year was performed.

3.3 Methods

3.3.1 CTD data collection.

Vertical profiles of temperature (θ), salinity (S) and dissolved oxygen concentration ($c(O_2)$) were obtained from 253 hydrographic stations in the Bellingshausen Sea (*RRS James Clark Ross*, cruise JR165). The cruise formed part of the ACES-FOCAS project (Antarctic Climate and the Earth System-Forcing from the Oceans, Clouds, Atmosphere and Sea-ice) of the British Antarctic Survey.

The BS is situated in the coastal area of the West Antarctic Peninsula (WAP) between 75º and 90º W. It is a transition region between the continental shelf, shelf break and open ocean. The sampling period consisted of 39 days (3 March – 9 April 2007), representing the transition from late summer to early autumn in 2007 (Figure 3.1). The hydrographic profiles were taken with a *Sea-Bird* 911+ CTD mounted on a rosette with 12, 10-l Niskin bottles for the collection of water samples.

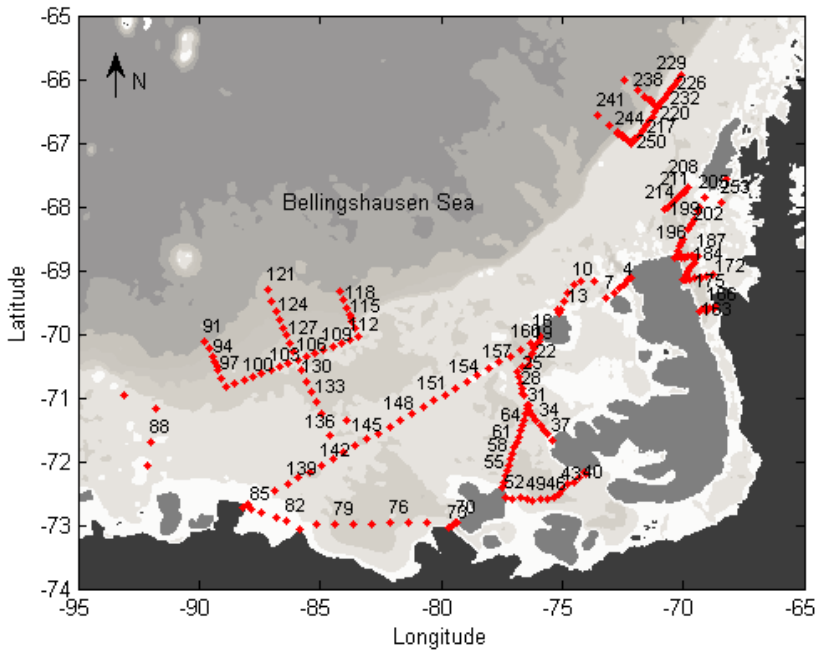

Figure 3.1 – 253 CTD stations obtained during cruise JR165 in the Bellingshausen Sea, west Antarctic Peninsula during late summer and early autumn, 2007. Labels indicate station numbers. Shading corresponds to the 200, 600, 1000, 2000, 3000 and 4000 m isobaths.

Calibration of the CTD salinity sensor was performed on board against discrete samples analyzed with a Guildline Autosal 8400B. A constant offset of 0.0337 was found when comparing with discrete salinity samples. The CTD was mounted with a high precision reversing thermometer sensor (Sea-Bird SBE35) and an O_2 sensor (CTD-O_2; Sea-Bird SBE43). The latter was calibrated by discrete samples from the Niskin bottles, which were analyzed on board for total O_2 concentrations using whole-bottle Winkler titration (Dickson, 1996) with photometric end-point detection. A total of 276 titrations were performed with an analytical precision of 0.29 µmol kg^{-1} based on 76 duplicate samples.

The up-cast O_2 profiles were calibrated by linear regression (r^2 = 0.997) obtained from the discrete sample O_2 concentration against the O_2 concentration as given by the CTD-O_2 sensor. The average offset between the non-calibrated O_2 data from the CTD sensor and the Winkler data was (3.9 ± 3.1) µmol kg^{-1}. The final profile data were interpolated vertically in steps of 2 dbar from 1 dbar to the corresponding maximum depth for each station.

3.3.2 MLD-O_2 criterion definition.

To find a MLD criterion suitable for air-sea gas exchange studies, I have investigated the vertical O_2 distribution from all the 253 CTD profiles in the BS. Only 251 stations were selected due to two stations where the surface data (top 50 m) was not available; thus hereinafter the number of working stations is referred as to 251 profiles. Objective (mathematical algorithm) and subjective (visual) observations were explored and compared to find a suitable MLD-O_2 criterion.

Previous to the identification of MLD-O_2, the vertical O_2 concentrations were calibrated previously against results from the O_2 method (section 2.4, Chapter 2). However, the MLD-O_2 criterion can be applied directly to non-calibrated vertical profiles, proven that the profiles were inspected before to remove bad data (i.e. spikes) given by sensor failure on the oxygen profiles.

3.3.3 Comparison with climatological and non-climatological data sets.

In order to contrast the MLD-O_2 criterion, I have compared the MLD results obtained from oxygen against the MLD obtained in the same vertical BS profiles, after applying various difference based criteria using potential temperature (MLD-θ) and density (MLD-σ_θ) (i.e. $\Delta\theta = 0.2$ ºC and $\Delta\sigma_\theta = 0.125$ kg m^{-3} with respect to the surface value and $\Delta\theta = 0.5$ ºC and $\Delta\sigma_\theta = 0.03$ kg m^{-3} with respect to the 10 m-depth value). These selected criteria to compare with are the ones proposed in the public climatologies (Monterey and Levitus, 1997; de Boyer Montégut *et al.*, 2004) (see Table 3.1 for further details).

In 2006, a criterion to define MLD by looking at the curvature of surface density and temperature profiles was proposed (Lorbacher *et al.*, 2006). It was defined from WOCE historical hydrographic data and offered reliable MLD for different vertical resolutions of investigated profiles (i.e. < 5 m to < 20 m of vertical resolution). Here, I have used the proposed algorithm by Lorbacher *et al.*, (**L06** hereinafter) in the BS profiles and contrast the obtained results to the MLD defined by O_2. I have also applied the only oxygen-based criterion in the literature so far, proposed by Talley (1999), to the BS profiles. This criterion proposed that the base of the mixed layer is the depth where the surface O_2 saturation is lower than 95 % ($c_{eq}(O_2) < 95$ %).

Results obtained from the comparisons mentioned above, show that MLD-O_2 is best correlated to MLD-σ_θ for the BS region. Therefore, a density based criterion to define MLD can be used in the absence of O_2 profiles for air-sea gas exchange. To corroborate this, it was done a comparison between the results of MLD-σ_θ and MLD-O_2 from the BS profiles against the MLD-σ_θ extracted from the monthly average global climatologies (i.e. ML97, BM04 and K03) for the same geographical location and month of the year.

To validate the MLD-O_2 criterion, the potential density criterion from BM04 was applied to density profiles calculated from temperature and salinity historical records (i.e. non-climatological data) from World Ocean Atlas, 2005 (WOA-05) (Antonov *et al.*, 2006; Locarnini *et al.*, 2006). WOA-05 provide a monthly objectively analyzed climatology with a spatial resolution of 1º by 1º degree, obtained from averaged profiles of temperature and salinity from 1965 to 2005. This data set corresponds to the latest updated climatological field for WOA, therefore the same data analysis for the interpolation, averaging and vertical resolution was applied as for ML97 (Monterey and Levitus, 1997).

Finally, the obtained MLD-σ_θ values were compared to MLD-O_2 values derived from historical O_2 profiles from the same WOA-05 data sets (WOA-O_2; Garcia *et al.*, 2006). The WOA-O_2 data set is the result of vertically averaged and interpolated O_2 profiles. The same standard depths and method for interpolation was used as for the temperature, salinity and density monthly climatologies by WOA (Monterey and Levitus, 1997). The O_2 data from the WOA-05 climatology corresponded only to results from chemical titration methods (i.e. Winkler method). No data from CTD-O_2 profiles are included. Details of all data sets used in the present work are shown in Table 3.1.

3.3.4 Influence of mixing and barrier layers for the MLD-O_2 definition.

To identify the presence of temperature inversions and possible interference of barrier layers (BL) with the observed MLD-O_2 in the area of study, the BL criterion according to(de Boyer Montégut *et al.*, 2007), was applied in the 251 CTD profiles distributed in the BS.

To identify a BL, the difference between its upper (D_σ) and bottom limit ($D_{T\text{-}02}$) must be defined in the potential density profiles. D_σ is defined as the depth where the σ_θ has increased from the reference depth (10 m) by a threshold equivalent to the density difference due to the change in temperature by 0.2 ºC. The bottom limit, $D_{T\text{-}02}$, is the depth where the increase of temperature by 0.2 ºC occurred with respect to the reference depth temperature (de Boyer Montégut *et al.*, 2007).

3.4 Results.

3.4.1 MLD-O_2 in BS profiles and comparison between subjective and objective observations.

After objective (mathematical algorithm) and subjective (visual) evaluation of each BS-O_2 profile, a suitable O_2 limit to define MLD-O_2 in the area of study was investigated. Here I suggest the MLD-O_2 to be the depth at which the O_2 concentration ML ($c_{MLD}(O_2)$) corresponds to a relative difference of 0.5 % with respect to the O_2 concentration ($\Delta c(O_2)$ = 0.5 %) at 11 dbar as the reference depth representing the uppermost limit of the ML ($c_{UL}(O_2)$).

The reference depth of 11 dbar (equivalent to 10.9 m) was chosen for convention. This depth is commonly used as the reference value after Brainerd and Gregg (1995) suggested it to avoid the noise caused by the sensors (when introduced to the water) and due to the ship's motion in the upper water column (Brainerd and Gregg, 1995). The diurnal cycle of the mixing layer occurs in the top few meters; therefore using a near-surface reference depth also helps to avoid this effect for the seasonal MLD definition. During the vertical O_2 calibration, noise on the signal due to the sensor instability caused by ship's motion was identified and removed on average in the top 4 dbar for most of the CTD stations. However, the depth reference considered for the as MLD-O_2 criterion is 11 dbar due to three reasons: 1) to compare the observations from oxygen with MLD criteria for climatological data that use the same reference depth, 2) to avoid the diurnal cycle of the mixing layer, which can be strong in high latitudes due to night time convection after wind stress and, 3) to avoid the melting sea-ice direct influence in the upper few meters.

After the comparison between objective MLD-O_2 extracted by the algorithm and the visual identification, both results agreed exactly for 235 out of 251 stations (94 %). In the remaining 16 stations the objective result was on average 1 ± 5 m shallower than the result by visual inspection (Figure 3.2).

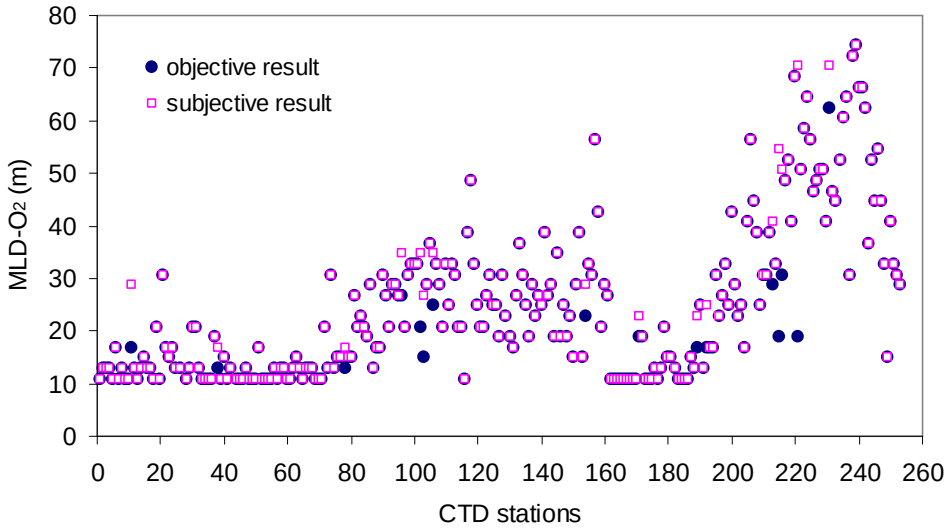

Figure 3.2 – Comparison between MLD-O_2 from algorithm (objective result) and MLD-O_2 from visual inspection (subjective result) in CTD stations distributed in the Bellingshausen Sea.

This result was mainly due to an intermediate slight decrease of oxygen due to the presence of low oxygenated subsurface waters (i.e. Winter Water) creating a weak upper oxycline. However, in the visual inspection this top temporal oxycline was avoided and the limit for MLD-O_2 was defined according to the deepest and clearer seasonal oxycline.

3.4.2 MLD-O_2 against potential density and temperature typical criteria in BS profiles.

We applied two typical potential temperature difference MLD criteria (MLD-θ) to the 251 study profiles in the BS region: a) $\Delta\theta = 0.5$ ºC with respect to the surface value and b) $\Delta\theta = 0.2$ ºC with respect to 11 dbar-depth value. A comparison of the results of MLD-θ and MLD-O_2 was done and a poor correlation between both criteria (r^2 = 0.001 and 0.111 for criterion a) and b), respectively) was identified.

In general, higher MLDs with respect to the MLD-O_2 were given by the temperature-based criteria (58±51 m deeper for a), and 26±34 m for b)) (Figure 3.3). These observations confirm the overestimation of MLD being defined solely by

temperature, and the importance of using potential density to define MLD in the SO (Figure 3.4a).

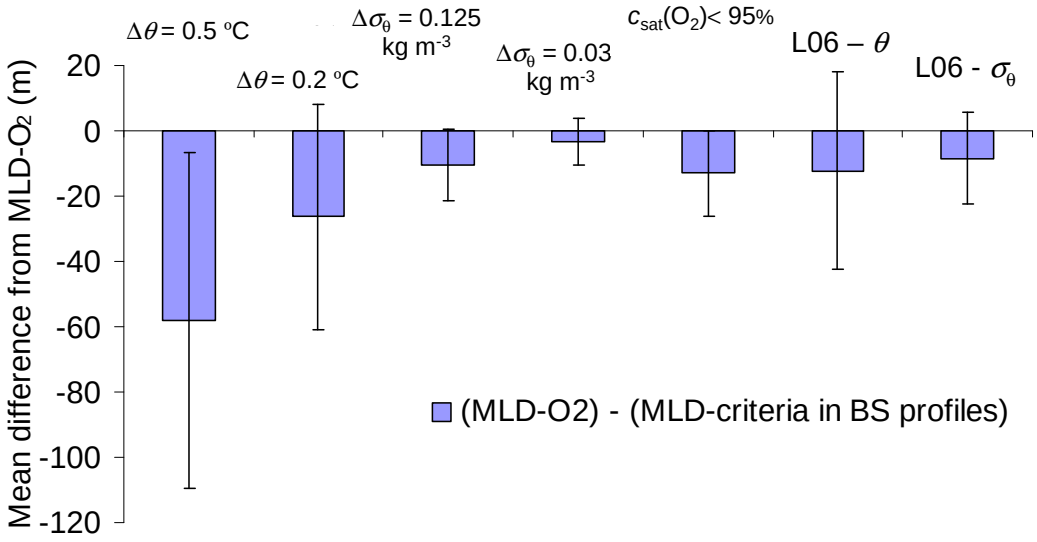

Figure 3.3 – Mean difference between MLD-O_2 in BS profiles and other MLD criteria based on: potential temperature, potential density and oxygen saturation. L06 is the Lorbacher et al., 2006 algorithm to define MLD from potential temperature (L06-θ) and potential density (L06-σ_θ). Error bars indicate ±1 standard deviation of the mean.

An underestimation of the average O_2 concentration within the MLD-θ compared to the one limited by the MLD-O_2 was observed. The average oxygen concentration within the MLD-θ was lower than the average concentration within the MLD-O_2 by as much as 37±25 μmol kg^{-1} in case of criterion a, and 19±22 μmol kg^{-1} for criterion b.

Therefore, the following two σ_θ threshold criteria were applied to the working BS profiles: c) $\Delta\sigma_\theta$ = 0.125 kg m^{-3} with respect to the surface value and d) $\Delta\sigma_\theta$ = 0.03 kg m^{-3} with respect to the 11 dbar-depth value.

The comparison between results from MLD-σ_θ against MLD-O_2 showed a better agreement than against MLD-θ. From this, a positive correlation was obtained (correlation coefficient, r^2 = 0.711 for criterion c) and 0.813 for criterion d). Criterion c) provided slightly higher MLD values (by as much as 11±11 m) than criterion d) that were only 3±7 m deeper compared to the MLD-O_2 (Figure 3.3 and 3.4b).

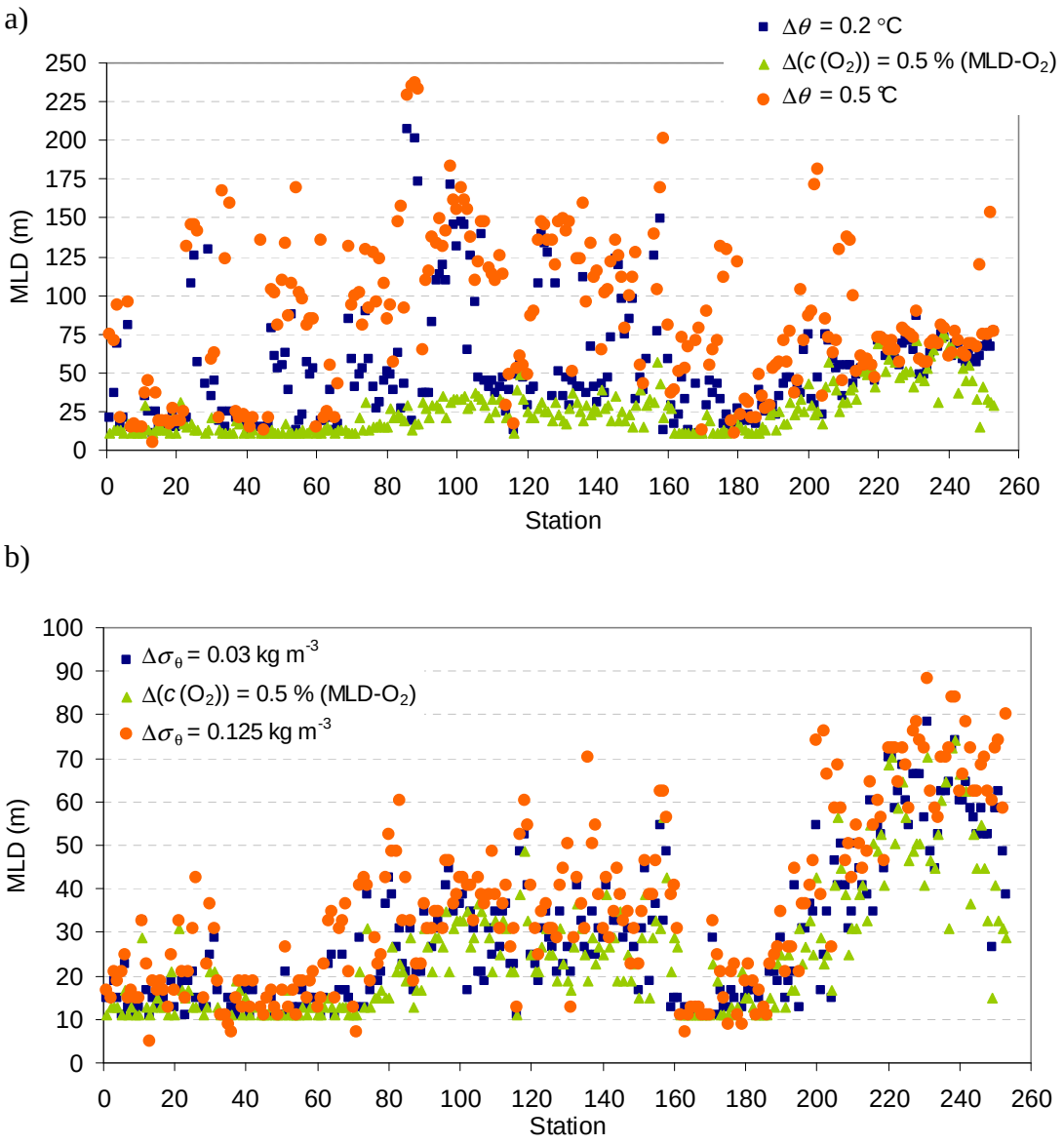

Figure 3.4 – Comparison between MLD-O_2 (green triangles) and typical MLD criteria applied to CTD profiles in the BS region: a) MLD-θ (blue squares, $\Delta\theta$ = 0.2 ºC and orange circles, $\Delta\theta$ = 0.5 ºC), and b) MLD-σ_θ (blue squares, $\Delta\sigma_\theta$ = 0.03 kg m^{-3} and orange circles, $\Delta\sigma_\theta$ = 0.125 kg m^{-3}).

The results obtained were visually confirmed after applying the corresponding algorithms for MLD-σ_θ criteria to the profiles. For both $\Delta\sigma_\theta$ criteria, the objective and subjective results are in close agreement. For $\Delta\sigma_\theta$ = 0.03 kg m^{-3}, the algorithm underestimates the MLD by as much as 2±5 m, while for $\Delta\sigma_\theta$ = 0.125 kg m^{-3} criteria the algorithm lead to an overestimation as much as 2±6 m.

After applying the algorithm to obtain MLD following the L06 criterion in the BS profiles, the results show deeper mixed layers from potential temperature (by as much as 12±30 m) and density profiles (8±14 m) when compared to the MLD-O_2 obtained from the oxygen profiles (Figure 3.3).

Therefore, MLD-O_2 reflects best the O_2 concentration within the ML of the observed profile than defined by the MLD-σ_θ criteria. In Figure 3.5, six typical profiles for the BS region are shown. Vertical profiles for stations 25, 76, 89, 188, 199 and 250, show the MLD-σ_θ (defined as $\Delta\sigma_\theta$ = 0.03 kg m^{-3}) lying in the oxycline region and deeper than the MLD-O_2.

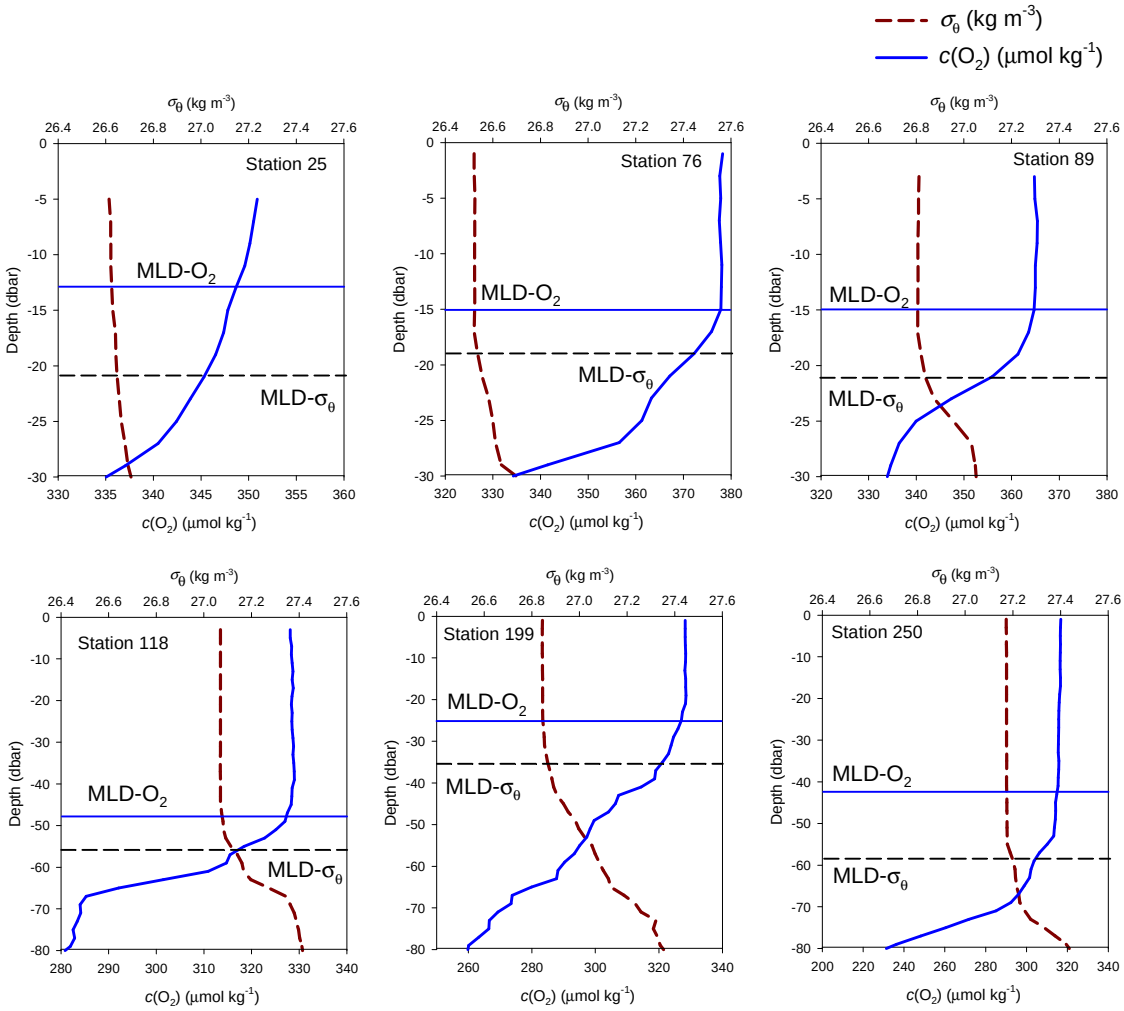

Figure 3.5 – Vertical profiles of O_2 concentration, $c(O_2)$ (full line, µmol kg^{-1}) and potential density (dashed line, σ_θ; kg m^{-3}) in stations located in the BS. Horizontal lines indicate the location of the MLD defined by $c(O_2)$ (full line) and σ_θ after BM04 criterion (dashed line).

The $c(O_2)$ at the depth where MLD-σ_θ is located following both criterion c and d, is on average lower (by as much as 14±36 μmol kg^{-1}) than the oxygen concentration at the MLD-O_2. Furthermore, an underestimation of the average O_2 concentration within the MLD-σ_θ compared to the one limited by the MLD-O_2 was expected. The average oxygen concentration within the MLD-σ_θ after criterion c is 8±13 μmol kg^{-1} and after criterion d is only 1±11 μmol kg^{-1} lower than the average $c(O_2)$ within the MLD-O_2.

3.4.3 MLD-$c_{eq}(O_2)$ criterion in BS profiles.

For the CTD stations analyzed in the present work, the surface oxygen saturation was found to be on average undersaturated by 100.4 ± 4.4 % during the sampling period for stations close to the ice shelves (1 to 90 and 164 to 198). The slight supersaturation was due to the characteristic high productivity close to the coast. Following Talley (1999), the depth at which the 95 % of O_2 saturation was reached in the BS profiles was at about 3 m. On average, the MLD-O_2 was found to be at 26 m. Thus, the MLD criterion from $c_{eq}(O_2)$ proposed by Talley (1999) is only suitable for the definition of winter and deep mixed layers when undersaturated water columns are likely to be observed. Despite this, in order to identify the location of the 95 % saturation with respect to $c_{eq}(O_2)$ and to avoid the top water column generally supersaturated in oxygen, here the reference depth was adjusted to be 10 m instead of the near-surface depth as suggested by Talley. The 95 % saturation depth for the MLD criterion showed deeper MLDs, by as much as 13±13 m than the MLD-O_2 proposed here (Figure 3.3).

3.4.4 MLD-O_2 and MLD-σ_θ from BS profiles against MLD from monthly climatologies based on density difference criteria.

We compared the MLD-σ_θ from BS profiles against the MLD extracted from the ML97 and BM04b monthly global climatologies based only on the $\Delta\sigma_\theta$ criterion, using the same CTD geographical location and sampling month of the year. A good agreement between BS profile observations and climatological monthly averages was observed in both cases, with r^2 = 0.604 against BM04b and r^2 = 0.628 against ML97 (data not shown). On average the MLD from BM04b was 0.7 ± 13.5 m shallower than the MLD-σ_θ ($\Delta\sigma_\theta$ = 0.03 kg m^{-3}) from BS. The ML97 climatology showed also shallower MLDs than the MLD-σ_θ ($\Delta\sigma_\theta$ = 0.125 kg m^{-3}) observed in BS profiles

(11.9 ± 11.6 m). The wider range of difference between the climatological MLD and the one observed from the BS-CTD profiles is probably due to averaging and interpolation in the ML97 climatology.

We then compared the MLD-O_2 from the BS profiles against the corresponding MLD-σ_θ from ML97, K03 and BM04b climatologies. Due to the lack of spatial coverage of profiles in the climatologies in the Southern Ocean, not all the 251 profiles in the BS had a corresponding value from the climatologies. BM04 climatology was the one with a higher number of the BS profiles found (208 profiles), while K03 and ML97 only showed a MLD result for 179 and 170 profiles, respectively. Therefore, only a comparison between the common profiles where a value for MLD was found on the three climatological data sets was performed.

The monthly averaged MLDs from ML97 and BM04 for the CTD station locations showed a positive correlation when compared with MLD-O_2 (r^2 = 0.561 and 0.542, respectively). Contrary to previous observations for the σ_θ criteria applied to the BS profiles, the MLD-σ_θ from climatological data was shallower than MLD-O_2, but only for ML97 and K03 (1±11 m and 14±14 m, respectively). In agreement to previous observations, the MLD-σ_θ from the BM04b climatology was deeper than the MLD-O_2, by as much as 7±11 m, for 170 profiles (Figure 3.6).

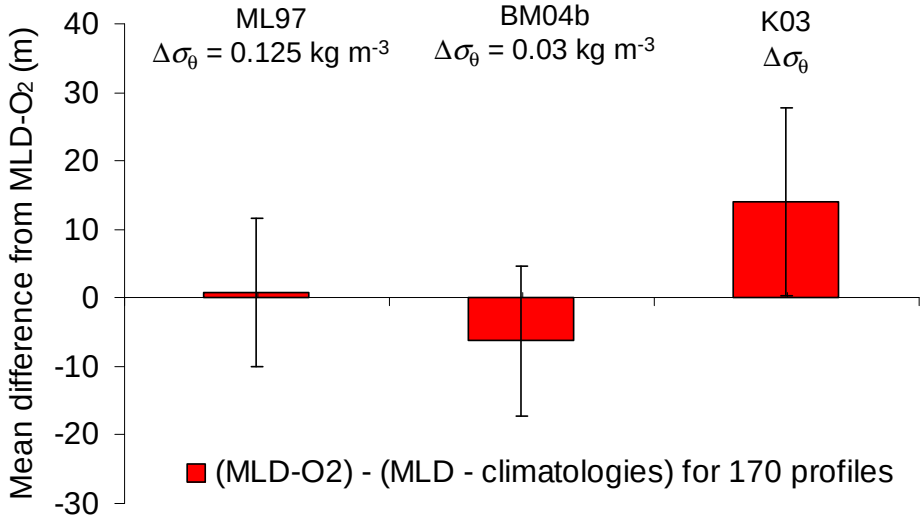

Figure 3.6 – Mean difference between MLD-O_2 in 170 CTD profiles in the BS and MLD for the same month and geographical location from monthly climatologies based on σ_θ difference criteria: ML97 (Monterey and Levitus, 1997); BM04b (de Boyer Montégut *et al.*, 2004 modified in 2008) and K03 (Kara *et al.*, 2003). Error bars indicate ±1 standard deviation of the mean.

A weak correlation was found between MLD-O_2 and the MLD-σ_θ extracted from K03 climatology (r^2 = 0.0001). The lack of agreement between ML97 and K03 climatologies to the MLD-O_2 is mainly due to the vertical resolution of profiles (after averaging and smoothing) used in both climatologies (0, 10, 20, 30, 50, 75, 100, 125, 150 m, every 50 m to 300 m, and then every 100 m to a depth of 1000 m), not allowing a fine identification of MLDs. For some stations, the MLD was overestimated by as much as 500 m, these data was removed from the MLD-O_2 comparisons since it was considered as an offset in the climatological set.

The observations shown here that MLDs based on the criterion $\Delta\sigma_\theta$ = 0.03 kg m^{-3} agrees best with the MLDs defined from $c(O_2)$ in the BS region. Furthermore, despite only 170 profiles were compared, the BM04b climatology showed the highest spatial profiles coverage (208 out of 251), and good vertical resolution, in the SO compared to the other climatologies.

3.4.5 MLD-O_2 compared to MLD-σ_θ criterion in historical profiles.

To compare the MLD-O_2 criterion with non-climatological data sets, the potential density criterion $\Delta\sigma_\theta$ = 0.03 kg m^{-3} was applied to density profiles taken from objectively analyzed fields of temperature and salinity data in WOA-05 (MLD-$\sigma_{\theta WOA05}$). A negative and poor correlation (r^2 = 0.043; n=120 profiles) was found between the MLD-O_2 and MLD-$\sigma_{\theta WOA05}$. This is probably due to the scarcity of data in the Southern Ocean region in the WOA-05 data sets and to the poor vertical resolution (10 m) compared to that in the O_2 profiles investigated here (2 dbar or 1.9 m).

By contrast to the observations above, the MLD-σ_θ criterion (i.e. $\Delta\sigma_\theta$ = 0.03 kg m^{-3}) applied to the WOA-05 density profiles led to shallower values than MLD-O_2 by as much as 14±16 m.

3.4.6 MLD-O_2 in oxygen historical profiles from WOA-05.

We applied the MLD-O_2 to historical O_2 profiles at the same geographical location, from the WOA-05. It was observed a positive correlation (r^2=0.412) between MLD-O_2 from the BS profiles against the MLD-O_2 from WOA-05 O_2 climatology. On

average the MLDs from the WOA-05 O_2 climatology were 8 ± 12 m shallower than the MLD-O_2 observed in the BS profiles during 2007 (Figure 3.7). In both cases, only 120 out of 251 profiles were found at the same geographical location, and the same month of the year, in the historical record of WOA-05. Although the ammount of data in the SO is poor for the WOA05-O_2 climatology, it is suggested here that the MLD-O_2 criterion is applicable for the SO coastal area, and results can be improved as the vertical resolution of the O_2 profiles is higher.

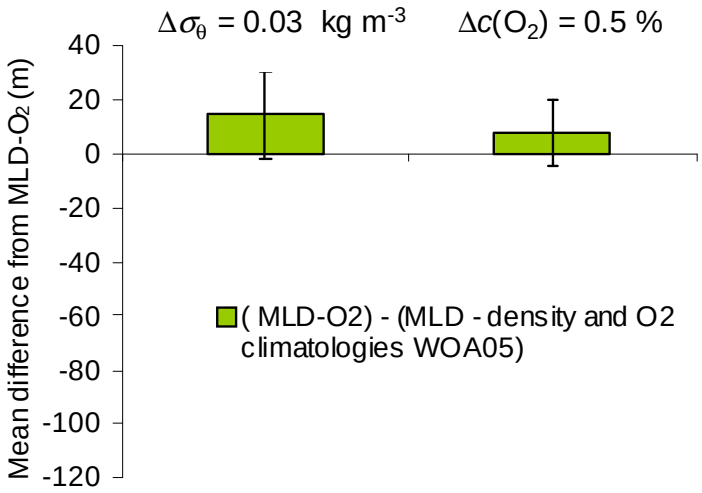

Figure 3.7 – Mean difference between MLD-O_2 minus MLD-σ_θ (after $\Delta\sigma_\theta$ = 0.03 kg m^{-3} criterion) and MLD-O_2 (after $\Delta c(O_2)$ = 0.5 % criterion) applied on World Ocean Atlas, 2005 (WOA-05) potential density (from temperature and salinity data) and oxygen historical profiles.

3.4.7 Barrier layers in the Bellingshausen Sea.

Based on the BM07 criterion for BL definition (de Boyer Montégut *et al.*, 2007), the presence of BLs was identified in 43 % of the profiles. The distribution of the stations with a BL was not associated with the distance from the coast. The range of BL thickness was from 2 to 93 m, with the thinnest (between 0 to 20 m) observed mostly in Marguerite Trough and west to the Adelaide Island region at the continental shelf break (station 200 to 251).

3.5 Discussion.

The definition of MLD based on potential density for air-sea gas exchange studies is not ideal. Typical potential density criteria to define the mixed layer lead to deeper values than the limits found from a criteria based exclusively on the vertical

distribution of $c(O_2)$. As a result, a MLD-σ_θ is located within the oxycline and tends to underestimate the average $c(O_2)$ contained within the MLD-O_2. This difference would increase in regions where stronger O_2 stratification occurs. Higher O_2 production in the upper waters or high respiration levels in waters below can also cause a stronger O_2 gradient in the oxycline, leading to shallower MLD-O_2 than MLD- σ_θ.

The results obtained from the algorithm for MLD definition proposed by Lorbacher *et al*. (2006) showed a similar overestimation of the mixed layer depth from the typical density and temperature criteria also evaluated here. Despite the L06 criterion it is able to deal with the different vertical resolution of the investigated profiles, it is still not suitable for gas exchange observations and does not describe the vertical distribution of gases in the upper water column.

Despite the modification here performed to the $c_{eq}(O_2)$ criterion proposed by Talley (1999) (i.e. $c_{eq}(O_2)$ < 95 % referencing the upper mixed layer limit as 10 m, instead of the surface value), it was concluded that defining MLD from O_2 saturation gives deeper MLDs than the ones obtained only from oxygen concentrations. Thus, defining the MLD from $c_{eq}(O_2)$ does not represent the faster changes in the water column caused by biogeochemical processes (photosynthesis and respiration), coastal upper water column dynamics such as upwelling and ice-melting water inducing stratification and air-sea gas exchange. In regions with slightly saturated O_2 surface waters, the 95 % O_2 saturation criterion is not appropriate and does not reflect the O_2-mixed layer.

Despite the good correlation between MLD-O_2 and MLD-σ_θ extracted from ML97 and BM04 climatologies, several advantages in the BM04 over the ML97 climatology are important to take into account: 1) the new BM04 climatology (BM04b) includes Argo data with a more complete data set in space and time; 2) data coverage in high latitudes (i.e. SO) is higher; from the ML97 climatology only 72 % of the occupied stations during JR165 had a MLD value, contrasting to the BM04 climatology where all the stations had a corresponding value for MLD; 3) non-interpolated and averaged profiles are used, avoiding the creation of smooth artificial profiles, this observation also applies for the K03 climatology. The BM04

climatology is obtained by an ordinary kriging of the data distributed in 2º boxes, with a prediction limited to 1000 km radius and missing data for the same radius with less than 5 grid point values. ML97 climatology (as well as in K03) considered a smaller radius of influence (771 km), however, interpolation of data and smoothing were performed within that radius leading to larger uncertainties in the observations; 4) with non-averaged profiles it is also easier to identify the presence of barrier layers and temperature inversions characteristic in the SO, and finally 5) a difference-criterion based on temperature or density with a wide threshold (such as ML97), can lead to an overestimation of MLD in the SO region. This was also observed by de Boyer Montégut *et al*. (2004) for the world's oceans, arguing than a wider interval in temperature or density for MLD criterion, such as in ML97, is best for averaged-profiles with a coarser and smoother resolution.

To take into account the spatial variability of density with water properties (density changes in terms of thermal expansion), Monterey and Levitus proposed a variable density criterion by considering a fixed temperature difference of 0.5 ºC, representing the thermal coefficient expansion of the water. However, as seen in section 3.2 by applying only the temperature difference criterion of 0.5 ºC, this temperature range corresponded to a high difference for the temperature vertical gradients in the waters of the BS.

The accuracy of MLD depends on the resolution of the parameter (given by the instruments) used in the criterion to define it. By using CTD observations, the resolution is sufficiently high to identify the vertical distribution of O_2 in the upper water column, and therefore define an adequate MLD in a less coarse vertical resolution than the integrated observations by climatologies.

The same observation was drawn from WOA-05 oxygen profiles. The low density of O_2 profiles in the WOA historical record for the SO region, and the low vertical resolution from titrations-only O_2 concentrations (10 m), make them unreliable when compared to the MLD-O_2 from CTD-O_2 vertical profiles. Moreover, the difference between MLD values between σ_θ and O_2 MLD criteria in the BS profiles and profiles from WOA-05 relies mainly in the interpolation method used to construct the temperature, salinity and oxygen fields in the latter. This artifact leads to higher error due to smooth and artificially created profiles just as in WOA-94 data.

The main factors controlling the initiation and maintenance of the high algal biomass in the BS region are physical dynamics, iron and light availability, which are driven by the MLD variability. According to previous observations by Boyd *et al*., (1995), the residence time of the primary production in the upper water column during austral summer is about 25 days in the Bellingshausen Sea. During this period of time the pigment levels, as an indicator of high chlorophyll concentration, remained relatively unchanged.

The presence of barrier layers is generally associated with temperature inversions. The latter are due to the presence of fresh and cold surface water from sea-ice melting which prevents the warming of subsurface waters. These cold and fresh waters lie above warmer and saltier ones advected from mid latitudes. As a result, temperature inversions are generally formed underneath the seasonal mixed layer. According to de Boyer Montégut *et al*. (2007), BLs are a quasi-permanent phenomenon (more than 10 months/year) in the Southern Ocean; however, the mechanisms for the BL formation and destruction in the SO are still not well understood.

The formation and thickness of the BL depends mainly on the diurnal variability of the upper water column, with the formation of a stable BL during the day due to the weaker wind stress and water column stabilization (de Boyer Montégut *et al.*, 2007). During the night this structure might disappear after night-time convection and overturning. In the continental shelf of the Bellingshausen Sea, only 17 % (43 stations) of the total number of stations were sampled during the considered “period of darkness” (about 5 hrs, from 11 pm to 4 am) during the austral summer. Furthermore, the BL was identified in both dark and light periods (Figure 3.8a).

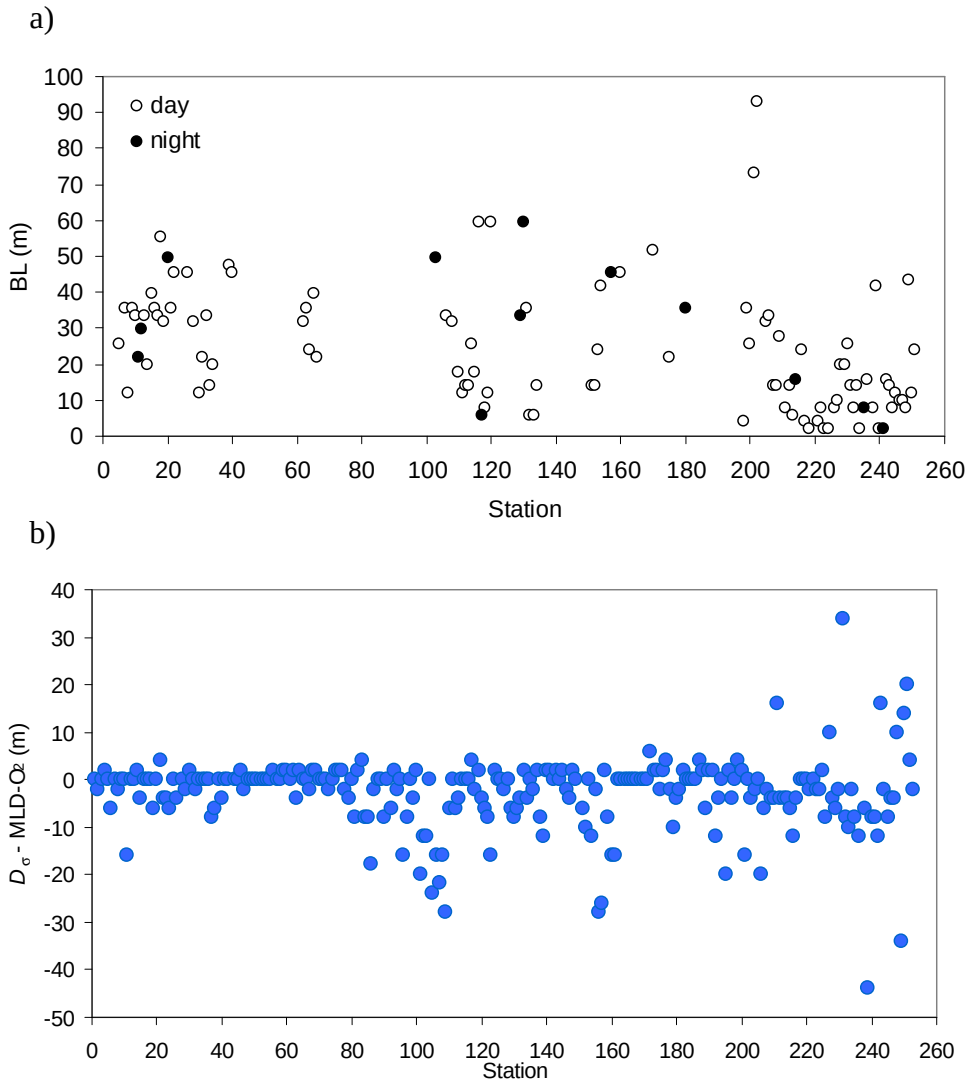

Figure 3.8 – a) Barrier Layer (BL) thickness in meters identified in vertical profiles of temperature and density in the Bellingshausen Sea during late summer and early autumn, 2007; b) the depth range difference between the upper limit of the temperature inversion at the BL and the MLD identified by the O_2 distribution for the same CTD stations.

The presence of short dark periods during the summer in the BS is clearly not an important factor for the development or destruction of BLs. BL formation in the Bellingshausen Sea may be stronger due to the upper water column stratification enhanced by the sea-ice dynamics rather than the water column diurnal variability. Furthermore, the BL in the area of study, reflect the presence of the seasonal thermocline which can act as a barrier for the mixing process between the seasonal ML and the waters below.

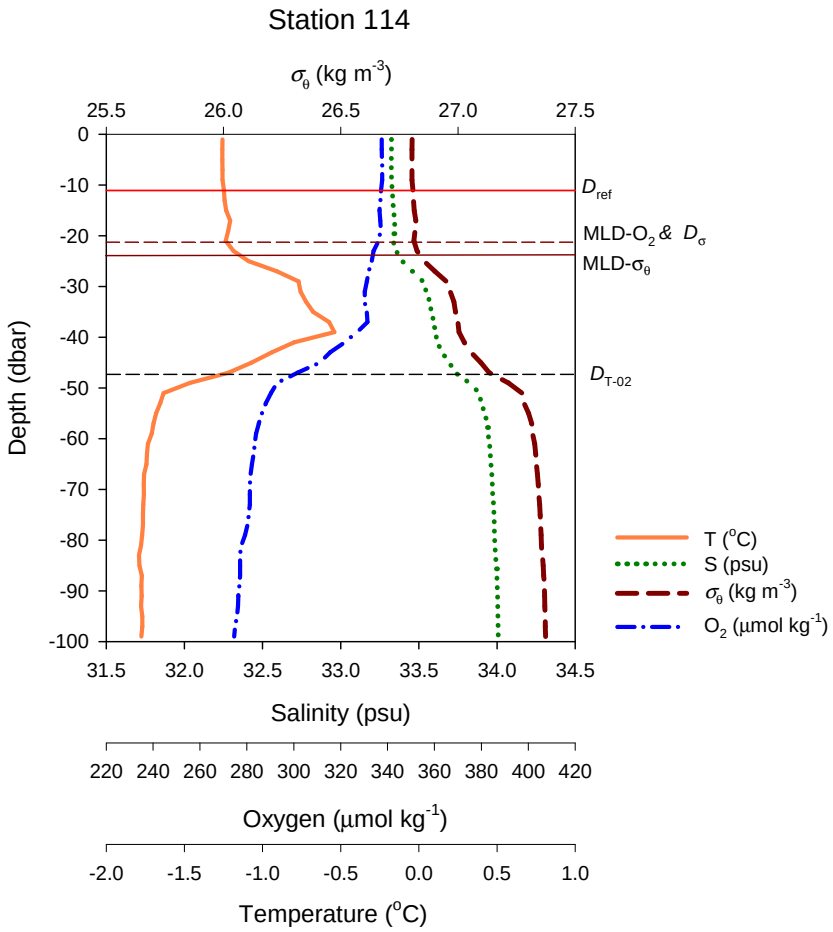

Figure 3.9 – Vertical profiles for CTD station 114, showing the typical distribution of potential density (σ_θ), temperature, salinity and oxygen for stations in the BS during late summer and early autumn. The typical location of the identified barrier layers (BLs), represented by the upper limit MLD-σ_θ, located below the MLD-O_2 is shown.

A typical vertical profile of the distribution of potential density, temperature, oxygen and salinity with the location of the BL and MLD-O_2 for the BS stations is shown (station 114, Figure 3.9).

In most stations the location of the MLD-O_2 was deeper than the upper BL's limit (D_σ) of the BL by an average of 2 ± 8 m (Figure 3.8b) indicating than the MLD-O_2 is located mainly within the BL, if the latter is present. Despite the identification of BLs in the BS region, their occurrence seemed to not influence the MLD-O_2 during summer and early autumn. The observations obtained here are in good agreement to those of Dong *et al.*, (2008). These authors concluded that the temperature inversions

did not influence the MLD defined by density derived from Argo profiles in the Southern Ocean. Moreover, the seasonal variability of the BL, influenced mainly by water column stratification is expected to correspond to the MLD-O_2 variability. The deepening of the MLD during strengthening of winds in autumn and winter will lead in O_2-low content waters entering in the ML from the BL zone and subsequent destruction of the BL.

Finally, a MLD based on O_2 can lead to a better understanding and approximation of the biogeochemical and physical processes in the upper water. The effect of using different MLD criteria in biogeochemical studies can be exemplified in estimates of net primary production (*N*). In the following table (Table 3.2) the biological O_2 flux (F_{bio} in mmol m^{-2} d^{-1}) has been calculated using the MLD criteria based on O_2, σ_θ and θ. The F_{bio} is calculated from the biological O_2 supersaturation ($\Delta O_2/Ar$) and a historical wind speed-weighted gas transfer coefficient (k_w in m d^{-1}) (see section 1.8 in Chapter 1 for further calculations description) in the BS.

Table 3.2 – Comparison of biological O_2 fluxes (F_{bio}) calculated using different criteria to define MLD in the BS. Bold indicate the closest values between columns.

Zone	Grouped CTD stations	Biological O_2 flux (F_{bio} in mmol m^{-2} d^{-1})				
		MLD-O_2	MLD-θ (θ > 0.5 ºC)	MLD-θ (θ > 0.2 ºC)	MLD- σ_θ (σ_θ > 0.125 kg $^{-3}$)	MLD- σ_θ (σ_θ > 0.03 kg m^{-3})
Wilkins Ice Shelf	1 to 36	**35.4**	44.2	**34.6**	38.7	**34.5**
Marguerite Bay north (1)	178 to 198	**21.4**	23.9	22.0	21.6	**21.5**
Belgica Trough	90 to 135	**−18.4**	−23.3	−21.2	−18.7	**−18.4**
West of Adelaide Island	214 to 252	**−20.0**	−19.2	−19.1	−19.0	**−19.3**
Marguerite Bay south (2)	199 to 213	**−12.7**	**−12.6**	−12.3	−12.1	**−12.5**

The MLD enters the calculation of k_w only indirectly (equation 1.5; Chapter 1). F_{bio} is not a direct function of MLD; thus, does not depend very strongly on MLD. However, as observed in the previous table the F_{bio} value in the grouped CTD stations differs according to the different MLD criteria used during the calculation. F_{bio} calculated using MLD-O_2 (column 3) and MLD-σ_θ defined by $\sigma_\theta < 0.03$ kg m^{-3} (column 7) agree very well, to within 0.4 mmol m^{-2} d^{-1}. For MLD based on $\theta > 0.5$ ºC, F_{bio} can differ from F_{bio} based on MLD-O_2 by as much as 8.8 mmol m^{-2} d^{-1} (or 25 %). A higher discrepancy due to different MLD criteria is expected for variables directly influenced by MLD such as estimates of time residence of a tracer.

3.6 Conclusion.

The vertical oxygen concentration in the coastal Southern Ocean is a better parameter to define MLD for gas exchange studies. For profiles in the Bellingshausen Sea collected during late summer and autumn (2007), the MLD was well defined by the depth where the absolute difference in the $c(O_2)$ was higher than 0.5 % of the $c(O_2)$ at 10 m-depth. The criterion was validated by further visual inspection with 94 % of the total working profiles agreeing well with the proposed criterion.

In coastal waters of the SO, the salinity stratification is a delimiting factor for the upper water dynamics due to the strong ice-melting water signal. After validation of the MLD-O_2 against traditional potential density and temperature criteria, a good agreement with the $\Delta\sigma_\theta = 0.03$ kg m^{-3} criterion was observed when applied on the same BS profiles and with the corresponding MLD extracted from the monthly climatology (BM04b;(de Boyer Montégut *et al.*, 2004).

Although a density based criterion can be suitable for the identification of the MLD in the area of study; vertical density can exhibit cases of vertical compensation and the MLD-O_2 gives a better reflection of the O_2 concentration within the ML of the observed profile.

Therefore, for gas exchange studies, dissolved gas budget or determination of marine production using dissolved gases as a proxy in the coastal SO, the use of the MLD-O_2 criterion is recommended. The proposed criterion is more sensitive to reflect

better upper mixed layer air-sea dynamics and the influence of biological and physical processes, rather than the traditional criteria based on potential temperature or density; particularly in regions where weak vertical gradients of temperature and density in the upper waters are suspected.

In the absence of oxygen profiles, the MLD criterion based on the $\Delta\sigma_\theta = 0.03$ kg m^{-3} criterion can be used. Furthermore, in the absence of CTD stations at all, the public monthly climatology BM04 (de Boyer Montégut *et al*., 2004), based on the same σ_θ-criterion, is encouraged to be used for determination of MLD in the coastal areas of the SO.

Chapter 4

Estimates of marine biological production in the Bellingshausen Sea from O_2/Ar ratios and triple oxygen isotopes

4.1 Abstract.

For the first time, detailed estimates of biological O_2 flux (F_{bio}) and gross oxygen production (G) integrated over the mixed layer of the Bellingshausen Sea (BS) are presented. For this, measurements of O_2/Ar ratios and triple oxygen isotopes in dissolved oxygen were done from late summer to early autumn (March to April) of 2007. Vertical O_2 profiles were also collected for 253 CTD stations in the continental shelf and shelf break regions.

The F_{bio} is used as a proxy of net community oxygen production (N) in the absence of vertical mixing. Here, an evaluation of the effect of local convective processes (i.e. diffusion by diapycnal flux (F_v) and convection by entrainment of O_2 (F_e) from subsurface waters) over F_{bio} is presented. An oxygen budget is constructed for the marine production estimates corrected by these non-biological effects. Overall, the F_v had less effect on N than F_e in the BS.

The distribution of N was well defined by the location of the marginal ice zone (MIZ). In close agreement to previous marine productivity estimates in the region, high N values were found along the coast of the Wilkins Ice Shelf (336 mg C m^{-2} d^{-1}) and in the southern part of the entrance to Marguerite Bay (245 mg C m^{-2} d^{-1}), both located in the sea ice zone (SIZ). The presence of sea-ice melt water along the coast was the main reason for enhanced stability of the water column and provided nutrients to sustain the late growing season. On the other hand, beyond the MIZ in the permanent open ocean zone (POOZ) N was negative only in the Belgica Trough area. This indicates a dominance of net heterotrophy and mixing with low oxygenated Winter Water entrained after deepening of the mixed layer.

Despite the positive N encountered in the northern part of the entrance to Marguerite Bay and in the area west of Adelaide Island, F_e seemed to play an important role for the mixed layer O_2 mass balance. However, the consumption of O_2 by heterotrophy is not neglected.

For marine productivity estimates from dissolved oxygen in coastal regions with influence of sea-ice, such as the Bellingshausen Sea, it is important to account for the local physical processes.

4.2 Introduction.

The Bellingshausen Sea (BS) is one of the major coastal shelf areas of the Western Antarctic Peninsula (WAP) in the Southern Ocean (SO). In the BS, high phytoplankton biomass has been observed around islands and in the ice fronts of the many ice shelves located in the region (Figure 4.1) (Holm-Hansen *et al.*, 2005). The high biomass and complex phytoplankton assemblage observed in the BS is mainly sustained by the water column stability, irradiance and nutrients distribution (Boyd *et al.*, 1995; Mengesha *et al.*, 1998; Garibotti *et al.*, 2003; Vernet *et al.*, 2008; Smith and Comiso, 2008b).

The WAP region is characterized by high concentrations of chlorophyll-*a* and iron in surface waters. These properties are also characteristic in other shelf areas of the Antarctic continent (i.e. Keguelen Plateau, Crozet plateau, Scotia Sea and Ross Sea) (Ardelan *et al.*, 2010); thus, the WAP is a representative area of most of the Antarctic shelf waters.

In the WAP region, the properties of the water column are influenced by local physical processes, bottom topography, seasonality of mixed layer depth (MLD) and sea-ice. In this region an increase of 0.5 °C in the sea surface temperature (top 100 m) it has been observed over the last decade and predominantly during winter (Meredith and King, 2005; Holland *et al.*, 2010; Montes-Hugo *et al.*, 2010). The observed seawater warming is believed to be due to the invasion and upwelling of the warm and low oxygenated Circumpolar Deep Water (CDW) onto the continental shelf of the WAP. As a consequence, this might contribute to the recently observed ice shelf thinning and increase of the sea ice-melt water (Jacobs *et al.*, 1996; Jenkins and Jacobs, 2008).

In the WAP, changes in sea-ice formation and retreat will not only affect the timeframe in terms of its extent and duration, but also will have important implications for the structure of the water column and marine productivity. The variability in the climate might lead to increased wind speeds (Le Quéré *et al.*, 2007); which can strongly affect the composition and abundance of phytoplankton communities in the WAP ecosystem through a stronger mixing regime. In turn, this will increase the surface nutrients content by upwelling (Arrigo *et al.*, 2008) and sea-ice retreat (Cook *et al.*, 2005). Changes in the oceanic O_2 inventories have been also

discussed previously (Matear *et al.*, 2000) with larger consequences in higher latitudes (Keeling and Garcia, 2002).

Previous estimates of marine biological primary production in the BS have been based on discrete measurements of ^{14}C assimilation, chlorophyll-*a* concentrations, quantification of the seasonal deficit in dissolved inorganic nutrients and biomass abundance of phytoplankton and zooplankton species (Boyd *et al.*, 1995; Turner and Owens, 1995; Garibotti *et al.*, 2003; Serebrennikova and Fanning, 2004; Vernet *et al.*, 2008). Marine production estimates in the BS have been also derived from remotely sensed ocean color (Arrigo *et al.*, 2008). The analytical limitations in the methods for marine productivity mentioned above are discussed in section 1.2 of Chapter 1.

In this chapter, I present net community (N) and gross oxygen production (G) in the Bellingshausen Sea during late summer and early autumn (February to April, 2007). Measurements of O_2/Ar ratios are used to constrain mixed-layer biological O_2 fluxes (F_{bio}). The latter reflects the O_2 exchange flux due to biological production and consumption of O_2 in the mixed layer; in the absence of vertical mixing this can be approximated to net community production (N). A detailed description of the basis of the method is described in Chapter 1.

The approach for estimation of N and G from mixed-layer O_2/Ar ratios and O_2 isotopes is relatively recent and has been applied successfully in some sectors of the SO (Cassar *et al.*, 2007; Reuer *et al.*, 2007a; Guéguen and Tortell, 2008; Tortell and Long, 2009), including the BS (Hendricks *et al.*, 2004) but only based on sparse discrete sampling. By using this approach it is possible to observe marine productivity gradients and high spatial resolution that have not been possible to identify using traditional incubation methods. Also, this method avoids bottle effects during the incubation process. In particular, previous productivity observations in BS have not fully resolved the interaction between processes associated with local features such as the ice-melt dynamics and biological productivity distribution. The estimates of N and G presented here were achieved over high resolution in space (on the order of 0.1 km) and time (temporal resolution of few minutes) thanks to the continuous measurements of surface water.

The F_{bio} and G estimates from the O_2 budget method assume steady state mixed-layer depth neglecting any vertical exchange from deep waters. However, local physical processes (i.e. diapycnal flux, turbulent mixing, vertical convection by entrainment, horizontal transport and upwelling) can be important for the upward transport of nutrients (particularly Fe), deep water enriched in CO_2 (Howard *et al.*, 2004; Naveira Garabato *et al.*, 2004; Bakker *et al.*, 2008) and can also exert an important contribution to the upper water O_2 mass balance. The oxygen isotopic composition can also be affected due to physical effects. In 2006, Sarma *et al*. found that as the physical processes influence the O_2 content in the mixed layer, the isotopic composition is also affected mainly by vertical mixing in the coastal region of Sagami Bay, Japan (Sarma *et al.*, 2006a).

Thus, the approximation of F_{bio} to N without considering vertical mixing can lead to significant under or overestimations to the productivity values in the BS. In order to improve the N from F_{bio} estimates the contribution of some physical processes is evaluated in this chapter.

First, the location of the Marginal Ice Zone (MIZ) (section 4.5.1) and results from direct observations of vertical profiles of oxygen and potential density (σ_θ) are presented for the Sea Ice Zone (section 4.5.2) and Permanent Open Ocean Zone (section 4.5.3).

Second, the buoyancy frequency was estimated in order to evaluate the stability of the water column influenced by the ice melt water (section 4.5.4) during the sampling period. The latter is known to be an important factor for the presence of phytoplankton communities. Furthermore, enhanced stratification will increase the buoyancy of the surface water due to surface warming and freshening and will also affect the O_2 solubility.

As step forward and in order to improve the marine production estimates from mixed-layer O_2 budget, here is evaluated the effect of only two small-scale convective processes over F_{bio} associated with the dynamics of the seasonal mixed layer: diapycnal flux by diffusion and entrainment of oxygen by vertical convection.
For this, in section 4.5.5 estimates of the vertical transfer caused by the eddy diffusivity, following the diapycnal flux (F_v) as a response of wind forcing of oxygen

trough the base of the mixed layer, are shown. Finally, in the same section the calculation of the entrainment oxygen (F_e) due to mixed layer deepening is presented. In section 4.5.6, a simple mixed-layer O_2 mass balance is used to evaluate the effect of F_v and F_e on F_{bio} and over N.

In section 4.5.8, the ratio of N to G (from $^{17}\Delta$ values, section 4.5.7) is then calculated as a proxy of the productivity index "*f*-ratio" (Eppley and Peterson, 1979) to evaluate the prevalence of heterotrophy or autotrophy (Hendricks *et al.*, 2004) in the BS during the sampling period. A comparison of the estimated gross production rates to previous estimates using the O_2 isotopes approach and traditional bottle incubation methods in the same area of study is shown.

4.3 Area of study.

The surveyed region was located between 65º and 73º S and between 66º and 95º W within the Bellingshausen Sea (BS) in the coastal area of the WAP. The present study was carried out during 38 days (3 March to 9 April 2007) on board *RRS James Clark Ross* (JCR) within the framework of the ACES-FOCAS project (Antarctic Climate and the Earth System-Forcing from the Oceans, Clouds, Atmosphere and Sea-ice) cruise JR165 of the British Antarctic Survey. The sampling period was coincident with the transition from summer to autumn during the late melting of winter ice from the previous season and the formation of new ice.

4.3.1 Physico-chemical characteristics of the water column in the BS.

The BS is located in the Antarctic Zone (AZ), in a transition region between the Antarctic continental shelf, the shelf break and the open ocean regime, the latter being delimited by the 3000 m isobath (Figure 4.1). Within the AZ on the continental shelf, two subsystems can be defined: the Permanent Open Ocean Zone (POOZ) influenced by the oceanic regime and limited by the shelf break, and the Sea Ice Zone (SIZ) towards the coast. The physical boundary between the POOZ and the SIZ is the Marginal Ice Zone (MIZ) defined by the location of the sea-ice associated to its seasonality (i.e. formation and retreat) (Vernet *et al.*, 2008; Hiraike and Ikeda, 2009). Although the MIZ is an active feature with no fixed location, it is normally encountered between 65º S to 70º S and 80º W to 87º W (Turner and Owens, 1995), extending about 100 km during summer and 200 km during winter.

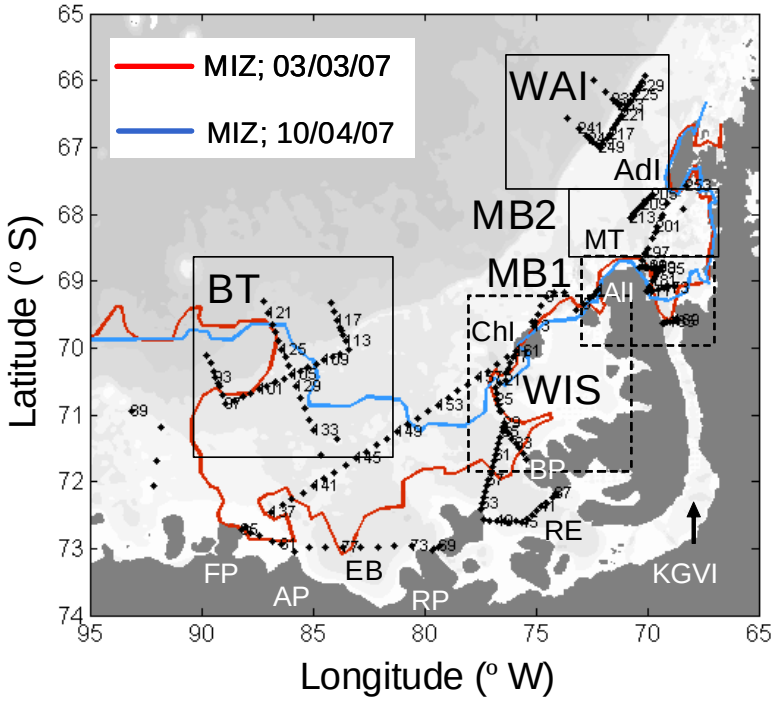

Figure 4.1 – Area of study for cruise JR165 in the Bellingshausen Sea during summer 2007. Land is dark grey. Bathymetry contours in a grey scale (200, 500, 1000, 2000 and 5000 m depth; light grey shallower to dark grey deeper). Diamonds are the location of CTD stations occupied during the cruise. Location of the Marginal Ice Zone (MIZ) from AMSR-E satellite images: red contour (beginning of cruise, 03 March 2007) and blue contour (end of cruise, 10 April 2007). Main coastal features (from west to east): FP, Fletcher Peninsula; AP, Allison Peninsula; EB, Eltanin Bay; RP, Rydberg Peninsula; RE, Ronne Entrance; BP, Beethoven Peninsula; KGVI, King George VI Sound; ChI, Charcot Island; AlI, Alexander Island; MT, Marguerite Trough; AdI, Adelaide Island. Squares group the stations for the areas indentified in this study; dashed-lined rectangles in Sea Ice Zone (SIZ): WIS, Wilkins Ice Shelf and MB1, Marguerite Bay 1; full-lined rectangle in Permanent Open Ocean Zone (POOZ): BT, Belgica Trough; MB2, Marguerite Bay 2 and WAI, West of Adelaide Island.

In Figure 4.1, the approximate location of the MIZ from the sea ice extent during the cruise JR165 (at the beginning and at the end of the sampling period) is shown. The approximate location was obtained from the satellite images provided by ENVISAT ASAR-E (Advance Synthetic Aperture Radar) from the ESA (European Space Agency) at 1 km spatial resolution for an ice concentration of 0.3 (i.e. percentage of area that is covered with sea ice) (http://www.seaice.dk). A rapid extent of the new sea-ice forming towards early autumn can be observed in the southern part of the study region.

The BS is a region characterized by complex hydrographic properties closely associated with the bottom topography, coastal configuration and sea-ice seasonality. It is relatively protected from the strong westward winds, storms and direct influence of the Antarctic Circumpolar Current (ACC) around the Antarctic continent. The formation, convection and overturning of water masses varies seasonally depending on the offshore-onshore freshwater input and vertical mixing. Here, a description of the general characteristics of the water column in the BS region will allow understanding of the distribution of the physico-chemical properties of the water column.

In the WAP region, the influence of the ACC is seen in the CDW entering close to the coast. The CDW is divided into its upper section (Upper Circumpolar Deep Water, UCDW) located at about 400 m depth in the permanent pycnocline region and its lower section (Lower Circumpolar Deep Water) located at the bottom of the water column (Orsi *et al.*, 1995). The UCDW is known to be warmer and fresher (θ >1.6 ºC and 34.6 < S < 34.72) than the LCDW (1 ºC > θ > 1.5 ºC and S > 34.72) (Serebrennikova and Fanning, 2004).

The UCDW extends well to the bottom of the Antarctic continental shelf slope and it mixes with the Antarctic Surface Water (AASW). As a result, the Modified Upper Circumpolar Deep Water is formed (MUCDW) (Smith *et al.*, 1999) and is characterized by slightly lower temperature values (0 to 1 ºC and in summer reaching up to 1.5 ºC) than the UCDW and LCDW, but similar salinities (34.6 to 34.72) and lower O_2 concentrations than the UCDW (Serebrennikova and Fanning, 2004).

The AASW is formed with the Antarctic Polar Front (APF) as its northern boundary and the Antarctic continent as its southern limit. Its formation on the continental shelf of the WAP starts by the beginning of the summer and is predominantly located in the upper 100 m (below the seasonal mixed layer) and up to 200 m depth. The AASW is characterized by higher O_2 content than the CDW (upper and lower parts), but remains undersaturated in oxygen levels (by as much as 10 %). The range of temperatures of the AASW is typically wide and with lower values than for the MCDW (−1.5 ºC < θ < 1 ºC). The value of θ that the AASW adopts depends on its location within the continental shelf and the time of the year with higher (lower)

values during summer (winter) and away (near) of the coastline. The salinity of the AASW normally ranges between 33 and 34.5. The distribution of the AASW defines the location of the AZ. Although two major fronts are located south of the APF: Southern Antarctic Circumpolar Current Front (SACCF) and the Southern boundary of the Antarctic Circumpolar Current (SbACC), their subsurface presence do not limit the AASW distribution in the surface waters (Orsi *et al.*, 1995; Whitworth III *et al.*, 1995). Another subsurface feature in the region (200 to 600 m depth) is the Antarctic Slope Front (ASF), located along the Antarctic continental slope, being characterized by a sharp horizontal gradient in temperature and salinity (Whitworth III *et al.*, 1998). The presence of the ASF does not limit either the onshore-offshore flow of the AASW; however, it appear to be absent in the WAP region (including the coast of the Bellingshausen Sea) (Orsi *et al.*, 1995).

During winter, most of the continental shelf is covered by pack ice, and underneath, the so-called Winter Water (WW) is formed towards the end of the season as a remnant of the isothermal winter mixed layer. The WW dominates the upper mixed layer during early spring replacing the AASW. The presence of the WW is characteristic of a deep (up to 100 m) well mixed layer during winter and spring. The WW is cold ($-1.8\ ^{o}C < T < -1.0\ ^{o}C$), salty ($34 < S < 34.2$) due to the brine rejection during sea-ice formation and with low O_2 content (60 to 85 % saturation) (Gordon *et al.*, 1984; Garibotti *et al.*, 2003).

The seasonality of sea-ice limits the light availability and melt water variability, and with it the temporal and spatial distribution of the biological communities that can adapt to different light regimes (Serebrennikova and Fanning, 2004; Garibotti *et al.*, 2005a; Vernet *et al.*, 2008). During early spring, the release of Fe and sea-ice algae, trapped in the ice during its formation in the previous season, start from the deep mixing by convection and melting of sea-ice close to the coast (Hopkinson *et al.*, 2007). This process and the surface presence of the WW enriched in macro nutrients (Serebrennikova and Fanning, 2004) in a well stratified water column, enhance the formation of phytoplankton blooms in the upper mixed layer (Martin *et al.*, 1991; Boyd *et al.*, 2000) particularly in the ice edge of the MIZ.

From October to March, the increase in day length and solar irradiance are also important factors that enhance the phytoplankton growing at the continental shelf. The peak of the growing season occurs in January (mid summer), and the chlorophyll-*a*, carbon biomass and phytoplankton abundance are highly variable from offshore to onshore waters; the latter is a common observation in previous works (i.e. Garibotti *et al.*, 2005a; Vernet *et al.*, 2008; Smith *et al.*, 2008a).

During the growing season, the phytoplankton blooms persist for several weeks and communities of diatoms dominate in the shelf waters of the BS (Mura *et al.*, 1995; Garibotti *et al.*, 2003; Garibotti *et al.*, 2005a; Smith *et al.*, 2008a). This group of primary producers can adapt to sea-ice covered regions and succeed in particular light regimes in a stable water column (Mengesha *et al.*, 1998; Vernet *et al.*, 2008).

As the growing season evolves, nutrients from the WW start to become depleted (mainly silica and nitrate) due to photosynthesis, remineralization of organic matter, vertical and lateral mixing. The Fe concentration starts to decrease to very low values (<0.1 nM) leading to phytoplankton biomass depletion (Smith *et al.*, 2000). By early autumn, the WW starts to disappear due to heating in surface waters and wind mixing. The mixing between sea-ice melt water (IMW) and the warmer AASW from below also starts. As the WW depletes during autumn, the AASW is located in most of the upper mixed layer, mainly in the POOZ.

From November to March (late spring to summer) the IMW starts to dominate close to the coast. Its presence in the SIZ, replaces the WW in the surface mixed layer and leaves underneath a remnant of the WW (Garibotti *et al.*, 2003; Vernet *et al.*, 2008). During summer, weaker wind speeds and the well stratified water column result in the characteristic shallow summer mixed layers (MLD < 50 m) (Holm-Hansen *et al.*, 2005). Away from the coast in the POOZ, the WW prevails in the upper mixed layer.

At the WAP continental shelf, the seasonality of the mixed layer is dominated by the influence of the IMW as the main factor to stabilize the water column, mainly in the SIZ. The IMW is well characterized for being fresher (S < 31.8) and with temperatures around −2 to −1.6 °C, close to the seawater freezing point (−1.8 °C). As the ice melts from the coast, glaciers and ice-shelves, the oxygen trapped as air bubbles in the ice is released to the surrounding water column and goes into solution.

Therefore, it is expected that the IMW has elevated oxygen levels, or close to equilibrium with the atmosphere.

Finally, the biological productivity results for the BS presented here are not only representative for the WAP region but for other Antarctic shelf areas. The marine pelagic ecosystem in the WAP characterized by krill, diatoms and various vertebrate consumers, is similar in structure and dynamics to most of the other Antarctic coastal areas, with exception of the Ross Sea where krill is normally less abundant. However, the WAP is experiencing the most rapid warming compared to other areas in the Antarctic shelf. In contrast to the Ross Sea where the winter sea-ice duration has increased, in the WAP region a sea-ice later advance and retreat is characteristic. Thus, the structure and abundance of biological communities in the WAP might face considerable changes in comparison to the rest of the Antarctic shelf areas (Ducklow *et al.*, 2007).

4.4 Methods.

4.4.1 Hydrographic stations.

During cruise JR165, vertical profiles of temperature (θ), salinity (S) and dissolved oxygen concentration ($c(O_2)$) were obtained from 253 CTD stations occupied at the continental shelf and shelf break of the Bellingshausen Sea (Figure 4.1). In Chapter 2 details of the rosette configuration (section 2.1.2) and salinity calibration (section 2.2.2) (JR165 cruise report; D. Shoosmith, *in preparation*) can be found.

To obtain the vertical profiles of O_2 concentration, the CTD was equipped with two oxygen sensors (Sea-bird SBE43). The up-cast O_2 profiles were calibrated by linear regression (r^2 = 0.997) from the comparison between O_2 concentration measured from the discrete samples by Winkler titration and the O_2 concentration as given by the CTD-O_2 sensor. A detailed description of the calibration procedure is presented in Chapter 2, section 2.4.

The analytical precision of the Winkler titration for this calibration was 0.29 μmol kg^{-1}. The final vertical profiles for all the variables measured were interpolated vertically in steps of 2 dbar to the corresponding maximum depth for each station.

4.4.2 Definition of mixed layer depth from O_2 vertical distribution.

An adequate criterion for the definition of mixed layer depth is needed for air-sea gas exchange studies and marine production estimates based on O_2 mass balance. In the coastal SO, the upper mixed layer is influenced by vertical transfer of water and the sea-ice dynamics. Traditional criteria to define the limit of the mixed layer based on temperature tend to overestimate its depth (Körtzinger *et al.*, 2008). This is more evident in the coastal waters of the SO where weak vertical temperature and salinity gradients are encountered (Chapter 3; Castro-Morales and Kaiser, 2010, *manuscript in preparation*).

In order to improve the marine production estimates in the mixed layer from oxygen measurements, here the MLD is defined based on the vertical O_2 distribution. The selection of the MLD from the vertical profiles of O_2 is the main subject of Chapter 3, with details and validation presented there. Chapter 3 is part of a manuscript in preparation, therefore here is also referred to as: Castro-Morales and Kaiser, 2010, *manuscript in preparation*).

Briefly, after objective (mathematical algorithm) and subjective (visual inspection) analysis of the 253 individual O_2 profiles in the BS, the upper MLD was defined as the depth where a change of $c(O_2)$ was higher than 0.5 % of the surface $c(O_2)$ at 10 m (or 11 dbar). In the BS, the MLD-O_2 yielded lower values than MLD defined by σ_θ (σ_θ < 0.03 kg m^{-3} with respect to the value at 10 m) by as much as 3±7 m. The latter threshold criterion based on potential density is used in the monthly mixed layer climatology from de Boyer Montégut *et al*. (2004) (BM04). The MLD-O_2 was also compared to the MLD-σ_θ directly extracted from the BM04 climatology for the same location and month of the year for the JR165-CTD stations. An average overestimation of MLD was observed by the climatological MLD-σ_θ when compared to MLD-O_2 (MLD-σ_θ in Chapter 3) by 7±11 m.

Bearing this in mind and due to the lack of historical oxygen profiles in the same area of study, the BM04 corrected by the previous offset was used as the historical MLD corresponding to 30 days before the sampling time for the estimation of the flux of O_2 by entrainment (F_e, section 4.4.7).

The term from now on to refer to the mixed layer depth will be z_{mix} and not MLD. In terms of defining the criterion, "MLD" was a more familiar acronym, however for the O_2 mass balance and to use this variable in more equations, I found it more appropriate to use z_{mix} instead.

4.4.3 Marine biological production from O_2 measurements.

The method used to estimate marine biological production was based on surface oxygen measurements, as well as O_2/Ar and the isotopic abundance of dissolved oxygen. The fundamentals for this approach have been extensively discussed in the literature (Luz and Barkan, 2002; Hendricks *et al.*, 2004; Reuer *et al.*, 2007a). A detailed description of the variables estimated in this chapter is presented in the introduction (Chapter 1) and methods (Chapter 2) of this thesis. A brief overview is given below with reference to the corresponding sections in the relevant chapters.
A mixed layer-O_2 mass balance is presented in section 4.4.9 where the complementary variables for the evaluation of the contribution of local physical processes over the marine productivity estimates are included.

4.4.4 Air-to-sea O_2 flux (F_g) determination from underway $c(O_2)$.

Continuous underway concentrations of dissolved O_2 ($c(O_2)$ in μmol kg^{-1}) were measured using an oxygen optode sensor (Model 3835, *Aanderaa* Instruments AS, Bergen, Norway). For the calibration of the continuous O_2 signal, a total of 186 discrete underway water samples were collected and the O_2 content was determined using Winkler titrations (Dickson, 1996) with photometric endpoint detection (see sections 2.3; chapter 2). The mean standard deviation (precision) of a duplicate analysis was 0.29 μmol kg^{-1}. Details of the calibration of the continuous underway $c(O_2)$ are given in section 2.5 (chapter 2). A high spatial resolution (on the order of 100 m) for the surface distribution of $c(O_2)$ was achieved considering the average ship speed (10 kn) along the cruise track, the time response of the optode sensor and the delay of the continuous underway seawater flow through the intake system to the measurement sampling point.

The supersaturation of O_2 (ΔO_2) with respect to the concentration at equilibrium with the atmosphere was calculated following equation 1.3 in section 1.7 (chapter 1). The ΔO_2 together with a weighted gas transfer coefficient (k_w, section 1.6; chapter 1) are

used to estimate the flux of oxygen through the air-sea interface (F_g) following equation 1.2 (section 1.7; chapter 1). Positive (negative) values of F_g represent a net flux of O_2 for that amount from the surface ocean (atmosphere) to the atmosphere (surface ocean).

4.4.5 Biological O_2 flux (F_{bio}) determination from O_2/Ar ratios.

Continuous measurements of the underway O_2/Ar ratios (Craig and Hayward, 1987; Emerson, 1987) were made by Membrane Inlet Mass Spectrometry (MIMS) (Kana *et al.*, 1994; Kaiser *et al.*, 2005; Tortell, 2005a) in the BS region. This was used to constrain the physical processes affecting the O_2 concentration in the mixed layer, Ar is used as an inert homologue. Seawater from the surface mixed layer was pumped by the ship's uncontaminated seawater supply (USW), located at a nominal depth of 6 m. The water was passed through a membrane chamber with a *Teflon AF®* membrane (*Random Technologies*) connected to the vacuum of a quadrupole mass spectrometer (QMS *Pfeiffer Vacuum Prisma*). Temperature effects and water vapour pressure variations in the measurements were reduced by keeping the membrane in a water bath at a constant temperature of 0 °C (further description in section 2.1.3, chapter 2). The continuous O_2/Ar ion current ratio measurements were made every 6 sec with a short-term stability of 0.05 %. A spatial resolution on the order of 300 m for the surface continuous O_2/Ar data was achieved from the average ship speed (10 kn) along the cruise track.

For calibration of the continuous O_2/Ar signal, mixed layer discrete samples in evacuated bottles were collected from the same underway water flow (see section 2.6.1 in chapter 2). After liquid and gas phase equilibration in the discrete samples, most of the water vapour, N_2 and CO_2 were removed as preparation step (section 2.6.2 of chapter 2), the remaining O_2 and Ar mixture was analyzed by Isotope Ratio Mass Spectrometry (IRMS) (*Thermo Finnigan* MAT 252) for identification of ion beam intensities *m/z* 32 and 40 by a peak jumping method on a single collector (Luz and Barkan, 2000). The calibration procedure for the continuous O_2/Ar ratios from MIMS based on discrete samples is described in section 2.7 (chapter 2).

The mixed-layer biological O_2 supersaturation (ΔO_2/Ar) (equation 1.4, section 1.8; chapter 1) is calculated from the ratio between the calibrated O_2/Ar ratios and the

saturation concentration ratio ($(O_2/Ar)_{eq}$ = $c_{eq}(O_2)$ / $c_{eq}(Ar)$) determined from the solubility equations for O_2 (Benson and Krause, 1984; Garcia and Gordon, 1992; Garcia and Gordon, 1993) and for Ar (Hamme and Emerson, 2004) as function of temperature, pressure and salinity.

Finally, continuous upper mixed layer biological O_2 fluxes, F_{bio} (mmol m^{-2} d^{-1}) were calculated using $\Delta O_2/Ar$ and k_w according to equation 1.5 in section 1.8 (chapter 1). Positive (negative) values of F_{bio} represent a net flux of O_2 biologically produced from the surface ocean (atmosphere) to the atmosphere (surface ocean).

4.4.6 Diapycnal flux (F_v) determination.

As mentioned before, the marine productivity estimates from the O_2 budget method neglects the vertical transfer of gas through the base of the mixed layer. However, previous studies have suggested that this assumption can lead to underestimation of the productivity estimates. Reuer *et al*. (2007) and Cassar *et al*. (2007) observed negative F_{bio} values in some regions of the SO and were unable to identify the contribution of net heterotrophy, upwelling or entrainment of low oxygenated waters. According to Reuer *et al*., the observed apparent "negative biological O_2 production", particularly in the Marginal Ice Zone (MIZ) south of New Zealand, can be due to vertical mixing rather than net heterotrophy. The authors suggested that the convection of low O_2 waters by upwelling near the ice margin and within the Antarctic Zone can be the main cause.

Thus, to account for the effect of the vertical flux of O_2 in the mixed layer-marine productivity estimates, the diapycnal flux of O_2 (F_v) is constrained here. F_v is an estimate of the transfer of gas due to eddy (or turbulent) diffusivity through the base of the mixed layer depth. F_v is calculated from the first Fick's law of diffusion following:

$$F_V = -K_Z \times \frac{\Delta c_{oxy}}{\Delta z_{oxy}} \qquad (4.1)$$

where Δc_{oxy} represents the gradient of O_2 in the oxycline obtained from the dissolved oxygen vertical profiles. Thus, Δc_{oxy} is given by the difference between the O_2 concentration at the oxycline's bottom limit ($c_{base}(O_2)$) minus the O_2 concentration in the upper limit ($c_{zmix}(O_2)$); (Δc_{oxy} = $c_{base}(O_2)$ − $c_{zmix}(O_2)$). The term $c_{zmix}(O_2)$ thus

represents the oxygen concentration integrated on the mixed layer depth at the sampling time.

The depth range of Δc_{oxy} corresponds to the thickness of the oxycline (Δz_{oxy}) given by the difference between the depth where the base of the oxycline was located (z_{base}) minus the depth of the mixed layer during sampling day (z_{mix}); ($\Delta z_{oxy} = z_{base} - z_{mix}$). Positive (negative) values of F_v represent an influx (efflux) of O_2 by eddy diffusivity into (out of) the mixed layer (contrary reference sign to F_g and F_{bio}, see Figure 4.2). The term K_z is the eddy diffusivity coefficient ($m^2\ s^{-1}$). Here, the mean K_z suggested by Howard *et al.* ($K_z \leq 1 \times 10^{-5}\ m^2\ s^{-1}$) was used. This value was obtained for the Marguerite Bay area during the Southern Ocean Global Ecosystem Dynamics program (GLOBEC) for fall and winter in 2001. This K_z value is in close agreement to the value suggested by Law *et al*. (2003) with a mean K_z of $1.1 \pm 2.0 \times 10^{-5}\ m^2\ s^{-1}$ obtained during the SF_6 tracer release experiment SOIREE (Southern Ocean Iron Enrichment Experiment) during the summer of 1999 in the Australian sector of the SO (Law *et al.*, 2003; Howard *et al.*, 2004).

Due to the lack of studies and the difficulty to estimate K_z directly in the field (particularly in the SO) here is considered that the selected K_z is the best approximation so far for the BS region. The range of wind speeds during the sampling time of JR165 (average between 4.6 and 8 $m\ s^{-1}$ obtained from the historical wind speed over 60 days before the cruise) were within the range of the wind speeds recorded during the SOIREE experiment (5 to 12 $m\ s^{-1}$). The squared of the buoyancy frequency (ν^2) during SOIREE registered values between $1 \times 10^{-3}\ s^{-2}$ for the seasonal pycnocline and up to $1 \times 10^{-5}\ s^{-2}$ in the mixed layer towards the end of the experiment. During GLOBEC, the buoyancy frequency (ν^2) was $< 10^{-4}\ s^{-2}$. These values are consistent with the range of ν^2 found for the BS region in this study (see section 4.5.4 below) being on the order of $10^{-4}\ s^{-2}$.

Since measurements of O_2/Ar ratios at different depths in the vertical profile were not done, it is not possible to estimate the diapycnal flux of the biological O_2 through the base of the mixed layer. However, it is considered that the Ar concentration of the water below the mixed layer is also affected by mixing. Therefore, the

concentration of Ar will vary only below the mixed layer and the gradient through the base of the mixed layer can be expressed in terms of dissolved O_2.

4.4.7 Entrainment of O_2 (F_e) due to mixed layer variability.

The flux of oxygen due to entrainment (F_e) by vertical convection after deepening of the mixed layer depth is evaluated here. Previous approaches used to estimate F_e (i.e. Emerson, 1987; Emerson *et al.*, 2008) account only for the gradient of oxygen given by the difference in concentration between the waters underneath the mixed layer (i.e. in the thermocline) minus the concentration within the mixed layer during sampling. However, this assumption leads to an underestimation of the total concentration of oxygen contained in the portion of the water column entrained after deepening of the mixed layer. Here, F_e after deepening of the mixed layer depth (Δz) is given by:

$$F_e = z_{mix} \frac{dc}{dt} = -\frac{1}{2} m(\Delta z)^2 \frac{dh}{dt} \qquad (4.2)$$

Where (dc/dt) represents the rate of change of the concentration of oxygen during the previous 30 days (dt) prior to the sampling time integrated over the mixed layer depth at the sampling time (z_{mix}); m is the slope given by the gradient of oxygen (Δc) in the oxycline during sampling day. The thickness of the water column entrained (Δz) is obtained from: $\Delta z = z_1 - z_0$; where z_0 corresponds to the depth of the mixed layer 30 days before the cruise and z_1 is the mixed layer depth at sampling time (i.e. z_{mix}). Thus, positive values of Δz would indicate deeper mixed layers compared to 30 days before the sampling time. Detailed derivation of equation 4.2 is shown in the Appendix A of this thesis.

The depth of the mixed layer (z_{mixcl}) during the 30th day before the sampling time was extracted from the monthly climatology given by de Boyer Montégut *et al.*, (2004) for the same geographical location of the ship track. To obtain z_0, the z_{mixcl} was corrected by 7.0 m (Chapter 3; Castro-Morales *et al.*, 2010, *manuscript in preparation*) according to the depth overestimation of z_{mix} as defined by σ_θ compared to the value obtained after the vertical oxygen distribution. Positive (negative) values of F_e represent an influx (efflux) of O_2 by convection into (out of) the mixed layer (opposite sign to F_g and F_{bio}, see Figure 4.2).

4.4.8 Gross O_2 production (G) determination from the isotopic abundance of dissolved O_2.

Analysis of the $^{17}O/^{16}O$ and $^{18}O/^{16}O$ isotope ratios ($\delta^{17}O$ and $\delta^{18}O$, in ‰) in the headspace of seawater discrete samples collected in the BS was done by multi collector IRMS (Luz and Barkan, 2000) (see section 2.6.2 of chapter 2 for detailed description and efficiencies of the analysis; section 2.9 shows the corrections to the measurements).

From the measured $\delta^{17}O$ and $\delta^{18}O$ the ^{17}O anomaly ($^{17}\Delta$ in per meg) is calculated in the headspace of the discrete seawater samples according to equation 1.18, section 1.10.2 in Chapter 1. Appropriate corrections for the $^{17}\Delta$ calculation are presented in section 2.9 of Chapter 2.

The quantification of $^{17}\Delta$ allows the identification of the origin of dissolved O_2; this is possible due to the different fractionation processes occurring in the environment. The O_2 formed by biological processes follows a mass-dependent fractionation with the $\delta^{17}O$ abundance being about half of the $\delta^{18}O$. However, the O_2 formed by photochemical reactions between O_3, O_2 and CO_2 in the stratosphere, follows a non-mass-dependent isotope fractionation; and, atmospheric O_2 shows a corresponding depletion in ^{17}O (Luz and Barkan, 2000) and $\delta^{17}O$ becomes almos equal than $\delta^{18}O$ (see section 1.10.2 in chapter 1 for further details).

The gross O_2 production (G, in mmol m^{-2} d^{-1}) integrated over the mixed layer was estimated from k_w, $c_{eq}(O_2)$, $^{17}\Delta_{max}$, $^{17}\Delta_{eq}$, and $^{17}\Delta$ of dissolved oxygen in discrete seawater samples, following equation 1.19 in section 1.10.4 (chapter 1).

The $^{17}\Delta$ is of relevance for the present study since it will help to elucidate the mixing with subsurface waters and air-sea gas exchange. The diapycnal mixing will not only bring deep waters to the surface, but will transport waters enriched in biological O_2 to waters below the mixed layer during summer. Since $^{17}\Delta$ is not affected by respiration (Luz and Barkan, 2000; Luz and Barkan, 2009), the anomaly is expected to accumulate despite the O_2 consumption in aphotic waters or in the remnant mixed layer. This accumulation can be transferred to upper waters as the season progresses

and the mixed layer deepens in response to higher wind stress and convective mixing.

4.4.9 Mixed layer-O_2 mass balance.

The fluxes mentioned above were included in a simple 1-D box-model to evaluate the O_2 mass balance in the mixed-layer of the BS (Figure 4.2). Based on the O_2 mass balance proposed previously by others (Hamme and Emerson, 2002; Hendricks *et al.*, 2004; Kaiser *et al.*, 2005), here the diapycnal O_2 flux (F_v, section 4.4.6) and entrainment of O_2 after the deepening of the mixed layer (F_e , section 4.4.7) are included in order to evaluate the effect of these local and small-scale physical processes over the O_2 concentration in the BS mixed layer and to finally improve the estimates of marine production by the oxygen measurements method. The mixed-layer O_2 mass balance at a specific time *t*, can be described as:

$$z_{mix} \times \frac{\partial c(O_2)}{\partial t} = G - R - F_g + F_v + F_e + F_{bubbles} \qquad (4.3)$$

The left hand side of the equation 4.3 indicates the temporal change of the $c(O_2)$ over the time in a z_{mix}. Considering steady state, the latter would equal to zero and the total O_2 in the mixed layer is given by the sum of F_g, $F_{bubbles}$, F_v and F_e. F_{bio}, as calculated in equation 4.3, is a rough estimate of G minus the rate of O_2 consumption by heterotrophy (respiration, R) integrated over the depth of the mixed layer. Thus, the net community production (N) is given by the difference between G and R.

The term $F_{bubbles}$ refers to the sum of the air-sea flux of O_2 from injection (F_{inj}) and exchange (F_{exch}) of bubbles into the mixed layer (Hamme and Emerson, 2002; Kaiser *et al.*, 2005).

$$F_{bubbles} = \chi(O_2) \times [F_{inj} + (F_{exch} \times \alpha(O_2) \times \sqrt{Sc(O_2)})] \qquad (4.4)$$

Both F_{inj} and F_{exch} are multiplied by the O_2 mixing ratio in air $\chi(O_2)$. F_{exch} is also multiplied times the Schmidt number for O_2 ($Sc(O_2)$) (Wanninkhof, 1992) and the Ostwald solubility coefficient for O_2 ($\alpha(O_2)$).

The physical transfer of O_2 by lateral advection and upwelling here are neglected. Further justification to the previous assumption and future recommendations for the O_2 mass balance are presented in the discussion section below. The next figure (Figure 4.2) shows a schematic representation of the O_2 mass balance as given by equation 4.3.

In the O_2 mass balance used here F_g and F_{bio} are referenced to the atmosphere, thus positive values indicate net transfer from the surface ocean to the overlying atmosphere. Contrary, F_v and F_e are fluxes referenced to the mixed layer; thus, positive values in these fluxes represent an influx of O_2 into the mixed layer.
Thus, the corrected F_{bio} by F_v and F_e gives a better approximation of N in the way: $N = F_{bio} - F_v - F_e$; without neglecting the physical contribution of O_2 in the mixed layer depth from the processes evaluated here.

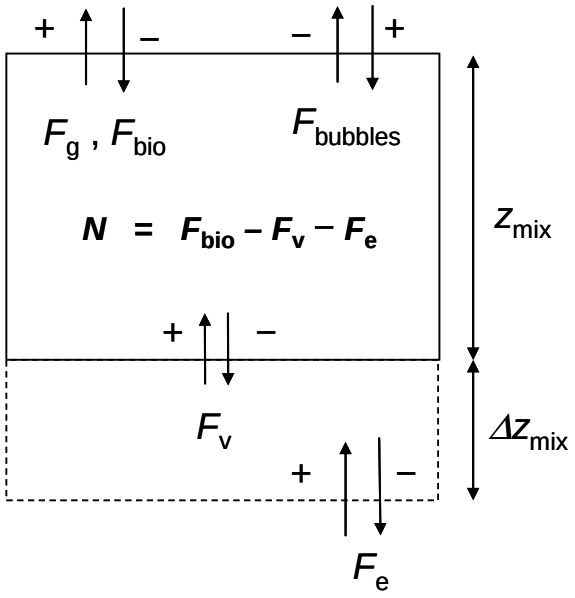

Figure 4.2 – Schematic of the mixed layer (z_{mix} in m) O_2 mass balance represented by the biological O_2 flux (F_{bio}) and flux of O_2 (F_g) relative to the atmosphere. Diapycnal flux (F_v) and flux by entrainment (F_e) due to the variability in the mixed layer (Δz_{mix} in m) are referenced to the mixed layer. All fluxes are given in mmol m^{-2} d^{-1}.

4.4.10 Auxiliary variables.

Supporting physical variables were measured from various sensors on board the JCR from the underway system: a continuous record of sea surface temperature (SST) from a sensor located at the bow of the ship close to the seawater intake, sea surface

salinity (*S*) from a thermosalinograph, as well as barometric pressure (*P*) and wind speed corrected to 10 m height (u_{10}) from the meteorological station on board. The corresponding corrections due to sensors' response lagtimes and height above the sea surface were accordingly performed. A consistent warming effect of 0.65 ºC was identified due to the 2 min delay of the surface water in the intake system until sampling. This offset was removed from the overall SST signal.

The gas transfer coefficient was calculated following the parameterization suggested by Sweeney *et al*. (2007). To account for the history of the mixed layer according to the residence time of O_2, a weighted gas transfer coefficient (k_w) was calculated using the method suggested by Reuer *et al*., (2007). For this, the historical wind speeds at 10 m height for an interval of 60 days prior to the sampling period (u_{10_60}) were used. These data were obtained from the European Centre for Medium-Range Weather Forecasts (ECMWF 6 hr resolution, operational analysis 1° grid field) wind speed product. The latter was selected after comparison of the instantaneous wind speed recorded by the ship's anemometer (u_{10}) during the sampling period to various wind speed products at different time resolutions (i.e. QuickSCAT 24 hr, NCEP 6 and 24 hr). The ECMWF wind speed extracted for the same days of the sampling period was in closer agreement to u_{10} by as much as 2.6 m s^{-1} as the mean of the difference between the standard deviation for each set of data. The latitudinal ($u_{\_10}$; east – west) and meridional ($v_{\_10}$; north – south) components of the wind speed vector were also extracted from the same wind product (see Chapter 2 for details).

4.5 Results.

4.5.1 Location of the Marginal Ice Zone (MIZ) associated with the spatial distribution of mixed layer biological O_2 supersaturation.

From the identification of the location of MIZ during the JR165 cruise (03 of March and 04 of April, 2007) (section 4.3.1, Figure 4.1) in the Bellingshausen Sea, the MIZ remained similar for the regions located between 95º and 87º W and 76º and 65º W. Therefore, no apparent retreat or advance occurred during the sampling period (38 days) for those areas. On the other hand, a sea-ice advance of about 215 km is observed in the central part of the area of study (region between 75º and 87º W) from the coast of Fletcher Peninsula, Allison Peninsula and Eltanin Bay towards the shelf break in Belgica Trough (Figure 4.1). During the sampling period, the rate of sea-ice

advance was about 5.6 km/day and is an indication of the formation of new ice during the beginning of autumn in the POOZ.

The MIZ represents the limit of the SIZ from the POOZ. The spatial distribution of O_2 and O_2/Ar supersaturations of these zones were heterogeneous. Overall, supersaturated values for total and biologically produced O_2 were observed towards the coast of the WAP (2.4±3.0 % and 5.7±3.4 % for ΔO_2 and ΔO_2/Ar, respectively) in the SIZ (Figure 4.3). There, the area of study is subdivided into two areas: 1) along the coast of Wilkins Ice Shelf (WIS, CTD stations 1 to 36) located in the southern part of the entrance of Marguerite Bay and 2) Marguerite Bay 1 (MB1, CTD stations 178 to 198) located close to the coast of Alexander Island.

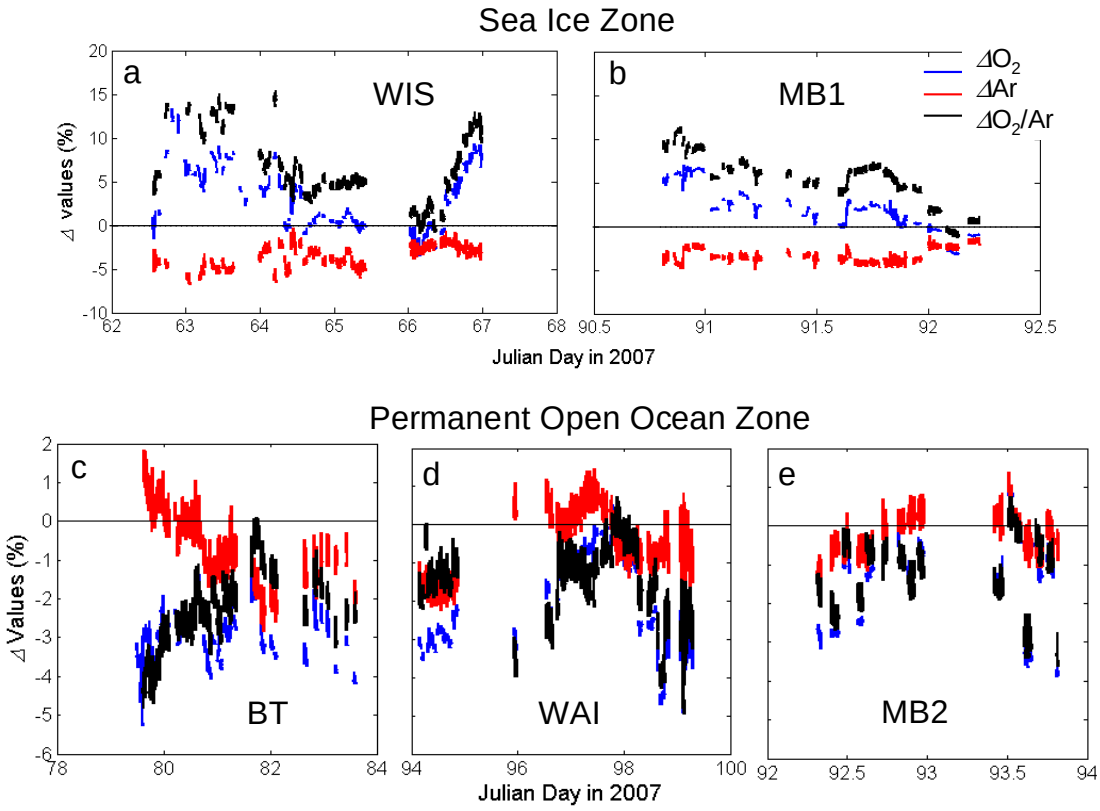

Figure 4.3 – Distribution of the surface mixed layer oxygen and oxygen/argon supersaturation (blue line, ΔO_2 and black line, ΔO_2/Ar) in the different subregions indentified. Top panels: a) WIS and b) MB1, corresponding to the SIZ. Bottom panels: c) BT, d) WAI and e) MB2, in the POOZ (note the difference in the y-axis scale for the top and bottom panels). ΔAr (red line) was inferred from ΔO_2 and ΔO_2/Ar. Horizontal solid line indicates the equilibrium with the atmosphere.

By contrast, undersaturated ΔO_2 and ΔO_2/Ar were identified in the POOZ off the coast (average ΔO_2 and ΔO_2/Ar of −2.0±0.9 % and −1.6±0.9 %, respectively). These values represent the average of the three areas subdivided in the POOZ: 1) Belgica Trough (BT, CTD stations 90 to 135), 2) Marguerite Bay 2 (MB2, CTD stations 199 to 213) located in the northern part of the entrance to Marguerite Bay and towards the coast of Adelaide Island and 3) West of Adelaide Island (WAI, CTD stations 214 to 252) located in the northernmost part of the sampling area (Figures 4.1 and 4.3).

As a consequence of the variable ΔO_2/Ar, the biological oxygen flux (F_{bio}) was also heterogeneous. High apparent biological O_2 production, given by positive values of F_{bio} (average of 27.3±14.0 mmol m^{-2} d^{-1}) was observed in the SIZ areas. On the other hand, negative values of F_{bio} (mean of −16.0±8.9 mmol m m^{-2} d^{-1}), were observed in the POOZ due to the undersaturated O_2/Ar (Table 4.2).
The decision to split Marguerite Bay region into two areas (MB1 and MB2) was due to the contrasting heterogeneous distribution of both ΔO_2 and ΔO_2/Ar. Positive ΔO_2/Ar was observed in MB1 at the southern part of the entrance to Marguerite Bay (5.3±2.9 %), while negative biological O_2 supersaturation was observed in MB2 at the northern part of Marguerite Bay (−1.2±0.9 %) (Figure 4.3). The boundary between MB1 and MB2 is coincident to the location of the MIZ at the entrance of Marguerite Bay. In this area, the MIZ remained close to Alexander Island and towards George VI ice-shelf during the sampling period (Figure 4.1).

In the following sections, the results for SIZ and POOZ are presented independently for each zone (section 4.5.2 and 4.5.3, respectively). The distribution of the water masses in the area of study (particularly in the upper 200 m) as identified from vertical sections of θ, S and $c(O_2)$ is also presented.

In section 4.5.5 the estimates of F_v for each CTD station according to the gradient of O_2 at the base of the mixed layer are shown. In the same section the estimates of F_e, for each CTD station, due to convection of deep water as a consequence of deepening of the mixed layer over a period of 30 days before the sampling day are also shown. The historical z_{mix} is based on climatological data (de Boyer Montégut *et al.*, 2004).

The contribution of F_v and F_e to the estimated F_{bio} is quantified. Average values and uncertainties (±1 standard deviation) for the estimated variables in the areas mentioned above are summarized in Tables 4.1 and 4.2. Details of individual errors and overall error propagation are also presented.

The results from $^{17}\Delta$ (section 4.5.7) and gross O_2 production (G) are shown with the rates of N/G ($f(O_2)$-ratio) calculated and presented in section 4.5.8. Using an oxygen-to-carbon ratio for N(C) the net carbon community production is calculated and compared to previous values in the region (section 4.7).

4.5.2 Sea Ice Zone.

In the SIZ of the area of study, the WIS section was sampled at the beginning of the survey during late summer (3 to 8 March, 2007), while the MB1 section was sampled 28 days later representing early autumn (31 March to 2 April, 2007).

The characteristics of the water column remained similar for WIS and MB1 despite the difference in sampling periods; therefore, the properties of the upper water column in the SIZ were not strongly affected during the seasonal transition from summer to autumn. From the observations in the vertical sections of θ, S and $c(O_2)$ (not shown), the upper 200 m of WIS (CTD stations 1 to 36) and MB1 (stations 178 to 198) showed a well stratified water column in the SIZ during the entire sampling period. Average values per area are shown in Table 4.1.

In order to identify the location of the main water masses in the water column of the SIZ and POOZ, Figure 4.4 shows the relationship between the $c(O_2)$ against θ (Figure 4.4a) and against S (Figure 4.4b) for the full depth profiles. The corresponding values exclusively in the mixed layer are also shown (Figures 4.4c and 4.4d).

The mixing lines according to the properties of the water masses as end members are shown as black dashed lines in Figure 4.4. The CDW (on its upper and lower part) was well identified in most part of the base of the continental shelf.

Table 4.1 – Average ± 1 standard deviation for the main variables measured and estimated in the Bellingshausen Sea for cruise JR165 in summer, 2007. Results categorized by areas: WIS, Wilkins Ice Shelf; MB1, Marguerite Bay 1; BT, Belgica Trough; MB2, Marguerite Bay 2 and WAI, West of Adelaide Island; (CTD stations in between the ones presented here are not included).

Area	CTD stations	SST (ºC)	Salinity	ΔO_2 [(1)] (%)	$c(O_2)$ [(2)] (µmol kg^{-1})	$\Delta O_2/Ar$ [(3)] (%)	ΔAr (%)	k_w [(4)] (m d^{-1})	F_g [(5)] (mmol O_2 m^{-2} d^{-1})	F_{Ar} (mmol m^{-2} d^{-1})	z_{mix} (m)	Δz_{mix} [(6)] (m)	v^2 ($\times 10^{-4}$ s^{-2})
Sea Ice Zone (SIZ)													
WIS	1-36	−0.9±0.6	32.5±0.4	2.9±3.6	367±18	6.2±3.9	−3.3±1.1	1.6±0.4	14±7	−3±3	15±5	−10±4	1.5±0.5
MB1	178-198	−1.1±0.2	33.0±0.2	1.9±2.5	352±7	5.3±2.9	−3.3±0.8	1.2±0.3	6±10	−3±2	19±7	4±7	1.2±0.3
Permanent Open Ocean Zone (POOZ)													
BT	90-135	−1.4±0.4	33.3±0.2	−2.9±0.6	339±5	−2.2±1.0	−0.6±0.9	2.0±0.2	−23±4	−2±1	28±7	8±7	0.8±0.3
MB2	199-213	−0.1±0.1	33.5±0.1	−1.4±1.1	329±4	−1.2±0.9	−0.2±0.5	2.8±0.5	−13±10	−3±1	33±8	21±10	0.2±0.1
WAI	214-252	0.4±0.2	33.8±0.1	−1.8±1.2	323±7	−1.5±1.0	−0.3±0.9	3.7±0.4	−23±15	−2±1	49±15	18±12	0.0±0.2

[(1)] The error in the oxygen supersaturation (ΔO_2) relies mainly in the uncertainty given by the dissolved O_2 measurements by the Winkler method (0.1 %). Positive values indicate the amount of dissolved O_2 supersaturated with respect to the concentration at equilibrium with the atmosphere.

[(2)] $c(O_2)$ per area represents the average within the mixed layer at the sampling time.

[(3)] The error in the biological O_2 supersaturation ($\Delta O_2/Ar$) is mainly due to the measurements of $c(O_2/Ar)$ in the IRMS and after the extraction line. The error is given after the analysis of a series of air-equilibrated waters which corresponded to 0.2 %.

[(4)] The error in the gas transfer coefficient according to Sweeney *et al*., 2007 ($k = 0.27\ (u_{10}^2)(Sc/660)^{-0.5}$) is about 15 %.

[(5)] The error for the sea-to-air flux of O_2 (F_g) relies mainly on the k_w (15 %); positive values indicate a flux from the ocean to the atmosphere.

[(6)] The error related to the difference in the mixed layer depth from the historical depth (30 days before) to the sampling time is 15 % considering the correction made to the mixed layer depth extracted from the climatological data (de Boyer Montégut *et al*., 2004). Positive values indicate a deepening of the mixed layer, by the given number in meters, during the sampling day with respect to the historical depth 30 days before.

In the upper waters, the main characteristic for the areas in the SIZ subsystem was the presence of IMW in the top 80 m dominating the mixed layer during the sampling period. The IMW was characterized by colder (−2 ºC), fresher (S<31.8) and O_2 supersaturated water (ΔO_2 up to 12 %) than the waters below (Figures 4.4c and d). Underneath the IMW the water column was dominated by the saltier (33.5 to 34) and colder version of the AASW (−1.5 to −1.0 ºC), this is probably due to the mixing with the overlying IMW.

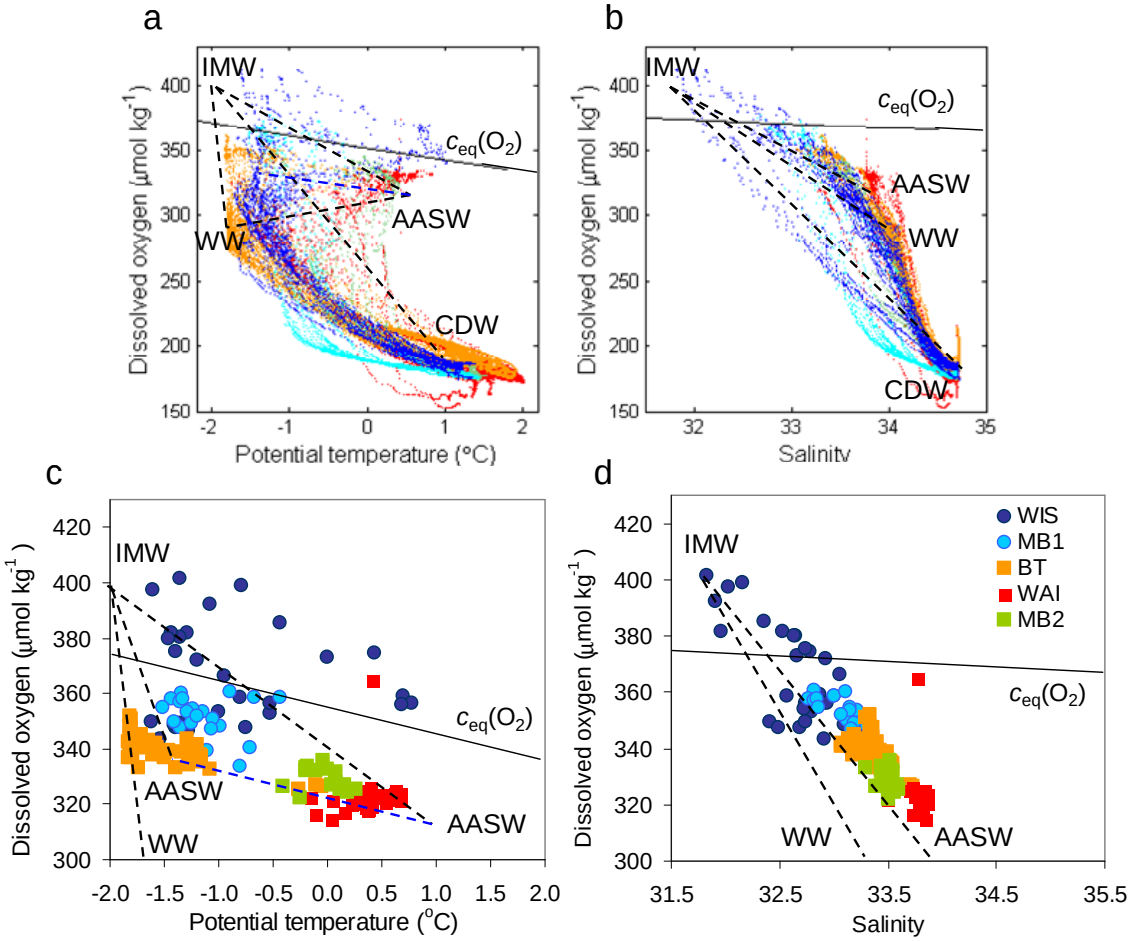

Figure 4.4 – Potential temperature and salinity plotted against dissolved oxygen for the stations representing the areas identified in the BS. (a, b) include all depths in the profiles for the identification of deep water masses; (c, d) zoom of top panels showing only the data corresponding to the mixed layer. Dashed lines correspond to the mixing lines with end-points marked as the characteristics of the identified water masses: IMW, Sea-ice meltwater; WW, Winter Water; AASW, Antarctic Surface Water; CDW, Circumpolar Deep Water. Full almost horizontal lines represent the changes in concentration of oxygen at saturation (only for reference) at: (a, c) constant salinity of 33.5; and (b, d) constant temperature at seawater surface freezing point (−1.8 ºC). Note in panel c the almost horizontal dashed line represents the wide range of temperatures that characterize the AASW, extending from colder (~ −1.5 ºC) to warmer (0.5 ºC) waters. Panel d, WIS and MB1 are supersaturated in O_2 considering the in situ temperature (< −0.9 ºC) is higher than the freezing point at which the $c_{eq}(O_2)$ line is plotted.

In the SIZ, the mixed layer depth was generally shallow with a mean depth ($z_{mix} \pm 1\sigma$) of (17 ± 6) m. In the WIS, clear temperature inversions ranging in an interval from −1 to 1 ºC in a depth range of few tenths of meters were observed in the upper 50 m due to the horizontal advection of IMW mainly from Charcot Island. Less influence from IMW was observed for Latady Island and Beethoven Peninsula in the western and southern parts of WIS, respectively and for Alexander Island in the north. However, the weak signal of IMW from these coastal features could be due to the mixing between IMW and AASW as was observed for the presence of the colder version of the latter. In turn, the characteristics of the AASW dominated the mixed layer, and the waters underneath (up to 180 m depth), in the coasts of Latady Island, Beethoven Peninsula and Alexander Island, reaching O_2 undersaturations down to −30 %.

In the upper 100 m of the SIZ, the presence of WW was not observed; this was expected as the presence of this water mass tends to disappear due to mixing with the IMW that dominates in the peak of the summer season. In the SIZ, the AASW was found to be lying above the MCDW, with the latter located below 180 m and characterized by being warmer (0.5 to 0.8 ºC), saltier (S > 34) and undersaturated in O_2 by as much as 40 %.

Contrary to WIS, in the MB1 section the Alexander Island appeared to be the main source of IMW into the mixed layer, extending horizontally and towards the northeast up to 31 km (from stations 194 to 199), and vertically up to 100 m depth. The intrusion of IMW continued in subsurface waters (between 100 to 150 m) from stations 199 to 201 underneath the AASW (into the area here identified as MB2); the latter dominated the mixed layer for the rest of the section towards Adelaide Island.

The strength and direction of the wind in the BS play an important role in the coastal upwelling, redistribution of the sea ice and the location of the MIZ, and with it also the distribution of the biological communities. The monthly mean wind direction (from the ECMWF wind product) showed a predominant and consistent presence of southerly winds over the WIS and MB areas during February, March and April, 2007 (Figure 4.5).

The mixed layer depth in the SO is generally deep and unstable; however the WIS and the MB1 in the SIZ are located in a more sheltered region due to the topographic features (islands and coast line structure) than the POOZ. In the SIZ, the wind stress was generally weaker, facilitating the local stabilization of the water column and the development of phytoplankton communities seeded by horizontally advected nutrients from the IMW.

As a consequence of weaker wind speeds over the geographically protected WIS and MB1 areas, the air-to-sea gas transfer was lower for these areas. The weighted gas transfer coefficient (k_w) (Sweeney *et al.*, 2007; Reuer *et al.*, 2007a), calculated from the historical wind speeds from the ECMWF product from 60 days before the sampling time, was 2 times lower in the WIS and MB1 region (average, 1.4±0.3 m d^{-1}) than in the areas located in the POOZ (BT, WAI and MB2; 2.8±0.3 m d^{-1}).

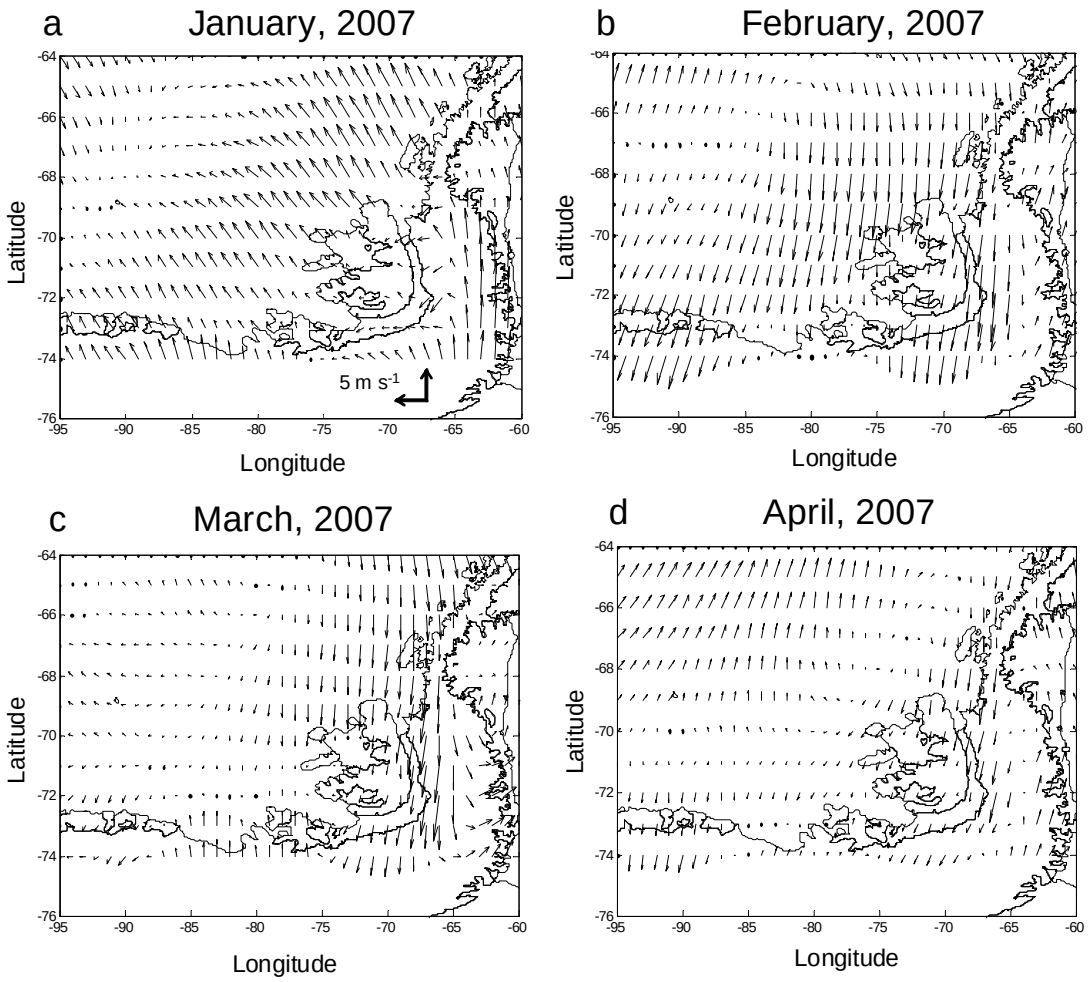

Figure 4.5 – Monthly mean wind speeds and direction in Bellingshausen Sea during 2007. Data from ECMWF wind product at 6 hr resolution; a) January; b) February; c) March and d) April. The data was only extracted with a lower latitude limit of 74º S.

Despite the weaker wind stress over the SIZ, a positive net flux of O_2 from the surface ocean to the atmosphere was observed (F_g of 14±7 and 6±10 mmol O_2 m^{-2} d^{-1} for the WIS and MB1, respectively) and biologically produced O_2 (F_{bio} of 37.6±22.4 mmol O_2 m^{-2} d^{-1} for WIS, and 21.1±10.6 mmol O_2 m^{-2} d^{-1} for MB1) (Figure 4.6; Table 4.2). This was due to the observed supersaturation in both ΔO_2 and ΔO_2/Ar (average for the WIS and the MB1; ΔO_2 = 2.4 ± 3.1 % and ΔO_2/Ar = 5.8 ± 3.4 %), indicating the presence of net autotrophy before and during JR165 cruise. To evaluate this hypothesis, estimates of *N* and *G* along with estimation of the diapycnal flux (F_v) and entrainment (F_e) as main controlling transport processes of oxygen (by eddy diffusivity and vertical convection of water, respectively), in the BS are presented in section 4.5.5 and discussed below (section 4.7).

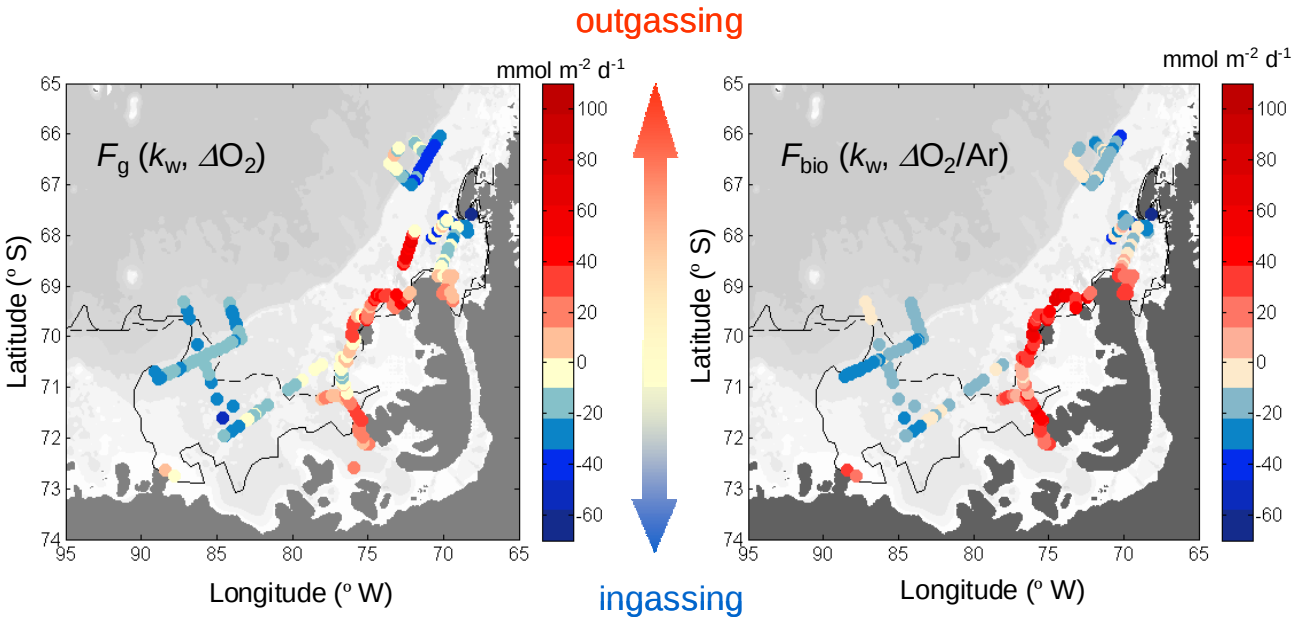

Figure 4.6 – Spatial distribution of the sea-to-air oxygen flux (F_g, left panel) and biological O_2 flux (F_{bio}, right panel) both in mmol O_2 m^{-2} d^{-1}, along the cruise track in the BS. The MIZ location at the beginning (solid black contour) and at the end (dashed black contour) of the JR165 cruise is shown.

4.5.3 Permanent Open Ocean Zone.

The three areas identified in the POOZ were represented by the following CTD stations: BT, 90 to 135 (20 to 24 March, 2007); MB2, stations 199 to 213 (1 to 3 April, 2007) and WAI, stations 214 to 252 (4 to 9 April, 2009). The observed MIZ advance in the POOZ affected mainly the BT area, while the WAI and MB2 areas remained under the open ocean regime during the entire sampling period.

In agreement with observations made by Vernet *et al*., (2008), an onshore-offshore gradient in z_{mix} was observed, with deeper z_{mix} in the POOZ (by as much as 20 m) when compared to z_{mix} in the SIZ region. The mixed layer depths as defined here by the vertical distribution in dissolved oxygen also showed a north-south gradient within the POOZ. Deeper and more variable mixed layers were observed in the WAI (49±15 m), and shallower mixed layers in the MB2 (33±8 m) and in the BT (28±7 m). This could be due to the stronger influence of the northerly winds in the WAI area. As seen before, the wind stress was weaker towards the coast in the more protected areas and towards the central part of the Bellingshausen Sea in the BT area during March and April (Figure 4.5).

As a consequence of being farther away from the coast, less influence of IMW from the ice shelves, coastline and glaciers was noted. Although MB2 is located closer to Adelaide Island, the presence of IMW was not observed near to this coastal feature. The mixed layer in the POOZ subsystem was dominated by AASW, characterized by a wide range of temperatures (from the coldest at −1.4 °C in the BT away from the IMW influence, followed by the MB2 with 0 °C and finally WAI with 0.4 °C) (Figure 4.4c). The latter extended up to 180 m depth lying above the MCDW.

With the data presented here it is not possible to define clearly the maximum extent of the IMW in the continental shelf during the peak of the summer season. However, it could be that as a consequence of high wind stress in the POOZ, turbulent mixing was promoted between surface waters and waters from below. As a result, deeper z_{mix} (Table 4.1) and an earlier invasion of AASW in the upper waters, was evident in contrast to the areas along the coast (Figures 4.4c and d).

The mixed layer in all the areas of the POOZ showed undersaturated oxygen, both in total and biologically produced O_2. The average ΔO_2 was −2.0±0.9 % corresponding to values between 310 to 350 μmol kg^{-1}, and −1.6±0.9 % for ΔO_2/Ar (Figure 4.3, see Table 4.1 for average values per area). The AASW is known to be undersaturated in O_2 by as much as −10 % at the higher temperature and salinity limits (1 °C and 34.5).

In the mixed layer of the POOZ, the lowest oxygen undersaturation was −4 % in the WAI area. The biological O_2 undersaturation, as given by the O_2/Ar ratios indicated the dominance of net heterotrophy or mixing with undersaturated waters.

The gas transfer coefficient was overall two times higher in the POOZ than in the SIZ (average of 2.8±0.4 m d^{-1}). As a consequence, consistent negative F_g and F_{bio} values characterized the BT, MB2 and WAI regions (F_g and F_{bio} averages, −20±10 mmol O_2 m^{-2} d^{-1} and −16.8±10.0 mmol O_2 m^{-2} d^{-1}, respectively).

To discriminate between net heterotrophy and non-biological processes (flux of oxygen by entrainment of subsurface waters and diapycnal flux due to diffusive and turbulent mixing) as controlling factors that could cause the observed "negative biological O_2 flux", first the stability of the water column is evaluated below.

4.5.4 Stability of the water column.

To investigate the stability of the water column during the JR165 sampling period, the square of the buoyancy frequency (or Brunt-Väisälä frequency, ν^2) is calculated, following: $\nu^2 \equiv (-g d\rho / \rho dz)$; where, g is the acceleration due to gravity (9.81 m s^{-2}) and ρ represents the average density in the top 50 m (z) of the water column, these factors multiplied by the change in density in the top 50 m ($d\rho$ / dz) for each region.

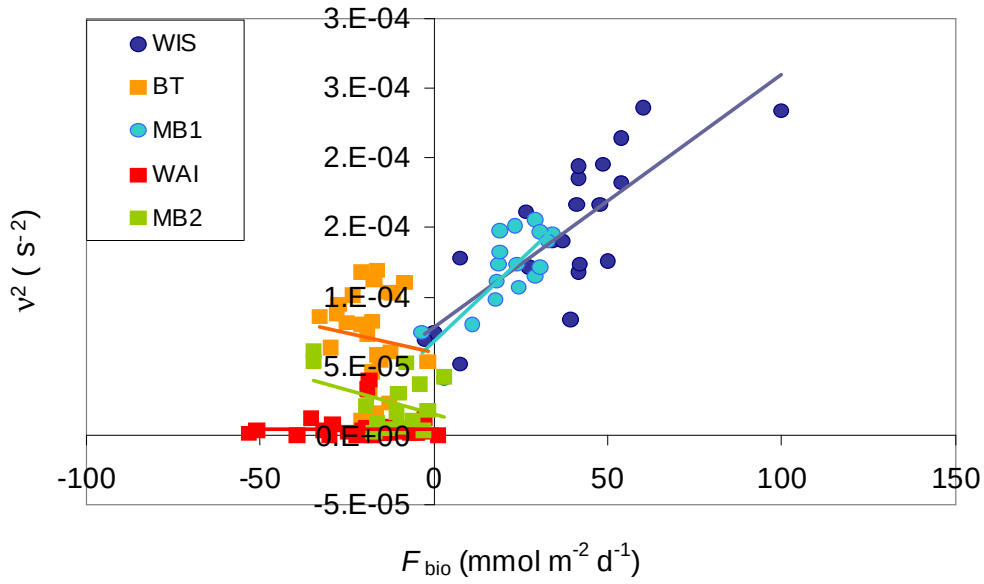

Figure 4.7 – Correlation between the square of the Brunt-Väisälä frequency (ν^2) and the biological oxygen flux (F_{bio}): dark and light blue circles represent the stations located in the WIS and MB1 areas (SIZ); squares in orange, green and red are the stations for the BT, MB2 and WAI areas respectively, in the POOZ.

According to the ν^2, the stability of the water column in the POOZ was four times lower than in the SIZ (Table 4.1). For both SIZ areas, the upper water column was more stable, (ν^2 averaged 1.5×10^{-4} s^{-2} and 1.3×10^{-4} s^{-2} for the WIS and MB1, respectively) than in the areas located in the POOZ (0.8×10^{-4} s^{-2}, 0.2×10^{-4} s^{-2} and 0.0×10^{-4} s^{-2}, for BT, WAI and MB2, respectively) (see table 4.1 for summary of results per area). A positive correlation between ν^2 and F_{bio} only for the SIZ areas (r^2=0.61 for WIS, and r^2=0.63 for MB1) was observed (Figure 4.7) supporting previous observations of the high biological production enhanced by water column stability.

4.5.5 Effect of diapycnal flux (F_v) and entrainment of subsurface waters (F_e) to the biological O_2 production.

The estimated average fluxes (i.e. F_g, F_{bio}, F_v, and F_e) for the areas within the SIZ and the POOZ are shown in Tables 4.1 and 4.2. The F_v was on average −1.5±1.1 mmol O_2 m^{-2} d^{-1} and −3.1±3.0 mmol O_2 m^{-2} d^{-1} in the MB1 and the BT, respectively. A negative F_v indicates that under steady state, the vertical flux of O_2 by diffusivity is from the mixed layer towards subsurface waters. This is due to the gradient of dissolved O_2 with higher concentration in the mixed layer relative to the concentration below it.

In the WIS the evasion of O_2 to deep waters was nearly two times smaller than in the MB1. Besides the exchange with the atmosphere and respiration, the vertical transfer of O_2 to subsurface waters is part of the main O_2 sinking processes to account for in the mixed layer O_2 budget in both the SIZ and POOZ of the BS. If most of the dissolved O_2 measured in the surface water of the SIZ is due to biological processes, then an average of 4 % in the WIS and 15 % in the MB1 of the O_2 produced biologically is exported by vertical diffusion out of the mixed layer.

For the F_e estimates, the Δz_{mix} calculation suggests that in the WIS the mixed layer became 10 m shallower along the peak of the summer season (from early January to the beginning of JR165 cruise in March). This result is consistent with the observations of enhanced water column stability due to the presence of IMW. On the other hand, the MB1 area showed a deepening of about 5 m on average, consistent with the less stable buoyancy frequency for this area as compared to the WIS.

Negative values of F_e, indicates an entrainment of low-oxygenated waters with consequent mixing and decrease in the mixed layer-O_2 concentration.

Following equation 4.2, an entrainment of −3.8±5.5 mmol O_2 m^{-2} d^{-1} was estimated for the MB1 due to the deepening of the mixed layer. The vertical sections of temperature and salinity for this area suggest that the entrained water into the mixed layer was still part of the IMW. The vertical extension of the IMW was up to 50 m depth, which is still in the range of the deeper mixed layer registered for this area (26 m). In the MB1, the entrained flux of oxygen due to the deepening of the mixed layer depth accounted for 18 % of the estimated F_{bio}.

The case of the POOZ is rather more complex. The F_v of O_2 to subsurface waters in the areas beyond the MIZ corresponds to 5 %, 9 % and 8 % of the F_{bio} for the BT, MB2 and WAI, respectively. Most of this could be seasonal O_2 biologically produced and exported out of the surface layers. In all the areas of the POOZ, according to the climatological data z_{mix} was deeper during the sampling time than 30 days before. In the WAI and MB2 the mixed layer was 18 and 21 m deeper, respectively; while in the BT was 8 m deeper (Table 4.1).

In the POOZ the vertical profiles of temperature, salinity and dissolved oxygen indicated that the mixed layer was rather dominated by AASW. The remnant WW is located between 50 and 100 m (where the minimum of dissolved O_2 is also located reaching undersaturation levels up to 30 %) below the mixed layer and the seasonal pycnocline. As can be observed in the vertical sections for temperature, salinity and oxygen for a transect in the WAI area (stations 214 to 227), the WW lay well beneath the mixed layer defined by the surface distribution of O_2 (Figure 4.8).

In contrast, the WW was absent in subsurface waters of the SIZ due to its earlier replacement by the AASW and the IMW during summer. This observation is in good agreement with Garibotti *et al*. (2003) where the authors found the subsurface presence of the WW between 50 to 150 m depth in the WAP region.

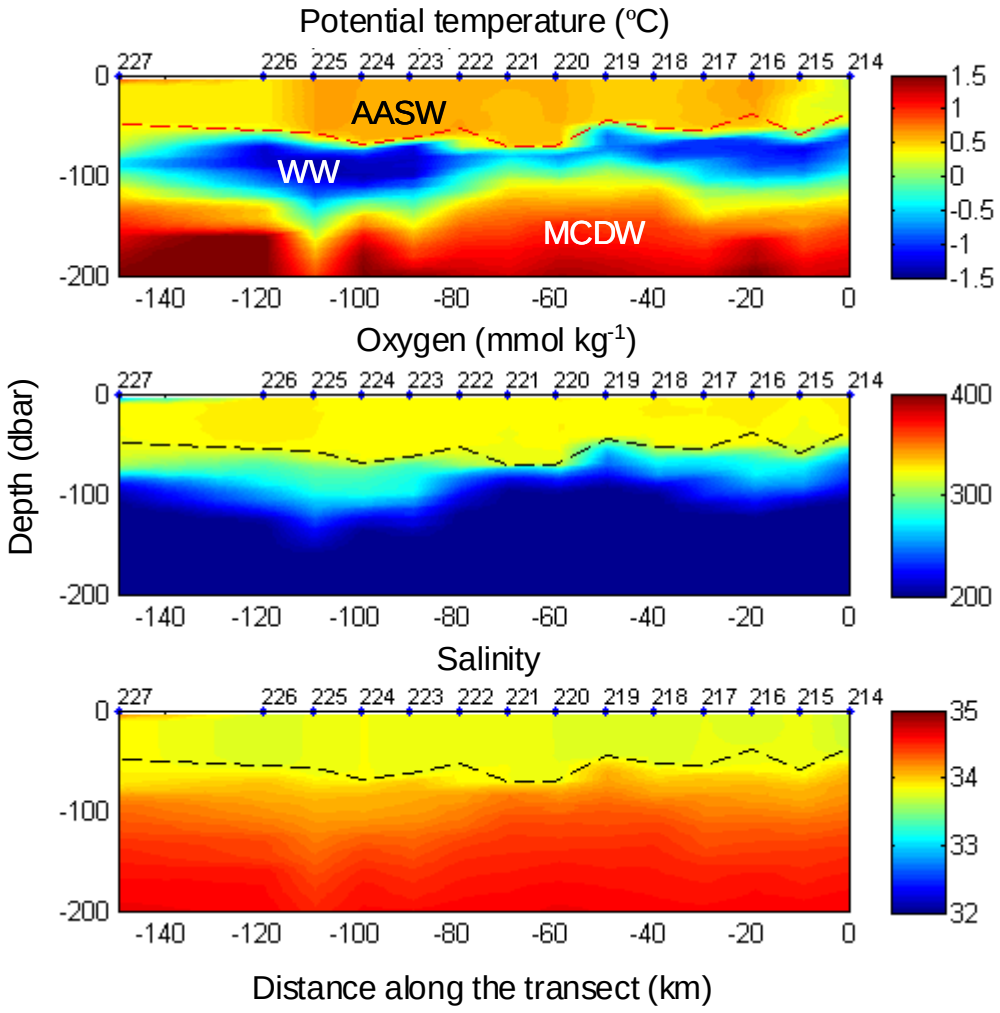

Figure 4.8 – Vertical sections showing the distribution of the water masses in the water column for the transect (stations 214 to 227, location marked in the top of each panel with blue dots) representing the West Adelaide Island area. Top panel, potential temperature, middle panel, dissolved oxygen and bottom panel, salinity. The dashed horizontal line represents the bottom of the mixed layer as defined by the distribution of oxygen. AASW dominates the mixed layer with the WW underlying and the MCDW from 150 m.

From the observations of the distribution of potential density in the mixed layer (Figure 4.9) the presence of the WW is evident in all POOZ areas. As discussed in section 4.5.3, the mixed layer was dominated by AASW from the warmer part in the WIS and MB2 areas to the colder in the BT area. In all the evaluated areas in the POOZ, the deepening of the mixed layer occurred mainly within the extension of the AASW in the water column.

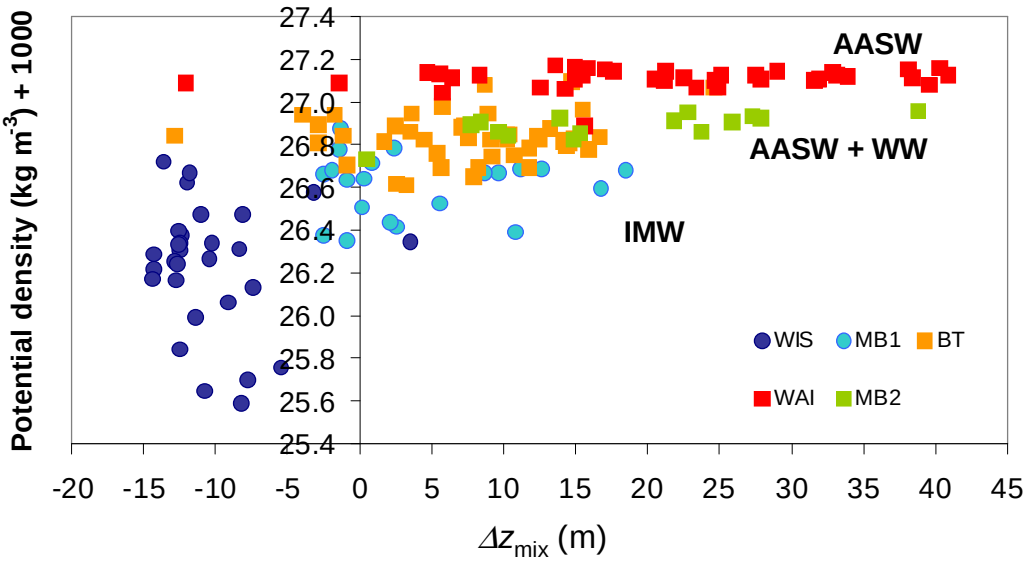

Figure 4.9 – Mixed layer potential density against the change in the mixed layer depth (Δz_{mix}) from 30 days before (from mixed layer depth climatology; de Boyer Montégut *et al.*, 2004) the sampling period for the areas identified. Positive values of Δz_{mix} indicate a deepening of the mixed layer compared to 30 days before.

In the mixing lines given by the distribution of potential density in the mixed layer against Δz_{mix}, the properties of the mixed layer in the POOZ areas correspond mainly to the dominance of AASW (Figure 4.4c). A consistent potential density range between 1026.6 to 1027.2 kg m^{-3} was observed as a result of well mixed upper water in the POOZ areas (Figure 4.9). Therefore, if it occurred, a small portion of the WW could intrude into the mixed layer and mix with the dominant and nutrients-depleted AASW.

From the results of Δz_{mix}, about 4 m of the mixed layer deepening in the WAI area would reach the extension of the WW (Figure 4.8) where the deeper mixed layers during the sampling period were registered. According to Gordon and Huber (1990) the approximate transfer of WW during winter months was about 45 m a^{-1}, bringing O_2 undersaturated waters, salinity and heat into the mixed layer of the Weddell gyre (Gordon and Huber, 1990). Based on the mixed layer from climatology data and for summer-to-autumn months, the transfer of WW into the BS mixed layer calculated here is about 49 m a^{-1}; this value is considering a linear deepening of the mixed layer up to 4 m over 30 days.

Finally, the average flux of O_2 by entrainment of subsurface waters into the POOZ mixed layer is about 13.9 mmol O_2 m^{-2} d^{-1} (Table 4.2) equivalent to 82 % of F_{bio}. Considering the moderate contribution of the diapycnal flux and flux of oxygen by entrainment to the mixed layer in the POOZ, an evaluation of the contribution of these physical processes to the observed negative F_{bio} and the effect to N is shown below.

4.5.6 Influence of F_v and F_e for N estimates.

From the method used here, the F_{bio} is equal to net community production in terms of O_2 (N) if vertical mixing is neglected (Hendricks *et al*., 2004; Reuer *et al*., 2007). However, from the results presented above both F_v and F_e can potentially affect the biological O_2 content in the mixed layer of the BS. Therefore, in order to make a better estimate of N, F_{bio} must be corrected due to the influence of F_v and F_e. Thus, the final N is equal to: $N = F_{bio} - F_v - F_e$ (Table 4.2); this is considering that F_v and F_e are referenced to the mixed layer, while F_{bio} is referenced to the atmosphere (Figure 4.2, equation 4.3).

In the SIZ, N values were positive and the highest productivity observed in the region was located in this zone (WIS, 39 and MB1, 28 mmol O_2 m^{-2} d^{-1}). F_v had an average effect over the total N of 4 % and 11 % in the WIS and MB1, respectively; while F_e contributed to the decrease of N by 14 % due to mixing with low-O_2 waters in the MB1 and had no effect in the WIS.

In the POOZ, the contribution of F_v and F_e to N was more heterogeneous. F_v had a higher effect by removing biological O_2 by diffusion out of the mixed layer of about 28 % of the total N in MB2 and 48 % in the WAI; in contrast to only 8 % in BT. On the other hand the effect of convection of subsurface waters appeared to have a higher effect on N by mixing and dilution with low oxygenated waters in the MB2 and WAI, and moderate effect on BT (Table 4.2).

In summary, about 86 % of the negative F_{bio} value could be accounted for by entrainment of low-oxygen deep waters. A further 8 % were caused by diapycnal mixing. This means that the actual net community production in this area was close to zero or slightly heterotrophic.

Table 4.2 – Flux estimates for the calculation of net community production (N) in the upper mixed layer of the BS, based on the proposed oxygen balance.

Area	F_{bio} [1] (mmol O_2 m^{-2} d^{-1})	F_v [2] (mmol O_2 m^{-2} d^{-1})	Δz_{mix} / Δt [3] (m/d)	F_e (mmol O_2 m^{-2} d^{-1})	N [4] (mmol O_2 m^{-2} d^{-1})	$^{17}\Delta$ [5] (per meg)	G [6] (mmol m^{-2} d^{-1})	N(C)=[N/1.4]×12 (mg C m^{-2} d^{-1})	f(O_2)-ratio (N/G)
Sea Ice Zone (SIZ)									
WIS	37.6±22.4	−1.5±1.1	−0.3	-	39±22	56±25	152±55	336	0.26
MB1	21.1±10.6	−3.1±3.0	0.1	−3.8±5.5	28±12	58±9	122±27	245	0.23
Permanent Open Ocean Zone (POOZ)									
BT	−18.4±6.9	−1.0±0.9	0.3	−5.2±5.4	−12±9	28±9	93±36	-	-
MB2	−12.4±10.9	−1.1±0.9	0.6	−15.3±22.1	3.9±25	25±8	106±20	33	0.31
WAI	−19.6±12.4	−1.6±1.0	0.7	−21.3 ±15.2	3.3±20	24±11	131±91	28	0.21

[1] The biological O_2 flux (F_{bio}) estimates have an error propagation of about 15 %, relying mainly on the uncertainty for the k_w estimates.
[2] The estimates of the diapycnal flux (F_v) had an overall error of 20 % which is mainly due to the eddy diffusivity coefficient following Law et al., 2003.
[3] The rate of change of z_{mix} over the time (30 days) is expressed in meters per day; negative, deeper z_{mix} over time. The entrainment for the MB1 was up to 50 m while for all the POOZ was up to 100 m depth.
[4] $N = F_{bio} - F_v - F_e$; negative values represent a flux out (into) of the ML for F_v and F_e (F_{bio}). The values correspond to the mean per area ± the standard error of the N estimate as the sum of the square root of the standard deviation of each term in the equation.
[5] The uncertainty in the $^{17}\Delta$ values rely in the measurements of the $^{17}O/^{16}O$ and $^{18}O/^{16}O$ measurements; in both cases the δ-values for the air-equilibrated set of samples was about 3 %.
[6] The error propagation for G is about 53 %, relying on the individual uncertainties for k_w, $^{17}\Delta_{eq}$, $^{17}\Delta$, $^{17}\Delta_{max}$ values. According to Luz and Barkan (2000) the $^{17}\Delta_{max}$ had an uncertainty of 6 % (249 ± 15 per meg); following the linear correlation to temperature (Luz and Barkan, 2009) and according to the authors observations, the uncertainty in the $^{17}\Delta_{eq}$ at 3.5 ºC was about 75 % (4 ± 3 per meg; n = 5); the uncertainty is higher as the temperature of the seawater decreases. The $^{17}\Delta$ measured here for air-equilibrated waters had an uncertainty of 45 % (20 ± 9 per meg).

Despite the corrections to N due to the effects of F_v and F_e, the remaining negative N in the BT (−12.3 mmol O_2 m^{-2} d^{-1}) represents net heterotrophy mainly due to the consumption of oxygen by respiration. Particularly in this area, net heterotrophy seemed to dominate with a large negative F_{bio} and only −6.2 mmol O_2 m^{-2} d^{-1} due to F_v and F_e. On the other hand, in the MB2 and WAI, the resulting N was similar and positive (3.9 and 3.3 mmol O_2 m^{-2} d^{-1}) indicating autotrophy over heterotrophy despite the physical effects in both areas (sum of F_v and F_e equals to −16.3 mmol O_2 m^{-2} d^{-1} and −22.9 mmol O_2 m^{-2} d^{-1} for the MB2 and WAI, respectively).

The total fluxes are summarized in the following figure (Figure 4.10). By combined bars, the contribution of each flux is represented for each area.

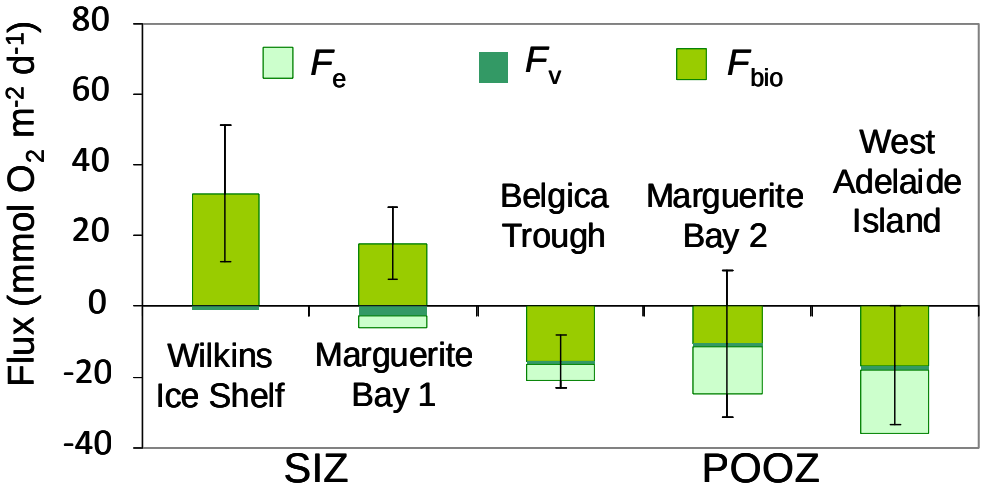

Figure 4.10 – Representation of evaluated fluxes (F_e, F_v and F_{bio} in mmol O_2 m^{-2} d^{-1}) per area in the Sea Ice Zone and Permanent Open Ocean Zone. Negative (positive) values indicate efflux (influx) out (into) of the mixed layer. The error bars represent the error of the N estimates after quantification of physical effects.

The uncertainty in the N estimates presented here accounts for 35 % and is mainly due to the wind speed-dependent parameterization of the gas transfer coefficient (k_w).

The gross oxygen production (G) from $^{17}\Delta$ estimates and f-ratios in terms of oxygen ($f(O_2)$-ratio) were calculated only for positive values of N after the correction by physical effects.

4.5.7 $^{17}\Delta$ of dissolved O_2 in the Bellingshausen Sea.

The highest $^{17}\Delta$ values in the area of study were located in the WIS and MB1, ranging from 31 to 81 per meg (Table 4.1). On average, the $^{17}\Delta$ values were two times smaller in the POOZ (26±9 per meg) than in the SIZ (57±17 per meg). These values are in agreement with the previous observations of the presence of O_2 produced mainly by photosynthesis during the sampling period as given by *N* in the SIZ.

The presence of the fresher and colder IMW into the mixed layer in the WIS and MB1 could have delivered enough nutrients to maintain high productivity levels. To evaluate this, a correlation between the mixed layer potential density and $^{17}\Delta$ values is shown in Figure 4.11. A good correlation (r^2 = 0.59) was observed indicating that at low seawater potential densities (from 1025.7 to 1026.8 kg m^{-3}) corresponded high $^{17}\Delta$ in dissolved oxygen.

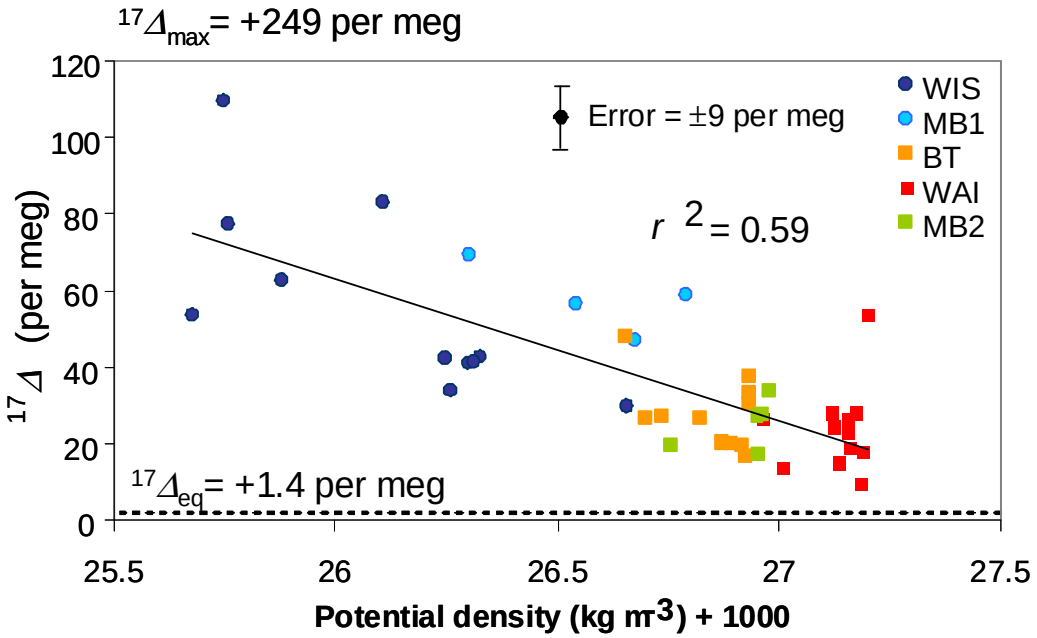

Figure 4.11 – Linear correlation (r^2 = 0.59) between potential density (σ_θ, kg m^{-3}) againstand $^{17}\Delta$ (per meg) in the surface water of the BS. A negative correlation is observed. Dashed horizontal line represents the average of the $^{17}\Delta_{eq}$ (1.4 per meg) in this study from *in situ* temperature (Luz and Barkan, 2009).

Following the linear fit between $^{17}\Delta_{eq}$ and the *in situ* surface water temperature (Luz and Barkan, 2009), the average $^{17}\Delta_{eq}$ for all the area of study was 1.4 per meg (Figure 4.11). In the SIZ, the $^{17}\Delta_{eq}$ was low (1 per meg) from a range of temperatures around

the seawater freezing point encountered in the surface water (−1.2 to −0.9 ºC). A departure of about 56 per meg from the measured $^{17}\Delta$ with respect to $^{17}\Delta_{eq}$ indicating the presence of oxygen produced by photosynthesis in the SIZ.

In the POOZ the values for $^{17}\Delta_{eq}$ were between 1 per meg (in BT) to 2 per meg (in the WAI) due to the wide range the temperatures in this zone (from −1.6 up to 0.5 ºC). Despite the apparent negative biological O_2 production as given by the $\Delta O_2/Ar$ in the POOZ, results for the ^{17}O anomaly in dissolved oxygen are well above the $^{17}\Delta_{eq}$ in both zones, by as much as 25 per meg in the POOZ and 118 per meg in the SIZ (Figures 4.11 and 4.12).

4.5.8 Estimates of *G* and *f*-ratios.

The gross oxygen production (*G*) was calculated from the $^{17}\Delta$ values. In the SIZ, slightly higher *G* values were observed (137±41 mmol m^{-2} d^{-1}) in comparison to the values in the POOZ (110±49 mmol m^{-2} d^{-1}) (Figure 4.12). These values are evidence of the presence of photosynthetic O_2 possibly due to a late phytoplankton growing season along the coast or stored and delivered from the subsurface to upper waters. The *G* values also confirm the importance of the IMW in the SIZ to enhance the marine productivity by providing nutrients and stability to the water column during late summer and early autumn.

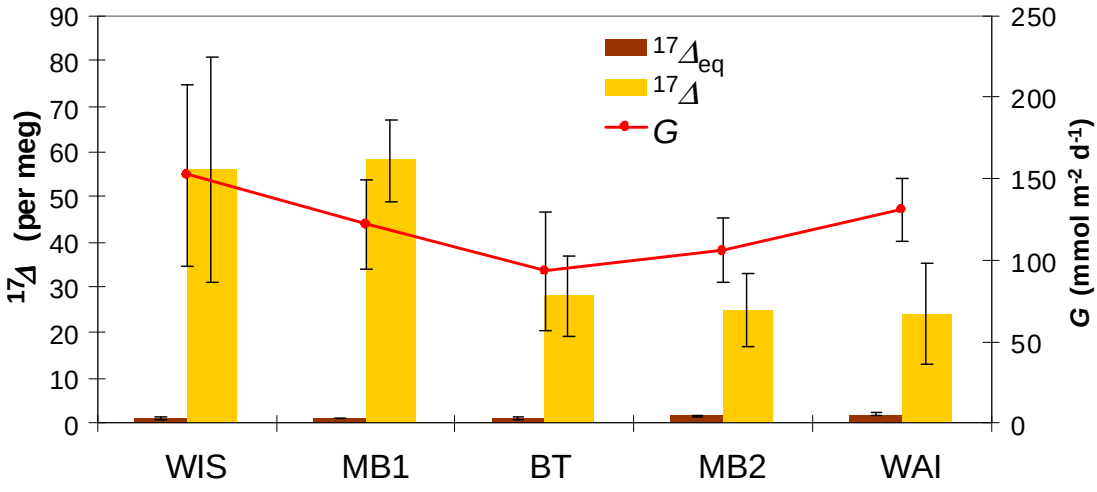

Figure 4.12 – Average of ^{17}O anomaly ($^{17}\Delta$ in per meg, left hand axis) from discrete samples of seawater (yellow bars) collected in the five areas identified in the BS. Brown bars represent the average of the ^{17}O anomaly value in equilibrium ($^{17}\Delta_{eq}$) calculated from in situ temperature (Luz and Barkan, 2009). The average of the gross oxygen production (*G*, right hand axis) is shown in red circles connected with red line. The error bars in all cases indicate ±1 standard deviation of the mean.

To calculate the net production in terms of carbon (N(C)), the N was divided by 1.4 (i.e. N(C) = N / 1.4). The factor 1.4 corresponds to the photosynthetic quotient suggested by Laws, 1991 .

For the WIS and the MB1 a daily community production obtained was 336 and 245 mg C m^{-2} d^{-1}. In the MB2 and the WAI, the production in terms of carbon is 33 and 28 mg C m^{-2} d^{-1}, respectively (Table 4.2).

Considering the z_{mix} at the sampling time as steady state and the gas transfer coefficient (k) at the sampling day (from wind speed recorded by the ship's anemometer), the residence time (τ) of the water in the upper mixed layer areas evaluated here was on average 25 days. Therefore the estimates of marine production presented here represent the biological O_2 produced during that period of time.

The N/G ratio for the areas in the SIZ corresponds to 0.22 and 0.16 for the WIS and the MB1 respectively, while for the POOZ is 0.26 on average for all areas. This fraction in terms of oxygen (f(O_2)-ratio) is similar to the f-ratio proposed by Eppley and Peterson (1979). The f-ratio was defined by the authors from nitrate assimilation and is an indicator of the ability of an ecosystem to retain or recycle organic matter by estimating the relative uptake of new versus total nitrogen (Eppley and Peterson, 1979). Here, f(O_2)-ratio is based on rates of O_2 production and consumption. High f(O_2) values (f(O_2) > 0.5) indicate high N or new O_2 produced by photosynthesis and low f(O_2) (< 0.5) values will indicate that most of the newly produced O_2 is consumed by respiration in the upper mixed layer so the recycling is fast. As discussed by Luz and Barkan (2009), despite the stoichiometric relationship between N(C) and N mentioned above, in the case of gross production in terms of carbon and oxygen in the ocean, there is no direct relationship; therefore, a comparison of the G results from carbon and oxygen measurements is not performed here.

In 2005, f(O_2)-ratios were calculated by Hendricks *et al*. in the equatorial Pacific with a mean value of 0.06 (Hendricks *et al.*, 2005). Reuer *et al.* (2007a) obtained an average value for f(O_2)-ratios equal to 0.13 in some regions of the Southern Ocean during summer. Luz and Barkan (2009) obtained values of 0.08 to 0.21 from samples collected at the site of the Bermuda-Atlantic Time Series (BATS) in the Atlantic

Ocean during May to October, 2000. The results from the present work are a factor of 2 higher; however, the oceanic $f(O_2)$-ratios are rather small and below 0.5.

4.5.9 Inferred Argon supersaturations in the BS.

The argon supersaturation (ΔAr) was inferred from the ΔO_2 and ΔO_2/Ar, according to: $\Delta Ar = (\Delta O_2 - \Delta O_2/Ar) / (1+\Delta O_2/Ar)$. In Figure 4.13, the relationship between the Δz_{mix} and the O_2, O_2/Ar and Ar supersaturations are shown. Because Ar is an inert gas, its concentration in seawater is affected only by diffusive and bubble-mediated gas exchange, pressure and temperature changes, lateral mixing and vertical diffusion. From the results presented here, in the SIZ Ar was equally undersaturated for both the WIS and the MB1 (−3.3 %). The estimated Ar undersaturation is higher than the uncertainty found in the ΔO_2/Ar after the set of air-equilibrated water (0.2 %); therefore, only a small fraction of the uncertainty can be explained by error in the analysis.

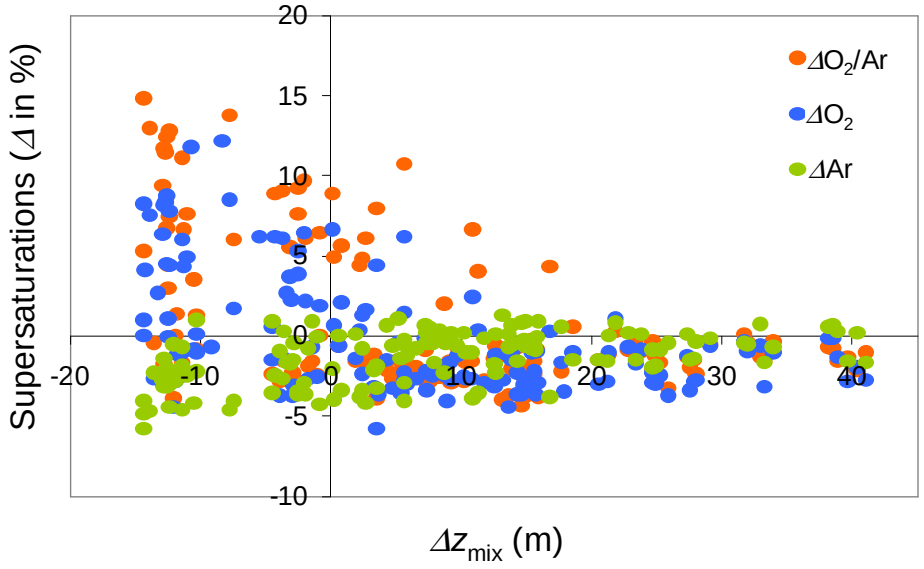

Figure 4.13 – Supersaturation of O_2, O_2/Ar and Ar (%; with respect to equilibrium with the atmosphere represented by zero in y-axis) against the change in the mixed layer depth from 30 days before the sampling period (from mixed layer climatology; de Boyer Montégut *et al.*, 2004). Positive Δz_{mix} indicate a deepening of the mixed layer observed towards the end of the summer compared to 30 days before.

Considering that the observed O_2 supersaturation corresponds mainly to O_2 that has been produced biologically, the presence of Ar undersaturated waters in the SIZ could be due to the the lack of vertical transfer of surface waters and ventilation of subsurface waters in a highly stratified water column in the SIZ. During both

summer, due to the upper presence of sea-ice melt water, and during the formation of new sea-ice towards winter, the Ar saturated surface waters are confined in the upper column of the SIZ. An increase of turbulence and vertical convection, due to an increase of coastal wind speeds, might enhance the transfer of Ar from the atmosphere to deep waters; however, as the rate of melt water production increases in response to higher surface waters temperature in the WAP region, this process is expected to be restricted. Thus, vertical measurements of Ar are needed in order to understand the physical processes occurring in the Antarctic shelf waters and implications to the environment response.

In a study made by Hamme and Emerson (2002) at BATS, the authors found that surface waters are generally supersaturated (by as much as 2 %) with respect to the atmospheric concentration. However, the concentration of dissolved Ar rapidly decreased towards subsurface waters with values up to −3 % in the top 500 m. With the data presented here and the lack of Ar estimates in subsurface waters from the SO, it is not possible to evidence the same vertical Ar distribution as in BATS.

Alternatively, the negative diapycnal flux observed in the shallow and stable mixed layers of the SIZ might also deliver Ar (besides O_2) to subsurface waters. However, the gas diffusion, following the eddy diffusivity coefficient, is a very slow process (on the order of 10^{-4} m s^{-1}) and would account only for a small fraction of the dissolved Ar delivered through the base of the mixed layer.

By contrast, the argon concentration in the POOZ was generally undersaturated, with values close to the equilibrium with the atmosphere (average for all the open ocean areas: −0.4± 0.8 %). This is mainly due to the high turbulent mixing between AASW and a small portion of remnant WW, and the instability created in the water column. From the ΔAr it is therefore possible to confirm the previous observation regarding the importance of vertical mixing and entrainment in the POOZ in the BS continental shelf. Thus, these processes control partially the distribution of the dissolved oxygen and argon in the upper water of the free-ice zone. According to the observations presented here, besides the low O_2 content in the WW, its remnant and subsurface AASW could have undersaturated Ar concentrations that are delivered to the upper waters by physical effects.

4.6 Discussion.

The wind stress over the surface water of the BS plays an important role to control the location of the MIZ. The effect of the continuous wind stress towards the coast of the Wilkins Ice Shelf and Marguerite Bay must have been the main cause of an almost neutral retreat or advance of the MIZ in those areas. As a consequence, the water properties in the SIZ mixed layer remained mostly unchanged during the entire sampling period. Furthermore, the predominant wind direction to the south would have kept the direction of surface waters by Ekman transport towards the coast (deflected to the left of the predominant wind direction) and this must have not being favourable to induce a wind-driven coastal upwelling during the sampling period.

In the POOZ, the structure of the water column was more influenced by the shelf break water mas dynamics (circumpolar currents), such as the entrainment of the UCDW onto the continental shelf from the open ocean CDW. The formation of the MCDW within the continental shelf and below 180 m depth also plays an important role in the structure of the POOZ water column.

In the present study, the stability of the water column (top 50 m) was also used as an indirect indicator of the success of phytoplankton communities. Previous studies, have discussed the importance of water column stability and vertical mixing as controlling factors for the temporal and spatial variability of Antarctic phytoplankton in the WAP region (i.e. Smith *et al.*, 1998; Garibotti *et al.*, 2003; Garibotti *et al.*, 2005b; Vernet *et al.*, 2008).

In 1990, Perissinotto *et al.* suggested that local physical processes in the WAP region control the accumulation and dissipation of phytoplankton communities, being a more important process for marine production than in situ growth (Perissinotto *et al.*, 1990). From the results in this study, the observations made by Perissinotto *et al.* are partially true for the BS area, with a heterogeneous distribution of the marine productivity estimates.

A less stable upper water column was observed in the BT, MB2 and WAI areas compared to the areas in the SIZ. In the SIZ, the observed shallow mixed layers and favourable geographical location being less exposed to the wind stress enhanced the

stability of the water column and success of the biological communities after the peak of the growing season, as noted by the higher productivity along the coast.

In the POOZ, a contribution of stronger wind stress and the lack of lateral advection of fresh water from the ice shelves might have caused a less stable water column. The deepening of the water column also played an important role in the POOZ. According to the mixed layer depth from the historical climatological data, the deepening of z_{mix} in the POOZ towards the beginning of autumn is likely the result of turbulent mixing and convection induced by the strengthening of the wind speed in a less protected area away from the coast.

In the POOZ, the presence of the WW below the mixed layer could have played a key role in the observed negative biological O_2 flux. The deepening of z_{mix} in this zone reached the upper limit of the WW (50 to 60 m) observed below the mixed layer; therefore, the oxygen-depleted and remnant of the denser WW could potentially entrain into the mixed layer and mix vertically with the summer mixed layer. Besides the limitation of irradiance due to the increase of z_{mix}, the turbulence would also induce vertical mixing in the euphotic zone, regulating the photosynthetic activity in the POOZ.

4.6.1 Influence of physical effects over *N* and *G* in the BS.

As a preliminar analysis of the influence of physics in marine productivity estimated by the O_2 budget method, here convective fluxes (by diffusion and convection) at local and small-scale were evaluated. From the observations presented here, the SIZ is characterized as net autotrophic during the sampling period. In the MB1 the observations of the flux of O_2 by entrainment (F_e) due to the depth variability of z_{mix}, along with the export by vertical diffusion (F_v) of (mainly) biological O_2 out of the mixed layer, are in close balance. Particularly, F_e from subsurface waters could be an important process by the import of nutrients from the deeper IMW to sustain a late growing season in the southern entrance of Marguerite Bay.

Despite the resulting positive *N* in the WAI and MB2, the non-biological processes evaluated here seemed to play an important role. In the WAI and MB2, F_v and F_e represented a larger fraction of O_2 to account for *N* with a main contribution due to the entrainment of subsurface waters than the evasion by diffusivity.

In agreement to Serebrennikova and Fanning (2004), Marguerite Bay showed a heterogeneous distribution of net community production. Without considering the physical effects, net heterotrophy seemed to dominate in the northern part of the bay (MB2), while new production due to entrainment of subsurface IMW rich in nutrients in the south (MB1). Serebrennikova and Fanning (2004) observed a nutrients-depleted current along the coast of Adelaide Island and flowing into Marguerite Bay, in the area identified as MB2. This current was observed in autumn during the end of the period with highest biological activity (spring-autumn). The authors observed a strong offshore/inshore trend in the nutrients distribution in the SIZ, with the highest nutrient utilization (and highest marine productivity) inside Marguerite Bay and along the coast of Wilkins Ice Shelf.

Considering the contribution of F_v and F_e in the POOZ (particularly in the MB2 area), the results indicate autotrophy, however it is not excluded the possibility that net heterotrophy accounts also for the observed O_2/Ar undersaturation.

According to Holm-Hansen *et al*., (2005), the predominant zooplankton species in the shelf regions of the BS is the krill *Euphausia superba.* The zooplankton biomass was found to be generally low on the shelf of the BS, with the exception inside and along the coast of MB (Serebrennikova and Fanning, 2004). Smith *et al*., (2008) found the dominance of net heterotrophy in the open ocean zone of the BS mainly due to the presence of dinoflagellates. In this study, only the BT area of the POOZ remained net heterotrophic after considering the physical effects. In this area, the consumption of O_2 by biological processes (i.e. respiration) seems to dominate over the local non-biological processes evaluated here. The O_2 delivered from waters below due to mixed layer deepening was in closer agreement with the loss of O_2 by diffusivity. Therefore, respiration rates can be high in the MB in comparison to the rest of the BS continental shelf; however, physical effects are important to take into account particularly in the MB2.

In terms of the ^{17}O anomaly, the $^{17}\Delta$ values encountered in the POOZ were overall two times smaller than in the SIZ. However, the difference with respect to the ^{17}O anomaly at the equilibrium with the atmosphere indicates the presence of photosynthetic O_2 in the mixed layer during the sampling period in all the study area,

including the POOZ. Physical processes (such as vertical mixing) must have caused the high $^{17}\Delta$ values observed in the POOZ, despite the undersaturated $\Delta O_2/Ar$.

From the *N* values an apparent net heterotrophy is characteristic in the BT of the POOZ, however the ^{17}O anomaly suggests the opposite with values well above the value in equilibrium (Figure 4.12). Similar observations were drawn from Hendricks *et al.* (2004); the authors suggested that the entrainment of oxygen undersaturated waters does not have a large impact on the upper $^{17}\Delta$ because already the O_2 content in the entrained waters is low. The authors assumed that the $^{17}\Delta$ of the added O_2 is probably not far from the equilibrium value. However, the results shown here suggest an incorporation of $^{17}\Delta$ from below the mixed layer as a result of the mixed layer deepening.

Luz and Barkan (2009) observed high values for $^{17}\Delta$ (above the equilibrium value) in samples from the BATS station with the maximum production of $^{17}\Delta$ in the thermocline. The authors suggested that the high $^{17}\Delta$ must have been stored below the mixed layer before it has being delivered to waters above. This might also explain the high ^{17}O anomaly observed in the BS. High $^{17}\Delta$ from photosynthetic O_2 could accumulate during the summer of the previous season (2005/2006) in the remnant mixed layer due to the attenuation of vertical mixing (evidenced by the shallower mixed layers). As the ΔO_2 below the mixed layer is undersaturated (and likely the $\Delta O_2/Ar$ as well) due to the predominant respiration, the signal of high ^{17}O anomaly might not be affected as respiration does not change the isotopic fractionation of the dissolved oxygen. During austral summer, the euphotic zone can be deeper than the mixed layer during some part of the day. Thus, photosynthetic O_2 can remain accumulated underneath the shallow summer mixed layer. As the season progresses and the mixed layer gets deeper towards autumn, the previously stored high $^{17}\Delta$ from the biological O_2 entrains into upper waters.

In the SO, there is still no data available of $^{17}\Delta$ in the vertical column. In 2004, Serebrennikova and Fanning concluded that the nutrient depletion from spring to autumn in the WW on the WAP region is negligible. The authors suggested that, although the WW could suffer erosion from the AASW from above until its replacement in the mixed layer during summer, the remnant underneath maintains its

properties with any significant change on any chemical property during the growing season. Thus, in the BS the high $^{17}\Delta$ in the POOZ could be due to the predominant entrainment observed in this zone of WW onto the AASW in the surface. This process might dominate over a late photosynthetic O_2 production.

4.6.2 Importance of upwelling and lateral advection in the BS.

In this study, upwelling and lateral advection were not included in the O_2 mass balance. However, those conservative processes could contribute also to the O_2 distribution and marine productivity in the upper water of BS.

Upwelling is a complex advective process acting at a regional scale and it is linked to the stress of wind in the surface and divergent Ekman transport. The wind-driven coastal upwelling can contribute to the upward flux of UCDW (Howard *et al.*, 2004). Previous studies have suggested that upwelling can lead to increased biological productivity due to nutrient-rich subsurface waters driven to the surface (Sokolov and Rintoul, 2007) particularly near islands and in the continental shelf of the West Antarctic Peninsula (Prézelin *et al.*, 2004; Jenkins and Jacobs, 2008; Wallace *et al.*, 2008).

The presence of sea-ice is an important factor to limit the wind-driven coastal upwelling in the continental shelf of the BS (Wallace *et al.*, 2008). This might have more effect in the SIZ rather than the POOZ that remains mostly free of sea-ice. Despite mixing rates of CDW to the surface have been observed in large-scale in regions (thousands of meters in the water column) above large topographic features (Sokolov and Rintoul, 2007), few works have tried to elucidate the influence and extent of the CDW into the mixed layer at smaller scale.

In 2008, Jenkins and Jacobs utilized observations of temperature and the ^{18}O isotopic signal as a tracer of glacial water to elucidate the distribution and extent of CDW intrusions in the Marguerite Bay region. Vertical heat and nutrient fluxes from the CDW are delivered to mid and upper waters impacting significantly at the BS continental shelf, particularly in Marguerite Bay and Ronne Entrance. As a consequence, additional contribution to the coastal upwelling beneath the ice and in the BS continental shelf are due to an increase in melting ice and changes in buoyancy of the water during all year (Jenkins and Jacobs, 2008). The authors

estimated a rate of upwelling of modified CDW onto the ML of Marguerite Bay (and beneath the ice shelf) to be 0.1 Sv. This is an average value for the entire ice shelf (~25,000 km^2) leading to a transport of water of 3.4 x 10^4 L m^{-2} d^{-1}. Since this value is based only on observations during one week, possibly this could be the result of intermittent intrusions of CDW into the continental shelf (Klinck *et al*., 2004; Jenkins and Jacobs, 2008).

For an average mixed layer depth of 50 m times the area of the continental shelf, the volume of water contained in the BS mixed layer is about 1.25 x 10^{10} m^3. Thus, considering the previous estimate, only about 0.0008 % of the total volume contained in an average mixed layer would correspond to the CDW delivered by upwelling. How true is this value? How much O_2 is delivered to the BS mixed layer by upwelling of CDW?. These are open questions for further investigations.

Observations of the fluxes of CDW due to upwelling have shown to be associated not only to an increase in subsurface temperature and nutrients but also with low dissolved oxygen concentrations. As the low oxygenated CDW intrudes towards the surface, the oxygen concentration increases due to the mixing of CDW with colder and more oxygenated AASW (Pollard *et al.*, 1995). Alternatively, the upwelling of CDW can also bring high levels of CO_2 to the surface during austral winter (Lenton and Matear, 2007), this contribution has been observed in Bransfield Strait (Bellerby *et al.*, 1995).

In a work published by Smith *et al*. in 2008, the authors concluded that the dynamics in coastal waters of Marguerite Bay might have a stronger influence by upward transport of CDW to the shelf from late summer to fall. High levels of pigment biomass were encountered during the seasonal transition (Smith *et al.*, 2008a). This period of time is coincident with the period of time corresponding to the results of the present study. Furthermore, in the work by Wallace *et al*. (2008) it is suggested that the process of upwelling and presence of oscillations of the water column after atmospheric forcing, are intermittent in the Marguerite Bay area. Observations corresponding to the same sampling time of cruise JR165, from a mooring located in the entrance of Marguerite Bay, the authors concluded that upwelling was only evident in March, but not during the previous two months in 2007.

A study made in the Weddell Sea and published in 2008 by Hewes *et al*. concluded that horizontal mixing can be an even more important process to deliver nutrient-rich waters to the surface rather than the upwelling of subsurface waters. This was observed during austral summer at the coast of Elephant Island and the South Shetland Islands (Hewes *et al.*, 2008).

The strength and periodicity of upwelling at the continental shelf of the BS, thus is still unclear and more studies from moorings or tracers on high spatial resolution, such as oxygen in the present study, can help to elucidate the contribution and effects of this process in surface waters of the BS. Estimates of the rate of upwelling and lateral advection from O_2 measurements must be complemented in the BS O_2 mass balance presented here to evaluate the contribution to *N* of these processes.

4.6.3 Comparison with previous marine production estimates in the region.

From shipboard measurements of ^{14}C in bottle incubations, Vernet *et al*. (2008) estimated an average daily integrated primary production for each January during 12 years (1994 to 2008) in the WAP continental shelf region of 745 mg C m^{-2} d^{-1}. The interannual production showed a maximum value of 1788 mg C m^{-2} d^{-1} in 2006 and minimum registered in 1999 with 248 mg C m^{-2} d^{-1}. An onshore-offshore gradient of the estimated rates of net primary production (*NPP*) was observed particularly in the Marguerite Bay region, with the highest values at the mouth of the bay. The results presented here are in agreement to the minimum limit, and this is probably due to the values obtained in this work represented only the months (March to April) after the peak of the growing season (January).

Arrigo *et al*., (2008) estimated the highest mean daily primary production over a 9 years time series (1997 to 2006) at the shelf of the Bellingshausen and Amundsen Seas of about 316 mg C m^{-2} d^{-1}. Their results are based on remotely sensed ocean color, sea surface temperature and sea-ice concentration data. Their estimates are the highest for this area compared to the pelagic and MIZ zones and the results presented here are in close agreement.

A quantitative comparison of net community production as measured here and other production values estimated from other methods, such as ^{14}C incubations, must be done with caution. The measurements done in this work represent values of net

community production integrated in the mixed layer defined by the oxygen distribution. In contrast, the productivity given by the incubation methods approximates to the primary productivity integrated to the depth of the euphotic zone. Furthermore, satellite data provide net productivity estimates only in the top few centimetres of the water column. Despite these differences, the observations of the present work are in close agreement with the results published by Vernet *et al.* (2008) and Arrigo *et al*., (2008) but only for the WIS area.

High primary production in inshore regions of the WAP, compared to the ones beyond the shelf break, has been also observed previously by other authors (i.e. Smith *et al*., 1998; Garibotti *et al*., 2003; Serebrennikova and Fanning, 2004; Mengesha *et al*., 2008). Particularly, the *G* estimates are in close agreement with the observations made by Agustí and Duarte (2005). The authors estimated a gross primary production for the SO of about 2.05 mmol m^{-3} d^{-1} from O_2 measurements in a microcosm experiment (Agustí and Duarte, 2005). For an average mixed layer depth of 50 m, this value is equivalent to 102.5 mmol m^{-2} d^{-1}. Thus, the presence of net heterotrophic communities plays an important role in the SO marine productivity.

Due to differences in the methods to estimate marine productivity so far applied in the WAP, the comparison to previous values of *N* and *G* in the Bellingshausen Sea is limited to results from the same approach used here. In 2004, Hendricks *et al*. (2004) published results of *N* and *G* using the O_2 budget method for samples collected in the BS during March in 2000. The authors showed a decrease in the *G* values towards the south (70º S) and west (98º W). The average *G* values shown by Hendricks *et al.* were about 25 mmol m^{-2} d^{-1} being about 5 times smaller than the values presented here. This difference is due to the $^{17}\Delta_{eq}$ value used for *G* calculation. The authors considered the standard value of +16 per meg following Luz and Barkan, 2000, while here is used an individually estimated $^{17}\Delta_{eq}$ for each sample depending on their corresponding sea surface temperature (Figure 4.11); therefore, the comparison is limited to the $^{17}\Delta$ values.

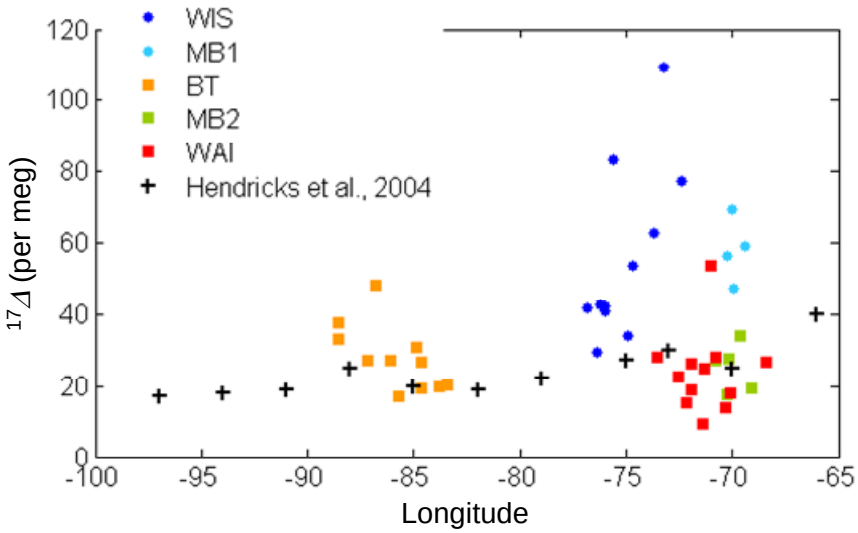

Figure 4.14 – Longitudinal distribution of ^{17}O anomaly ($^{17}\Delta$, per meg) in the Bellingshausen Sea during March to April 2007 (this study; colours represent the identified areas), comparing with results obtained by Hendricks *et al*. (2004) during March, 2000 (black crosses).

In Hendricks *et al*., (2004) a poor spatial resolution of only 11 discrete points were distributed in the POOZ of the BS, with an average 24 per meg for $^{17}\Delta$. Comparable trends on $^{17}\Delta$ values were observed with the results here presented for the areas in the POOZ (Figure 4.14).

4.7 Conclusion.

In this chapter, the first high resolution study (in time and space) of *N* from oxygen measurements in the BS were presented. The distribution of *N* was heterogeneous and limited by the location of the MIZ. Along the BS coast and in the SIZ, *N* was higher representing net autotrophy. In this zone, the stability of the water column played a more important role to enhance the productivity, while the physical processes acting over the surface O_2 distribution seem to play a minor role.

As the rate of melt water production increases due to predicted rise of sea surface temperature and a delay of sea-ice formation by strengthening of winds, the productivity along the BS coast might be also enhanced. By lengthening the growing season towards autumn, implications for sequestration of more carbon from the atmosphere and export to deep waters are also consequences of the increase in the melt water.

From both physical processes evaluated, diapycnal flux by diffusivity (F_v) seems to play a less important role in the BS than entrainment due to vertical convection of low oxygenated waters and mixing (F_e), particularly in the POOZ. However, net heterotrophy may also play an important role in all areas.

The results presented here are estimates of mixed layer productivity as snapshot for the seasonal transition from summer to autumn in 2007 and represent the integration of the time residence (of about 25 days) of oxygen in the mixed layer. Despite the high uncertainty from the *N* estimates (35 %), the method used here was successful to identify the heterogeneity of the marine productivity in the BS. It is strongly suggested that the values must be corrected by the physical processes as evaluated here. Inclusion of upwelling and lateral advection must be also considered in the O_2 mass balance.

Chapter 5

Spatial distribution of net community and gross oxygen production in Drake Passage

5.1 Abstract.

From surface O_2/Ar ratios and the ^{17}O anomaly ($^{17}\Delta$) of dissolved oxygen are here presented mixed layer biological O_2 fluxes (F_{bio}) and gross oxygen (G) production on three Drake Passage (DP) transects (DP1, DP2 and DP3) during summer and autumn 2007. A seasonal transition from late summer to early autumn occurred from the second to the third transect, represented by surface water cooling and deepening of the mixed layer.

The distribution of F_{bio} was associated with the location of the frontal zones and boundaries. The highest F_{bio} value was observed near the Polar Front during mid February (83 mmol m^{-2} d^{-1}) in transect DP1 east of the Shackleton Transverse Ridge. In this site, a value for G corresponds to 208 mmol m^{-2} d^{-1}.

The spatial distribution of F_{bio} north of the Polar Front was characterized to be homogenous (~4 mmol m^{-2} d^{-1}). This pattern was well associated with a deepening of the mixed layer and possible import of nutrients from deeper waters during April. In contrast, in the southern part of DP the variability of the mixed layer was negligible despite the seasonal transition. In this zone, net heterotrophy and the beginning of ice formation seem to be important processes than net autotrophy.

The *in situ* productivity estimates presented here are higher than results previously obtained from *in vitro* techniques. The G values from $^{17}\Delta$ are two fold higher than the values from the ^{18}O incubation method. The net community production in terms of carbon (N(C)) was four fold higher than the productivity from assimilation of ^{14}C obtained in past studies.

The results presented here offer valuable information on *in situ* marine productivity. The high spatial and temporal resolution resolves the fast changes and heterogeneous distribution in a dynamic region such as Drake Passage. This data can also contribute to the improvement of algorithms for productivity models and to the understanding of the role of environmental controls on the marine productivity in the Southern Ocean.

5.2 Introduction.

Drake Passage (DP) is one of the most dynamic oceanic regions in the world and plays an important role for the global carbon cycle. It is geographically located in the Pacific Sector of the Southern Ocean (SO) and represents the narrowest path (≈700 km) (Sprintall, 2003; Barré *et al.*, 2008) of the Antarctic Circumpolar Current (ACC) flowing eastward around the Antarctic continent. Accelerated water flows accompanied by complex topographic features make it a relevant area from the oceanographic and climatic point of view.

The ventilation of deep waters and the sinking of anthropogenic CO_2 in response to convergence of water and subsequent upwelling that occurs in the frontal zones of the ACC are important processes occurring in the DP. Recent changes observed in the oxygen pool in response to surface warming and stratification (Gille, 2002; Keeling and Garcia, 2002) and changes in Southern Ocean winds (Toggweiler *et al.*, 2006) have significant implications on the local marine communities.

The DP is one of the most studied areas in the Southern Ocean. Its water masses and large scale circulation are well defined (Orsi *et al.*, 1995; Sprintall, 2003; Zhou *et al.*, 2010). However, many physical and biogeochemical processes are not completely understood, particularly the meso- and small-scale processes (< 20 km).

For the understanding of the link between the physical and biogeochemical processes in the DP, small scale processes are important including jets, meanders, eddies, regional upwelling, horizontal transport (Zhou *et al.*, 2010) and diapycnal mixing (Thompson *et al.*, 2007). The southern DP is particularly interesting because the Shackleton Transverse Ridge (STR, Figure 5.1) exhibits a heterogeneous distribution of marine productivity due to intense mixing between water masses in this region (Zhou *et al.*, 2010). To the south, a high productive region is present around the South Shetland Islands and Elephant Island. In contrast, to the west of the STR a region of low productivity has been identified due to the presence of the Antarctic Surface Water (AASW). This water mass extends eastward to the southern part of the Scotia Sea with high productivity values (Holm-Hansen *et al.*, 2004; Hewes *et al.*, 2008; Zhou *et al.*, 2010).

Net community and primary production (*NCP* and *NPP*, respectively) in the DP have been quantified using various methods: distribution of chlorophyll from satellite ocean colour measurements (Letelier *et al.*, 1997; Holm-Hansen *et al.*, 2004; Holm-Hansen *et al.*, 2005; Kahru *et al.*, 2007; Sokolov and Rintoul, 2007) on site chlorophyll measurements (Hewes *et al.*, 2009) *in vitro* ^{14}C bottle incubations (Arístegui *et al.*, 1996) and nutrient distribution (Hopkinson *et al.*, 2007; Hewes *et al.*, 2008; Dulaiova *et al.*, 2009). Productivities using oxygen measurements have also been estimated from *in vitro* ^{18}O-labeled discrete water samples (Dickson and Orchardo, 2001) to constrain gross photosynthetic and net community oxygen production (*G* and *N*, respectively).

Common observations in the previous studies are high variability as latitudinal gradients of the water properties limited by the frontal zones. The presence of features such as eddies and jets have also been associated with the productivity distributions. Generally, high surface chlorophyll concentrations have been found in the frontal zones, with highest values (> 500 μg l^{-1}) in the Polar and Subtropical Fronts (PF and STF) respectively.

As discussed in Chapter 1 (section 1.2), the marine productivity estimates from traditional methods (i.e. assimilation of ^{14}C by bottle incubations, satellite observations) rely on various analytical uncertainties. By the limited *in situ* sampling achieved from these methods it is difficult to identify the shorter timescales of productivity changes in the DP. Thus, there is a need to improve the marine productivity estimates, particularly in the SO due to the lack of spatial resolution for the *in vitro* methods, as well as the lack of better *in situ* estimates to validate algorithms and models. Therefore, developing new methods that offer higher spatial coverage on faster time resolution are needed.

High resolution marine biological productivity estimates from surface ocean oxygen-based measurements in the DP are presented here. For this, measurements of continuous surface O_2/Ar ratios were performed to derive biological oxygen sea-air fluxes (F_{bio}) along three latitudinal sections in the DP during summer and autumn of 2007. In a steady state mixed layer (i.e. absence of vertical mixing) F_{bio} can be used as a proxy of *N*. Detailed description of this approach is given in Chapter 1, section 1.8.

To derive gross oxygen production (*G*) estimates, dissolved O_2 isotopologues in the mixed layer from discrete samples were measured. For this, the ^{17}O anomaly ($^{17}\Delta$) is used as a proxy to differentiate between the oxygen produced exclusively from photosynthesis and the dissolved oxygen from stratospheric source. More details about this approach are presented in section 1.10 of Chapter 1. Results for *N* and *G* represent rates of production integrated over the surface mixed layer (z_{mix}) and are complemented with hydrographic data and wind-speed gas exchange parameterizations.

The O_2/Ar and oxygen isotopes method and its fundamentals for *N* and *G* estimates have been thoroughly described (Craig and Hayward, 1987; Luz *et al.*, 1999; Luz and Barkan, 2000) and applied previously in various regions of the world's oceans (Hendricks *et al.*, 2005; Kaiser *et al.*, 2005; Sarma *et al.*, 2006a; Sarma *et al.*, 2006b; Sarma *et al.*, 2008; Luz and Barkan, 2009; Juranek and Quay, 2010). In the DP, a few transects have been done using the same method but were based on sampling of discrete data points only (Hendricks *et al.*, 2004; Reuer *et al.*, 2007a).

The method used here offers a unique perspective on the high variability of the physical and biogeochemical processes occurring in the DP that could not be achieved with traditional productivity tracers. The results from this work resolve fast changes in the dynamic DP region on the order of days and few hundreds of kilometres and contribute to the understanding of the challenging complexity that the DP poses.

The aims of the present work are: 1) to improve the scarce previous productivity estimates in the DP, 2) to evaluate the role of the variability in the mixed layer associated with the seasonal transition and 3) to compare with previous productivity observations in the area. For the last, a comparison to productivity values using the same method here was performed. Between the years 2000 and 2004, results from six DP transects are used to evaluate the inter-seasonal variation of *N* in the DP (Reuer *et al.*, 2007a; Reuer, 2007b) (see description in Table 5.1 and 5.2 in section 5.6.1 below; the geographical location of the transects is shown in Figure 5.7)

Finally, the results from the present work are also compared to previous productivity estimates in the DP from ^{18}O (gross oxygen productions) and ^{14}C incubations and to modelled net primary production (*NPP*) data from surface ocean colour images (Figure 5.8).

5.3 Area of study.

Three transects across the DP were occupied on board *RRS James Clark Ross* (*JCR*) from February to April in 2007. The first DP transect (DP1) was located in the area of the Scotia Sea, for the JR158 cruise in the framework of the ADELIE project (Antarctic Drifter Experiment: Links to Isobaths and Ecosystems), departing from South Scotia Ridge towards the Falklands Plateau in northward direction. The following two transects were part of the JR165 cruise in the framework of the ACES-FOCAS project (Antarctic Climate and the Earth System-Forcing from the Oceans, Clouds, Atmosphere and Sea-ice): **DP2** in southward direction and **DP3** in northward direction. Both transects were from (and to) the Falkland Islands and West of the Antarctic Peninsula (Figure 5.1).

Sampling dates and seasonal stage during the occupation of each DP transect are shown in Table 5.1 (section 5.6.1). The three crossings represent a temporal transition from mid summer (February), after the peak of the growing season, to the beginning of autumn (April).

In Figure 5.1, are also shown the main topographic features: in the southern part of the Drake Passage, the South Shetland Islands (SSI) formed from west to east by Livingston, King George and Elephant Islands; in the central DP the Shackleton Transverse Ridge dividing to the east Ona basin (south) and Yaghan basin (north) and the Drake Passage to the west; as well as Burwood Bank (BB).

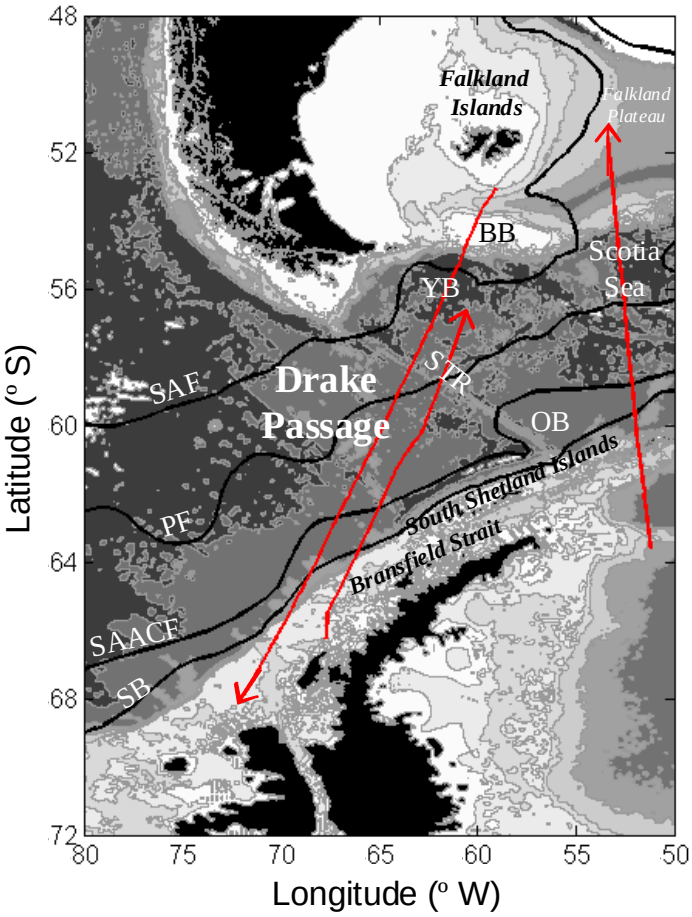

Figure 5.1 – Area of study for the three Drake Passage crosses (red lines) occupied during summer, 2007. From left to right: DP2, southbound from 17 February to 03 March 2007; DP3, northbound from 12 to 15 April 2007 and DP1, northbound from 13 to 15 February 2007. Isobaths at 200, 500, 1000, 2000, 3000, 4000 and 5000 m. Thick black lines represent the climatological location of fronts (Orsi *et al*., 1995) from north to south: SAF, Subantarctic Front; PF, Polar Front; SACCF, Southern Antarctic Circumpolar Current Front and SB, Southern Boundary front. Main topographic features: Yaghan Basin (YB), Ona Basin (OB), Burwood Bank (BB), and Shackleton Transverse Ridge (STR).

5.3.1 Oceanographic characteristics

The DP is limited to the north by the southern part of the American continent and to the south by the Antarctic Peninsula. Its rough bottom topography is characterized by sea mounts and depressions which strongly control the paths of the water masses, currents (Heywood *et al.*, 2004; Naveira Garabato *et al.*, 2004; Zhou *et al.*, 2010) and location of frontal zones (Orsi *et al.*, 1995).

The fronts in the ACC are circumpolar features (jets) flowing eastwards. They are characterized by sharp changes in temperature and salinity, and define the boundary between different water masses in bands of flow or frontal zones where deep convection and consequent upwelling take part. The fast changes across the fronts not only occur in conservative properties, but also in oxygen concentration and biological properties (Zhang *et al*., 2008).

The three main fronts from north to south in the Drake Passage are: Subantarctic Front (SAF), Polar Front (PF) and Southern ACC Front (SACCF). A fourth, and subsurface feature such as the SACCF, is the Southern boundary of the ACC front (SB) (Orsi *et al.*, 1995; Sokolov and Rintoul, 2009). The climatological location of the three main ACC fronts (SAF, PF and SACCF), according to Orsi *et al*. (1995) is shown in Figure 5.1. Locations of the corresponding zones bounded by the fronts are also shown, from north to south: Subantarctic Zone (SAZ), Polar Frontal Zone (PFZ), Antarctic Zone (AZ) and Southern Antarctic Circumpolar Current Zone (SACCZ).

The SAF is defined by Orsi *et al*. (1995) by a change in the temperature of about 4 to 5 °C, and the surface salinity above 300 m is lower than 34.2. This front bounds to the south the Subantarctic Zone (SAZ) characterized by strong convergence and is the transition from subtropical waters to colder Antarctic waters, therefore is an important area for the sink of anthropogenic CO_2 (McNeil *et al.*, 2007).

The PF is on average located between 60° S and 61° S, where the sea surface temperature changes from 4.5 to 2 °C (or a change in ~2.5 °C) over a distance of < 60 km. The PFZ is bounded to the south by the PF and to the north by the SAF, and is characterized by strong lateral mixing and convergence (subduction) with salinity values < 34 and represents the core of the ACC. In this zone one typically finds the presence of mesoscale meanders and eddies (Orsi *et al.*, 1995; Sprintall, 2003; Dulaiova *et al.*, 2009).

During summer, the surface waters of the SAZ and PFZ are dominated by Subantarctic Surface Water (SASW), known for a high concentration of nitrate and low silicate and chlorophyll content (Dugdale *et al.*, 1995). The success and abundance of the biomass in this region is mainly controlled by light and mixed layer

depth as wells as by the abundance of iron and silica (Boyd *et al.*, 1999). South of the PF, the upper water column is dominated by Antarctic Surface Water (AASW). Therefore, the PF is probably one of the clearest fronts to identify in surface waters since it acts as the core boundary between the cold Antarctic surface waters to the south and the warmer Subantarctic waters to the north (Orsi *et al.*, 1995).

The SACCF is a subsurface feature, observed below 500 m and is on average located between 62.5° S and 63.5° S where the temperature drops from 2 to 0.5 °C. This front does not separate surface water masses; therefore the surface between the PF and the Antarctic continental shelf is fully dominated by Antarctic Surface Water (AASW). Salinity gradients are also pronounced in the SAF and SACCF but not for the PF (Orsi *et al.*, 1995; Hendricks *et al.*, 2004).

The Antarctic Zone (AZ) is located south of the PF and up to the SACCF. Here, the Circumpolar Deep Water (CDW) mixes with ice melt and precipitation water to form a fresher AASW that dominates the surface waters of this zone during summer (Chaigneau *et al.*, 2004). By contrast, the Winter Water (WW) dominates most of the AZ mixed layer during autumn and winter.

The Southern Antarctic Circumpolar Current Zone (SACCZ) is located south of the AZ. This zone is bounded by the SACCF to the north and the Southern Boundary of the ACC (SB) to the south. The latter marks the boundary of the Antarctic Continental slope (Orsi *et al.*, 1995; Hendricks *et al.*, 2004).

The Southern Boundary front (SB) limits the northern edge of the Antarctic Continental Zone (ACZ) with the Antarctic continent delimiting the southern edge. It is located where a step change in depth of the continental slope occurs, from 1000 m to 200 m. In this zone, a separate water mass of uniform temperature and low salinity ($S < 33.8$) is found in the upper 500 m (Tomckzak and Godfrey, 1994).

The Antarctic fronts are dynamic features and tend to shift from their mean location as given by Orsi *et al.* (1995). For instance, the PF tends to shift by 50 to 100 km in both north and south directions from its climatological location (Gille, 1994a; Zhang and Klinck, 2008).

Various methods have been applied for the identification of SO fronts such as: advanced microwave radiometer to estimate sea surface temperature (SST) from space (Dong *et al.*, 2006), hydrographic data (Orsi *et al.*, 1995; Thompson *et al.*, 2007), expendable bathythermography and altimetry data (Gille, 1994b; Sprintall, 2003), sea surface height (Sokolov and Rintoul, 2009). Here, the surface location of the SAF and PF from sharp changes in SST at the sampling time is presented. The location of SACCF and SB is induced from the observations of marine productivity.

5.4 Methods.

The mixed layer air-to-sea flux of biological oxygen (F_{bio}) in the DP was estimated from continuous measurements of surface O_2/Ar ratios and further estimates of the biological O_2 supersaturation (ΔO_2/Ar). In the absence of vertical mixing F_{bio} is used as a proxy of net community production (N) in terms of oxygen. The gross oxygen production (G) was estimated from discrete samples for dissolved oxygen isotope quantification and ^{17}O anomaly determination ($^{17}\Delta$). The total flux of oxygen (F_g) was estimated from the oxygen supersaturation with respect to the concentration in equilibrium with the atmosphere ($c_{eq}(O_2)$) (Benson and Krause, 1984; Garcia and Gordon, 1992). All fluxes are integrated over the whole mixed layer depth (MLD) and were estimated by using a weighted gas transfer coefficient (k_w) to account for the historical change of the oxygen in the mixed layer due to changes in the wind speed. A detailed description of the variables estimated in this chapter is presented in the introduction (Chapter 1) and methods (Chapter 2) of this thesis.

The DP transects subject of this study were part of transits between hydrographic stations made for JR158 and JR165 cruises. Thus, no CTD profiles, including data for vertical oxygen, are available for DP1, DP2 and DP3. In the absence of CTD oxygen profiles in the DP transects, the values for MLD were obtained from the World Ocean Circulation Experiment - National Oceanographic Data Center (WOCE-NODC) monthly mixed layer global climatology (de Boyer Montégut *et al.*, 2004). For this data set the mixed layer is defined at the depth where the potential density (σ_θ) is lower than 0.03 kg m^{-3} with respect to the density value at 10 m depth. Details of the comparison between MLDs defined from oxygen profiles and MLDs from the climatological data are shown in Chapter 3. Hereinafter, MLD is referred to as z_{mix}.

The calibration of SST and *S* in the DP transects was done by removing the corresponding offsets as discussed in Chapter 2 (sections 2.2.1 and 2.2.2, respectively). Due to the lack of vertical data, here the vertical contribution of oxygen by physical processes (diapycnal flux and entrainment by vertical convection into the mixed layer) was not evaluated. However their contribution to *N* in the DP should not be neglected. Furthermore, due to the lack of corrections by physical processes here is not approximated F_{bio} to *N* and hereinafter in this chapter will be referred only as to F_{bio}.

5.5 Results.

5.5.1 Identification of Southern Ocean fronts from sea surface temperature.

The locations of the SAF and PF were identified from sharp changes in SST distribution along the three DP transects. Figure 5.2 depicts the latitudinal distribution of SST and the identified location of the fronts. The latter is compared to the climatological position as given by Orsi *et al*., (1995).

The SAF was observed only in DP2, with a change in temperature from 6.8 to 6.1 ºC over a distance of 10 km. This position is about 32 km to the north of the climatological position (Figure 5.2b).

In all three transects, the PF was observed as a clear sharp gradient in temperature over a generally variable latitudinal temperature distribution. This is probably due to the presence of mesoscale eddies, particularly between 55 and 59º S.
For DP1, the location of the PF was around 58º S with a change in temperature from 5.6 to 4.2 ºC. This location was almost 140 km south of the climatological position (Figure 5.2a).

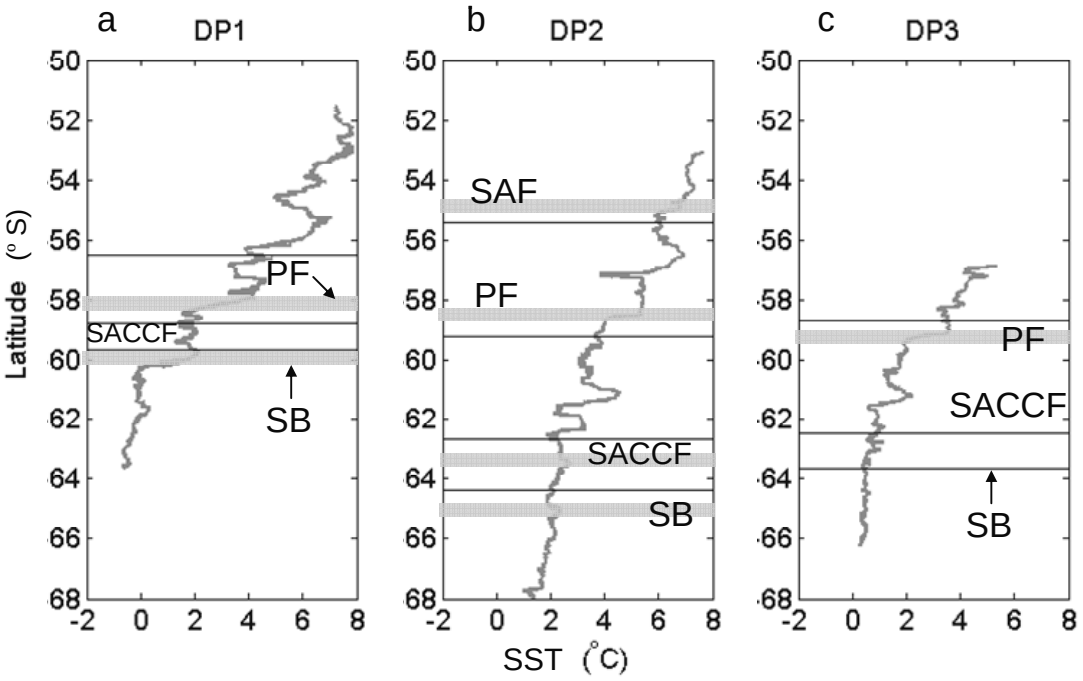

Figure 5.2 – Latitudinal distribution of sea surface temperature (SST in ºC): (a) DP1, (b) DP2 and (c) DP3. Horizontal thin black lines are the climatological location of the fronts according to Orsi *et al.*, 1995; grey horizontal bands are the location of fronts here identified from the SST distribution.

In DP2, the PF was identified as a sharp change in temperature of about 1.1 ºC (from 5.3 to 4.2 ºC) over a distance of 7.7 km. For this transect, the front was located about 71 km to the north with respect to the climatological location (Figure 5.2b).

In DP3, the PF was identified for a similar change in temperature (0.9 ºC) but in a range of colder temperature values (3.5 to 2.6 ºC) over a distance of 6.6 km. Contrary to DP2, the location of the PF in DP3 was to the south from the climatological position at a distance of 54 km (Figure 5.2c).

The shifting horizontal position here observed of the PF with respect to the climatological location is within the range (i.e. between 50 and 100 km) of previous observations by other authors (Gille, 1994a; Zhang and Klinck, 2008). Despite that using the SST in the three DP it is difficult to identify the presence of mesoscale features such as meanders and eddies (scale of 50 to 100 km), in all three profiles evaluated here sharp increase and decrease of temperature along the transects are characteristic. The scale of these gradients covered a horizontal distance of ~10 to 100 km and they were observed consistently within the PFZ and SACCZ where most

eddies are located in the DP. Thus, the observations of these temperature gradients might be an indication of the presence of eddies during the sampling period (K. Heywood, *personal communication*).

Since the SACCF and SB are only subsurface features (<500 m depth), their positions with respect to SST were not clearly identified for all three DP transects. However, in DP1 a strong gradient in temperature around 60.1º S was observed, probably associated with the subsurface influence of SB. If so, it was located at about 48 km to the south from its climatological position (Figure 5.2a). In case of DP2, the SST distribution was variable possibly due to the presence of small features such as meanders. In this case, the locations of SACCF and SB are indistinct (Figure 5.2b).

The spatial distribution of F_{bio} and G for DP1, DP2 and DP3 are shown in the following sections. Their distribution is in good agreement with the location of the frontal zones in the DP.

5.5.2 Inter-seasonal variability of physical properties

A comparison of the latitudinal distribution of SST, salinity (S), mixed layer depth (z_{mix}) and the gas transfer coefficient (k_w) between the three DP transects (Figure 5.3) was performed in order to observe the seasonal transition between the transects within the sampling period.

The transect DP1 was sampled 12 days before DP2 and the SST in the former was generally 1.8 ºC colder than the latter (Figure 5.3a). The salinity changes between DP1 and DP2 are less evident between both transects, except in the PFZ between 58 and 62º S. In the Scotia Sea region (where the DP1 is located) higher salinities were observed (up to 34.5; Figure 5.3b), indicating the presence of different characteristics on the AASW east and west of the STR.

The z_{mix} for both transects during the sampling period (according to the climatological data) did not differ greatly and showed an average value of 41±6 m (Figure 5.3c). In contrast, k_w was on average 0.8 m d^{-1} higher in DP1 than DP2 (Figure 5.3d) due to the higher wind speeds encountered east of the STR.

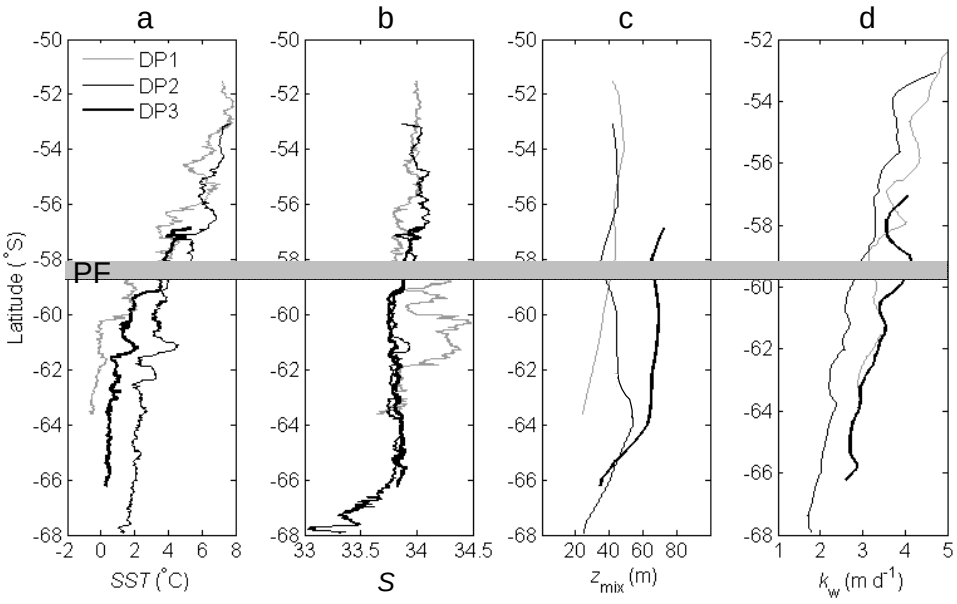

Figure 5.3 – Comparison of the latitudinal distribution between DP1 (grey thin line), DP2 (black thin line) and DP3 (thick black line) for: (a) sea surface temperature (SST), (b) sea surface salinity (*S*), (c) mixed layer depth (z_{mix}) and (d) gas transfer coefficient (k_w). Grey horizontal band indicates the identified location of the Polar Front (PF) for transects DP2 and DP3.

From DP2 to DP3, the seasonal transition between end of summer to autumn was more evident. Both transects were almost parallel with a distance between each other of 100 km (Figure 5.1) and a difference of sampling time of 44 days. Although both transects are not located exactly in the same geographical position, similar latitudinal patterns in the hydrographic properties is expected. South of 60º S, the latitudinal distribution of SST and *S* show similar structural patterns with meanders and eddies in the SAACZ (Figure 5.3a and b). Despite the identified similar features between DP2 and DP3, a constant decrease of temperature of about 2.4 ºC from DP2 to DP3 was observed. This was due to the formation of WW and the surface water cooling. As a response, the increase in wind speed at the beginning of autumn is translated to a higher gas transfer coefficient (mean offset of 0.75 m d^{-1}) during DP2 (k_w = 3.7 m d^{-1}) than during mid summer in DP2 (k_w = 2.9 m d^{-1}) (Figure 5.3d). As a consequence, according to the mixed layer climatology the z_{mix} in the SAZ, PFZ and AZ (up to 64º S) deepened by as much as 26 m in 44 days; from early March in DP2 (median of z_{mix} of 68 m) to mid April (median on the z_{mix} values of 43 m) in DP3 (Figure 5.3c). By contrast, in the SACCZ the depth of the mixed layer remained

almost constant during the sampling period. The changes observed in z_{mix} and k_w are expected to have direct implications over the conservative properties, as well as over the spatial distribution of the fluxes of total oxygen, biological oxygen and gross oxygen production. The observations for these variables are described in the following sections.

5.5.3 Latitudinal distribution of air-to-sea fluxes of total (F_g) and biological oxygen (F_{bio}).

The spatial distribution of the oxygen supersaturation (ΔO_2) and biological oxygen supersaturation (ΔO_2/Ar) are shown in figure 5.4a and b respectively. The corresponding fluxes (i.e. F_g and F_{bio}) are shown in figure 5.4c and d respectively.

In agreement with previous observations (Hendricks et al., 2004; Reuer et al., 2007; Cassar et al., 2008), a strong latitudinal gradient in the oxygen supersaturation and biological oxygen supersaturation was observed. This was also observed for k_w, where the highest values were found north of the SAZ compared to the lowest in the SACCZ close to the Antarctic continent (Figure 5.3d). High spatial resolution observations for ΔO_2/Ar (300 m) and ΔO_2 (100 m) allowed the identification of strong gradients between the DP frontal zones and transects. Results for each zone are presented below.

a) Subantarctic Zone (SAZ)

Only during DP2 data for ΔO_2 and ΔO_2/Ar in the SAZ it was collected. Within this area, the lowest ΔO_2/Ar was observed in the SAF (−3 %) around 54º S, corresponding to a negative biological O_2 flux (F_{bio} = −36 mmol m^{-2} d^{-1}). A similar pattern is observed in the ΔO_2 and F_g distributions (Figure 5.4). A heterogeneous distribution of mixed layer biological oxygen is observed with ΔO_2/Ar values ranging from slight under to super-saturations (−3 % to 1.8 %) in a spatial structure of alternate oxygen super- and under-saturations over a horizontal distance of 200 km. During DP2, shallow mixed layers (40 m) were still present, therefore the variability in the surface oxygen distribution might be the result of mesoscale structures such as eddies or meanders typical of this zone. Such mesoscale features are the result of steep changes in the topography of the region from the deep Yaghan basin (YB) (> 4000 m) to the shallow (< 200 m) Burwood Bank (BB) (Figure 5.1).

Therefore, it is expected that the physical processes have a strong control over the distribution of the productivity. In the SAZ for the three DP transects, the k_w values were between 3 to 5 m d^{-1}, with a clear decrease with increase on latitude (Figure 5.3d).

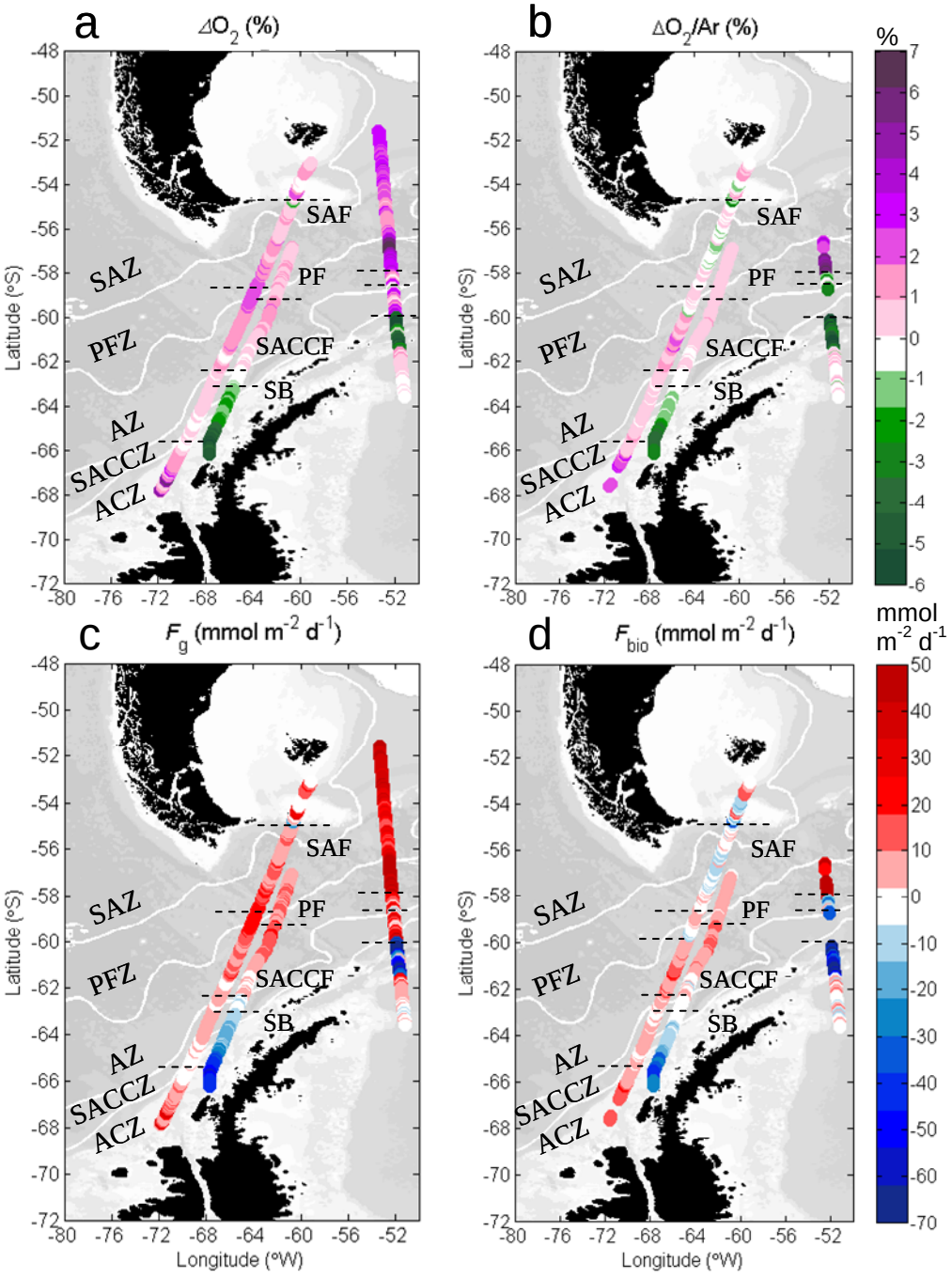

Figure 5.4 – Spatial distribution of: a) dissolved oxygen supersaturation (ΔO_2); b) biological oxygen supersaturation (ΔO_2/Ar)c) sea-to-air flux of oxygen (F_g) and d) flux of biological oxygen (F_{bio}) during DP1, DP2 and DP3. White lines indicate the climatological location of fronts; thin dashed horizontal black lines represent the location of fronts as identified in the present study. In all panels are shown the location of the frontal zones bounded by the fronts, from north to south: Subantarctic Zone (SAZ), Polar Frontal Zone (PFZ), Antarctic Zone (AZ), Southern Antarctic Circumpolar Current Zone (SACCZ) and Antarctic Coastal Zone (ACZ).

b) Polar Frontal Zone (PFZ)

From the spatial distribution of the oxygen supersaturation and fluxes (Figure 5.4), a contrasting pattern is observed east and west of the STR. The distribution of ΔO_2 was positive in the three DP transects, however during DP1 is five fold higher (6 %) than the average values for DP2 and DP3 (0.5 to 2 %). The spatial distribution of O_2 in the PFZ is more homogeneous than in the SAZ, except for DP1 where a north to south gradient in the ΔO_2 distribution was observed with the highest values towards the Falklands Plateau and lower values approaching the PF east of the Scotia Ridge. ΔO_2 was up to 7.4 % in the region where the climatological PF is located (Figure 5.4a). In this front, as upwelling and vertical mixing bring nutrients to the surface, most of the ΔO_2 could have been from biological origin due to autotrophy.

In agreement with previous observations (Zahn *et al*., 2010), higher productivities are normally encountered in the Scotia Sea east of the STR where the AASW exhibits a higher concentration of nutrients. Unfortunately, due to analytical problems with the MIMS on board, no data was acquired for continuous O_2/Ar ratios at the PFZ during the DP1 transit. However, three discrete samples were collected for analysis of O_2/Ar in this zone and the results show a positive biological O_2 supersaturation (1.9±1.0 %) confirming that in the mixed layer of the PFZ most of the observed supersaturated oxygen is from biological sources during DP1.

The biological O_2 supersaturation showed a contrasting pattern between DP2 and DP3. During DP2 in mid summer, shallow mixed layer depths (42 m) (Figure 5.3c) were present. A heterogeneous distribution of ΔO_2/Ar (from −1.5 % up to 1 %) indicates a slight biological O_2 production with intervals of O_2 consumption by heterotrophy or interaction of physical processes (Figure 5.4b). The F_{bio} estimates in this zone led to values between −15 to 0 mmol m^{-2} d^{-1} (Figure 5.4d).

In the PF during DP2 (between 57.7 and 58.5º S), the oxygen concentration in surface waters (both total and biologically produced) increased from north to south (Figures 5.4a and b). This translates to a positive band of F_{bio} in the PF (up to 8 mmol m^{-2} d^{-1}) (Figure 5.4d). Despite positive values that were observed in the PF for ΔO_2 and ΔO_2/Ar, only half of the ΔO_2 corresponds to biological processes. The remaining supersaturated oxygen in the PF might be due to the low SST and

entrainment of bubbles from the atmosphere bringing more dissolved O_2 in the surface waters with respect to the atmospheric concentration.

In DP3 during autumn, the ΔO_2 in the PF (between 57 and 61.5º S) was also supersaturated, with the highest values (2.9 %) where the steeper gradient of temperature was observed. As in DP2, oxygen undersaturated waters were identified north and south of the front (0 %< ΔO_2 < 1 %). Interestingly, 44 days later F_{bio} in the PFZ was higher during DP3 than during DP2. In the PFZ a homogeneous F_{bio} distribution (5±2 mmol m^{-2} d^{-1}) was observed during autumn compared to the heterogeneous distribution during mid summer.

c) Antarctic Zone (AZ)

The distribution of F_{bio} and F_g in the AZ, show a similar pattern within the three DP transects and between each other. Total and biological O_2 supersaturations were observed. The highest values of ΔO_2/Ar (up to 6.3 %) and F_{bio} (80 mmol m^{-2} d^{-1}) were observed during DP1 in comparison to DP2 and DP3. These values also correspond to the highest biological oxygen production observed for the three transects (Figure 5.4b and d).

During DP2 and DP3, the ΔO_2 and ΔO_2/Ar in the AZ had a homogeneous spatial distribution. Values between 0.1 to 1.3 % for ΔO_2/Ar (F_{bio} = 10±6 mmol m^{-2} d^{-1} for DP2 and 7±3 mmol m^{-2} d^{-1} for DP3) and 0.3 to 1.5 % for ΔO_2 (F_g = 11±3 mmol m^{-2} d^{-1} for DP2 and 11±6 mmol m^{-2} d^{-1} for DP3). Thus, in surface waters of the AZ most of the excess dissolved oxygen is of biological origin.

d) Southern Antarctic Circumpolar Zone (SACCZ) and Antarctic Continental Zone (ACZ)

The location of the SACCF and SB fronts has been a clear influence over the distribution of marine biomass in surface waters, by delimiting zones with high phytoplankton abundance from less productive waters. The ΔO_2 and F_g are higher in the SACCZ of the DP1 than in DP2 and DP3 by as much as 5 % and 46 mmol m^{-2} d^{-1}, respectively. The spatial distribution of F_{bio} is generally homogeneous during both DP2 and DP3, ranging from 0 to 3 mmol m^{-2} d^{-1}. Undersaturated biological O_2 (ΔO_2/Ar up to −11.7 % at 60º S) was observed in the ACZ and extending up to 62º S;

this might be an indication of the apparent dominance of oxygen consumption by respiration in this zone.

During DP1 and DP3, the SB is represented by a step change in the biological oxygen supersaturation at about 60º S from autotrophic waters in the AZ to heterotrophic waters in the ACZ. This change coincides well with the climatological location of the SB front. During DP3, the $\Delta O_2/Ar$ is as low as −4 % (−44 mmol m^{-2} d^{-1} for F_{bio}) at the southernmost limit of the transect (65.7º S).

In contrast, during DP2 the biological production of O_2 seemed to be still active in the ACZ. The highest productivities along this transect were found in this zone (19 mmol m^{-2} d^{-1} at 66º S) enhanced by the influence of the lateral advection of coastal waters from icebergs and sea-ice during summer from the coast of Antarctic Peninsula. The same coastal influence seemed to have occurred south of 61.6º S in DP1, where F_{bio} increased to 0.9 mmol m^{-2} d^{-1} (Figure 5.4b). From the previous observation, the variability of the mixed layer depth seems to play an important role over the productivity in the surface waters of the DP. This is evaluated in the following section.

5.5.4 Influence of deepening of the mixed layer over F_{bio}

The change in F_{bio} ($\Delta F_{bio} = F_{bio}$ (DP2) – F_{bio} (DP3)) with respect to the change of z_{mix} ($\Delta z_{mix} = z_{mix}$ (DP2) – z_{mix} (DP3)) between DP2 and DP3 was calculated to evaluate the influence of the deepening of mixed layer towards autumn over the mixed layer oxygen production (Figure 5.5). The latitudinal distribution of Δz_{mix} and ΔF_{bio} are similar, with smaller values in the north and an increase towards south.

The negative Δz_{mix} indicates that z_{mix} was deeper towards April with respect to the summer mixed layer. A bigger change between z_{mix} occurred in the northern DP, corresponding to the SAZ and PFZ. This led to a decreased of F_{bio} possibly due to the dominance of net heterotrophy and/or convective mixing leading to an apparent consumption of biological oxygen during beginning of March in the SAZ and PFZ.

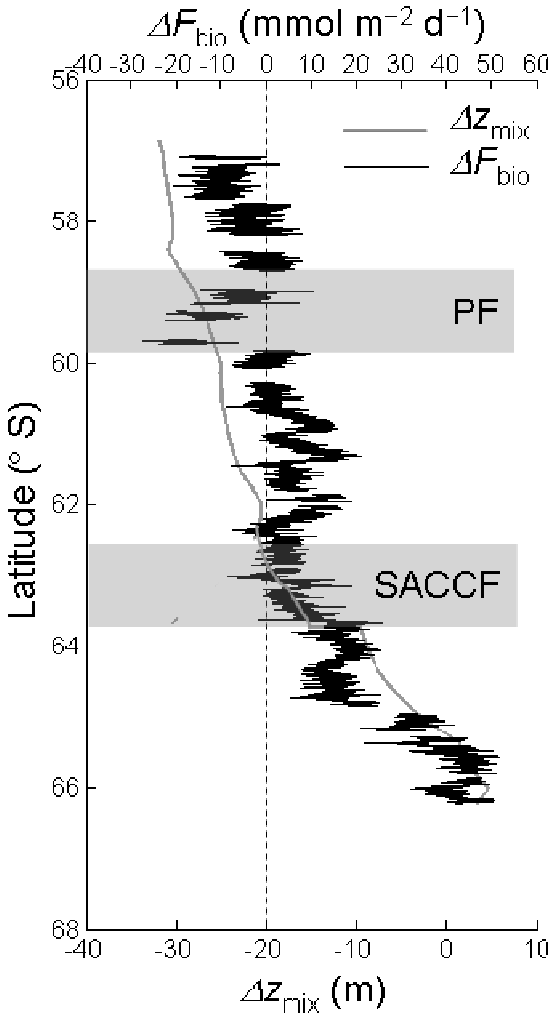

Figure 5.5 – Latitudinal distribution of the change of mixed layer depth (Δz_{mix}) (bottom axis) and the change of flux of biological oxygen (ΔF_{bio}) (top axis) from mid February (DP2) to mid April (DP3) in 2007. Grey thick bands represent the location of the Polar Front (PF) and the Southern Antarctic Circumpolar Current Front (SACCF).

In the SACCZ and ACZ, Δz_{mix} increased towards south, as indicated by the lack of change in the z_{mix} from summer to autumn. ΔF_{bio} is more positive towards south, as a response of higher F_{bio} during DP2 associated with stable and shallow z_{mix} that remained until mid autumn.

5.5.5 Latitudinal distribution of ^{17}O anomaly and gross O_2 production.

The ^{17}O anomaly ($^{17}\Delta$) was calculated from the isotopic abundance of dissolved oxygen in discrete samples (equation 1.18, Chapter 1) from the surface ocean collected along the three DP chapters. Details of the analysis (section 2.6.2, Chapter 2) and calculations (section 2.9, Chapter 2) are described in the methods chapter of this thesis.

The gross O_2 production (G, in mmol m^{-2} d^{-1}) integrated in the mixed layer was estimated from the $^{17}\Delta$, k_w and $c_{sat}(O_2)$, $^{17}\Delta_{max}$ and $^{17}\Delta_{eq}$ (equation 1.19, section 1.10.4, Chapter 1). The $^{17}\Delta$ was well above the estimated $^{17}\Delta_{eq}$ in all three transects, indicating the presence of photosynthetic oxygen in the mixed layer during the sampling time. Although the continuous data for $\Delta O_2/Ar$ was only acquired up to 57º S during DP1 and DP3, three seawater discrete samples, for each transect, were collected for the ^{17}O anomaly analysis north of this latitude (Figure 5.6).

The latitudinal distribution of $^{17}\Delta$ and G shows a similar pattern for DP1 and DP3, while DP2 is generally homogeneous south of 546º S. Similar latitudinal features to the distribution of F_{bio} were observed, despite the discrete samples for oxygen isotopic analyses were sparse (average collection time of 6 hrs between samples).

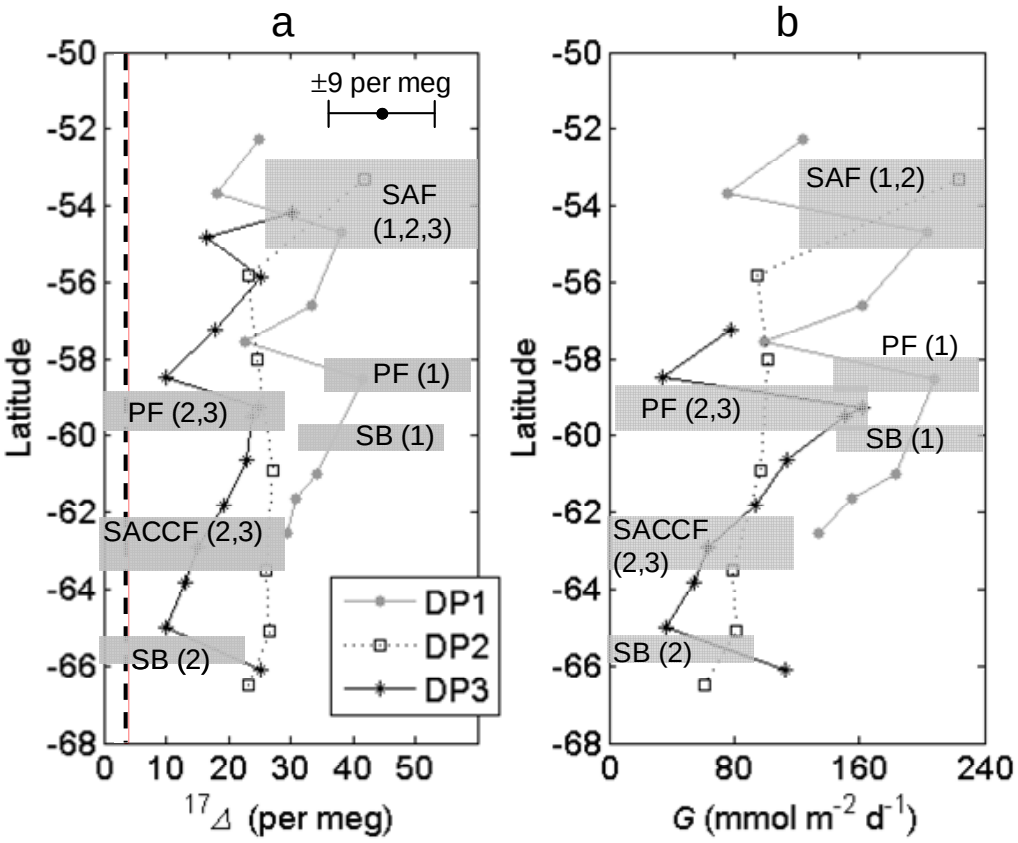

Figure 5.6 – Latitudinal distribution of a) $^{17}\Delta$ from discrete samples along DP1, DP2 and DP3; top right, black circle with error bars indicates the precision of the measurements (±9 per meg) as given by the air-equilibrated water analysis; vertical black-dashed line represents the average ^{17}O anomaly of dissolved oxygen at equilibrium with the atmosphere ($^{17}\Delta_{eq}$ = 3.8±1.5 per meg) calculated from in situ temperature (θ); b) gross oxygen production (G) estimated from $^{17}\Delta$ and k_w.

High values of $^{17}\Delta$ and *G* were found in the northern section of the transects with average values for the three transects of (35±9) per meg for $^{17}\Delta$ and (129±85) mmol m^{-2} d^{-1} for *G* (Figure 5.6a and b). These maxima values might be due to the presence of eddies in the SAZ (as observed in the SACCF), enclosing high biomass concentration in an area typically dominated by low productivities due to the convergence of surface waters.

High *G* values in the PF of the three DP transects were observed in good agreement to the observations for the spatial distribution of F_{bio}. In this area it was identified the highest *G* corresponding to DP1 in mid summer (208 mmol m^{-2} d^{-1} and 42 per meg for $^{17}\Delta$). This value was four times higher than the one observed in the same location during DP3 in autumn (48 mmol m^{-2} d^{-1} and 25 per meg for $^{17}\Delta$).

In DP1 and DP3, a negative north-to-south gradient for $^{17}\Delta$ and *G* was observed within the PFZ, SACCZ and AZ. A less steep gradient was observed along DP2. During DP1 the higher values of *G* (149±46 mmol m^{-2} d^{-1}) were observed, followed by a decrease by as much as 37 mmol m^{-2} d^{-1} in DP2 and 44 mmol m^{-2} d^{-1} for DP3 (112±54 mmol m^{-2} d^{-1} and 105±45 mmol m^{-2} d^{-1}, respectively). This trend was also observed from the latitudinal distribution of F_{bio} (from the corresponding discrete samples) with 16±12 mmol m^{-2} d^{-1} for DP1, 11±5 mmol m^{-2} d^{-1} in DP2 and 7±4 mmol m^{-2} d^{-1} in DP3. For this calculation the negative F_{bio} values observed, mainly in the SACCZ and ACZ during DP3, were not taken into account.

In the next sections are shown the average values for F_{bio} and *G* per zones in the three DP transects. A comparison to previous productivity results in DP is also shown below.

5.5.6 Estimates of *f*-ratios from F_{bio} and *G*

The ratio between F_{bio} and *G*, as analogy to the *f*-ratio defined by Eppley and Peterson (1979) was calculated. The latter was defined by the authors from nitrate assimilation and is an indicator of the ability of an ecosystem to retain or recycle organic matter by estimating the relative uptake of new versus total nitrogen (Eppley and Peterson, 1979).

Despite in this chapter no corrections due to physical processes were done to better approximate F_{bio} to N, this approximation is done in order to calculate the f-ratio in terms of O_2 (i.e. $f(O_2)$-ratio = F_{bio} / G). Here, $f(O_2)$-ratios are based on rates of O_2 production and consumption (Luz and Barkan, 2009) where high $f(O_2)$ values (> 0.5) indicate high or new O_2 produced by photosynthesis and low $f(O_2)$ values (< 0.5) will indicate that most of the newly produced O_2 is consumed by respiration and a dominance or grazing pressure by heterotrophers. In the DP, the $f(O_2)$-ratios were generally low (< 0.2). The average values per transect were 0.13±0.10, 0.11±0.08 and 0.07±0.02 for DP1, DP2 and DP3, respectively.

5.6 Discussion.

The distribution of F_{bio} and G in the DP are heterogeneous and each zone represented different environment where physical processes seemed to control the observed productivity.

In the SAF deep convective mixed layers (>500 m) occur during winter and relatively shallow mixed layers during summer. The deep mixed layers are subducted northward moving to subtropical waters and therefore this is an important zone for the ventilation of surface waters. According to McNeil *et al*. (2007) the SAF and SAZ act as sink of CO_2, controlled mainly by the strength of the meridional Ekman transport across the PFZ (McNeil *et al.*, 2007). From the heterogeneous surface distribution of ΔO_2/Ar and ΔO_2 in the SAZ, the vertical convection might also play an important role over the productivity of this dynamic zone.

In agreement to the high F_{bio} observed in the PF, previous works have characterized this area by the presence of phytoplankton blooms and high chlorophyll concentrations. This is due to cross-frontal mixing and upwelling of subsurface waters induced by mesoscale structures such as meanders, bringing nutrients into surface waters (Moore and Abbott, 2002). In the PF, silica concentrations are high during winter and spring and low during summer, particularly north of the front (i.e. in the PFZ) (Hutchins *et al.*, 2001) where it has been observed a low diatom growth (Boyd *et al.*, 2001; Moore and Abbott, 2002).

In contrast to the PF, the PFZ is characterized by convergence of surface waters and convective mixing. The surface waters of the PFZ are dominated by the AASW and are generally less productive than the waters located ad the front (Boyd *et al.*, 1999; Moore and Abbott, 2002).

In the AZ, F_{bio} showed a homogeneous regional distribution even during the transition from summer to autumn. The AZ is characterized by upwelling of warm and saltier Circumpolar Deep Water (CDW) during most part of the year. The typical divergence in this area is due to the compensation of the equatorward Ekman transport. The AZ is also characterized by stable mixed layers which favours the biological production (Chaigneau *et al.*, 2004; McNeil *et al.*, 2007). Although the upwelling CDW can bring low oxygen, the delivery of high content of nutrients to the surface waters of the AZ appeared to be a dominant process to sustain the high productivity during summer and towards autumn. The observed deepening of the mixed layer from DP2 to DP3, appear to not have a strong influence over the marine productivity in this zone; however, this process might help to sustain the late growing season in this zone. McNeil *et al*. (2007) observed that in the AZ is where much of the CO_2 outgases to the atmosphere due to the wintertime ventilation of deep waters. Contrary, the AZ acts as an important sink of CO_2 during summer. The results here presented agree with this observation, leading to a high net oxygen production by photosynthesis observed during the DP transects from summer to autumn by the biological assimilation of CO_2.

From the results in the PFZ and AZ two main observations can be drawn: 1) during mid summer, despite the presence of more stable and shallow mixed layers, the PFZ PF and AZ exhibit a heterogeneous distribution in the surface oxygen concentrations. Low biological production is present in the PFZ, while high productivities are located in the PF and AZ; 2) towards the beginning of autumn, the mixed layer deepened in the SAZ, PFZ and AZ favoured by the strengthening of winds. An increase in turbulence and delivery of nutrients from deep waters leads to “new production” in a homogeneous mixed layer. The observations here presented support that the dynamics of the mixed layer play an important role to sustain the productivity and late growing season in the PFZ and AZ towards the beginning of autumn.

South of the AZ the increase in productivity, as given by F_{bio} in the SACCF, might be due to the presence of mesoscale structures as eddies. The latitudinal distribution of SST along the DP transects in the present work showed the probable presence of eddies in this zone. From chlorophyll satellite data, Kahru *et al*. (2007) observed an enhanced accumulation of phytoplankton biomass due to the presence of cyclonic eddies in the SACCF. The accumulation of high chlorophyll *a* particularly occurred within the eddy (Kahru *et al.*, 2007).

According to previous works, in the DP there is a strong seasonal cycle of solar radiation and mixed layer depths. A direct effect over the light and nutrients availability, as well as the grazing pressure, are the main controls for the biomass accumulation (Boyd *et al.*, 2001; Hutchins *et al.*, 2001; Moore and Abbott, 2002). In 1996, Banse found no relationship between the depth of the mixed layer and chlorophyll concentration in the PF (Banse, 1996). This might be true only for the PF in the results presented here, where the observed deepening of the z_{mix} might had a negligible effect over the high productivity encountered in the PF in all transects.

However, this is not true for all the other zones and fronts. The results presented in this study, show that the variability of z_{mix} plays an important role for biological oxygen fluxes where a deepening of z_{mix} is observed. If negligible deepening on z_{mix} occurs, heterotrophy might be the main reason for negative F_{bio} values. North of the DP, in the SAZ, PFZ and AZ, the mixed layer was deeper towards April accompanied with the increase in turbulence and vertical mixing. As a response, F_{bio} increased with respect to the value encountered during February. The import of nutrients from deeper waters and the further homogenization in the mixed layer, could maintain the productivity of photosynthetic oxygen to sustain the late growing season in April.

In contrast, in the SAACZ and ACZ, the mixed layer depth did not change from February to April according to the climatological data. F_{bio} is generally high close to the coast during summer due to the stability of the water column, light and availability of nutrients from melting ice. As the season progresses, F_{bio} decreases towards autumn due to net heterotrophy or mixing with deep low oxygenated waters. In the ACZ, formation of the Antarctic Bottom Water (AABW) takes place. Cold and

denser waters sink due to the formation of ice and salt rejection, this occurs during autumn and winter. From the results here presented is confirmed the lack of biological O_2 production in this area towards autumn, where export production or net heterotrophy cause a negative F_{bio} during autumn.

Despite the O_2 consumption and lack of replenishment of nutrients towards the end of the growing season (particularly in the southern DP), the latitudinal patterns for F_{bio} and G remain similar in the DP zones for the three transects. A clear inter-seasonal change upon the end of summer and beginning of autumn was observed, particularly from DP1 to DP3. As the latitudinal distribution of F_{bio} and G in DP2 was homogeneous in contrast to the strong gradients in DP1 and DP3, this is an indication of the fast changes that the productivity in the DP faces in a timescale of weeks. The homogeneity in DP2, might mark the transitional stage from summer to autumn. The O_2 budget method used here proofed to be adequate to identify these changes. However, it must be complemented to the quantification of the physical contribution particularly by upwelling and lateral advection. For this purpose, vertical profiles of O_2 and O_2/Ar are recommended.

Although the observations made above meant to explain the observed distribution of F_{bio} in the DP, with the method used here to estimate N is not possible to differentiate the contribution of processes (biological or physical) responsible for observed negative F_{bio}, unless physical processes are directly quantified. The negative F_{bio} in the PFZ during March and in the ACZ during February and April could be due either to net heterotrophy, degassing of surface waters to the atmosphere or entrainment of low oxygenated subsurface waters, leading to an apparent consumption of the photosynthetic oxygen to negative values. Furthermore, the lateral advection of waters from the coast can play a substantial role for the distribution of phytoplankton and further estimates of this physical process are recommended.

Finally, the total error in the F_g and F_{bio} estimates relies mainly in the k_w estimates and is about 15 %. The total error for G is about 53 % relying on the individual uncertainties for k_w, $^{17}\Delta_{eq}$, $^{17}\Delta$, $^{17}\Delta_{max}$ values. According to Luz and Barkan (2000) the $^{17}\Delta_{max}$ had an uncertainty of 15 per meg. Following Luz and Barkan (2009) the uncertainty in the $^{17}\Delta_{eq}$ at 3.5 ºC was about 3 per meg. The uncertainty is higher as

the temperature of the seawater decreases. The $^{17}\Delta$ here measured for air-equilibrated waters had an uncertainty of 9 per meg.

5.6.1 Comparison to previous ocean productivity data from oxygen measurements.

a) *$^{17}\Delta$ and O_2/Ar measurements*

In order to contrast the results obtained here to previous productivity measurements, first a comparison to other results in the DP, obtained from measurements of $^{17}\Delta$ and O_2/Ar ratios, is done next. The only previous work in the literature offering these results is Reuer *et al*. (2007a and 2007b) (presenting an amended version of the data published by Hendricks *et al.*, 2004). The authors showed the *N* and *G* from discrete samples collected along six DP transects between 2000 and 2004 (see Table 5.1 for details of the transects subject of Reuer's work) mainly during the summer months (from January to March). For consistency and simplification, Reuer's transects are referred as to R01 to R06 hereinafter. The cruise identification as given originally in Reuer's work is shown in parenthesis in column 1 of Table 5.1. The geographical location together to the three DP transects of the present work are shown in Figure 5.7.

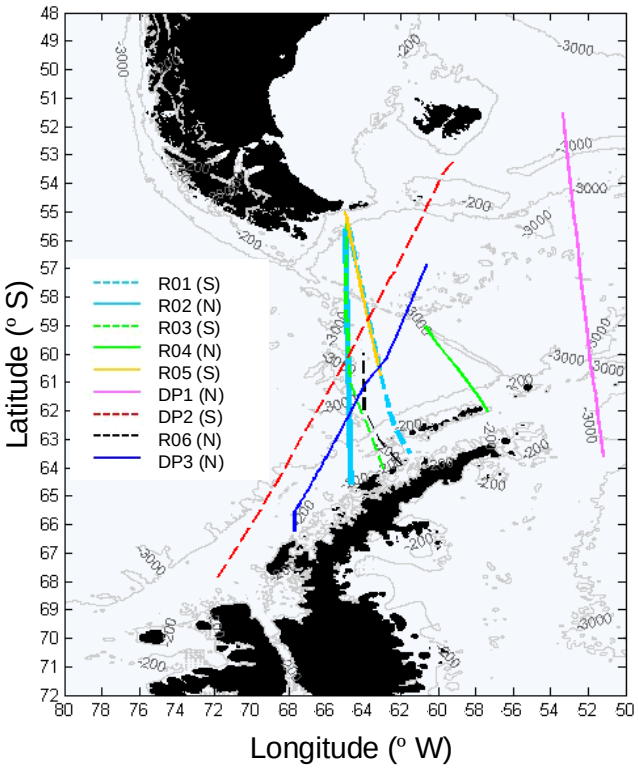

Figure 5.7 – Geographical location of the DP transects from the present work (DP1 to DP3) and DP transects published by Reuer *et al*. (2007a) (R01 to R06). The direction of the cruise track during each transect is in the legend indicated in parenthesis. For identification of each transect, see Table 5.1 for specific dates.

Table 5.1 – Average ± 1 standard deviation (were appropriate) of biological O_2 flux and gross oxygen productions (F_{bio} and G) from discrete samples. Included also data published by Reuer *et al*., 2007b with values of G recalculated for best comparison considering the $^{17}\Delta_{eq}$ at *in situ* temperature.

Transect ID (direction)	**Dates**	**Season**	**F_{bio} (mmol m^{-2} d^{-1})**				**G (mmol m^{-2} d^{-1})**			
			SAZ	**PFZ**	**AZ**	**SAACZ**	**SAZ**	**PFZ**	**AZ**	**SAACZ**
DP1 (N)	13-15/Feb 2007	summer*	14±1	24±13		-21±31	134±64	156±55		158±25
DP2 (S)	27/Feb to 03/Mar 2007	summer	11	8±2	9±5	9±9	223	98±5	88±12	71±14
DP3 (N)	12-15/Apr 2007	autumn		7±4	0±0	-19±17		106±61	104±14	67±33
Reuer *et al*., 2007b (Re-calculated *G*)										
R01 (S) (LMG0209)	25-29/Nov 2002	spring		21±15	8±9			143±91	95±42	
R02 (N) (LMG0209)	29/Nov to 22/Dec 2002	late spring		17±10	-4±8			68±35	71±27	
R03 (S) (LGM0401)	03-26/Jan/2004	summer*		28±15	5±4			126±51	115±76	
R04 (N) (LMG0401)	27/Jan to 04/Feb 2004	summer*			-3±3				83±52	
R05 (N) (LMG0301)	05-06/Feb/2003	summer*	3±8	-19±4	-13±6		57±44	72±35	35±9	
R06 (S) (NBP001)	25-29/Mar/2000	summer			-20±16				129±61	

All transects were located west of the Shackleton Transverse Ridge and most of them from the tip of South America to the Bransfield strait west of the tip of Antarctic Peninsula.

The values of F_{bio}, G and $f(O_2)$-ratio averaged by zone during each transect were compared to the results of the present work. As stated above, the $^{17}\Delta_{eq}$ is a sensitive parameter for the calculation of G. In the work by Reuer *et al*., the authors used 8 per meg as an average value of $^{17}\Delta_{eq}$ from the analysis of air-equilibrated water. Therefore, to compare the present results to the authors' results, a re-calculation was done for their G values using the temperature dependent of $^{17}\Delta_{eq}$ as suggested by Luz and Barkan (2009). From this calculation, an underestimation of G in the PFZ and AZ by as much as 17 and 50 %, respectively (equivalent to: 16±4 mmol m^{-2} d^{-1} and 26±9 mmol m^{-2} d^{-1}, respectively) was identified due to the usage of a fixed $^{17}\Delta_{eq}$ instead of the one obtained from the *in situ* temperature. The average values F_{bio}, G and $f(O_2)$-ratios per zone on each transect obtained in the present work and by Reuer *et al*. are shown in Tables 5.1 and 5.2.

b) Seasonal variability of F_{bio} and G

With the intention to construct a seasonal transition of productivity values from O2-budget method in the DP, the results from the transects from the present work and the results published by Reuer *et al.* were arranged by the month on which were sampled. The seasonal transition starts from late spring (end of November, transect R01), trough early autumn (end of March, transect R06) and extends to mid autumn (April, transect DP3) (Figure 5.6 and Table 5.1 for further details on specific dates). For this seasonal arrangement, DP1 was not taken into account since it was located west of Weddell Sea and off the region of the DP where the rest of the transects were located.

According to Sprintall (2003) from observations of temperature variability in the DP, most of the seasonal variation in this region occurs in the upper 200 m. A seasonal cycle in the DP is represented mainly by: during winter, the AASW reaches its lower temperature limits in the southern surface layers; in spring, the distribution of the AASW becomes patchy at 150 m depth and finally during summer, the AASW is

capped in the south while in north DP the surface waters become warmer (Sprintall, 2003).

From the previous arrangement of transects in the DP is expected to observe a seasonal trend in the F_{bio} (here also approximated to *N*) and *G*. The latter was true for the PFZ, where an inter-seasonal trend in net community and gross oxygen productions was observed. High values were identified during spring (21 mmol m^{-2} d^{-1} and 143 mmol m^{-2} d^{-1}, respectively), when the phytoplankton blooms start to form. Towards the peak of the growing season (between January to February), high productivity values were still present (28 mmol m^{-2} d^{-1} and 126 mmol m^{-2} d^{-1} for *N* and *G*) followed by a decrease towards mid autumn (4 mmol m^{-2} d^{-1} and 56 mmol m^{-2} d^{-1}). This pattern is probably due to the evolution of the biological community in the surface mixed layer. The production in the SO is limited by Fe rather than nitrogen (Martin *et al.*, 1991; de Baar *et al.*, 1999). If an early bloom occurs during spring, it depletes the Fe concentrations so during summer, the growth of phytoplankton is limited by grazing until nutrients are replenished from below.

A decrease in both net and gross oxygen productions in the PFZ, was observed towards the end of spring (transect R02; 18 mmol m^{-2} d^{-1} in *N* and 68 mmol m^{-2} d^{-1} in *G*). This decrease was also observed at the end of the peak of growing season in transect R04 with negative *N* (−19 mmol m^{-2} d^{-1}) and the lowest *G* value (35 mmol m^{-2} d^{-1}) before they peak again towards the end of summer. The presence of undersaturated biological O_2 during the R04 transect could be due to the dominant vertical mixing and increase in O_2 degasification to the atmosphere, or to the increase in the respiration of O_2 towards the end of the growing season.

Despite the analytical uncertainties and the difference in sampling times, it was identified an inter-seasonal variability in the productivity estimates from oxygen measurements north of the DP. In contrast, in the ACZ the seasonal transition from spring to autumn is less evident. In this zone, physical processes such as vertical mixing, lateral advection and the influence of coastal upwelling and sea-ice melting waters appear to play a major role over the productivity. For the R01 to R06 data, no distinction was made between the SACCZ and ACZ.

Table 5.2 – Average ± 1 standard deviation of $f(O_2)$-ratios and calculated net community production (N(C)) in terms of carbon from F_{bio} as approximated to N. Recalculated $f(O_2)$-ratios for Reuer *et al.*, 2007b from the new G value shown in Table 5.1.

Transect ID (direction)	**Dates**	**Seasonal stage**	**$f(O_2) = F_{bio}/G$**				**$N(C) = (F_{bio}/1.4) \times 12$ (mg C m^{-2} d^{-1})**			
			SAZ	**PFZ**	**AZ**	**SAACZ**	**SAZ**	**PFZ**	**AZ**	**SAACZ**
DP1 (N)	13-15/Feb 2007	summer*	0.12±0.07	0.17±0.13		0.01		204±113		
DP2 (S)	27/Feb to 03/Mar 2007	summer	0.05	0.09±0.03	0.10±0.04	0.15±0.16	118±62	73±18	78±43	79±81
DP3 (N)	12-15/Apr 2007	autumn		0.08±0.02	0.00	-0.36±0.4	97	60±33		
Reuer *et al.*, 2007b (Recalculated $f(O_2)$-ratios)										
R01 (S) (LMG0209)	25-29/Nov 2002	spring		0.78±1.56	0.31±0.78			184±128	71±76	
R02 (N) (LMG0209)	29/Nov to 22/Dec 2002	late spring		0.15±0.27	-0.01±0.10			148±86		
R03 (S) (LGM0401)	03-26/Jan/2004	summer*		0.23±0.14	0.06±0.05			239±132	41±32	
R04 (N) (LMG0401)	27/Jan to 04/Feb 2004	summer*			-0.05±0.04					
R05 (N) (LMG0301)	05-06/Feb/2003	summer*	0.05±0.07	-0.39±0.28	-0.36±0.24		24±70			
R06 (S) (NBP001)	25-29/Mar/2000	summer			-0.21±0.26					

For transects DP2 and DP3, the highest biological oxygen production in the AZ was observed during summer (9.1 mmol m^{-2} d^{-1} for DP2) followed by a decrease during autumn (5 mmol m^{-2} d^{-1} in DP3). For the AZ, the seasonal variability in *G* did not show a clear tendency, with values between 35 mmol m^{-2} d^{-1} in summer (R05) to 130 m^{-2} d^{-1} during autumn (DP3).

c) Seasonal variability of f(O_2)-ratios

Before discussing the seasonal variability between the results from Reuer *et al.*, a discussion solely of the ratios encountered for the DP transects subject of the present work is done below. The range of values for *f*(O_2)-ratio in the three DP transects were as expected for areas with low productivity compared to other oceanic regions. In the Southern Ocean, areas influenced by Antarctic Divergence or in the ice-edge systems such as in the Weddell and Ross Seas, generally have high *f*-ratios (0.4 – 0.7) resembling a large portion of produced organic matter exported into deep waters (Jacques, 1991).

Despite the individual gradients within the transects observed from F_{bio} and *G*, the *f*(O_2)-ratios indicates a lack of meridional gradients. The results here presented are comparable to the observations by Reuer *et al*. (2007a). The authors suggested that the lack of latitudinal variability in *f*(O_2)-ratios is due to an equilibrium between the regenerated or exported productivity from the DP mixed layer. Here is suggested that due to the high vertical mixing in the DP, a fast recycling of nutrients (in the order of few days) from the mixed layer to waters below is a predominant characteristic, leading to unclear dominance between heterotrophy and autotrophy.

In the comparison between *f*(O_2)-ratios from all the transects, a decrease from spring to summer was observed. This agrees with the observations made by Dickson and Orchardo (2001) during spring and autumn of 1997 and 1998 along the 170º W meridian during the Joint Global Ocean Flux Study (JGOFS) program (Dickson and Orchardo, 2001). The authors used ^{18}O bottle incubations and surface oxygen supersaturations to quantify *N* and *G*. Despite the difference to the method used here, the *N* values obtained by Dickson and Orchardo were in close agreement (0.34 to 0.77) with the recalculated ratio using Reuer *et al*. (2007b) data for spring (0.78).

A decrease in $f(O_2)$-ratios towards summer, with values from negative to close to zero shows low export production during summer. High $f(O_2)$-ratios during spring comparing to summer, is a common feature not only in the SO, but in other regions of the world's oceans (i.e. Equatorial Pacific during spring and fall in 1992, Bender *et al*., 1999; during summer in the Ross Sea, Bender *et al.*, 2000 ; and other regions of the SO, Williams, 1998; Dickson and Orchardo, 2001). This pattern indicates that despite the lower levels of productivity in different regions, a high $f(O_2)$-ratio in springtime shows dominant autotrophy at the beginning of the growing season.

A study published in 1998 by Mengesha *et al*. revealed a differential nitrogen uptake by phytoplankton from spring to summer in the Indian sector of the Southern Ocean (Mengesha *et al.*, 1998). Large spatial and seasonal variations showed a lead of new production due to the uptake of nitrate during spring that will resemble high *f*-ratios. Contrary during summer, regenerated production was more dominant due to the preferential uptake of ammonium by the phytoplanktonic communities despite the nitrate availability. The latter will lead to low values for *f*-ratios. Therefore, the $f(O_2)$-ratio here are in good agreement with the seasonal comparison between transects and is a good indicator of the state of the euphotic zone.

d) Comparison to production measurements from ^{18}O-incubation and O_2 saturation measurements.

The *N* and *G* values here presented are compared to marine productivity estimates from other methods. From the results of Dickson and Orchardo (2001), integrated *G* from ^{18}O-assimilation method during summer was lower than in spring. The highest rates of production were observed in the SAZ and PFZ (for *G*, 229 and 258 mmol m^{-2} d^{-1}). In the DP transects from the present work, north of the PF the *G* values determined from $^{17}\Delta$ were from as low as 40 mmol m^{-2} d^{-1} (during DP3) and up to 223 mmol m^{-2} d^{-1} (during DP1). Although DP1, DP2 and DP3 transects were all sampled during summer, a decrease from the first to the last north of the PF was observed. These pattern and values, agree with the observation by Dickson and Orchardo with a decrease in productivity as the season progresses from spring to summer. However, a higher overestimation between results was found for the PF. The *G* values here presented were about four times higher (102 mmol m^{-2} d^{-1} in DP2 to 162 mmol m^{-2} d^{-1} in DP3) than the *in vitro* ^{18}O estimates (38 mmol m^{-2} d^{-1}) measured by Dickson and Orchardo.

In agreement with Juranek and Quay (2005) and Quay *et al*., (2010), the gross O_2 production determined from $^{17}\Delta$ tends to be equal or greater (by as much as 1.5 to 2 times) than the results obtained from ^{18}O-incubation method. Each method has its own analytical uncertainties such as the bottle effect characteristic in the *in vitro* methods (i.e. captured phytoplanktonic communities that do not represent the heterogeneity in natural environment, photoinhibition and photorespiration caused by light stress due to the continuous exposure to the same irradiance) and in the preparation process for the O_2 isotopic analysis. The determination of *G* by ^{18}O incubations measures the total O_2 production; therefore the results obtained from this method tend to overestimate the Gross Production when converted by a photosynthetic quotient to in terms of carbon. However, in the comparison between *G* obtained by O_2 measurements this conversion is irrelevant to explain the discrepancy between results from both methods.

Perhaps, the discrepancy between *G* values from both methods is due to systematic biases due to violation of steady-state assumption and neglection of transport effects in the $^{17}\Delta$ method, especially if vertical exchange of O_2 between the mixed layer and waters below is important. In addition, *G* values from $^{17}\Delta$ and from ^{18}O method are integrated over differente time and space scale. The first integrates production over a much longer time period (on the order of weeks, depending on the wind speed and mixed layer depth), while the last represents *G* on the order of 24 h and for a small volume (Juranek and Quay, 2005; Quay *et al.*, 2010).

Despite the discrepancy in *G* values from $^{17}\Delta$ and from ^{18}O method, the *G* values here presented are within the range of values observed in different regions of the world's oceans. In 2010, Juranek and Quay made a compilation of oceanic *G* values at different latitudes, both from oxygen and from carbon measurements. In the case of the *G* from oxygen measurements (using $^{17}\Delta$), the range of average values is from as low as 67 mmol O_2 m^{-2} d^{-1} in the northern subtropics (10º to 30º N) during August 2004 to as high as 408 mmol O_2 m^{-2} d^{-1} in the tropics (2º N to 2º S) during February in 2005. The authors concluded that the regional variability of values is also as high as the uncertainty in the $^{17}\Delta$ method (30 to 40 %), being also an important part of the discrepancy compared to other methods for estimation of *G*.

The uncertainty in *G* estimates from $^{17}\Delta$ method would decrease as the spatial resolution of $^{17}\Delta$ increases. The results obtained in this thesis and Dickson and Orchardo's rely strongly in the scarcity of samples collected along the transect. Here, from 7 and up to 10 samples were collected per transect, while the authors made their estimates based on only 5 samples distributed along the DP. Thus, in order to improve the previous observations and resolve better the distribution of *G* and its heterogeneous nature in the DP, more data points are needed.

In the case of *N*, the average values estimated from ΔO_2 by Dickson and Orchardo along their DP transects were from −11±31 mmol m^{-2} d^{-1}. Here, all the DP transects for the present work averaged 5±9 mmol m^{-2} d^{-1} from ΔO_2/Ar estimates. This translates to a wider range of values obtained by Dickson and Orchardo with 2 times overestimation and 9 times underestimation with respect to the values from biological O_2 supersaturation.

The spatial distribution from the ΔO_2 method was in excellent agreement with the ΔO_2/Ar method and both methods integrate the observations in the mixed layer. In good agreement, during late summer high rates of O_2 production were observed north of the PF and undersaturation south of the PF. However, the higher uncertainty on *N* estimates from O_2 supersaturation relies on the lack of use Ar to discriminate between the biological from the physical contributions of O_2 in the mixed layer such as in the biological O_2 supersaturation method.

The latitudinal distribution of productivity values from the authors during summer was in clear disagreement to the DP transects of this study. Dickson and Orchardo found the lowest productivity values within the PF; in contrast, the results here presented here show an increase of gross O_2 production within the PF associated with the continuous upwelling of nutrients-rich subsurface waters (Figure 5.6).

Other estimates of *N* in the Pacific sector of the Southern Ocean have been previously reported and were estimated from the deficit in CO_2 and nutrients (i.e. phosphate, nitrate, silicic acid). Rubin *et al.* (1998) observed a range of values from 80 to 290 mg C m^{-2} d^{-1} estimated in autumn and end of summer (Rubin *et al.*, 1998).

In 2002, Ishii reported a range of values from 60 to 500 (Ishii *et al.*, 2002). These results are in close agreement to the results presented in this thesis.

In the Ross Sea, as representative of another region in the Southern Ocean, *N* values estimated from deficit of nutrients (i.e. nitrogen and silicon) falled from 130 mg C m^{-2} d^{-1} to as high as 2600 mg C m^{-2} d^{-1} as average daily annual production. The extreme levels encountered in this region are expected since the Ross Sea continental shelf is perhaps the most important carbon sink in Antarctica, thus large biological productivity is expected (Smith *et al.*, 2011) in comparison to the Drake Passage. High *N* values (but lower than Smith *et al.* 2011 values) were also observed but 11 years before by Sweeney *et al.* (2000). The values were estimated from the drawdown of CO_2 and nutrients and the highest *N* was about 1100 mg C m^{-2} d^{-1} in the Ross Sea from mid-October to mid-February (Sweeney *et al.*, 2000).

In the case of the Weddell Sea, *N* has been previously estimated from depletion of total CO_2, nitrate, phosphate and silicate during early autumn in 2005. The *N* values are in close agreement to the ones observed in this thesis (Table 5.2), being 1.8 and 3.5 mol C m^{-2} yr^{-1} (equivalent to 59 to 115 mg C m^{-2} d^{-1}) for the interior and near-margin region respectively (Hoppema *et al.*, 2007). In the Scotia Sea, Shim *et al.* (2006) estimated *N* values from measurements of pCO_2 during summer (December) in 2001 and were of about 1.0 to 1.2 mol m^{-2} south of the Polar Front (~ 480 mg C m^{-2} d^{-1}).

Despite the differences in results by different methods due to analytical artifacts (i.e. bottle effect, integration time) the *N* values obtained in this thesis fall into the range of observed values, not only in the SO, but in the world's oceans. To mention some: in 2005, Juranek and Quay observed *NCP* values using O_2/Ar measurements from −120 mg C m^{-2} d^{-1} to 180 mg C m^{-2} d^{-1} (−12.5 to 18.8 mmol O_2 m^{-2} d^{-1} using 1.25 as PQ) in the North Pacific gyre at the HOT sation.

Only as reference, other results of *N* in the world ocean's are mentioned. In the Sargasso Sea, at the North Atlantic, Mouriño-Carballido and Anderson (2009) reported *N* data obtained from a 1-D model using O_2 profiles and from in vitro incubations. The average values were on average 4 mmol O_2 m^{-2} d^{-1} integrated during a period of 43 days (Mouriño-Carballido and Anderson, 2009).

5.6.2 Net community productions from carbon and observations from space.

a) Comparison to productivity from traditional carbon measurements

From *N*, the net community production in terms of carbon (*N*(C)) is calculated. For this, F_{bio} is divided by 1.4 ($N(C) = F_{bio} / 1.4$) where the factor 1.4 corresponds to the photosynthetic quotient suggested by Laws, 1991 . Results from this calculation are shown in Table 5.2.

For the JGOFS study during 1997 and 1998, Hiscock *et al*., (2003) published results corresponding to carbon productivity rates from bottle incubations for ^{14}C assimilation in discrete samples collected from the SAZ to the ACZ in the DP (Hiscock *et al.*, 2003). A common feature with the data from the present study was the rapid productivity decrease from mid February to end of February.

In the present work, the net carbon production estimated from oxygen was nearly four times higher than the results obtained by Hiscock *et al*., from ^{14}C incubations. During late summer in the AZ, *N*(C) was estimated to be 97 mg C m^{-2} d^{-1}, while Hiscock *et al*. obtained a mean value of 25 mg C m^{-2} d^{-1}; in the PFZ, was obtained a value of 73 mg C m^{-2} d^{-1} while the authors obtained 21 mg C m^{-2} d^{-1}. Finally, in the SACCZ it was estimated a value of 79 mg C m^{-2} d^{-1} compared to 18 mg C m^{-2} d^{-1} observed from the ^{14}C incubation experiments.

Besides the difference in the methodological approaches, the main difference relies in the depth the results are representing and the depth integrated. As in the case of the ^{18}O incubation methods, the ^{14}C method integrates production over a timescale on the order of 24 h in the euphotic layer. In contrast, the marine productivity estimates from F_{bio} represent the productivity integrated on the order of weeks depending on the equilibration time of the O_2 in the mixed layer at a specific mixed layer depth and wind speed. The method used here allows the integration of various episodic events of *in situ* productivity, while the incubation methods only a single event per day. Therefore, the results between these methods are not directly comparable and represent the productivity over different timescales.

b) Comparison to modelled primary productivity data from satellite ocean colour

Finally, the results of *N*(C) were compared to satellite and modelled derived Net primary production (*NPP*, in mg C m^{-2} d^{-1}).

The *NPP* values, corresponding to the same sampling month and year of the DP transects of this study and were extracted from data publicly available (http://www.science.oregonstate.edu/ocean.productivity) at 8 days resolution over a spatial grid of 1/6 of a degree (1080 × 2160). The phytoplankton carbon biomass for this data set was obtained from the Carbon-based productivity model (CbPM) using chlorophyll and particulate backscattering coefficients from GSM v5 from SeaWiFS. Detailed description of the model and origin of the data is provided in Behrenfeld *et al.*, 2005 .

In Figure 5.8 is shown the spatial distribution of integrated *NPP* for the 10 to 17 of February (Figure 5.8a) comparable to the dates when DP1 was occupied. Figures 5.8b and 5.8d correspond to the interval of dates within the sampling time for DP2 and DP3 (26 February to 5 March and 15 to 22 of April, respectively). The location of the DP transects are plotted (full black lines) on top of the spatial distribution of *NPP*. The SO fronts, according to their climatological position, are also plotted (dashed black and white lines).

Several differences in the analytical approaches between the estimates from *NPP* by remote sensing (*NPP*-RS) and *N*(C) from oxygen measurements are important to mention. The *N*(C) represent the productivity, not only by phytoplankton (net community production) in the mixed layer depth.

The *NPP*-RS observations are based on chlorophyll estimates from satellite ocean colour. As suggested by Mengesha *et al.* (1998) in the Indian sector of the Southern Ocean, the measurements of chlorophyll *a* do not fully elucidate the total phytoplankton biomass with a shift between chlorophyll distribution and cell abundance. Furthermore, the chlorophyll surface distribution can show low levels in a high biomass area, leading to underestimation of productivity values. According to previous observations, the primary production estimates derived from remote sensing models range over a factor of 2 in comparison to *in situ* productivity measurements (Carr *et al.*, 2006). Reuer *et al.* (2007a) confirmed that estimates of *G* from models based on remotely sensed chlorophyll underestimate the results from $^{17}\Delta$.

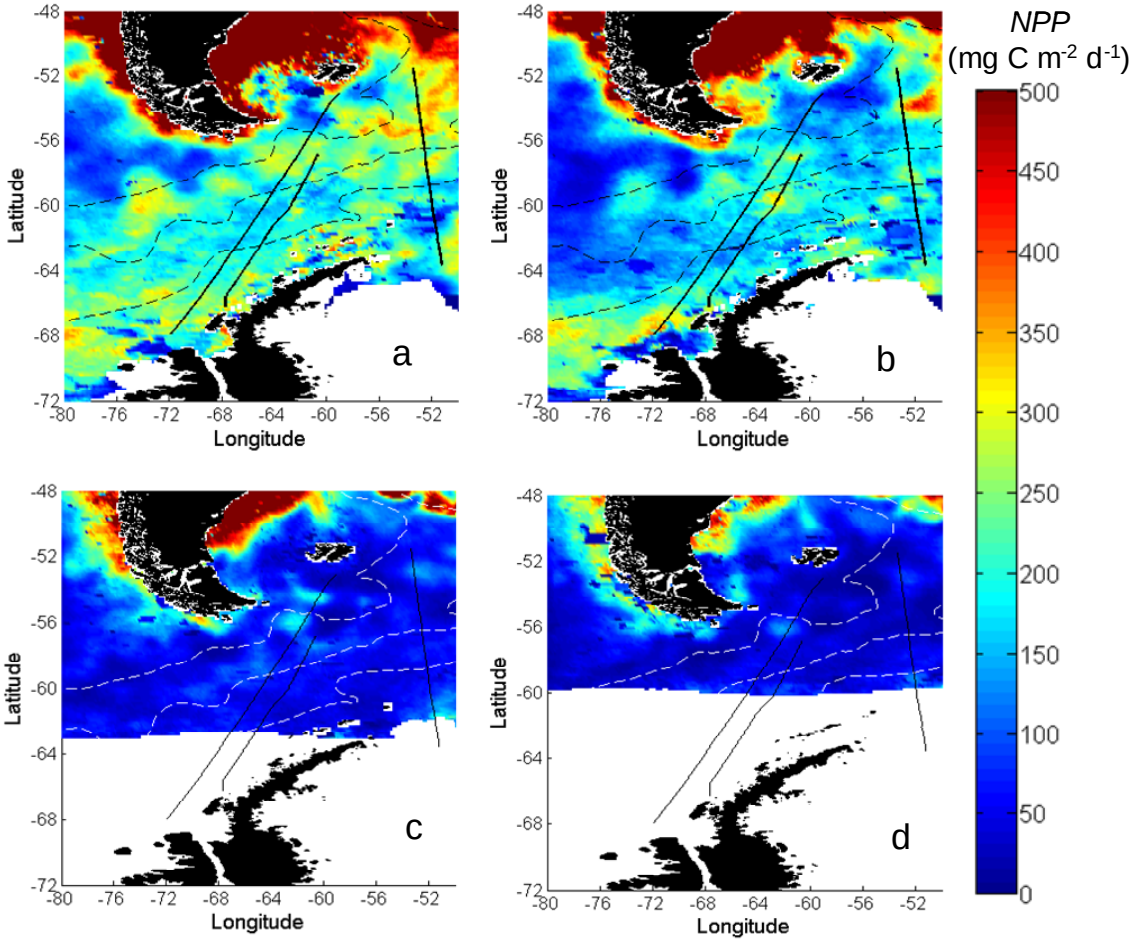

Figure 5.8 – Spatial distribution of net primary production (*NPP*; mg C m^{-2} d^{-1}) from model output based on remote sensing chlorophyll (Behrenfeld et al., 2005), corresponding to 8 day averages; a) 10 to 17 of February, 2007, b) 26 of February to 5 of March, c) 7 to 14 of April, and d) 15 to 22 of April. White (c and d) and black (a and b) dashed lines are the climatological location of fronts.

In the next figure (Figure 5.9), a quantitative comparison between *N*(C) and the corresponding *NPP*-RS for the same month and geographical location is shown. According to the geographical location of the DP transects in this study, the *NPP* from remote sensing are generally in disagreement to the *in situ* estimates of *N*(C). During summer and at the beginning of February, the high productivity observed north of the PF against the low apparent phytoplankton biomass in the AZ (Figure 5.4d) can be, at first sight, comparable for both results. However, the quantitative comparison shows lower productivity values, by as much as 400 mg C m^{-2} d^{-1}, than the *in situ* values (Figure 5.9a).

For DP2, the trend of the observed and satellite data remains similar and with constant offset of about 200 mg C m^{-2} d^{-1} between results. A general overestimation of the satellite results is observed in this case. A closer agreement between satellite and data derived from O_2/Ar is observed in the ACZ close to the Antarctic coastline, where high accumulation of phytoplankton led to high productivity (Figure 5.9b). Unfortunately, in the *NPP*-RS data it was not possible to compare with the *N*(C) observations south of 60º S during DP3 due to lack of data in the first by cloud coverage (Figure 5.8d). This is a common analytical disadvantage on the observations from space.

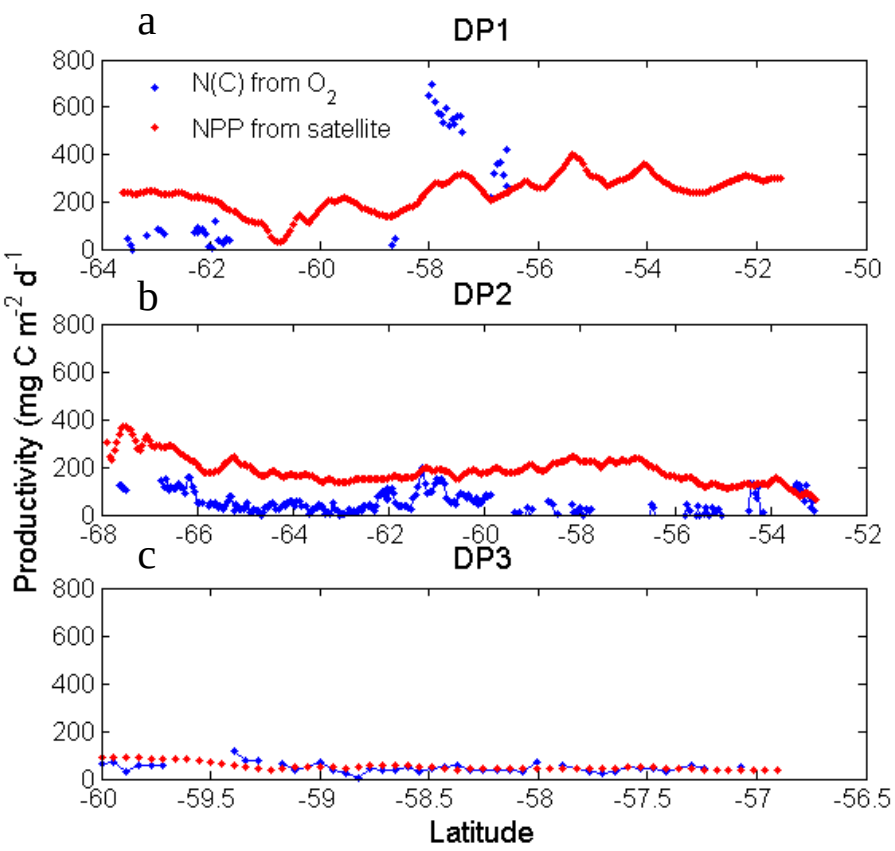

Figure 5.9 – Comparison of net community production (mg C m^{-2} d^{-1}) from O_2/Ar ratios (*N*(C)) and satellite observations of sea surface colour (*NPP-RS*) for three transects in the Drake Passage during summer 2007; a) DP1, b) DP2 and c) DP3.

Finally, the best agreement between N from space and *in situ* observations can be observed in for DP3 (Figure 5.9c) where a very close agreement between productivity values is found during the period where biological productivity decreased towards the end of the growing season.

Due to the inherent differences in the methods to obtain *N*(C) and *NPP*-RS, a quantitative comparison between *N*(C) and *NPP*-RS results must be done with caution, and as observed above, no clear difference between results (i.e. over and underestimation) is observed. Visual inspection based on similarities on the spatial distribution in productivity results from both methods is then encouraged.

Perhaps the most important output from the comparison of the spatial distributions of productivity between both methods is to corroborate the presence of mesoscale features, such as eddies, by the accumulation of phytoplankton as given by the patchiness of high chlorophyll levels. As previously suggested from the patchiness in the SST and the latitudinal distribution of F_{bio}, in the PFZ, AZ and SAACZ from mid February to beginning of March, an apparent accumulation of phytoplankton biomass was associated with the presence of mesoscale structures. In Figure 5.8a and b, can be observed patches of high productivity as given by the accumulation of chlorophyll, indicating the presence of eddies as suggested by Kahru *et al*. (2007). The location of the phytoplankton blooms during the sampling period are in good agreement to the sites of the maxima F_{bio} observed here, such as at 58 ºS for DP1 (i.e. location of the PF) and at 67 ºS for DP2 close to the coast.

The contrasting differences between the *NPP* as given by the 8 days averages are also an evidence of the rapid changes that occur in the DP as observed in the transects DP1 to DP3.

The estimation of primary production from space it is indeed a reliable method due to the advantage of visualize the spatial distribution in wide coverage of data in almost real time for different locations. However, improvements in the current algorithms are needed and high resolution *in situ* productivity measurements, such as the ones presented here, will contribute to achieve this goal.

c) Continuous productivity estimates from free-floating drifters

In order to improve the productivity estimates due to the disagreement between observations from traditional incubation methods, recent attention of the scientific community has been centred on developing and improvement of *in situ* methods. With this intention, a new method has been tested for the estimates of productivity

from dissolved inorganic measurements (DIC) made with free-floating drifters. During 2006 and 2007, net community production in terms of carbon (N(C)) was estimated in the South Atlantic and Indian Oceans as part of the CARIOCA (CARbon Interface OCean Atmosphere) experiment (Boutin and Merlivat, 2009). The integrated N(C) values during December were between 30 to 50 mmol m^{-2} d^{-1}, with the maximum value observed in April equivalent to 120 mmol m^{-2} d^{-1}. The values from the three DP transects presented in this work are consistently lower than those, ranging from 6 mmol m^{-2} d^{-1} (in the AZ) to 17 mmol m^{-2} d^{-1} (PFZ) during summer and 5 mmol m^{-2} d^{-1} during April (all values in terms of mmol of C). Despite both methods rely on high resolution estimates a direct comparison between them is still not possible. First, the latitudinal range of the drifters from the CARIOCA project did not cover the DP region; second, the high temporal variability of biological processes across the SO lead to wide range of values. However, this is the first time that productivity results from $^{17}\Delta$ and O_2/Ar measurements are compared to drifter measurements, and future comparisons are needed in order to improve both methods.

5.7 Conclusion.

The distribution of biological O_2 flux, approximated to the mixed layer net community production (*N*), was heterogeneous along three Drake Passage (DP) transects during summer and autumn 2007. This was possible to observe due to the high spatial (on the order of 0.1 km) and temporal (few minutes) resolutions achieved from continuous surface measurements of O_2/Ar ratios. These results were complemented with discrete observations of gross O_2 production (*G*) from the measurements of the isotopic abundance on dissolved O_2.

From sharp changes in the latitudinal distribution of SST and F_{bio} were identified the main fronts and zones in the region; most of them located near the climatological position. The differences observed in the spatial distribution of productivity between the frontal zones might be controlled by different physical processes along the DP. During summer, high biological O_2 production was observed in the upwelling areas such as the PF, AZ and SACCZ due to continuous replenishment of nutrients in a stratified water column with shallow mixed layer. Apparent net heterotrophy and degassing of oxygen was observed in the convergence areas north of the PF (i.e. SAZ).

The differences between sampling time of the three DP transects investigated here allowed the identification of the seasonal changes in the productivity from summer to autumn. In the PFZ and AZ an increase of biological O_2 production was well associated with the deepening of the mixed layer. As consequence, the input of nutrients from waters below could sustain the phytoplankton growth during mid April.

Contrary, in SACCZ and ACZ the mixed layer dynamics had less influence over the distribution of F_{bio}. During autumn, apparent net heterotrophy or degassing from the ocean to the atmosphere, were dominant processes in the southern part of the DP. This could be due to the consumption of nutrients during summer and lack of replenishment during the beginning of the ice formation, the vertical transfer of low oxygenated waters, lateral advection and convective mixing.

From the observations in the present work, the mixed layer variability seems to play an important role but only in northern DP (north of the SACCF). Due to the similarity in some zones and the strong seasonal changes, lateral advection of waters and upwelling driven by favourable wind direction may play also a key role. The patchiness of the productivity distribution was well associated with the location of phytoplankton blooms confirmed by ocean productivity from satellite data.

In agreement with previous observations from other works, the *in vitro* productivity estimates from previous studies tend to be lower than the *in situ* data. The gross O_2 production determined from ^{17}O anomaly was four-fold higher than previous results from ^{18}O-incubation method in the DP. The estimates of net community carbon production (N(C)) from oxygen measurements were nearly four-fold higher than the results obtained from ^{14}C incubations in past studies by other authors for the same region.

The O_2/Ar and oxygen isotopes method to estimate productivity is a reliable *in situ* method for N and G estimates. With the high resolution achieved here it is possible to identify the fast changes in productivity associated with the heterogeneity and low productivity in the dynamic DP. The results presented here, are an invaluable contribution to the currently available and scarce *in situ* productivity data in the DP and can also contribute to the improvement of current regional and global productivity models, observations from space, as well as new observations from free-floating drifters.

Upwelling, as well as lateral advection, can also contribute greatly to N estimates from F_{bio} in the DP and have to be evaluated in future productivity estimates from O_2 budget in this area. In order to elucidate the contribution of physical (i.e. vertical mixing, upwelling, lateral advection) over biological processes (i.e. net heterotrophy) in regions were negative F_{bio} was observed (i.e. SACCZ and ACZ) a more complete sampling scheme including vertical sampling for O_2/Ar and ^{17}O anomaly, as well as the estimate of physical processes such as upwelling and lateral advection are strongly recommended in future works. Parallel measurements such as nutrients distribution, phytoplankton abundance and productivity estimates by other methods for direct comparison are also desirable.

Chapter 6

Conclusions and future work

6.1 Conclusions.

The objective of this research was to investigate marine biological production in two regions of the Southern Ocean: Bellingshausen Sea and Drake Passage. Net community production (N, from biological O_2 flux, F_{bio}) and gross oxygen production (G) were estimated from O_2/Ar ratios and O_2 isotopes respectively. This is the first time a large data set for productivity estimates on high spatial and temporal resolution is presented for two important regions in the Southern Ocean.

In contrast to previous studies using oxygen triple isotopes for G estimates in the Southern Ocean, a temperature-dependent value for the ^{17}O anomaly in equilibrium with the atmosphere ($^{17}\Delta_{eq}$) was used, as suggested by Luz and Barkan (2009).

Because the results presented here represent productivity values integrated over the mixed layer, the criterion used to define the mixed layer depth (MLD) is important. In order to improve the gas exchange flux calculations, a criterion to define mixed layer depth (MLD) based on the vertical distribution of oxygen was proposed. The criterion suggested here defines the depth where the dissolved O_2 concentration has changed by at least 0.5 % compared to its value at 10 m. MLD-O_2 agreed better with the MLD derived from visual inspection of the oxygen profile in the mixed layer than MLD criteria based on temperature or potential density. The latter tend to overestimate MLD and been generally located at or beneath the oxycline. As a result, underestimate the average O_2 concentration in the MLD for considering lower O_2 waters from the oxycline. The use of MLD-O_2 is suitable for air-sea gas exchange studies and marine productivity estimates from O_2 measurements in the coastal area of the Southern Ocean.

The best agreement between MLD-O_2 and MLD based on criteria using potential density properties was observed for a change of 0.03 kg m^{-3} with respect to the value at 10 m depth. The latter is used in the monthly mixed layer climatology published by de Boyer Montégut *et al.* (2004). In the absence of vertical O_2 profiles, the use of this criterion would therefore seem appropriate.

F_{bio} approximates net community production (N) under steady-state conditions and assuming that physical mixing processes can be neglected. However, in both Bellingshausen Sea and Drake Passage physical processes do actually play an important role for the distribution of mixed-layer productivity. To evaluate the contribution of vertical mixing to F_{bio}, the diapycnal flux of oxygen (F_v) and the entrainment of oxygen (F_e) by vertical convection of subsurface waters after deepening of the mixed layer were estimated only in the BS.

In the Bellingshausen Sea, the distribution of F_{bio} was heterogeneous. High biological O_2 production was found along the coast, while negative values were located off shore in the Permanent Open Ocean Zone (POOZ). About 86 % of the negative F_{bio} value could be accounted for by entrainment of low-oxygen deep waters. A further 8 % were caused by diapycnal mixing. This means that the actual net community production in this area was close to zero or slightly heterotrophic. As the mixed layer deepened and the water column de-stratified due to the strengthening of winds, the entrainment of low-oxygenated Winter Water exerted an important contribution to the mixed layer O_2 mass balance. Not only low oxygen waters entrained due to this process, but the waters also had apparently high $^{17}\Delta$ values formed during the previous growing season and stored in the upper thermocline, leading to apparently high values of G, which, however, probably do not reflect actual in-situ production. In order to corroborate this hypothesis, vertical samples for $^{17}\Delta$ analysis would have been desirable, particularly from waters below the mixed layer, but could not have been measured for logistical reasons.

In the Drake Passage region, the distribution of F_{bio} was in agreement with the location of the Antarctic fronts and zones for the three transects evaluated here. Due to the lack of vertical O_2 concentrations, the effect of physical mixing processes could not be evaluated as in the Bellingshausen Sea. However, the role of the deepening of the mixed layer upon the seasonal transition from summer to autumn was investigated. Taking advantage of the close agreement between MLD-O_2 and the MLD from monthly climatology (de Boyer Montégut *et al.,* 2004), the depth at the sampling time and 30 days before was extracted from these data sets. A north-to-south gradient in F_{bio} and G was observed with higher productivities towards the south during late summer and an opposite pattern in early autumn. The deepening of

the mixed layer seemed to play an important role on this pattern. The deepening of the MLD was more evident in the northern part of the DP (the Subantarctic Zone, SAZ). Even though the entrainment of deep waters should have lowered the biological O_2 content of the mixed layer, it would have also brought nutrients to the surface. This seems to have fuelled O_2 production since light levels were still sufficient towards the beginning of autumn. In contrast, in the southern DP a deepening of the MLD was not observed. A considerable decrease from positive F_{bio} in summer to negative values in the SACCZ and ACZ is likely due to limited light availability and the consumption of nutrients at the end of the growing season, thus net heterotrophy seems to dominate in this region.

To derive N from F_{bio} it is strongly recommended to estimate the contribution of physical effects to the mixed layer O_2 budget. The quantification of the contribution of oxygen by upwelling and lateral advection is desirable for future applications. If no physical processes are evaluated, the biological O_2 flux should be referred as it is and not approximated as N unless it is known that in the study region the physical contribution might not play an important role.

Using the O_2/Ar method, it was possible to obtain *in situ* productivity estimates in high spatial (on the order of 0.1 km) and temporal (on the order of minutes) resolution. This is the main advantage in comparison to the sparse sampling that can only be achieved by incubation methods. However, another important advantage attributed to the O_2 approach over the traditional incubation methods is that it is free of analytical artefacts such as bottle effects. It is also relatively easy to maintain and easy to use in the field despite the daily attention that it requires.

Another important advantage of the O_2/Ar and $^{17}\Delta$ method is the depth and time that productivity estimates from this method represent in comparison to *in vitro* methods. Firstly, the given productivity values represent the O_2 produced by photosynthesis over the order of a couple of weeks which resembles the lifetime of O_2 in the mixed layer depth and under certain wind speed conditions. In contrast, the productivity estimates from incubation methods represent the productivity in the euphotic zone during a period of time of only 12 to 24 h. Due to the difference in time integration, the O_2 approach represents an average of episodic productivity events rather than a daily event, leading to a more complete picture of the productivity in the area of

interest. In the DP the G values from $^{17}\Delta$ were nearly four times higher than G obtained by Dickson and Orchardo (2001) from the ^{18}O incubation method. In the case of N, it was also nearly four times higher when estimated from in situ O_2/Ar measurements than the primary productivity results obtained by Hiscock *et al.* (2003) from the ^{14}C incubation method. Productivity estimates based on satellite observations of chlorophyll or particulate carbon biomass offer large spatial coverage compared to the results from the O_2 approach used here, which is limited to transects along cruise tracks. However, more *in situ* data are necessary to offer an alternative way of calibrating the satellite-based productivity models, which are usually validated using ^{14}C-primary production measurements. A direct quantitative comparison between the O_2 approach and observations from space should be performed, taking into account the integration depth of the O_2 method (MLD) and that of the optical measurements (optical thickness). What is true is that the results from satellite observations provide valuable information of high spatial coverage useful for inspection of oceanic features that can complement the observations from *in situ* O_2 observations. In addition, more data from *in situ* productivity estimates will help to improve the model based productivity values.

The O_2 budget method also has important limitations and uncertainties. Analytical errors during the isotopic analysis and the estimate of gas transfer coefficient are the most important to mention. In this work, the uncertainty estimated for F_{bio} is about 15 % and for G is 53 % due to uncertainties in the gas transfer coefficient and $^{17}\Delta$ and $^{17}\Delta_{eq}$ in the case of G. When correcting F_{bio} to derive N (considering F_v and F_e), the uncertainty of N amounts to about 35 %. As more physical controls such as upwelling and lateral advection are added to the mixed layer O_2 mass balance, the uncertainties in the productivity estimates will increase. Therefore more work to improve the inherent uncertainties for each component of the mass balance should be done.

It is still challenging to obtain reliable productivity estimates in the field and so far no definitive method can be suggested. Efforts to improve the uncertainties on productivity estimates and to validate them by comparison to other methods are still needed in the face of future environmental changes.

6.2 Future work.

Despite its inherent complexity and uncertainties, the O_2/Ar and $^{17}\Delta$ method is becoming more popular. It has been adopted by more research groups and applied in several oceanic regions around the world.

From the current work, important suggestions for future applications can be made. The vertical oxygen concentration from CTD-O_2 or optical sensors such as optodes is recommended in order to identify a suitable MLD. To constrain the physical effects in the productivity estimates, vertical samples for O_2/Ar ratios and $^{17}\Delta$ determinations are desirable. Taking advantage of the fast time response of the MIMS method (i.e. on the order of seconds), vertical water samples from Niskin bottles can be sampled and immediately measured. From this approach, the vertical distribution of oxygen photosynthetically produced can provide a valuable insight of the vertical transfer from or to upper waters.

Finally, physical and biological complementary variables from other techniques are desirable. Underway measurements of active fluorometry by the FRRF technique (Fast Repetition Rate Fluorometer) have been used to measure active fluorometry in order to estimate the abundance of phytoplankton in surface waters from fluorometry measurements over high spatial and temporal resolution compatible to the continuous measurements of O_2/Ar ratios by MIMS.

Other common oceanographic measurements such as: ADCP (Acoustic Doppler Current Profiler) for better estimates of lateral water advection, traditional quantification of macro and micro nutrients or *in situ* chlorophyll determinations are also ideal in order to have a more complete perspective of the state of the mixed layer at the sampling time. Parallel marine productivity estimates from traditional *in vitro* methods can be suitable.

Appendix A

In this appendix, is explained how equation 4.2 in Chapter 4, was derived in order to estimate the entrainment of oxygen (F_e) by vertical transport of water due to the change in the mixed layer depth.

In 2008, Emerson *et al.* represented the entrainment flux of a tracer to upper waters due to the change in mixed layer depth over the time (*dz/dt*) as:

$$E = \frac{dz}{dt}(c_T - c)$$

Where c_T represents the concentration of oxygen in the thermocline below the mixed layer depth and c is the concentration of oxygen before the deepening event (Emerson *et al.*, 2008).

In this thesis, the flux of oxygen due to deepening of mixed layer depth (F_e) is given by the change of the concentration of oxygen over the time (*dc/dt*) in the mixed layer (z_{mix}) due to entrainment of subsurface waters after deepening of the mixed layer in 30 days (*dt*). It is also considered here the slope of the oxycline (m) given by the oxygen profile during sampling time. The explanation of the calculation of Fe according to equation 4.2 (Chapter 4) is given below.

As the deepening of the mixed layer depth occurs over the time (*dh*/*dt*), the concentration of oxygen decreases due to spreading the previous concentration in the mixed layer (c_0) over a greater depth; and it increases due to addition of tracer from the upper oxycline below. Thus, the resulting concentration of oxygen ($c1$) after deepening of the mixed layer to a final depth (z_1) from an initial depth (z_0) is given by:

$$z_1c_1 = z_0c_0 + \Delta z c_T \qquad \text{(A1)}$$

Where, Δz is the change in depth of the mixed layer (i.e. $\Delta z = z_1 - z_o$) and c_T in this case represents the average O_2 concentration in the oxycline given by: $c_T = \frac{1}{2}(c_0 + c_b)$. The term c_b is the concentration of oxygen at the base of the oxycline observed during sampling time. Expanding A1:

$$z_1c_1 = (z_1 - \Delta z)c_0 + \Delta z c_T \qquad \text{(A2)}$$

The change in the oxygen concentration due to the deepening Δz is expressed as: $\Delta c = c_1 - c_0$; thus replacing this expression in A2 and simplifiying:

$$z_1\Delta c = \Delta z(c_T - c_0) \qquad \text{(A3)}$$

The slope of the oxycline (m) at the sampling day is given by: $m = \left.\frac{dc}{dz}\right|_{z_0}$, and the concentration at a depth Δz below z_0 is given by:

$$m = \frac{c_b - c_0}{\Delta z} \qquad \text{(A4)}$$

Thus, the average concentration over the depth interval Δz is then given by:

$$c_T = \frac{1}{2}(c_0 + c_b) = c_0 + \frac{1}{2}\Delta c = c_0 + \frac{1}{2} m \Delta z \qquad \text{(A5)}$$

Replacing equation A5 in A3:

$$z_1 \Delta c = \Delta z (c_0 + \frac{1}{2} m \Delta z - c_0)$$

$$z_1 \Delta c = \frac{1}{2} m (\Delta z)^2 \qquad \text{(A6)}$$

Thus, the entrainment flux (F_e) of oxygen is given by:

$$F_e = z_{mix} \frac{dc}{dt} = -\frac{1}{2} m (\Delta z)^2 \frac{dh}{dt} \qquad \text{(A7)}$$

Note that the minus sign is added in order to reference the flux of the tracer to the waters below the mixed layer (i.e. positive values represent an influx of O_2 from subsurface waters into the mixed later).

In order to use the equation A7 there must be considered the slope of the oxycline (m) is constant. This assumption relies on the unknown slope of the oxycline at any time before the sampling day. Therefore, it is implied here that the rate of oxygen consumption below any given mixed layer depth remains the same at any given time t.

List of acronyms[1]

ECMWF	European Centre for Medium Range Weather Forecast
IRMS	Isotope Ratio Mass Spectrometry
MIMS	Membrane Inlet Mass Spectrometry
MLD	Mixed Layer Depth (referred also as to z_{mix} for equations and in mass balance)
MS	Mass spectrometer
NCEP	National Centre for Environmental Prediction
QMS	Quadrupole Mass Spectrometer
QSCAT	QuikSCAT
TSG	Thermosalinograph sensor
USW	Underway Surface Seawater
USW-SS	Underway Surface Seawater - Sampling System
WOA	World Ocean Atlas
WOCE	World Ocean Circulation Experiment

[1] Acronymns used in specific sections are not included here

List of variables[1]

$^{17}\Delta$	^{17}O anomaly in dissolved oxygen (per meg)
$^{17}\Delta_{max}$	^{17}O anomaly for pure photosynthetic oxygen (per meg)
$^{17}\Delta_{eq}$	^{17}O anomaly (per meg)
α	Ostwald solubility coefficient (dimensionless)
$c(O_2)$	mixed-layer dissolved O_2 concentration (continuous calibrated) (µmol kg^{-1})
$c_{sa}(O_2)$	dissolved O_2 concentration in discrete samples from USW measured by Winkler method (µmol kg^{-1})
$c_{CTD}(O_2)$	dissolved O_2 concentration of discrete samples from CTD-surface Niskin bottle measured by Winkler method (µmol kg^{-1})
$c_{eq}(O_2)$	O_2 concentration at equilibrium with the atmosphere at *in situ* temperature and salinity (µmol kg^{-1}) (Benson and Krause, 1984; Garcia and Gordon, 1992)
O_2/Ar	continuous O_2/Ar ratio from shipboard USW measurements
$(O_2/Ar)_{sa}$	O_2/Ar ratio for discrete water samples (after solubility correction)
$(O_2/Ar)_{CTD}$	O_2/Ar ratio for discrete water samples (after solubility correction) from Niskin bottle corresponding to surface water
$(O_2/Ar)_{eq}$	O_2/Ar ratio at saturation, estimated from the individual saturation concentration for O_2 and Ar ($c_{sa}(O_2)$ and $c_{sa}(Ar)$ respectively) at in situ temperature, salinity and pressure
$(O_2/Ar)_{Cair}$	O_2/Ar ratio for compressed air aliquots, representing the O_2/Ar ratio in atmospheric air (22.42)
$(O_2/Ar)_{Eqwat}$	O_2/Ar ratio from air-equilibrated water aliquots
$c(Ar)$	mixed layer Ar concentration (µmol kg^{-1})
$c_{sa}(Ar)$	Ar concentration for discrete samples collected from USW and Niskin surface bottles (µmol kg^{-1})
$c_{eq}(Ar)$	Ar concentration at equilibrium with the atmosphere at *in situ* temperature and salinity (µmol kg^{-1}) (Hamme and Emerson, 2004).
$\delta^{18}O$	^{18}O relative abundance referenced to ^{16}O in sample with respect to a working reference (‰)
$\delta^{17}O$	^{17}O relative abundance referenced to ^{16}O in sample with respect to a working reference (‰)
ΔO_2	O_2 supersaturation (%)
$\Delta_{sa}(O_2)$	O_2 supersaturation in discrete samples from USW (%)
$\Delta_{CTD}(O_2)$	O_2 supersaturation in discrete samples from surface Niskin bottle (%)
$\Delta_{diff}(O_2)$	$\Delta_{sa}(O_2)$ minus $\Delta_{CTD}(O_2)$ for comparisons between surface water discrete samples (µmol kg^{-1})
$\Delta O_2/Ar$	Biological O_2 supersaturation from USW continuous measurements (%)
$\Delta_{sa}(O_2/Ar)$	Biological O_2 supersaturation from USW discrete sample (%)
$\Delta_{CTD}(O_2/Ar)$	Biological O_2 supersaturation from surface Niskin sample (%)
$\Delta_{diff}(O_2/Ar)$	$\Delta_{sa}(O_2/Ar)$ minus $\Delta_{CTD}(O_2/Ar)$ for comparisons between surface water discrete samples (%)

[1] Most symbols are included here except specific ones that are explained in the corresponding location.

Δ_{sa}(Ar)	Ar supersaturation for discrete samples collected from USW and Niskin surface bottles (%)
ΔAr	Ar supersaturation for continuous USW sampling (%)
f_{buoy}	buoyancy correction (1.00105)
f	volume ratio of water to headspace in sampling bottles (V_{sw}/V_g)
$f(O_2)$-ratio	net community production (N) / gross oxygen production (G)
h	ship's anemometer and barometer height above sea level (m)
ϕ	internally calculated phase (DPhase) for *Aanderaa* optode based on manufacturer coefficients and ϕ_{raw}
ϕ_{sa}	Raw DPhase from *Aanderaa* optode corresponding to the time at discrete samples collection for dissolved O_2 analysis
g	acceleration of the gravity; 9.80665 m s^{-2}
G	Gross photosynthetic oxygen production (mmol m^{-2} d^{-1})
N	Net Community Production (mmol m^{-2} d^{-1})
P	Atmospheric pressure at the barometer height (mbar)
P_0	Atmospheric pressure at the sea surface (mbar)
ρ_{air}	density of air (1.2 kg m^{-3} at 20 ºC)
ρ	Density of water (kg m^{-3})
ρ_{sw}	Density of seawater (kg m^{-3})
ρ_{fw}	Density of fresh water (kg m^{-3}) (≈ 1000 kg m^{-3} at 20 ºC)
S	Sea surface salinity
S_{sa}	Salinity of discrete samples extracted from the *SSS*, corresponding to each discrete samples collection time, t_{sa}
SST	Sea Surface Temperature calibrated (°C)
θ_{int}	Sea Surface Temperature from USW intake sensor (°C)
t_{sa}	time at which the discrete samples for Winkler analysis were taken from the USW flow (Julian days)
t_{evbot}	time at which the discrete samples for O_2/Ar analysis were taken from the USW flow (Julian days)
t_{firing}	firing time of Niskin bottles
T_{air}	Air absolute temperature (K)
θ_{sa}	Temperature of the sample at pickling time (θ_{opt} for USW samples and θ_{surf} for surface Niskin sample), calibrated
θ_{cal}	Temperature calibrated extracted from the *SST* (°C), corresponding to each discrete samples collection time, t_{sa}
θ	Temperature (°C)
θ_{opt}	Sea Surface Temperature from optode (°C) (continuous raw, used as the temperature of the sample for the Winkler measurements)
θ_{CTD}	Temperature from surface Niskin given by the CTD temperature sensor (SBE-35) (°C)
θ_{TSG}	Sea Surface Temperature from TSG (°C)
τ	Underway wind direction given by ship's anemometer (degrees)
τ_{true}	True wind direction relative to ground (degrees)
u	east / west component of the wind velocity relative to the ship
u_{ship}	east / west ship's velocity component
v	north / south component of the wind velocity relative to the ship
v_{ship}	north / south ship's velocity component
u_{10}	Wind speed at 10 m above mean se level (m s^{-1})
U_{32}	Voltage from the ion beam intensity for *m/z* 32 (V)

U_{40}	Voltage from the ion beam intensity for *m/z* 40 (V)
U_{28}	Voltage from the ion beam intensity for *m/z* 28 (V)
V_{20}	volume of Winkler flask at calibration temperature (θ_{cal} = 20 ºC) (ml)
V_1	initial volume of $S_2O_3^{2-}$ during blanks titration (first volume discharged) (ml)
V_2	final volume of $S_2O_3^{2-}$ during blanks titration (second volume discharged) (ml)
V_{blank}	Volume difference between the V_1 and V_2 of the $S_2O_3^{2-}$, discharged to titrate the blanks (ml)
V_{flask}	final volume of Winkler flasks after buoyancy and thermal correction (ml)
V_{KIO3}	volume of the aliquot of the standard solution of KIO_3 (ml)
V_{thio}	volume of $Na_2S_2O_3$ (titrant) discharged (ml)
V_{evbot}	volume of the evacuated bottles (ml)
V_{sw}	Volume of seawater in evacuated sampling bottles
V_g	Volume of headspace in evacuated sampling bottles
z_{mix}	mixed layer depth (m); referred as to MLD as acronymn

References

Agustí, S. and Duarte, C.M., 2005. Threshold of gross primary production for planktonic metabolic balance in the Southern Ocean: An experimental test. *Limnology and Oceanography,* 50, 4, 1334-1339.

An, S., Gardner, W.S. and Kana, T.M., 2001. Simultaneous measurements of denitrification and nitrogen fixation using isotope pairing with membrane inlet mass spectrometry analysis. *Applied Environmental Microbiology,* 67, 3, 1171-1178.

Angert, A., Rachmilevitch, S., Barkan, E. and Luz, B., 2003. Effects of photorespiration, the cytochrome pathway, and the alterntive pathway on the triple isotopic composition of atmospheric O_2. *Global Biogeochemical Cycles,* 17, 1, 30-1 to 30-14.

Antonov, J.I., Locarnini, R.A., Boyer, T.P., Mishonov, A.V. and García, H.E., 2006. Salinity, Levitus, S. In: World Ocean Atlas, 2005, 2 Washington, D.C., 182.

Ardelan, M.V., Holm-Hansen, O., Hewes, C.D., Reiss, C.S., Silva, N.S., Dulaiova, H., Steinnes, E. and Sakshaug, E., 2010. Natural iron enrichment around the Antarctic Peninsula in the Southern Ocean. *Biogeosciences,* 7, 11-25.

Arístegui, J., Montero, M.F., Ballesteros, S., Basterretxea, G. and van Lenning, K., 1996. Planktonic primary production and microbial respiration measures by ^{14}C assimilation and dissolved oxygen changes in coastal waters of the Antarctic Peninsula during austral summer: implications for carbon flux studies. *Marine Ecology Progress Series,* 132, 191-201.

Arrigo, K.R., van Dijken, G.L. and Bushinsky, S., 2008. Primary production in the Southern Ocean, 1997-1996. Journal of Geophysical Research. *Journal of Geophysical Research,* 113, C08004, 1-27.

Assonov, S.S. and Brenninkmeijer, C.A.M., 2003. On the ^{17}O correction for CO_2 mass-spectrometric analysis. *Rapid Communications in Mass Spectrometry,* 17, 1007-1016.

Bakker, D.C.E., Hoppema, M., Schröder, M., Geibert, W. and de Baar, H.J.W., 2008. A rapid transition from ice covered CO_2-rich waters to a biologically mediated CO_2 sink in the eastern Weddell Gyre. *Biogeosciences,* 5, 1373-1386.

Balch, W., Evans, R., Brown, J., Feldman, G., McClain, C. and Esaias, W., 1992. The remote sensing of ocean primary productivity: use of a new data compilation to test satellite algorithms. *Journal of Geophysical Research,* 97, C2, 2279-2293.

Banse, K., 1996. Low seasonality of low concentrations of surface chlorophyll in the Subantarctic water ring: underwater irradiance, iron, or grazing? *Progress in Oceanography,* 37, 241-291.

Barkan, E. and Luz, B., 2003. High-precision measurements of $^{17}O/^{16}O$ and $^{18}O/^{16}O$ of O_2 and O_2/Ar ratio in air. *Rapid Communications in Mass Spectrometry*, 17, 2809-2814.

Barkan, E. and Luz, B., 2005. High precision measurements of $^{17}O/^{16}O$ and $^{18}O/^{16}O$ ratios in H_2O. *Rapid Communications in Mass Spectrometry*, 19, 3737-3742.

Barré, N., Provost, C., Sennechael, N. and Hak Lee, J., 2008. Circulation in the Ona Basin, southern Drake Passage. *Journal of Geophysical Research*, 113, C04033, 1 - 25.

Behrenfeld, M.J., Boss, E., Siegel, D.A. and Shea, D.M., 2005. Carbon-based ocean productivity and phytoplankton physiology from space. *Global Biogeochemical Cycles*, 19, GB1006, 1 - 14.

Bellerby, R.G.J., Turner, D.R. and Robertson, J.E., 1995. Surface pH and pCO_2 distributions in the Bellingshausen Sea, Southern Ocean, during the early Austral summer. *Deep-Sea Research II*, 42, 4-5, 1093-1107.

Bender, M., Orchardo, J., Dickson, M.-L., Barber, R. and Lindley, S., 1999. In vitro O_2 fluxes compared with ^{14}C production and other rate terms during the JGOFS Equatorial Pacific experiment. *Deep-Sea Research Part I: Oceanographic Research Papers*, 46, 4, 637-654.

Bender, M., Sowers, T. and Labeyrie, L., 1994b. The Dole effect and its variations during the last 130,000 years as measured in the Vostok ice core. *Global Biogeochemical Cycles*, 8, 3, 363-376.

Bender, M.L., Dickson, M.-L. and Orchardo, J., 2000. Net and gross production in the Ross Sea as determined by incubation experiments and dissolved O_2 studies. *Deep-Sea Research II*, 47, 3147-3158.

Bender, M.L., Tans, P.P., Ellis, T.J., Orchardo, J. and Habfast, K., 1994a. A high precision isotope ratio mass spectrometry method for measuring the O_2/N_2 ratio of air. *Geochimica et Cosmochimica Acta*, 58, 21, 4751-4758.

Benson, B.B. and Krause, D.J., 1984. The concentration and isotopic fractionation of oxygen dissolved in freshwater and seawater in equilibrium with the atmosphere. *Limnology and Oceanography*, 29, 3, 620-632.

Bigeleisen, J. and Mayer, M.G., 1947. Calculation of equilibrium constants for isotopic exchange reactions. *Journal of Chemical Physics*, 15, 5, 261-267.

Blain, S., Quéguiner, B., Armand, L., Belviso, S., Bombled, B., Bopp, L., Bowie, A.R., Brunet, C., Brussaard, C., Carlotti, F., Christaki, U., Corbiere, A., Durand, I., Ebersbach, F., Fuda, J., Garcia, N., Gerringa, L., Griffiths, B., Guigue, C., Guillerm, C., Jacquet, S., Jeandel, C., Laan, P., Lefevre, D., Lo Monaco, C., Maltis, A., Mosseri, J., Obernosterer, I., Park, Y., Picheral, M., Pondaven, P., Remenyi, T., Sandroni, V., Sarthou, G., Savoye, N., Scouarnec, L., Souhaut, M., Thuiller, D., Timmermanns, K.R., Trull, T.W., Uitz, J., van Beek, P., Veldhuis, M., Vincent, D.,

Viollier, E., Vong, L. and Wagener, T., 2007. Effect of natural iron fertilization on carbon sequestration in the Southern Ocean. *Nature*, 446, 1070-1074.

Blunier, T., Barnett, B., Bender, M.L. and Hendricks, M.B., 2002. Biological oxygen productivity during the last 60,000 years from triple oxygen measurements. *Global Biogeochemical Cycles*, 16, 3, 3-1 - 3-15.

Boutin, J. and Merlivat, L., 2009. New in situ estimates of carbon biological production rates in the Southern Ocean from CARIOCA drifter measurements. *Geophysical Research Letters*, 36, L13608, 1 - 6.

Boyd, P.W., Crossley, A.C., DiTullio, G.R., Griffiths, F.B., Hutchins, D.A., Queguiner, B., Sedwick, P.N. and Trull, T.W., 2001. Control of phytoplankton growth by iron supply and irradiance in the subantarctic Southern Ocean: Experimental results fron the SAZ project. *Journal of Geophysical Research*, 106, C12, 31573-31583.

Boyd, P.W., LaRoche, J., Gall, M., Frew, R. and McKay, R.M., 1999. Role of iron, light, and silicate in controlling algal biomass in subantarctic waters SE of New Zealand. *Journal of Geophysical Research*, 104, C6, 13395-13408.

Boyd, P.W., Robinson, C., Savidge, G. and Williams, P.J.l., 1995. Water column and sea-ice primary production during Austral spring in the Bellingshausen Sea. *Deep Sea Research Part II: Topical Studies in Oceanography*, 42, 4-5, 1177-1200.

Boyd, P.W., Watson, A.J., Law, C.S., Abraham, E.R., Trull, T.W., Murdoch, R., Bakker, D.C.E., Bowie, A.R., Buesseler, K.O., Chang, H., Charette, M., Croot, P., Downing, K., Frew, R., Gall, M., Hadfield, M., Hall, J., Harvey, M., Jameson, G., LaRoche, J., Liddicoat, M.I., Ling, R., Maldonado, M.T., McKay, R.M., Nodder, S., Pickmere, S., Pridmore, R., Rintoul, S.R., Safi, K., Sutton, P., Strzepek, R., Tanneberger, K., Turner, S., Waite, A. and Zeldis, J., 2000. A mesoscale phytoplankton bloom in the polar Southern Ocean stimulated by iron fertilization. *Nature*, 407, 695-702.

Brainerd, K.E. and Gregg, M.C., 1995. Surface mixed and mixing layer depths. *Deep-Sea Research I*, 42, 4-5, 1177-1200.

Brimblecombe, P., 1996. Air composition and chemistry. 2nd ed., Cambridge environmental chemistry series 6, Cambridge: Cambridge University Press, 249.

Broecker, W.S. and Peng, T.H., 1982. Tracers in the Sea. ed., Palisades, New York: Lamont-Doherty Geological Laboratory, Columbia University,

Campbell, J., Antoine, D., Armstrong, R., Arrigo, K.R., Balch, W., Barber, R., Behrenfeld, M., Bidigare, R., Bishop, J., Carr, M., Esaias, W., Falkowski, P.G., Hoepffner, N., Iverson, R., Kiefer, D., Lohrenz, S., Marra, J., Morel, A., Ryan, J., Vedernikov, V., Waters, K., Yentsch, C.S. and Yoder, J., 2002. Comparison of algorithms for estimating ocean primary production from surface chlorophyll, temperature, and irradiance. *Global Biogeochemical Cycles*, 16, 3, 1035.

Carpenter, J.H., 1965. The accuracy of the Winkler method for dissolved oxygen analysis. *Limnology and Oceanography,* 10, 135-140.

Carr, M., Friedrichs, M.A.M., Schmeltz, M., A.M., N., Antoine, D., Arrigo, K.R., Asanuma, I., Aumont, O., Barber, R.T., Behrenfeld, M., Bidigare, R., Buitenhuis, E.T., Campbell, J., Ciotti, A., Dierssen, H., Dowell, M., Dunne, J., Esaias, W., Gentili, B., Gregg, W., Groom, S., Hoepffner, N., Ishizaka, J., Kameda, T., Le Quéré, C., Lohrenz, S., Marra, J., Mélin, F., Moore, J.K., Morel, A., Reddy, T.E., Ryan, J., Scardi, M., Smyth, T.J., Turpie, K., Tilstone, G.H., Waters, K. and Yamanaka, Y., 2006. A comparison of global estimates of marine primary production from ocean color. *Deep-Sea Research II,* 53, 741-770,

Cartaxana, P. and Lloyd, D., 1999. N_2, N_2O and O_2 profiles in a Tagus estuary salt marsh. *Estuarine, Coastal and Shelf Science,* 48, 6, 751.

Cassar, N., Barnett, B., Bender, M.L., Kaiser, J., Hamme, R.C. and Tilbrook, B., 2009. Continuous High-Frequency Dissolved O_2/Ar Measurements by Equilibrator Inlet Mass Spectrometry. *Analytical Chemistry,* 81, 1855-1864.

Cassar, N., Bender, M.L., Barnett, B., Fan, S., Moxim, W.J., Levy II, H. and Tilbrook, B., 2007. The Southern Ocean biological response to aeolian iron deposition. *Science,* 317, 1067-1070,

Castro-Morales, K. and Kaiser, J., 2010, *manuscript in preparation*. Using dissolved oxygen measurements to determine mixed layer depths in the Bellingshausen Sea. *Manuscript in preparation.,*

Chaigneau, A., Morrow, R.A. and Rintoul, S.R., 2004. Seasonal and interannual evolution of the mixed layer in the Antarctic Zone south of Tasmania. *Deep-Sea Research I,* 51, 2047-2072.

Chester, R., 2000. Marine Geochemistry. Second edition ed., Oxford, UK: Blackwell Science Ltd, 506

Cisewski, B., Strass, V.H., Losch, M. and Prandke, H., 2008. Mixed layer analysis of a mesoscale eddy in the Antarctic Polar Front Zone. *Journal of Geophysical Research,* 113, C05017, 1-19.

Cisewski, B., Strass, V.H. and Prandke, H., 2005. Upper-ocean vertical mixing in the Antarcic Polar Front Zone. *Deep-Sea Research II,* 52, 1087-1108.

Cliff, S.S. and Thiemens, M.H., 1997. First measurements of the $^{18}O/^{16}O$ and $^{17}O/^{16}O$ ratios in stratospheric nitrous oxide: A mass-independent anomaly. *Journal of Geophysical Research,* 104, D13, 16171-16175.

Coale, K.H., Johnson, K.S., Chavez, F.P., Buesseler, K.O., Barber, R.T., Brzezinski, M.A., Cochlan, W.P., Millero, F.J., Falkowski, P.G., Bauer, J.E., Wanninkhof, R., Kudela, R.M., Altabet, M.A., Hales, B.E., Takahashi, T., Landry, M.R., Bidigare, R.B., Wang, X., Chase, Z., Strutton, P.G., Friederich, G.E., Gorbunov, M.Y., Lance, V.P., Hilting, A.K., Hiscock, M.R., Demarest, M., Hiscock, W.T., Sullivan, K.F.,

Tanner, S.J., Gordon, R.M., Hunter, C.N., Elrod, V.A., Fitzwater, S.E., Jones, J.L., Tozzi, S., Koblizek, M., Roberts, A.E., Herndon, J., Brewster, J., Ladizinsky, N., Smith, G., Cooper, D., Timothy, D., Brown, S.L., Selph, K.E., Sheridan, C.C., Twining, B.S. and Johnson, Z.I., 2004. Southern Ocean Iron Enrichment Experiment: carbon cycling in high- and low-Si waters. *Science,* 304, 408-414.

Cook, A.J., A.G Fox, D.G. Vaughan and J.G. Ferrigno, 2005. Retreating Glacier Fronts on the Antarctic Peninsula over the Past Half-Century. *Science,* 308, 541-544.

Craig, H. and Hayward, T., 1987. Oxygen supersaturation in the ocean: Biological versus physical contributions. *Science,* 235, 4785, 199-202.

Culberson, C.H., 1991. Dissolved Oxygen. *WHP Operation Methods,* 1-15.

de Baar, H.J.W., de Jong, J.T.M., Nolting, R.F., Timmermanns, K.R., M.A., v.L., Bathmann, U.V., van der Loeff, M.R. and Sildam, J., 1999. Low dissolved Fe and the absence of diatom blooms in remote Pacific waters of the Southern Ocean. *Marine Chemistry,* 66, 1-34.

de Boyer Montégut, C., Madec, G., Fisher, A.S., Lazar, A. and Iudicone, D., 2004. Mixed layer depth over the global ocean: an examination of profile data and profile-based climatology. *Journal of Geophysical Research,* 109, C12003, 1-20.

de Boyer Montégut, C., Mignot, J., Lazar, A. and Cravatte, S., 2007. Control of salinity on the mixed layer depth in the world ocean: 1. General description. *Journal of Geophysical Research,* 112, C06011, 1-12.

Dickson, A.G., 1996. Determination of dissolved oxygen in seawater by Winkler titration, World Ocean Circulation Experiment. In: WOCE Operations Manual. Volume 3: The Observational Programme. Section 3.1: WOCE Hydrographic Programme. Part 3.1.3: WHP Operations and Methods, 3 Woods Hole, Massachussetts, USA, 1-13.

Dickson, M.-L. and Orchardo, J., 2001. Oxygen production and respiration in the Antarctic Polar Front during the austral spring and summer. *Deep-Sea Research II,* 48, 4101-4126.

Dole, M. and Jenks, G., 1944. Isotopic compostion of photosynthetic oxygen. *Science,* 100, 409.

Dong, S., Gille, S.T., Sprintall, J. and Gentemann, C., 2006. Validation of the advanced microwave scanning radiometer for the earth observing system (AMSR-E) sea surface temperature in the Southern Ocean. *Journal of Geophysical Research,* 111, C04002, 1-16.

Dong, S., Sprintall, J., Gille, S.T. and Talley, L., 2008. Southern Ocean mixed-layer depth from Argo float profiles. *Journal of Geophysical Research,* 113, C06013, 1-12.

Drennan, W.M., Taylor, P.K. and Yelland, M.J., 2005. Parameterizing the Sea Surface Roughness. *Journal of Physical Oceanography,* 35, 835-848.

Ducklow, H.W., Baker, K.S., Martinson, D.G., Quetin, L.B., Ross, R.M., Smith, R.C., Stammerjohn, S., Vernet, M. and Fraser, W., 2007. Marine pelagic ecosystem: the West Antarctic Peninsula. *Philosophical Transactions of The Royal Society*, 362, 67-94.

Ducklow, H.W., Fraser, W., Karl, D.M., Quetin, L.B., Ross, R.M., Smith, R.C., Stammerjohn, S., Vernet, M. and Daniels, R.M., 2006. Water-column processes in the West Antarctic Peninsula and the Ross Sea: Interannual variations and foodweb structure. *Deep-Sea Research II*, 53, 834-852.

Dugdale, R.C., Wilkerson, F.P. and Minas, H.J., 1995. The role of a silicate pump in driving new production. *Deep-Sea Research I*, 42, 5, 697-719.

Dulaiova, H., Ardelan, M.V., Henderson, P.B. and Charette, M.A., 2009. Shelf-derived iron inputs drive biological productivity in the southern Drake Passage. *Global Biogeochemical Cycles*, 23, GB4014, 1-14.

Emerson, S., 1987. Seasonal oxygen cycles and biological new production in surface waters of the subarctic Pacific Ocean. *Journal of Geophysical Research*, 92, C6, 6535-6544.

Emerson, S. and Hedges, J.I., 2008. Chemical Oceanography and the Marine Carbon Cycle. ed., New York: Cambridge University Press, 453

Emerson, S., Quay, P., Stump, C., Wilbur, D. and Schudlich, R., 1995. Chemical tracers of productivity and respiration in the subtropical Pacific Ocean. *Journal of Geophysical Research*, 100, C8, 15,873-15,887.

Emerson, S., Stump, C. and Nicholson, D., 2008. Net biological oxygen production in the ocean: Remote in situ measurements of O_2 and N_2 in surface waters. *Global Biogeochemical Cycles*, 22, GB3023, 1-13.

Emerson, S., Stump, C., Wilbur, D. and Quay, P., 1991. Accurate measurement of O_2, N_2 and Ar gases in water and the solubility of N_2. *Marine Chemistry*, 64, 331-347.

Emerson, S., Stump, C., Wilbur, D. and Quay, P., 1999. Accurate measurement of O_2, N_2, and Ar gases in water and the solubility of N_2. *Marine Chemistry*, 64, 4, 337-347.

Eppley, R.W. and Peterson, B.J., 1979. Particulate organic matter flux and planktonic new production in the deep ocean. *Nature*, 282, 677-680.

Gaarder, T. and Gran, H.H., 1927. Investigation of the production of plankton in the Oslo Fjord. *Rapp. P.v.cons.Int.Explor.Mer.*, 42, 1-48.

Garcia, H.E., Boyer, T.P., Levitus, S., Locarnini, R.A. and Antonov, J.I., 2005b. Climatological annual cycle of upper ocean oxygen content anomaly. *Geophysical Research Letters*, 32, L05611, 1-4.

Garcia, H.E. and Gordon, L.I., 1992. Oxygen solubility in seawater: better fitting equations. *Limnology and Oceanography,* 37, 6, 1307-1312.

Garcia, H.E. and Gordon, L.I., 1993. Erratum: Oxygen solubility in seawater: Better fitting equations. *Limnology and Oceanography,* 38, 3, 656.

Garcia, H.E. and Keeling, R.F., 2001. On the global oxygen anomaly and air-sea flux. *Journal of Geophysical Research,* 106, C12, 31155-31166.

Garcia, H.E., Locarnini, R.A., Boyer, T.P. and Antonov, J.I., 2006. Dissolved Oxygen, Apparent Oxygen Utilization and Oxygen Saturation, Levitus, S. In: World Ocean Atlas, 2005, 3 Washington, D.C., 342.

Garibotti, I.A., Vernet, M. and Ferrario, M.E., 2005. Annually recurrent phytoplanktonic assemblages during summer in the seasonal ice zone west of the Antarctic Peninsula (Southern Ocean). *Deep Sea Research I,* 52, 1823-1841.

Garibotti, I.A., Vernet, M. and Ferrario, M.E., 2005a. Annually recurrent phytoplanktonic assemblages during summer in the seasonal ice zone west of the Antarctic Peninsula (Southern Ocean). *Deep Sea Research I,* 52, 1823-1841.

Garibotti, I.A., Vernet, M., Ferrario, M.E., Smith, R.C., Ross, R.M. and Quetin, L.B., 2003. Phytoplankton spatial distribution patterns along the western Antarctic Peninsula (Southern Ocean). *Marine Ecology Progress Series,* 261, 21-39.

Garibotti, I.A., Vernet, M., Smith, R.C. and Ferrario, M.E., 2005b. Interannual variability in the distribution of the phytoplankton standing stock across the seasonal sea-ice zone west of the Antarctic Peninsula. *Journal of Plankton Research,* 27, 8, 825-843.

Gille, S.T., 1994a. Mean sea surface height of the Antarctic Circumpolar Current from Geosat data: method and application. *Journal of Geophysical Research,* 99, C9, 18255 - 18273.

Gille, S.T., 1994b. Mean sea surface height of the Antarctic Circumpolar Current from Geosat data: method and application. *Journal of Geophysical Research,* 99, C9, 18255-18273.

Gille, S.T., 2002. Warming of the Southern Ocean since the 1950s. *Science,* 295, 1275-1277.

Glueckauf, E., 1951. The composition of atmospheric air, Malone, T.F. In: Compendium of Meteorology, Boston, MA., 3-10.

Gordon, A.L., Chen, C.T.A. and Metcalf, W.G., 1984. Winter Mixed Layer Entrainment of Weddell Deep Water. *Journal of Geophysical Research,* 89, C1, 637-640.

Gordon, A.L. and Huber, B.A., 1990. Southern Ocean winter mixed layer. *Journal of Geophysical Research,* 95, C7, 11655-11672.

Green, E.J. and Carrit, D.E., 1967. Oxygen solubility in sea water: thermodynamic influence of sea salt. *Science,* 157, 3785, 134-230.

Guéguen, C. and Tortell, P.D., 2008. High-resolution measurements of Southern Ocean CO_2 and O_2/Ar by membrane inlet mass spectrometry. *Marine Chemistry,* 108, 184-194.

Guy, R.D., Fogel, M.L. and Berry, J.A., 1993. Photosynthetic fractionation of the stable isotopes of oxygen and carbon. *Plant Physiol.,* 101, 1, 37-47.

Hamme, R.C. and Emerson, S., 2002. Mechanisms controlling the global oceanic distribution of the inert gases argon, nitrogen and neon. *Geophysical Research Letters,* 29, 23, 1-4.

Hamme, R.C. and Emerson, S.R., 2004. The solubility of neon, nitrogen and argon in distilled water and seawater. *Deep-Sea Research Part I: Oceanographic Research Papers,* 51, 11, 1517-1528.

Hamme, R.C. and Emerson, S.R., 2006. Constraining bubble dynamics and mixing with dissolved gases: Implications for productivity measurements by oxygen mass balance. *Journal of Marine Research,* 64, 73-95.

Hanawa, K. and Talley, L., 2001. 5.4 Mode Waters, Siedler, G., Church, J. and Gould, J. In: Ocean Circulation and Climate: Section 5, Formation and transport of water masses, 77 London,

Hartnett, H., E. and Seitzinger, S.P., 2003. High-resolution nitrogen gas profiles in sediment porewaters using a new membrane probe for membrane-inlet mass spectrometry. *Marine Chemistry,* 83, 23-30.

Heimann, M., 1995. The global atmospheric tracer model TM2. *Tech. Rep.,* 10-53.

Helman, Y., Barkan, E., Eisendstadt, D., Luz, B. and Kaplan, A., 2005. Fractionation of the three stable oxygen isotopes by oxygen-producing and oxygen-consuming reactions in photosynthetic organisms. *Plant Physiology,* 138, 2292-2298.

Hendricks, M.B., Bender, M.L. and Barnett, B., 2005. Triple oxygen isotope composition of dissolved O_2 in the equatorial Pacific: A tracer of mixing, production, and respiration. *Journal of Geophysical Research,* 110, C12021, 1-17.

Hendricks, M.B., Bender, M.L. and Barnett, B.A., 2004. Net and gross O_2 production in the Southern Ocean from measurements of biological O_2 saturation and its triple isotope composition. *Deep-Sea Research Part I: Oceanographic Research Papers,* 51, 11, 1541-1561.

Hense, I., Timmermann, R., Beckmann, A. and Bathmann, U.V., 2003. Regioanl ecosystem dynamics in the ACC: simulations with a three-dimensional ocean-plankton model. *Journal of Marine Systems,* 42, 31-51,

Hewes, C.D., Reiss, C.S. and Holm-Hansen, O., 2009. A quantitative analysis of sources for summertime phytoplankton variability over 18 years in the South Shetland Islands (Antarctica) region. *Deep-Sea Research I,* 56, 1230-1241,

Hewes, C.D., Reiss, C.S., Kahru, M., Mitchell, B.G. and Holm-Hansen, O., 2008. Control of phytoplankton biomass by dillution and mixed layer depth in the western Weddell-Scotia Confluence. *Marine Ecology Progress Series,* 366, 15-29.

Heywood, K.J., Naveira Garabato, A.C., Stevens, D.P. and Muench, R.D., 2004. On the fate of the Antarctic Slope Front and the origin of the Weddell Front. *Journal of Geophysical Research,* 109, C06021, 1-13.

Hiraike, Y. and Ikeda, M., 2009. Descending surface water at the Antarctic Marginal Ice Zone and its contribution to I
Intermediate Water: an ice-ocean model. *Journal of Oceanography,* 65, 587-603.

Hiscock, M.R., Marra, J., W.O., S., Goericke, R., Measures, C.I., Vink, S., Olson, R.J., Sosik, H.M. and Barber, R.T., 2003. Primary productivity and its regulation in the Pacific Sector of the Southern Ocean. *Deep-Sea Research II,* 50, 533-558.

Holland, P.R., Jenkins, A. and Holland, D.M., 2010. Ice and ocean processes in the Bellingshausen Sea, Antarctica. *Journal of Geophysical Research,* 115, C05020, 1-16.

Holm-Hansen, O., Kahru, M. and Hewes, C.D., 2005. Deep chlorophyll a maxima (DCMs) in pelagic Antarctic waters. II. Relation to bathymetric reatures and dissolved iron concentrations. *Marine Ecology Progress Series,* 297, 71-81.

Holm-Hansen, O., Kahru, M., Hewes, C.D., Kawaguchi, S., Kameda, T., Sushin, V.A., Krasovski, I., Priddle, J., Korb, R., Hewitt, R.P. and Mitchell, B.G., 2004. Temporal and spatial distribution of chlorophyll-a in surface waters of the Scotia Sea as determined by both shipboard measurements and satellite data. *Deep-Sea Research II,* 51, 1323-1331.

Holte, J. and Talley, L., 2009. A new algorithm for finding mixed layer depths with applications to Argo data and Subantarctic Mode Water. *Journal of Atmospheric and Oceanic Technology,* 29, 9, 1920-1939.

Hopkinson, B., Greg Mitchell, B., Reynolds, R.A., Wang, H., Selph, K.E., Measures, C.I., Hewes, C.D., Holm-Hansen, O. and Barbeau, K.A., 2007. Iron limitation across chlorphyll gradients in the southern Drake Passage: Phytoplankton responses to iron addition and photosynthetic indicators of iron stress. *Limnology and Oceanography,* 55, 6, 2540-2554.

Hoppema, M., Middag, R., De Baar, H.J.W., Fahrbach, E., van Weerlee, E.M. and Thomas, H., 2007. Whole season net community production in the Weddell Sea. *Polar Biology,* 31, 101-111.

Howard, S.L., Hyatt, J. and Padman, L., 2004. Mixing in the pycnocline over the western Antarctic Peninsula shelf during Southern Ocean GLOBEC. *Deep-Sea Research II,* 51, 1965-1979.

Hutchins, D.A., Sedwick, P.N., DiTullio, G.R., Boyd, P.W., Queguiner, B., Griffiths, F.B. and Crossley, A.C., 2001. Control of phytoplankton growth by iron and silicic acid availability in the subantarctic Southern Ocean: Experimental results from the SAZ project. *Journal of Geophysical Research,* 106, C12, 31559-31572.

Ishii, M., Inoue, H.Y. and Matsueda, H., 2002. Net community production in the marginal ice zone and its importance for the variability of the oceanic pCO_2 in the southern Ocean south of Australia. *Deep-Sea Research II,* 49, 1691-1706.

Jacobs, S.S., Hellmer, H.H. and Jenkins, A., 1996. Antarctic ice sheet melting in the Southeast Pacific. *Geophysical Research Letters,* 23, 9, 957-960.

Jacques, G., 1991. Is the concept of new production-regenerated production valid for the Southern Ocean? *Marine Chemistry,* 35, 273-286.

Jenkins, A. and Jacobs, S.S., 2008. Circulation and melting beneath George VI Ice Shelf, Antarctica. *Journal of Geophysical Research,* 113, C04013, 1-18.

Johnson, H.K., 1999. Simple expressions for correcting wind speed data for elevation. *Coastal Engineering,* 36, 263-269.

Johnson, R.C., Cooks, R.G., Allen, T.M., Cisper, M.E. and Hemberger, P.H., 2000. Membrane introduction mass spectrometry: trends and applications. *Mass Spectrometry Reviews,* 19, 1-37.

Juranek, L.W., Hamme, R.C., Kaiser, J., Wanninkhof, R. and Quay, P.D., 2010. Evidence of O2 consumption in underway seawater lines: Implications for air-sea O2 and CO2 fluxes. *Geophysical Research Letters,* 37, L01601, 1-5.

Juranek, L.W. and Quay, P.D., 2005. In vitro and in situ gross primary and net community production in the North Pacific Subtropical Gyre using labeled and natural abundance isotopes of dissolved O_2. *Global Biogeochemical Cycles,* 19, GB3009, 1-15.

Juranek, L.W. and Quay, P.D., 2010. Basin-wide photosynthetic production rates in the subtropical and tropical Pacific Ocean determined from dissolved oxygen isotope ratio measurements. *Global Biogeochemical Cycles,* 24, GB2006, 1-17.

Kahru, M., Mitchell, B.G., Gille, S.T., Hewes, C.D. and Holm-Hansen, O., 2007. Eddies enhance biological production in the Weddell-Scotia Confluence of the Southern Ocean. *Geophysical Research Letters,* 34, L14603, 1 - 6.

Kaiser, J., Reuer, M.K., Barnett, B. and Bender, M.L., 2005. Marine productivity estimates from continuous oxygen/argon ratio measurements by shipboard membrane inlet mass spectrometry. *Geophysical Research Letters,* 32, L19605, 1-5.

Kaiser, J., Röckmann, T. and Brenninkmeijer, C.A.M., 2004. Contribution of mass-dependent fractionation to the oxygen isotope anomaly of atmospheric nitrous oxide. *Journal of Geophysical Research,* 109, D3, D03305

Kana, T.M., 1990. Light-dependent oxygen cycling measured by and oxygen-18 isotope dilution technique. *Marine Ecology Progress Series,* 64, 293-300.

Kana, T.M., Darkangelo, C., Hunt, M.D., Oldham, J.B., Bennett, G.E. and Cornwell, J.C., 1994. Membrane inlet mass spectrometer for rapid high-precision determination of N_2, O_2, and Ar in environmental water samples. *Analytical Chemistry*, 66, 23, 4166-4170.

Kara, A.B., Rochford, P.A. and Hurlburt, H.E., 2003. Mixed layer depth variability over the global ocean. *Journal of Geophysical Research,* 108, C3, 3079, doi:10.1029/2000JC000736.

Keeling, R.F. and Garcia, H.E., 2002. The change in oceanic O_2 inventory associated with recent global warming. *Proc. U.S. Natl. Acad. Sci.,* 99, 7848-7853.

Keeling, R.F. and Shertz, S.R., 1992. Seasonal and interannual cariations in atmospheric oxygen and implications for the global carbon cycle. *Nature,* 358, 6389, 723-727.

Ketola, R.A., Kotiaho, T., Cisper, M.E. and Allen, T.M., 2002. Environmental applications of membrane introduction mass spectrometry. *Journal of Mass Spectrometry*, 37, 457-476.

Ketola, R.A., Mansikka, T., Ojala, M., Kotiaho, T. and Kostiainen, R., 1997. Analysis of volatile organic sulfur compounds in air by membrane inlet mass spectrometry. *Rapid Communications in Mass Spectrometry,* 69, 22, 4536-4539.

Kibelka, G.P.G., Short, R.T., Toler, S.K., Edkins, J.E. and Byrne, R.H., 2004. Field-deployed underwater mass spectrometers for investigations of transient chemical systems. *Talanta,* 64, 4, 961-969.

Kirkwood, D.S., 1992. Stability of solutions of nutrient salts during storage. *Marine Chemistry,* 38, 151-164.

Körtzinger, A., Schimanski, J. and Send, U., 2005. High quality oxygen measurements from profiling floats: a promising new technique. *Journal of Atmospheric and Oceanic Technology,* 22, 302-308.

Körtzinger, A., Send, U., Wallace, D.W.R., Karstensen, J. and DeGrandpre, M., 2008. Seasonal cycle of O_2 and pCO_2 in the central Labrador Sea: Atmospheric, biological, and physical implications. *Global Biogeochemical Cycles,* 22, GB1014, 1-16.

Lämmerzahl, P., Röckmann, T., Brenninkmeijer, C.A.M., Krankowsky, D. and Mauersberger, K., 2002. Oxygen isotope composition of stratospheric carbon dioxide. *Geophysical Research Letters,* 29, 12, 10.1029/2001GL014343.

Law, C.S., Abraham, E.R., Watson, A.J. and Liddicoat, M.I., 2003. Vertical eddy diffusion and nutrient supply to the surface mixed layer of the Antarctic Circumpolar Current. *Journal of Geophysical Research,* 108, C8, 3272, 28 (1-14).

Laws, E.A., 1991. Photosynthetic quotients, new production and net community production in the open ocean. *Deep-Sea Research,* 38, 1, 143-167.

Le Quéré, C., Aumont, O., Monfray, P. and Orr, J.C., 2003. Propagation of climatic events on ocean stratification, marine biology, and CO_2: case studies over the 1979-1999 period. *Journal of Geophysical Research,* 108, C12, 1-7.

Le Quéré, C., Rödenbeck, C., Buitenhuis, E.T., Conway, T.J., Langenfelds, R., Gomez, A., Lbuschagne, C., Ramonet, M., Nakazawa, T., Metzl, N., Gillet, N. and Heimann, M., 2007. Saturation of the Southern Ocean CO_2 sink due to recent climate change. *Science,* 316, 1735-1738.

Legendre, L., Demers, S., Yentsch, M. and Yentsch, C.S., 1983. The ^{14}C method: patterns of dark CO_2 fixation and DCMU correction to replace the dark bottle. *Limnology and Oceanography,* 28, 5, 996-1003.

Lenton, A. and Matear, R.J., 2007. Role of the Southern Annular Mode (SAM) in Southern Ocean CO_2 uptake. *Global Biogeochemical Cycles,* 21, GB2016, 1-17.

Letelier, R.M., Abbott, M.R. and Karl, D.M., 1997. Chlorophyll natural fluorescence response to upwelling events in the Southern Ocean. *Geophysical Research Letters,* 24, 4, 409-412.

Levitus, S., 1992. Climatological atlas of the world ocean. NOAA. Technical report 13, Washington, D.C., 173.

Li, W.J. and Meijer, H.A.J., 1998. The use of electrolysis for accurate $\delta^{17}O$ and $\delta^{18}O$ isotope measurements in water. *Isotopes in Environmental and Health Studies,* 34, 349-369.

Liss, P.S., 2001. Chapter 3: "The earth system: a physiological perspective", Ehlers, E. and Krafft, T. In: Understanding the earth system: compartments, processes and interactions, Berlin, 272.

Liss, P.S., Chuck, A.L., Turner, S.M. and Watson, A.J., 2004. Air-sea gas exchange in Antarctic waters. *Antarctic Science,* 16, 4, 517-529.

Liss, P.S. and Merlivat, L., 1986. Air-sea exchange rates: introduction and synthesis. ed., The role of Air-Sea Echange in Geochemical Cycling, D. Reidel Dordrecht, 113-127

Liss, P.S. and Slater, P.G., 1974. Flux of Gases across the Air-Sea interface. *Nature,* 247, 181-184.

Locarnini, R.A., Mishonov, A.V., Antonov, J.I., Boyer, T.P. and García, H.E., 2006. Temperature, Levitus, S. In: World Ocean Atlas, 2005, 1 Washington, D.C., 182.

Lorbacher, K., Dommenget, D., Niiler, P. and Köhl, A., 2006. Ocean mixed layer depth: A subsurface proxy of ocean-atmosphere variability. *Journal of Geophysical Research,* 111, C07010, 1-22.

Lovenduski, N.S., Gruber, N., Doney, S.C. and Lima, I.D., 2007. Enhanced CO_2 outgassing in the Southern Ocean from a positive phase of the Southern Annular Mode. *Global Biogeochemical Cycles,* 21, GB2026, 1-14.

Lukas, R. and Lindstrom, E., 1999. The mixed layer of the western equatorial Pacific Ocean. *Journal of Geophysical Research,* 96, 3343-3357.

Luz, B. and Barkan, E., 2000. Assessment of oceanic productivity with the triple-isotope composition of dissolved oxygen. *Science,* 288, 5473, 2028-2031.

Luz, B. and Barkan, E., 2002. Tracing mixing in the upper ocean with the three oxygen isotopes. *Geochimica et Cosmochimica Acta,* 66, 16, supplement, A466.

Luz, B. and Barkan, E., 2005. The isotopic ratios $^{17}O/^{16}O$ and $^{18}O/^{16}O$ in molecular oxygen and their significance in biogeochemistry. *Geochimica et Cosmochimica Acta,* 69, 5, 1099.

Luz, B. and Barkan, E., 2009. Net and gross oxygen production from O_2/Ar, $^{17}O/^{16}O$ and $^{18}O/^{16}O$ ratios. *Aquatic Microbial Ecology,* 56, 133-145.

Luz, B., Barkan, E., Bender, M.L., Thiemens, M.H. and Boering, K.A., 1999. Triple-isotope composition of atmospheric oxygen as a tracer of biosphere productivity. *Nature,* 400, 547-550.

Luz, B., Barkan, E. and Sagi, Y., 2002. Evaluation of community respiratory mechanisms with oxygen isotopes: A case study in Lake Kinneret. *Limnology and Oceanography,* 47, 1, 33-42.

Marrari, M., Hu, C. and Daly, K., 2006. Validation of SeaWiFS chlorophyll a concentrations in the Southern Ocean: A revisit *Remote Sensing of Environment,* 105, 367-375.

Martin, J.H., Fitzwater, S.E. and Gordon, M.B., 1990a. Iron deficiency limits phytoplankton growth in Antarctic waters. *Global Biogeochemical Cycles,* 4, 1, 5-12.

Martin, J.H., Gordon, R.M. and Fitzwater, S.E., 1991. The case for iron. *Limnology and Oceanography,* 36, 8, 1793-1802.

Matear, R.J., Hirst, A.C. and McNeil, B.I., 2000. Changes in dissolved oxygen in the Southern Ocean with climate change. *Geochemistry Geophysics Geosystems,* 1, 2000GC000086, 1-12.

McLinden, C.A., Prather, M.J. and Johnson, M.S., 2003. Global modeling of the isotopic analogues of N_2O: Stratospheric distributions, budgets, and the ^{17}O-^{18}O mass-independent anomaly. *Journal of Geophysical Research,* 108, D8, 4233, doi:10.1029/2002JD002560.

McNeil, B.I., Metzl, N., Key, R.M., Matear, R.J. and Corbiere, A., 2007. An empirical estimate of the Southern Ocean air-sea CO_2 flux. *Global Biogeochemical Cycles,* 21, GB3011, 1-16.

Mengesha, S., Dehairs, F., Fiala, M., Elskens, M. and Goeyens, L., 1998. Seasonal variation of phytoplankton community structure and nitrogen uptake regime in the Indian sector of the Southern Ocean. *Polar Biology,* 20, 20, 259-272.

Meredith, M.P. and King, J.C., 2005. Rapid climate change in the ocean west of the Antarctic Peninsula during the second half of the 20th century. *Geophysical Research Letters,* 32, L19604, 1-5.

Meskhidze, N., Nenes, A., Chameides, W.L., Luo, C. and Mahowald, N., 2007. Atlantic Southern Ocean productrivity: Fertilization from above or below? *Global Biogeochemical Cycles,* 21, GB2006, 1-9.

Miller, M.F., 2002. Isotopic fractionation and quantification of ^{17}O anomalies in the oxygen three-isotope system: an appraisal and geochemical significance. *Geochimica et Cosmochimica Acta,* 66, 11,

Monterey, G.I. and Levitus, S., 1997. Climatological cycle of mixed layer depth in the world ocean. NOAA. Report, Silver Spring, Md., 5.

Montes-Hugo, M., Sweeney, C., Doney, S.C., Ducklow, H.W., Frouin, R., Martinson, D.G., Stammerjohn, S. and Schofield, O., 2010. Seasonal forcing of summer dissolved inorganic carbon and chlorophyll *a* on the western shelf of the Antarctic Peninsula. *Journal of Geophysical Research,* 115, C03024,

Moore, J.K. and Abbott, M.R., 2002. Surface chlorophyll concentrations in relation to the Antarctic Polar Front: seasonal and spatial patterns from satellite observations. *Journal of Marine Systems,* 37, 69-86.

Mountford, K., 1969. Measuring dissolved oxygen and indicator of primary productivity. *Chesapeake Science,* 10, 3 & 4, 327-330.

Mouriño-Carballido, B. and Anderson, L.A., 2009. Net community production of oxygen derived from in vitro and in situ 1-D modeling techniques in a cyclonic mesoscale eddy in the Sargasso Sea. *Biogeosciences,* 6, 1799-1810.

Müller-Karger, F., Varela, R., Thunell, R., Astor, Y., Zhang, H., Luerssen, R. and Hu, C., 2004. Processes of coastal upwelling and carbon flux in the Cariaco Basin. *Deep-Sea Research II,* 51, 927-943.

Mura, M.P., Satta, M.P. and Agustí, S., 1995. Water-mass influences on summer Antarctic phytoplankton biomass and community structure. *Polar Biology,* 15, 15-20.

Nakata, K. and Doi, T., 2006. Estimation of primary production in the ocean using a physical-biological coupled ocean carbon cycle model. *Environmental modelling and software,* 21, 204-228.

Naveira Garabato, A.C., Polzin, K.L., King, B.A., Heywood, K.J. and Visbeck, M., 2004. Widespread Intense Turbulent Mixing in the Southern Ocean. *Science,* 303, 210-213.

Nightingale, P.D., Malin, G., Law, C.S., Watson, A.J., Liss, P.S., Liddicoat, M.I., Boutin, J. and Upstill-Goddard, R.C., 2000. In situ evaluation of air-sea gas exchange parameterizations using novel conservative and volatile tracers. *Global Biogeochemical Cycles,* 14, 1, 373-387.

Noh, Y. and Lee, W., 2008. Mixed and mixing layer depths simulated by and OGCM. *Journal of Oceanography,* 64, 217-225.

Nybakken, J.W. and Bertness, M.D., 2005. Marine Biology an ecological approach. Sixth ed., San Francisco, CA: 579

Orsi, A.H., Whitworth III, T. and Nowlin, W.D.J., 1995. On the meridional extent and fronts of the Antarctic Circumpolar Current. *Deep-Sea Research I,* 42, 5, 641-673.

Perissinotto, R., Duncombe Rae, C.M., Boden, B.P. and Allanson, B.R., 1990. Vertical stability as a controlling factor of the marine phytoplankton production at the Prince Edward Archipielago (Southern Ocean). *Marine Ecology Progress Series,* 60, 205-209.

Pollard, R., Sanders, R., Lucas, M. and Statham, P., 2007. The Crozet natural iron bloom and export experiment (CROZEX). *Deep-Sea Research II: Topical Studies in Oceanography,* 54, 18-20, 1905-1914.

Pollard, R.T., Read, J.F., Allen, J.T., Griffiths, G. and Morrison, A.I., 1995. On the physical structure of a front in the Bellingshausen Sea *Deep-Sea Research II,* 42, 4-5, 955-982.

Prézelin, B.B., Hofmann, E.E., Moline, M. and Klinck, J.M., 2004. Physical forcing of phytoplankton community structure and primary production in continental shelf waters of the Western Antarctic Peninsula. *Journal of Marine Research,* 62, 419-460.

Quay, P., Emerson, S., Wilbur, D. and Stump, G., 1993. The $\delta^{18}O$ of dissolved O_2 in the surface waters of the Subarctic Pacific: a tracer of biological productivity. *Journal of Geophysical Research,* 98, C5, 8447-8458.

Quay, P.D., Peacock, C., Björkman, K. and Karl, D.M., 2010. Measuring primary production rates in the ocean: enigmatic results between incubation and non-incubation methods at station ALOHA. *Global Biogeochemical Cycles*, 24, GB3014, 1-14.

Reid, J.L., 1982. On the use of dissolved oxygen concentration as an indicator of winter convection. Naval Research Reviews, Vol. 34, 28-29.

Reuer, M.K., 2007b. Erratum to "New estimates of Southern Ocean biological production rates from O_2/Ar ratios and the triple isotope composition of O_2". *Deep-Sea Research I,* 54, 1853-1858.

Reuer, M.K., Barnett, B.A., Bender, M.L., Falkowski, P.G. and Hendricks, M.B., 2007a. New estimates of Southern Ocean biological production rates from O_2/Ar ratios and the triple isotope composition of O_2. *Deep-Sea Research I,* 54, 951-974.

Rintoul, S.R. and Trull, T.W., 2001. Seasonal evolution of the mixed layer in the Subantarctic Zone south of Australia. *Journal of Geophysical Research,* 106, C12, 31447-31462.

Robinson, C., Tilstone, G.H., Rees, A.P., Smyth, T.J., Fishwick, J.R., Tarran, G.A., Luz, B., Barkan, E. and David, E., 2009. Comparison of *in vitro* and *in situ* plankton production determinations. *Aquatic Microbial Ecology*, 54, 13-34,

Rubin, S.I., Takahashi, T., Chipman, D.W. and Goddard, J.G., 1998. Primary productivity and nutrient utilization ratios in the Pacific sector of the Southern Ocean based on seasonal changes in seawater chemistry. *Deep-Sea Research I,* 45, 1211-1234.

Sarma, V.V.S.S., Abe, O., Hinuma, A. and Saino, T., 2006a. Short-term variation of triple oxygen isotopes and gross oxygen production in the Sagami Bay, central Japan. *Limnology and Oceanography*, 51, 3, 1432-1442.

Sarma, V.V.S.S., Abe, O. and Saino, T., 2008. Spatial variations in time-integrated plankton metabolic rates in Sagami Bay using triple oxygen isotopes and O_2 : Ar ratios. *Limnology and Oceanography*, 53, 5, 1776-1783.

Sarma, V.V.S.S., Abe, O., Yoshida, N. and Saino, T., 2006b. Continuous shipboard sampling system for determination of triple oxygen isotopes and O_2/Ar ratio by dual-inlet mass spectrometry. *Rapid Communications in Mass Spectrometry*, 20, 23, 3503-3508.

Sarmiento, J.L. and Gruber, N., 2006. Ocean Biogeochemical Dynamics. ed., Princeton, USA: 503

Sarmiento, J.L., Hughes, T.M.C., Stouffer, R.J. and Manabe, S., 1998. Simulated response of the ocean carbon cycle to anthropogenic climate warming. *Nature*, 393, 6682, 245.

Sarmiento, J.L. and Le Quéré, C., 1996. Oceanic carbon dioxide uptake in a model of century-scale global warming. *Science*, 274, 1346-1350.

Sarmiento, J.L. and Orr, J.C., 2001. Three-dimensional ocean model simulations of the impact of Southern Ocean nutrient depletion on atmospheric CO_2 and ocean chemistry. *Limnology and Oceanography*, 36, 1928-1950.

Schmitz Jr., W.J., 1996. On the World Ocean Circulation: Volume I, Some Global Features/North Atlantic Circulation. ed., Technical Report WHOI-96-03, 141

Serebrennikova, Y.M. and Fanning, K.A., 2004. Nutrients in the Southern Ocean GLOBEC region: variations, water circulation, and cycling. *Deep Sea Research Part II*, 51, 1981-2002.

Shulenberger, E. and Reid, J.L., 1981. The Pacific shallow oxygen minimum, deep chlophyll maximum, and primary productivity, reconsidered. *Deep-Sea Research*, 28, 901-919.

Smith, D.A., Hofmann, E.E., Klinck, J.M. and Lascara, C.M., 1999. Hydrography and circulation of the West Antarctic Peninsula Continental Shelf. *Deep Sea Research I*, 46, 925-949.

Smith, R.C., Baker, K.S. and Vernet, M., 1998. Seasonal and interannual variability of phytoplankton biomass west of the Antarctic Peninsula. *Journal of Marine Systems*, 17, 229-243.

Smith, R.C., Martinson, D.G., Stammerjohn, S., Iannuzzi, R.A. and Ireson, K., 2008a. Bellingshausen and western Antarctic Peninsula region: Pigment biomass and sea-ice spatial/temporal distributions and interannual variability. *Deep-Sea Research II*, 55, 1949-1963.

Smith, W.O. and Comiso, J.C., 2008b. Influence of sea ice on primary production in the Southern Ocean: A satellite perspective. *Journal of Geophysical Research*, 113, C05S93, 1-19.

Smith, W.O., Marra, J., Hiscock, M.R. and Barber, R., 2000. The seasonal cycle of phytoplankton biomass and primary productivity in the Ross Sea, Antarctica. *Deep-Sea Research II*, 47, 3119-3140.

Smith, W.O., Shields, A.R., Dreyer, J.C., Peloquin, J.A. and Asper, V., 2011. Interannual variability in vertical export in the Ross Sea: Magnitude, composition, and environmental correlates. *Deep-Sea Research I*, 58, 147-159.

Sohrin, Y., Iwamoto, S., Mtsui, M., Obata, H., Nakayama, E., Suzuki, K., Handa, N. and Ishii, M., 2000. The distribution of Fe in the Australian sector of the Southern Ocean. *Deep-Sea Research I*, 47, 55-84.

Sokolov, S. and Rintoul, S.R., 2007. On the relationship between fronts of the Antarctic Circumpolar Current and surface chlorophyll concentrations in the Southern Ocean. *Journal of Geophysical Research*, 112, C07030, 1-17.

Sokolov, S. and Rintoul, S.R., 2009. Circumpolar structure and distribution of the Antarctic Circumpolar Current fronts: 1. Mean circumpolar paths. *Journal of Geophysical Research,* 114, C11018, 1-19.

Speer, K., Rintoul, S.R. and Sloyan, B., 2000. The diabatic Deacon cell. *Journal of Physical Oceanography,* 30, 3212-3222.

Sprintall, J., 2003. Seasonal to interannual upper-ocean variability in the Drake Passage. *Journal of Marine Research,* 61, 27-57.

Stramma, L., Johnson, G.C., Sprintall, J. and Mohrholz, V., 2008. Expanding oxygen-minimum zones in the tropical oceans. *Science,* 320, 655-658.

Swain, D., Ali, M.M. and Weller, R.A., 2006. Estimation of mixed-layer depth from surface parameters. *Journal of Marine Research,* 64, 745-758,

Sweeney, C., Gloor, E., Jacobson, A.R., Key, R.M., McKinley, G., Sarmiento, J.L. and Wanninkhof, R., 2007. Constraining global air-sea gas exchange for CO_2 with recent bomb ^{14}C measurements. *Global Biogeochemical Cycles,* 21, GB2015, 1-10.

Sweeney, C., Hansell, D.A., Carlson, C.A., Codispoti, L.A., Gordon, L.I., Marra, J., Millero, F.J., W.O., S. and Takahashi, T., 2000. Biogeochemical regimes, net community production and carbon export in the Ross Sea, Antarctica. *Deep-Sea Research II,* 47, 3369-3394.

Talley, L., 1999. Some aspects of ocean heat transport by the shallow, intermediate and deep overturning circulations, Clark, P.U., Webb, R.S. and Keigwin, L.D. In: Mechanisms of Global Climate Change at Millennial Time Scales, 112 Washington, D.C.,

Tans, P.P., Conway, T.J. and Nakazawa, T., 1990. Latitudinal distribution of the sources and sinks of atmospheric transport model. *Journal of Geophysical Research,* 94, 5151-5172.

Thiemens, M.H., 2001. The mass-independent ozone isotope effect. *Science,* 293, 5528.

Thiemens, M.H. and Heidenreich III, J.E., 1983. The mass-independent fractionation of oxygen: a novel isotope effect and its possible cosmochemical implications. *Science,* 219, 1073-1075.

Thompson, A.F., Gille, S.T., MacKinnon, J.A. and Sprintall, J., 2007. Spatial and Temporal Patterns of Small-Scale Mixing in Drake Passage. *Journal of Physical Oceanography,* 37, 572-592.

Thomson, R.E. and Fine, I.V., 2003. Estimating mixed layer depth from oceanic profile data. *Journal of Atmospheric and Oceanic Technology,* 20, 319-329.

Toggweiler, J.R., Russell, J.L. and Carson, S.R., 2006. Midlatitude westerlies, atmospheric CO_2, and climate change during the ice edges. *Paleoceanography,* 21, PA2005, 1-15.

Tomckzak, M. and Godfrey, J.S., 1994. Regional Oceanography: An introduction. ed., London, Great Britain: Elsevier Science Ltd., 382

Tortell, P.D., 2005a. Dissolved gas measurements in oceanic waters made by membrane inlet mass spectrometry. *Limnology and Oceanography: Methods,* 3, 24-37.

Tortell, P.D., 2005b. Small scale-heterogeneity of dissolved gas concentrations in marine continental shelf waters. *Geochemistry Geophysics Geosystems,* 6, 11, Q11M04, doi:10.1029/2005GC000953.

Tortell, P.D. and Long, M.C., 2009. Spatial and temporal variability of biogenic gases during the Southern Ocean spring bloom. *Geophysical Research Letters,* 36, L01603, 1-5.

Turner, D.R. and Owens, N.J.P., 1995. A biogeochemical study in the Bellingshausen Sea: overview of the STERNA 1992 expedition. *Deep-Sea Research II,* 42, 4-5, 907-932.

Urey, H.C., 1947. The thermodynamic properties of isotopic substances. *Journal of the Chemical Society,* 562-581.

Verdy, A., Dutkiewicz, S., Follows, M.J., Marshall, J. and Czaja, A., 2007. Carbon dioxide and oxygen fluxes in the Southern Ocean: Mechanisms of interannual variability. *Global Biogeochemical Cycles,* 21, GB2020, 1-10.

Vernet, M., D. Martinson, R. Iannuzzi, S. Stammerjohn, W. Kozlowiski, K. Sines, R. Smith and Garibotti, I., 2008. Primary production within the sea-ice zone west of the Antarctic Peninsula: I-Sea ice, summer mixed layer, and irradiance. *Deep-Sea Research II,* 55, 2068-2085.

Wallace, M.I., Meredith, M.P., Brandon, M.A., Sherwin, T.J., Dale, A. and Clarke, A., 2008. On the characteristics of internal tides and coastal upwelling behaviour in Marguerite Bay, west Antarctic Peninsula. *Deep-Sea Research II,* 55, 2023-2040.

Wanninkhof, R., 1992. Relationship between wind speed and gas exchange over the ocean. *Journal of Geophysical Research,* 97, C5, 7373-7382.

Watson, A.J. and Naveira, G.A.C., 2006. The role of Southern Ocean mixing and upwelling in glacial-interglacial atmospheric CO_2 change. *Tellus,* 58B, 73-87.

Weiss, R.F., 1970. The solubility of nitrogen, oxygen and argon in water and seawater. *Deep-Sea Research* 17, 4, 721-735.

Whitworth III, T., A.H. Orsi, A.J. Kim and Nowlin, W.D.J., 1995. Water masses and mixing near the Antarctic Slope Front. Ocean, ice and atmosphere: interactions at the Antarctic continental margin. *Antarctic Research Series*, 75, 1-27.

Whitworth III, T., Orsi, A.H., Kim, S.J. and Nowlin, W.D.J., 1998. Water masses and mixing near the Antarctic Sope Front. ed., Ocean, Ice and Atmosphere: Interactions at the Antarctic Continental Margin, AGU Antarctic Research Series, 1-27

Williams, G.D., Nicol, S., Raymond, B. and Meiners, K., 2008. Summertime mixed layer development in the marginal sea ice zone off the Mawson coast, East Antarctica. *Deep-Sea Research II*, 55, 365-376.

Williams, P.J.l., 1998. The balance of plankton respiration and photosynthesis in the open oceans. *Nature*, 394, 55-57,

Wong, G.T.F. and Li, K.Y., 2009. Winkler's method overestimates dissolved oxygen in seawater: Iodate interference and its oceanographic implications. *Marine Chemistry*, 115, 86-91.

Yelland, M.J., Moat, B.I., Pascal, R.W. and Berry, D.I., 2002. CFD Model estimates of the airflow distortion over research ships and the impact on momentum flux measurements. *Journal of Atmospheric and Oceanic Technology*, 19, 1477-1499.

Zawada, D.G., Roland, J., Zaneveld, V. and Boss, E., 2005. A comparison of hydrographically and optically derived mixed layer depths. *Journal of Geophysical Research*, 110, C11001, 1-13.

Zhang, B. and Klinck, J.M., 2008. The effect of Antarctic Circumpolar Current transport on the frontal variability in Drake Passage. *Dynamics of Atmospheres and Oceans*, 45, 208 - 228.

Zhou, M., Zhu, Y., Dorland, R.D. and Measures, C.I., 2010. Dynamics of the current system in the southern Drake Passage. *Deep Sea Research I, In press*,